Vibrational effects in quantum transport through single-molecule junctions



Jakub K. Sowa

Hertford College

University of Oxford

A thesis submitted for the degree of

Doctor of Philosophy

Hilary Term 2019

Abstract

Vibrational effects in quantum transport through single-molecule junctions

Jakub K. Sowa

Herford College, University of Oxford

A thesis submitted for the degree of
Doctor of Philosophy

Hilary term 2019

This thesis is concerned with vibrational effects in resonant charge transport through molecular junctions. The first research chapter examines the role of non-equilibrium vibrational dynamics in charge transport through a molecular double quantum dot. We demonstrate that non-equilibrium vibrational effects in such a system can result in current suppression and negative differential conductance. The second research chapter describes how vibrational dynamics can be incorporated into the theoretical description of molecular junctions based on a Pariser-Parr-Pople Hamiltonian. As a case study, we consider a prototypical spiro-conjugated molecular junction. We demonstrate that the transport properties of this system are governed by an interplay between destructive quantum interference and Jahn-Teller distortion (an effect of vibronic origin). In the next chapter, we examine the role of collective vibrational coupling in charge transport through a two-site molecular system akin to the one considered in the first research chapter. We demonstrate that such interactions can significantly enhance the efficiency of transport through such a system, and also take this opportunity to analyse various theoretical descriptions of electron-vibrational interactions commonly used in the transport setting. In the fourth research chapter, we consider a single-site molecular system coupled to a collection of thermalised vibrational modes. We formulate a relatively simple yet powerful theoretical framework describing charge transport through such a system. We recover the Marcus and Landauer-Büttiker theories of transport in the limit of high-temperature and vanishing electron-vibrational coupling, respectively. We further show how lifetime broadening can be consistently incorporated into Marcus theory, and we derive a low-temperature correction to the semi-classical Marcus hopping rates. In the last research chapter, elements of this framework are applied to experimental measurements of charge transport through zinc-porphyrin molecular junctions. This joint experimental-theoretical study provides, for the first time, a full understanding of the resonant transport regime of graphene-based molecular junctions.

Acknowledgements

First and foremost, I must thank my supervisors Erik Gauger, Jan Mol, and Andrew Briggs for their support and encouragement over the last three and a half years. I am especially grateful to Erik who has been supervising my work all the way from Edinburgh. If it weren't for you, Erik, I would have probably been forced to become an experimentalist (with detrimental effects on my mental health and potentially the physical well-being of others). I would like to further thank Jan for always keeping me on track of what's experimentally relevant, and to him and Erik for proof-reading my thesis. I am also grateful to Andrew for the special interest he took in my future academic career.

Secondly, I would like to acknowledge my experimental collaborators: James Thomas, Bart Limburg, Achim Harzheim, and Harry Anderson. Putting one's theory into practice is a rather satisfying task and I am very grateful to you for giving me the opportunity of doing so.

In the words of Rudolph Marcus whose name will keep appearing on the pages of this thesis: *Oxford is just wonderful!* I wish to express in this place my gratitude to Claire Vallance for inviting me nearly eight years ago to pursue my undergraduate degree here in Oxford. I would also like to thank her and Peter Hore for their continued support over the years.

For comments on the publications that have arisen from this work I wish to thank Colin Lambert, Roald Hoffmann, Neill Lambert, Marc Garner, James Thomas, Bart Limburg, Pascal Gehring, and Rudolph Marcus.

I would also like to recognise here the entire Wolfson crew: Adam, Grace, Holly, Joie, Katie, Kerstin, Kevin, Lucho, Maryam and Sarah for their support and the time spent together. My special thanks, however, go to Lesley MacGregor who unsolicitedly proof-read this entire D.Phil thesis – in no way could I have hoped for a better friend.

Finally, I would like to thank my family, my parents and my sister, for twenty-seven years of love and support. None of this would have been possible without you.

List of publications

This thesis is based on the following publications:

Chapter 4: [1] *Vibrational effects in charge transport through a molecular double quantum dot.* J. K. Sowa, J. A. Mol, G. A. D. Briggs, E. M. Gauger, *Phys. Rev. B*, 95, 085423 (2017).

Author contributions: JKS conceived the study, derived the analytical results, performed the calculations, and wrote the manuscript with input from EMG. JKS, JAM, and EMG discussed the results. JAM, GADB, and EMG commented on the manuscript.

Chapter 5: [2] *Spiro-conjugated molecular junctions: between Jahn-Teller distortion and destructive quantum interference.* J. K. Sowa, J. A. Mol, G. A. D. Briggs, E. M. Gauger, *J. Phys. Chem. Lett.* 2018, 9, 1859–1865.

Author contributions: JKS conceived the study, performed the calculations, and wrote the manuscript. JKS, JAM, GADB and EMG discussed the results. JAM, GADB, and EMG commented on the manuscript.

Chapter 6: [3] *Environment-assisted quantum transport through single-molecule junctions.* J. K. Sowa, J. A. Mol, G. A. D. Briggs, E. M. Gauger, *Phys. Chem. Chem. Phys.*, 19, 29534–29539 (2017).

Author contributions: JKS conceived the study, derived the analytical results, performed the calculations, and wrote the manuscript. JKS, JAM, and EMG discussed the results. JAM, GADB, and EMG commented on the manuscript.

Chapter 7: [4] *Beyond Marcus theory and the Landauer-Büttiker approach in molecular junctions: A unified framework.* J. K. Sowa, J. A. Mol, G. A. D. Briggs, E. M. Gauger, *J. Chem. Phys.*, 149, 15, 154112 (2018). **Editor's Pick**.

Author contributions: JKS conceived the study, derived the analytical results, performed the calculations, and wrote the manuscript. JKS, JAM, and EMG discussed the results. JAM, GADB, and EMG commented on the manuscript.

Chapter 8: [5] *Understanding resonant charge transport through single-molecule junctions.* J. O. Thomas, B. Limburg, J. K. Sowa†, K. Willick, J. Baugh, G. A. D. Briggs, E. M. Gauger, H. L. Anderson, J. A. Mol, Manuscript submitted to *Nature Communications*.

Author contributions: JOT, BL, JKS, and JAM conceived the study. JOT and BL synthesised the porphyrin compounds, and performed the experiments. JOT, BL, and KW fabricated the devices. JKS developed the theoretical approach. JKS and BL analysed the data. JOT performed the DFT calculations. JOT, BL, JKS, and JAM wrote the manuscript. All authors discussed the results and commented on the manuscript.

The following publications were also produced during the doctoral training, but are not covered in great detail in this thesis:

[6] *Distinguishing lead and molecule states in graphene-based single-electron transistors* P. Gehring, J. K. Sowa, J. Cremers, Q. Wu, H. Sadeghi, Y. Sheng, J. H. Warner, C. J. Lambert, G. A. D. Briggs, and J. A. Mol, *ACS Nano*, 11, 5 4739–4745 (2017).

[7] *Marcus theory of thermoelectricity in molecular junctions* J. K. Sowa, J. A. Mol, and E. M. Gauger, *J. Phys. Chem. C*, 123, 4103–4108 (2019).

[8] *Thermoelectric characterisation of electroburnt graphene quantum dots* A. Harzheim, J. K. Sowa, J. L. Swett, G. A. D. Briggs, J. A. Mol, and P. Gehring, *Manuscript in preparation.*

[9] *Charge-state assignment of nanoscale single-electron transistors from their current-voltage characteristics* B. Limburg, J. O. Thomas, J. K. Sowa, K. Willick, J. Baugh, E. M. Gauger, G. A. D. Briggs, J. A. Mol, and H. L. Anderson, *Manuscript in preparation.*

† – joint-first authorship

The text in this thesis was written exclusively by the author.

Contents

1 Introduction **1**

1.1 Outline 2

2 Theoretical background **5**

2.1 Charge transport through nanostructures 6

2.2 The quantum-mechanical description 9

2.3 Electron-vibrational dynamics 17

2.4 Density matrix formalism 22

2.5 Quantum master equations 23

2.6 Observables & Full counting statistics 27

3 Experimental studies on single-molecule junctions **32**

3.1 Overview of experimental techniques 33

3.2 Transport properties of molecular junctions 37

3.3 Vibrational effects in off-resonant regime 39

3.4 Vibrational effects in resonant regime 40

3.5 Current noise 44

4 Double quantum dot: non-equilibrium vibrational effects **46**

4.1 Theoretical model 47

4.2 Results and Discussion 54

4.3 Conclusions 63

5 Pariser-Parr-Pople-based approach **65**

5.1 Pariser-Parr-Pople Hamiltonian 66

5.2 The case study: Spiro[4.4]nonatetraene 67

5.3 Electronic transport properties 71

5.4 Jahn–Teller distortion 75

5.5 Symmetry breaking 79

5.6 Conclusions 81

6 Environment-assisted quantum transport **82**
6.1 Theoretical model 83
6.2 Quantum master equations 86
6.3 Results 95
6.4 Conclusions 105

7 Collective vibrational effects: Theory **106**
7.1 Model 107
7.2 Derivation 109
7.3 Comparison with NEGF 115
7.4 Microscopically-motivated coupling 118
7.5 High(er)-temperature limits 122
7.6 Conclusions 133

8 Collective vibrational effects: Experimental evidence **134**
8.1 Zinc-porphyrin molecular junctions 135
8.2 Deviation from the single-level model 137
8.3 Inelastic resonant charge transport 140
8.4 Conclusions 151

9 Conclusions **153**

A Displacement operators **156**

B Hansson-Stafström parametrisation **158**

C Phononic correlation functions **160**

Bibliography **162**

Chapter 1

Introduction

You'll have a hard time, but you'll do OK.

— Steven Weinberg

Over forty years ago, in a work that would subsequently lead to the development of an entirely new field of molecular electronics, Aviram and Ratner envisioned the possibility of constructing a single-molecule rectifier [10]. The proposed device comprised a single (donor–acceptor) molecule spanning a gap between two metallic electrodes. Due to the energetic mismatch between the donor and acceptor sites, it was designed to allow for current flow only in one direction and thus exhibit rectifying behaviour.

Practical realisations of such devices (single-molecule junctions) had not been technically possible until the development of the scanning tunnelling microscope (STM) which emerged a decade later [11]. Since then a number of ways of fabricating single-molecule devices have been developed [12]. Following a series experimental breakthroughs that occurred at the turn of the millennium [13–18], molecular electronics entered the mainstream of physical sciences, and is now a vibrant and fast-paced field.

Before proceeding further, as with any scientific endeavour, we must ask the question: *why?* Why should we devote our time and resources (not to mention the taxpayers money!) to this particular branch of science? In the case of molecular electronics the

answer is two-fold. First and foremost, single-molecule junctions allow us to study molecular systems from a fundamentally novel perspective. The molecular structures are investigated in an unusual heterogeneous environment (sandwiched or suspended between two metallic electrodes) and by radically different means (for instance, by measuring the junction conductance or thermoelectric properties). Secondly, as first suggested by Aviram and Ratner, molecular junctions could form a basis of functional electronic circuits. While the idea of single-molecule transistors, for example, outperforming their silicon counterparts still remains rather far-fetched, other directions of development, such as thermoelectric materials based on self-assembled monolayers of molecular compounds, may eventually give rise to practical technologies.

This Thesis focuses predominantly on the role of the electron-vibrational (electron-phonon) coupling in the resonant transport through single-molecule junctions. As we shall demonstrate, these interactions significantly affect the transport properties of molecular junctions, and it is therefore necessary to analyse in detail the role they play in single-molecule devices.

1.1 Outline

We start in Chapter 2 by outlining the basics of mesoscopic transport theory. We also discuss the origin of electron-vibrational interactions in molecular systems and derive the electron-vibrational coupling Hamiltonian. We then give the general introduction to the theory of open quantum systems, derive the (Born-Markov) second-order quantum master equation, and introduce the concept of full counting statistics.

Chapter 3 gives a general overview of experimental studies on molecular junctions. We discuss the techniques used to fabricate single-molecule junctions, and their transport properties. Special emphasis is placed on the observations and evidence of vibrational effects in these systems.

In the first research chapter, Chapter 4, we study transport properties of a two-site (double quantum dot) system in which both sites interact with a single vibrational

mode. We examine the effects of non-equilibrium vibrational dynamics on the behaviour of this model system and demonstrate that intra-molecular dynamics can play a surprisingly large role in such extended molecular systems.

Chapter 5 discusses how the microscopic details of the molecular system can be included in the theoretical description of the junction. This is done by employing the celebrated Pariser-Parr-Pople Hamiltonian which enables us to go beyond the phenomenological 'site' models. As a case-study for this approach, we investigate charge transport through a prototypical spiro-conjugated molecular junction. It is demonstrated that the unusual electronic structure of the considered system results in a complete destructive interference between its doubly-degenerate electronic levels. Populating these levels, however, results in Jahn-Teller distortion – an effect of a vibronic origin. In this context, it is demonstrated how electron-vibrational interactions can be included in the above approach. Finally, the interplay between destructive quantum interference effects and dynamic Jahn-Teller distortion is analysed in detail.

In Chapter 6 we move to consider the effects of coupling of the electronic degrees of freedom to thermalised phonon baths. In this context, we again study charge transport through a two-site molecular system but assume that two sites interact with separate thermalised vibrational environments. It is demonstrated that such interaction can significantly enhance the efficiency of charge transport through the molecular junction in an analogy to the phenomenon of environment-assisted quantum transport.

In Chapter 7 we return to a single-site model described in Chapters 2 and 3. It is shown how one can go beyond the previously used second-order (Born-Markov) approximation and incorporate lifetime broadening in the theoretical description of the junction. Assuming coupling to a thermalised collection of vibrational modes, we arrive at a relatively compact expression for the resonant current flowing through the junction. We then consider higher-temperature limits of this original result and demonstrate that at high temperature our result can be reduced to the well-known Marcus theory. We further demonstrate how lifetime broadening and low-temperature corrections can be incorporated into Marcus theory.

In Chapter 8, elements of the above framework are applied to experimental measurements of charge transport through zinc-porphyrin molecular junctions. It is demonstrated that the conventional (non-interacting Landauer-Büttiker and classical Marcus) approaches fail to describe the empirically-observed transport behaviour. Conversely, the theoretical approach developed in the previous chapter yields an excellent agreement with the experimental measurements, highlighting the importance of the quantum-mechanical nature of the electron propagation and the nuclear dynamics in single-molecule transistors.

Since every chapter of this thesis considers somewhat different model system, in order to avoid any confusion, any non-obvious notation is defined separately in each of them. Furthermore, each of the research chapters is accompanied by its own conclusion section. The overall conclusions of this thesis are briefly discussed in Chapter 9.

Chapter 2

Theoretical background

I had finally come to the point where I thought it was alright if a student knew more about Fourier transforms than about stopcock grease.

— Edgar Bright Wilson

In this chapter, we will discuss the theory behind charge transport through nanoscopic systems and single-molecule junctions in particular. We begin with the electrostatic considerations of nanostructures studied in a transport setting and proceed to discuss their quantum-mechanical description. We then derive an electron-phonon coupling Hamiltonian and discuss the polaron (Lang-Firsov) transformation. We also discuss the nature of the vibrational environment in single-molecule junctions and the Franck-Condon description of electronic-vibrational transitions.

Next, we introduce the density-matrix formalism and introduce basic concepts of the theory of open quantum systems, including a derivation of the second-order quantum master equation (within the Born-Markov approximation). This chapter is concluded with a brief discussion of full counting statistics and relevant observables considered in the quantum transport studies.

2.1 Charge transport through nanostructures

Quantum dots (QDs), artificial solid-state structures which can accommodate additional electrons or holes, in many ways bear significant resemblance to molecular systems. They often possess discrete electronic structure, their electronic degrees of freedom are coupled to a vibrational environment, and finally (in an analogy to single-molecule junctions) QDs can also be considered in a transport setting [19]. The field of single-molecule electronics has therefore hugely benefited from developments in the field of nanoscopic physics [20–23], many of which have taken place more than a decade prior to the seminal works in the field of molecular electronics discussed in Chapter 1. We therefore begin this chapter with a brief overview of transport properties of quantum dots.

In what follows, we consider a quantum dot in a three-terminal setting: capacitatively coupled to the source, drain and gate electrodes (with capacitances C_s, C_d and C_g, respectively), and electronically coupled to the source and drain electrodes as schematically shown in Figure 2.1. It will be useful to introduce the electrostatic aspects of charge transport through quantum dots using the so-called constant interaction model. In what follows, we will closely follow Ref. [19]. Within this approach it is assumed that the interactions between electrons are parametrised solely by the total capacitance C:

$$C = C_\mathrm{s} + C_\mathrm{d} + C_\mathrm{g} \ , \tag{2.1}$$

and that the single-particle energy spectrum is independent of electron-electron interactions (and therefore also of the total number of the electrons on the quantum dot, N). The total energy of the dot populated with N electrons is determined by the applied source (V_s), drain (V_d), and gate (V_g) voltages:

$$U(N) = \frac{[e(N - N_0) + C_\mathrm{s}V_\mathrm{s} + C_\mathrm{d}V_\mathrm{d} + C_\mathrm{g}V_\mathrm{g}]^2}{2C} + \sum_{n=1}^{N} E_n \ . \tag{2.2}$$

In the above, e is the electron charge, N_0 is the number of positive background charges.

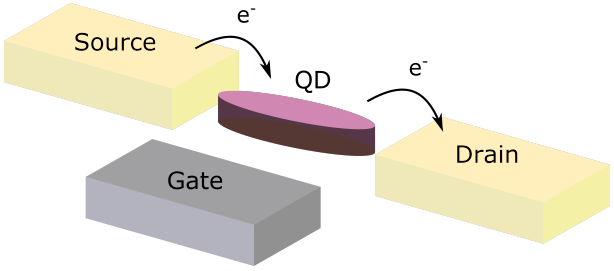


Figure 2.1: Schematic illustration of a three-terminal quantum dot setup.

The first term on the right-hand-side of Eq. (2.2) accounts for the electrostatic electron-electron repulsion, while the final term is simply a sum over the occupied single-particle energy levels. The electrochemical potential for the transition between the N-electron and the $(N-1)$-electron states is then given by:

$$\mu(N) = U(N) - U(N-1) = E_{\mathrm{C}}\left(N - N_0 - \frac{1}{2}\right) - \frac{E_{\mathrm{C}}}{e}\left(C_{\mathrm{s}}V_{\mathrm{s}} + C_{\mathrm{d}}V_{\mathrm{d}} + C_{\mathrm{g}}V_{\mathrm{g}}\right) + E_N \ , \tag{2.3}$$

where $E_{\mathrm{C}} = e^2/C$ is the charging energy. It is important to note that the electrochemical potential $\mu(N)$ varies linearly with the gate voltage V_{g}. It is also useful to define the so-called addition energy E_{add} which corresponds to the spacing between electrochemical potentials for successive transitions:

$$E_{\mathrm{add}}(N) = \mu(N+1) - \mu(N) = E_{\mathrm{C}} + \Delta E \ . \tag{2.4}$$

As can be seen above, it is given by a sum of the charging energy E_{C}, and the spacing between the discrete single-particle energy levels, ΔE.

What transport properties are predicted by the constant interaction model? The sequential electron transport through the quantum dot can only take place when the electron states in one of the leads (which are aligned with the electrochemical potential of the QD) are filled whereas the electron states in the other lead are empty. Therefore the current flows whenever the electrochemical potential of the quantum dot $\mu(N)$ can be found between those of the source μ_{s} and drain μ_{d} electrodes (i.e. within the bias window).[1] The latter are determined by the applied bias voltage V_{b} where $\mu_{\mathrm{s}} - \mu_{\mathrm{d}} =$

[1]Naturally, this statement is strictly valid only in the limit of low temperature and weak QD-lead

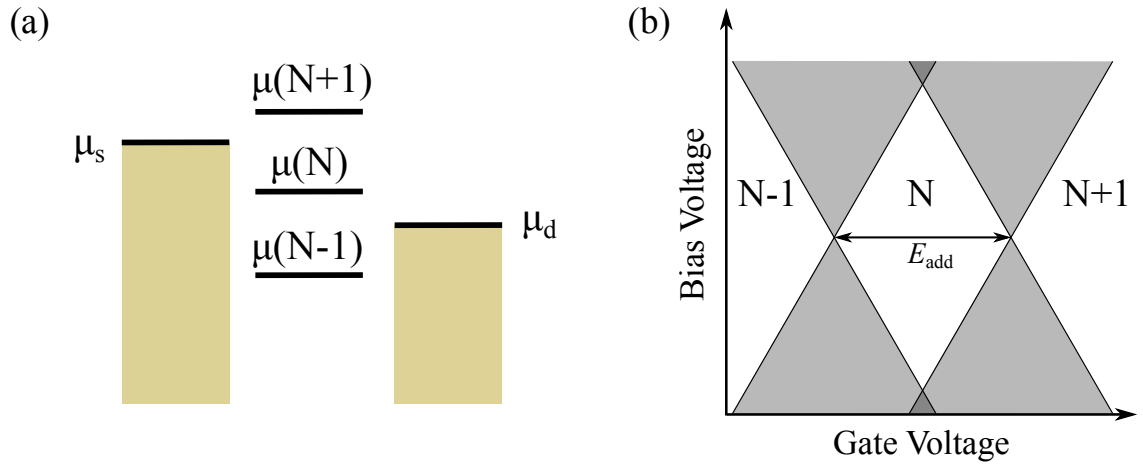


Figure 2.2: (a) Schematic energy diagram of a quantum dot in the sequential tunnelling regime: $\mu_{\rm s} > \mu(N) > \mu_{\rm d}$. (b) Schematic illustration of a stability diagram of a quantum dot. Shaded regions corresponds to regions of sequential tunnelling (high electric current). $E_{\rm add}$ is the addition energy, as given in Eq. (2.4).

$|e|V_{\rm b}$. This is schematically shown in Figure 2.2(a). Otherwise, the charge state of the QD remains fixed as the electron tunnelling onto the dot cannot take place and the system is found in what is known as the *Coulomb blockade* [21, 24]. A measurement of electric current flowing through the QD while simultaneously varying the bias and gate voltages is known as a *charge stability diagram*. The phenomenon of Coulomb blockade is typically observed in the stability diagrams as diamond-shaped regions of low electric conductance (*Coulomb diamonds*), see Figure 2.2(b).

Furthermore, we can use the constant interaction model to determine the slopes of the edges of the Coulomb diamonds: $\mathrm{d}(-|e|V_{\rm b})/\mathrm{d}V_{\rm g}$, as schematically pictured in Figure 2.2(b). Experimentally, one typically sets $V_{\rm d} = 0$ and therefore, using Eq. (2.3), the two slopes are given (in terms of the capacitances) by $-|e|C_{\rm g}/(C - C_{\rm s})$ and $|e|C_{\rm g}/C_{\rm s}$, respectively. We note however that throughout this thesis (with the exception of Chapter 8 where we will model experimental studies on zinc-porphyrin transistors) we shall assume that $C_{\rm s} = C_{\rm d} \gg C_{\rm g}$. Within the wide-band approximation, this will simply correspond to applying the bias voltage symmetrically: $\mu_l = \pm eV_{\rm b}/2$ where $l = \mathrm{s}, \mathrm{d}$.

It is clear from the above considerations that Coulomb blockade in transport through nanoscopic systems can arise whenever the charging energy $E_{\rm add}$ of the quantum dot

interactions.

exceeds the thermal energy $k_{\mathrm{B}}T$ and the strength of the dot-lead coupling – technically, charge quantisation is the only prerequisite for observing the Coulomb blockade. In molecular systems, however, the final term in Eq. (2.4) can often dominate.

While the constant interaction model explains the phenomenon of Coulomb blockade and constitutes a useful framework for describing the electrostatic behaviour of nanoscopic systems, it does not capture many of the intricacies of molecular systems. In particular, one should expect the assumption of an N-independent single-particle energy spectrum to break down in the case of molecular junctions (*c.f.* Chapter 5 where this problem will be approached more rigorously using a many-body electronic Hamiltonian).

2.2 The quantum-mechanical description

Throughout this thesis, we will investigate a range of molecular junctions each described by a distinct Hamiltonian. Systems studied in this thesis can be all described however by a Hamiltonian which can be generally written as:

$$H = H_{\mathrm{e}} + H_{\mathrm{vib}} + H_{\mathrm{lead}} + H_{\mathrm{e-vib}} + H_{\mathrm{tun}} \ . \tag{2.5}$$

The first three terms on the right-hand side of Eq. (2.5) describe the individual subsystems: H_{e} describes the electronic degrees of freedom of the molecule, H_{vib} accounts for the relevant vibrational modes (phononic environment), and H_{lead} describes the source and drain electrodes (leads). $H_{\mathrm{e-vib}}$ represents the electron-vibrational interactions, H_{tun} is the molecule-lead coupling (tunnelling) Hamiltonian.

2.2.1 Electronic Hamiltonians

Generally speaking, and disregarding the spin degrees of freedom, the full molecular Hamiltonian can be written directly as a sum of terms describing the kinetic energy of the electrons and the nuclei and potential energy associated with the electron-electron,

electron-nuclear, and nuclear-nuclear electrostatic interactions [25]. Throughout this thesis, we will be working within the Born-Oppenheimer approximation which allows us to separate the electron and nuclear dynamics (see more detailed discussion in Section 2.2.3).

We are generally interested in a transition between two (N and $N+1$) charge states. Typically, the N-charge states will correspond to the neutral molecular species and it is therefore useful to define it as the electronic reference state (which will depend parametrically on the nuclear positions $\mathbf{R}$). In the second-quantisation notation, it can be written as:

$$|\Psi_{\text{ref}}(\mathbf{R})\rangle = \prod_h a_h^\dagger(\mathbf{R})|0\rangle, \tag{2.6}$$

where $|0\rangle$ is the vacuum (zero-particle) state, $a_h^\dagger(\mathbf{R})$ is a fermionic creation operator for an electron in the state h, and the product in Eq. (2.6) runs over the occupied levels of the reference state. We can now write the molecular electronic Hamiltonian [defined with respect to that reference state in Eq. (2.6) and limited to the $N+1$ charge state] simply as [26]:

$$H_{\text{elec}}(\mathbf{R}) = \sum_i \varepsilon_i(\mathbf{R})\, a_i^\dagger(\mathbf{R}) a_i(\mathbf{R}) \ , \tag{2.7}$$

where $a_i^\dagger(\mathbf{R})$ ($a_i(\mathbf{R})$) is the fermionic creation (annihilation) operator for an electron in orbital i with energy $\varepsilon_i(\mathbf{R})$ which all parametrically depend on $\mathbf{R}$. It will be useful however (see Section 2.2.3) to define the electronic Hamiltonian evaluated for the equilibrium nuclear positions $\mathbf{R} = \mathbf{R_0}$:

$$H_{\text{e}} = \sum_i \varepsilon_i\, a_i^\dagger a_i \ , \tag{2.8}$$

where, for simplicity, we have dropped the parametrical dependence on the nuclear positions. Since the Hamiltonian in Eq. (2.8) is given with respect to the ground state of the N charge state, ε_i should be more rigorously understood as the chemical potential for the transition between the ground state of N charge state and the i-level in the $N+1$ charge state. Naturally, additional charge states can be incorporated

within the Fock space spanned by the electronic Hamiltonian. That would require simply including additional electron-electron repulsion terms in Eq. (2.8) but is largely unnecessary for the purposes of this thesis. An alternative, although largely equivalent, way in which one can construct a many-body molecular electronic Hamiltonian will be discussed in Chapter 5.

The source and drain electrodes are described as reservoirs of non-interacting electron gases. They are therefore governed by the Hamiltonian:

$$H_{\text{lead}} = \sum_{l=\text{s,d}} \sum_{k_l} \epsilon_{k_l} \, c_{k_l}^\dagger c_{k_l} \ , \tag{2.9}$$

where k_l denotes the energy levels within the lead l, and $c_{k_l}^\dagger$ and c_{k_l} are the (fermionic) creation and annihilation operators for an electron in the lead l with energy ϵ_{k_l}, respectively. They obey the fermionic anticommutation relation:

$$\{c_n, c_m^\dagger\} = \delta_{nm} \ ; \tag{2.10}$$

$$\{c_n^\dagger, c_m^\dagger\} = \{c_n, c_m\} = 0 \ . \tag{2.11}$$

The electrodes are typically mesoscopic objects and significantly larger than the molecular structure of interest. One can therefore safely assume them to be in a thermal equilibrium state. The electron occupation number in the electrode l is then given by the Fermi-Dirac distribution:

$$f_l(\epsilon) = \frac{1}{e^{(\epsilon - \mu_l)/k_{\text{B}}T} + 1} \ , \tag{2.12}$$

where μ_l is the chemical potential determined by the applied bias voltage, as discussed in the previous section.

The origin of the tunnelling Hamiltonian H_{tun} can be traced to the spatial overlap between the molecular orbitals and the conduction band states of the metallic electrodes. This results in a hybridisation of the molecular and electrode states which is

described by the following off-diagonal Hamiltonian:

$$H_{\text{tun}} = \sum_{l=\text{s,d}} \sum_{k_l} \left(V_{k_l}\, c_{k_l}^{\dagger} a_l + \text{H.c.} \right) \ . \tag{2.13}$$

The linear coupling term given above describes the coupling between the molecular orbitals and a continuum of energy levels in the leads with the strength V_{k_l} and has exactly the same ubiquitous form as it is present, for instance, in the celebrated Anderson model [27]. We note here that the definition of $a_l^{\dagger}$ and a_l [in terms of $a_i^{\dagger}$ and a_i where states i are the eigenstates of the molecular electronic Hamiltonian (2.8)] will depend on the specific problem at hand.

2.2.2 Vibrational modes

The nuclear potential energy of a polyatomic molecule will depend on the positions of all its nuclei x_i. In the limit of small displacement from their equilibrium positions, it can be written as [25]:

$$V_{\text{nuc}}(x_1, x_2, ...) = V(0) + \sum_i \left(\frac{\partial V}{\partial x_i} \right)_0 x_i + \frac{1}{2} \sum_{i,j} \left(\frac{\partial^2 V}{\partial x_i \partial x_j} \right)_0 x_i x_j + ... \ , \tag{2.14}$$

where $V(0)$ is the potential energy at the equilibrium geometry. Setting the latter to zero, and noticing that the second term on the right-hand-side of Eq. (2.14) vanishes, we write:

$$V_{\text{nuc}}(x_1, x_2, ...) \approx \frac{1}{2} \sum_{i,j} k_{ij} x_i x_j \ , \tag{2.15}$$

where k_{ij} is the generalised force constant: $k_{ij} = \left(\dfrac{\partial^2 V}{\partial x_i \partial x_j} \right)_0$. Defining the mass-weighted coordinates, $z_i = m_i^{1/2} x_i$ (where m_i is the mass of nucleus i), the nuclear energy can then be written as:

$$E_{\text{nuc}} = \frac{1}{2} \sum_i \dot{z}_i^2 + \frac{1}{2} \sum_{i,j} K_{ij} z_i z_j \ . \tag{2.16}$$

where $K_{ij} = \left(\frac{\partial^2 V}{\partial z_i \partial z_j}\right)_0$. In general, it is possible to find linear combinations (normal coordinates) Q_i of mass-weighted coordinates z_i such that cross-terms ($i \neq j$) in Eq. 2.16 vanish. In these coordinates the nuclear energy becomes:

$$E_{\text{nuc}} = \frac{1}{2}\sum_q \dot{Q}_q^2 + \frac{1}{2}\sum_q K_q Q_q^2 \ . \tag{2.17}$$

The corresponding nuclear Hamiltonian is given by:

$$H_{\text{nuc}} = \sum_q \left[-\frac{1}{2}\frac{\partial^2}{\partial Q_q^2} + \frac{1}{2}K_q Q_q^2\right] \ , \tag{2.18}$$

and effectively describes a set of independent harmonic oscillators. Defining $\omega_q = \sqrt{K_q}$, we can solve the Hamiltonian in Eq. (2.18) with the help of the phononic creation and annihilation operators:

$$b_q^\dagger = \frac{1}{\sqrt{2}}\left(\sqrt{\omega_q}Q_q - \frac{1}{\sqrt{\omega_q}}\frac{\partial}{\partial Q_q}\right) \ ; \tag{2.19}$$

$$b_q = \frac{1}{\sqrt{2}}\left(\sqrt{\omega_q}Q_q + \frac{1}{\sqrt{\omega_q}}\frac{\partial}{\partial Q_q}\right) \ . \tag{2.20}$$

Substituting them into Eq. (2.18) yields:

$$H_{\text{nuc}} = \sum_q \omega_q \left(b_q^\dagger b_q + \frac{1}{2}\right). \tag{2.21}$$

The above Hamiltonian simply describes a set of independent phonon modes in the second-quantisation notation. Throughout this thesis, we will be working with respect to the zero-point energy ground state. The vibrational Hamiltonian is therefore given simply by:

$$H_{\text{vib}} = \sum_q \omega_q \, b_q^\dagger b_q \ . \tag{2.22}$$

The eigenstates of the above Hamiltonian form a set of equally-spaced singly-degenerate levels, as discussed in any undergraduate quantum-mechanics textbook. Finally, we note that the phononic creation and annihilation operators obey the bosonic commu-

tation relation:

$$[b_q, b_{q'}^\dagger] = \delta_{qq'} \ . \tag{2.23}$$

Finally, although not accounted for in the Hamiltonian in Eq. (2.5), the vibrational modes discussed here can (besides interacting with the electronic degrees of freedom, see Section 2.2.3) also be coupled to a secondary vibrational environment, itself described by

$$H_{\text{env}} = \sum_{q'} \Omega_{q'} \, d_{q'}^\dagger d_{q'} \ , \tag{2.24}$$

with strengths $Q_{q,q'}$ via the Hamiltonian [28–30]:

$$H_{\text{vib-env}} = \sum_{q \neq q'} (b_q^\dagger + b_q) Q_{q,q'} \, (d_{q'}^\dagger + d_{q'}) \ , \tag{2.25}$$

where $d_{q'}$ ($d_{q'}^\dagger$) is the annihilation (creation) operator for the mode q'.[2] The interactions described by Hamiltonian (2.25) can lead to thermalisation of the vibrational modes q. This effect will be treated in this thesis in a phenomenological manner (*vide infra*).

2.2.3 Electron-vibrational coupling

As the molecular system undergoes a transition from one electronic state to another (for instance due to charging or an electronic excitation), the distribution of the electron density on the molecule changes and this electronic transition is associated with a distortion of the molecular geometry. This, in turn, leads to a displacement of the vibrational modes (to which we will interchangeably also refer to as the phonon modes) within the system and thus gives rise to the coupling between the electronic and vibrational degrees of freedom.

Molecular structures differ from typical solid-state systems in that the electronic degrees of freedom are typically coupled to specific vibrational modes (although interactions with background phonons, originating from the substrate on which the molecular

[2] This secondary vibrational environment can correspond to the phonon modes of the metallic leads, the substrate on which the molecule is deposited, or the solution in which the junction is immersed. Naturally, these vibrational modes themselves can also interact with the electronic degrees of freedom.

system is deposited or the solvent in which it is immersed, can also play an important role in these systems as will be discussed in Chapters 6 and 8). In this respect, they share certain characteristics with carbon nanotube quantum dots [31, 32].

In this section, we derive a generic interaction term to describe electron-vibrational coupling Hamiltonian (following Ref. [33]). When investigating the electronic structure of molecular systems one often resorts to the Born-Oppenheimer approximation. Due to an enormous mass difference between the electrons and the nuclei (over three orders of magnitude), the former move on a much slower timescale so that the electronic Hamiltonian may be assumed to depend only parametrically on nuclear positions. We write $H_{\text{elec}} = H_{\text{elec}}(\mathbf{Q})$ where $\mathbf{Q} = \mathbf{R} - \mathbf{R_0}$ is a displacement vector away from the equilibrium nuclear positions $\mathbf{R_0}$. Now, we can expand the full electronic Hamiltonian around the equilibrium nuclear geometry so that in the limit of small displacement $\mathbf{Q}$ it becomes:

$$H_{\text{elec}} \approx H_{\text{e}} + \sum_{I,\nu} \left.\frac{\partial H_{\text{elec}}}{\partial Q_{I,\nu}}\right|_{Q=0} Q_{I,\nu} \ . \tag{2.26}$$

Here, H_{e} is the electronic Hamiltonian in the equilibrium geometry case, index I denotes the nuclei in the molecule, ν refers to the spatial direction $\nu = \{x, y, z\}$. After performing a transformation into the normal mode coordinates, Eq. (2.26) can be written as:

$$H_{\text{elec}} \approx H_{\text{e}} + \sum_{I,\nu} \left.\frac{\partial H_{\text{elec}}}{\partial Q_{I,\nu}}\right|_{Q=0} \sum_{q} \mathbf{v}^{q}_{I,\nu} \sqrt{\frac{\hbar}{2M_I\omega_q}} \, (b^{\dagger}_{q} + b_q) \ , \tag{2.27}$$

where the summation over q runs over all vibrational modes with creation (annihilation) operators $b^{\dagger}_{q}$ (b_q) and frequency ω_q. M_I is the mass of ion I and $\mathbf{v}^{q}_{I,\nu}$ is the ionic displacement unit vector. From Eq. (2.27) we can now extract the electron-vibrational coupling Hamiltonian which can be written as:

$$H_{\text{e-vib}} = \sum_{q} \sum_{i,j} M^{q}_{ij} \, a^{\dagger}_{i} a_j \, (b^{\dagger}_{q} + b_q) \ , \tag{2.28}$$

where the coupling element is given by:

$$M^q_{ij} = \sum_{I,\nu} \langle i| \frac{\partial H_{\text{elec}}}{\partial Q_{I,\nu}} |j\rangle_{Q=0} \, \mathbf{v}^q_{I,\nu} \sqrt{\frac{\hbar}{2M_I\omega_q}} \, , \tag{2.29}$$

and i, j refer to molecular orbitals (eigenstates of H_{e}).

Using the Hellmann-Feynman theorem,[3] it can be shown that within the Born-Oppenheimer approximation the coupling matrix $\mathbf{M}^q$ is diagonal. Then, the Hamiltonian (2.28) can be written as:

$$H_{\text{e-vib}} = \sum_{i,q} g_{i,q} \, a^\dagger_i a_i \, (b^\dagger_q + b_q) \, , \tag{2.30}$$

where $g_{i,q}$ are the diagonal elements of $\mathbf{M}^q$. On the other hand, the non-adiabatic (off-diagonal) electron-vibrational coupling induces transitions between the eigenstates of the electronic Hamiltoninan [34, 35]. Such (vibronic) effects will not be considered in this thesis.

It will also prove useful to define a dimensionless electron-vibrational coupling parameter $\Lambda_{i,q}$ which quantifies the (dimensionless) displacement along the vibrational coordinate:

$$\Lambda_{i,q} = \frac{g_{i,q}}{\omega_q} \, . \tag{2.31}$$

The electron-vibrational coupling is usually referred to as strong for $\Lambda_{i,q} > 1$. The coupling constants $g_{i,q}$ describing the strength of interactions between the electronic and vibrational degrees of freedom can be obtained relatively straightforwardly in the case of periodic solid-state systems, see for example Ref. [36]. Electron-vibrational coupling constants in a molecular setting must be, in turn, calculated using more sophisticated *ab initio* methods [33, 37–39]. For practical reasons, these calculations are typically performed in the absence of the leads (i.e. on molecular structures in the gas phase) [40–42]. Examples of such calculation are given and briefly discussed in Chap-

[3] Hellmann-Feynman theorem states that given that the Hamiltonian H_κ, its eigenstate $|\phi_\kappa\rangle$ and corresponding eigenvalue E_κ depend continuously on a parameter κ, then $\frac{\mathrm{d}E_\kappa}{\mathrm{d}\kappa} = \langle\phi_\kappa|\frac{\mathrm{d}H_\kappa}{\mathrm{d}\kappa}|\phi_\kappa\rangle$.

ters 7 and 8. A few atomic layers of the metallic electrodes are however sometimes included in the *ab initio* modelling of the electron-vibrational coupling [43]. This has been shown to yield a good agreement with the experimental data for certain molecular wires [44].

We finish this discussion with two general remarks. Firstly, one can sometimes use symmetry (group-theoretical) considerations to identify vibrational modes that are not coupled to the degrees of freedom of the charge carriers. This can be done by exploiting the fact that in order for a given vibrational coupling to be non-zero, the considered matrix element must transform as the totally symmetric irreducible representation [45], we will make use of this fact in Chapter 5. Secondly, as can be seen from Eq. (2.29), the electronic degrees of freedom are typically most strongly coupled to low-lying vibrational modes such as centre-of-mass motion. This has indeed been found to be the case in a number of single-molecule junctions as well as carbon nanotubes [37, 41, 42, 46].

2.3 Electron-vibrational dynamics

2.3.1 Polaron transformation

In the absence of coupling to the leads (and ignoring the secondary vibrational environment), the Hamiltonian (2.5) can be diagonalised by employing the so-called polaron (or Lang-Firsov) transformation [36, 47, 48]. Similarly, in the presence of coupling to the leads, the polaron transformation enables us to treat the vibrational dynamics non-perturbatively and is therefore of paramount importance in theoretical descriptions of weakly-coupled molecular junctions.

Here, we introduce the polaron transformation by considering a generic Hamiltonian describing the single-molecule junction as a collection of energy levels interacting with a number of vibrational modes. This generic molecular-junction Hamiltonian can be

written as:

$$H = \sum_i \varepsilon_i a_i^\dagger a_i + \sum_q \omega_q b_q^\dagger b_q + \sum_{i,q} g_{i,q} a_i^\dagger a_i (b_q^\dagger + b_q) + \sum_{l,k_l} \epsilon_{k_l} c_{k_l}^\dagger c_{k_l} + \sum_{l,k_l} \left(V_{k_l} \, c_{k_l}^\dagger a_i + \text{H.c.} \right) \, , \tag{2.32}$$

where we follow the notation introduced throughout Section 2.2.

Then, the polaron transformation is performed by considering the following unitary transformation:

$$\bar{H} = e^S H e^{-S} \, , \qquad \text{where} \;\; S = \sum_{i,q} \frac{g_{i,q}}{\omega_q} \, a_i^\dagger a_i (b_q^\dagger - b_q) \, . \tag{2.33}$$

The transformation in Eq. (2.33) can be evaluated by making use of the Baker-Campbell-Hausdorff identity:

$$e^S H e^{-S} = H + [S, H] + \frac{1}{2!}[S, [S, H]] + \ldots \, . \tag{2.34}$$

We note that the polaron transformation is linear, so that $\overline{f(A, B, C)} = f(\overline{A}, \overline{B}, \overline{C})$. In the present case, one therefore only needs to evaluate the effect of the polaron transformation on a small number of (single-particle) operators:

$$\bar{a}_i^\dagger = a_i^\dagger \exp\left(\sum_q \frac{g_{i,q}}{\omega_q} \left(b_q^\dagger - b_q \right) \right) \; ; \tag{2.35}$$

$$\bar{b}_q^\dagger = b_q^\dagger - \sum_i \frac{g_{i,q}}{\omega_q} \, a_i^\dagger a_i \; ; \tag{2.36}$$

$$\bar{c}_{k_l}^\dagger = c_{k_l}^\dagger \, , \tag{2.37}$$

and equivalently for $\bar{a}_i$, $\bar{b}_q$, and $\bar{c}_{k_l}$. In the polaron-transformed frame, the Hamiltonian (2.32) hence becomes:

$$H = \sum_i \bar{\varepsilon}_i \, a_i^\dagger a_i + \sum_q \omega_q \, b_q^\dagger b_q + \sum_{l,k_l} \epsilon_{k_l} \, c_{k_l}^\dagger c_{k_l} + \sum_{l,k_l} \left(V_{k_l} \, c_{k_l}^\dagger X_i a_i + \text{H.c.} \right) \, . \tag{2.38}$$

As can be seen above, the polaron transformation has therefore a three-fold effect on

the Hamiltonian. Firstly, it decouples the electronic and vibrational degrees of freedom (the $H_{\mathrm{e-vib}}$ term vanishes). In other words, it diagonalises the Hamiltonian, at least in the absence of the molecule-lead coupling. Secondly, it renormalises the energy levels of the molecule $\varepsilon_i \to \bar{\varepsilon}_i$ where

$$\bar{\varepsilon}_i = \varepsilon_i - \sum_q \frac{|g_{i,q}|^2}{\omega_q} \ . \tag{2.39}$$

Thirdly, it introduces the (so-called) displacement operators [49] into the tunnelling Hamiltonian:

$$X_i^\dagger = \exp\left(\sum_q \frac{g_{i,q}}{\omega_q}\left(b_q^\dagger - b_q\right)\right) \ . \tag{2.40}$$

As is clear from Eq. (2.40), the displacement operators X_i and $X_i^\dagger$ act solely on the vibrational subspace, as translation operators on the vibrational wavefunctions. The matrix elements of the displacement operator $X_i^\dagger$, $\langle v_1|X_i|v_2\rangle$ where v_1 and v_2 are the relevant vibrational quantum numbers, account for the Franck-Condon overlap between relevant vibrational states in the two electronic states (*vide infra*). They can be explicitly evaluated (in a vibrational basis, for a given v_1, v_2, and $\Lambda_{i,q}$) in a way described in Appendix A.

2.3.2 Electronic-vibrational transitions

To understand the basics of electron-vibrational dynamics in single-molecule junctions, we begin by considering transport through a prototypical molecule with a single energy level coupled to a single vibrational mode with frequency ω_0 (and the source and drain electrodes). In the case of relatively weak molecule-lead coupling, the overall transport can be understood as a sequence of electron transfers occurring at the source and drain electrodes. Since the electronic level considered here is coupled to the vibrational mode (with strength g) each of these electron-transfer events is in fact an electronic-vibrational transition which is associated with a simultaneous change in the electronic (charge) and vibrational state of the system. This is schematically shown in Figure

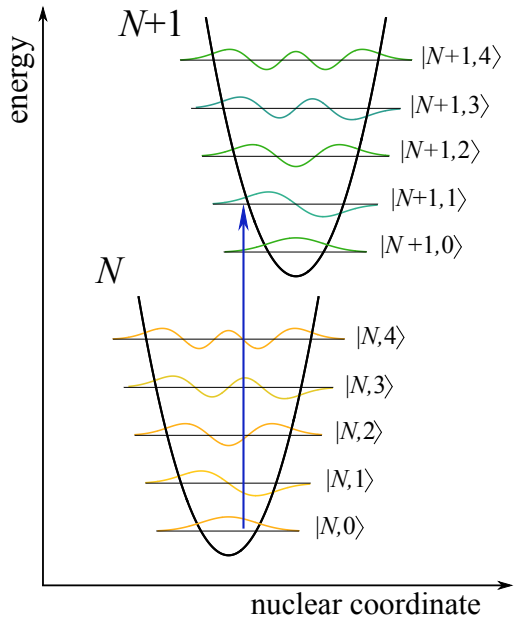


Figure 2.3: Schematic illustration of an example of an electronic-vibration transition occurring during charging of the molecular system.

2.3(a) for the $|N,0\rangle \rightarrow |N+1,1\rangle$ transition where $|M,v\rangle$ corresponds to a molecular system in M charge state and the vibrational mode in level v. The efficiency of a given $|M,v\rangle \rightarrow |M',v'\rangle$ transition depends therefore on the Franck-Condon overlap between the relevant states, which in turn is determined by the displacement of the vibrational coordinate. Mathematically, the Franck-Condon overlap is calculated as an expectation value of the displacement operator:

$$\mathrm{FC}_{v,v'} = |\langle v|X_i|v'\rangle|^2 \ , \tag{2.41}$$

and will therefore depend on the dimensionless electron-vibrational coupling parameter $\Lambda_{i,q}$. The explicit formulae are given in Appendix A and here we limit ourselves to several qualitative comments. Generally, the value of the Franck-Condon overlap depends non-trivially on v and v'. Nonetheless, for weak electron vibrational coupling $\Lambda_{i,q} < 1$, the most efficient (i.e. with the largest Franck-Condon factor) transition is the one between the two vibrational ground states. Conversely, for $\Lambda_{i,q} \gg 1$, the ground-state-to-ground-state transition occurs with a very small probability, see discussion in Section 3.4.1.

2.3.3 Vibrational dynamics

Generally speaking, vibrational modes interacting with the electronic degrees of freedom can be either strongly damped by the secondary vibrational environment or interact with it very weakly (naturally, intermediate situations are also possible). In the former case, one can assume that the vibrational modes can always be found in thermalised state as any non-equilibrium phononic populations will be rapidly quenched by the strong environmental interactions. Conversely, in the case of weak vibrational damping, large non-equilibrium vibrational populations can be developed.

In order to capture the effects of non-equilibrium vibrational dynamics, it is typically necessary to include the relevant vibrational degrees of freedom in the considered Hilbert space. This is the approach that will be taken in Chapters 4 and 5. If the phononic modes are assumed to be thermalised, however, it is possible to trace out the vibrational degrees of freedom and drastically decrease the dimension of the Hilbert space. This is how we shall proceed in Chapters 6, 7, and 8.

When dealing with a continuum of vibrational modes (phonon baths, usually corresponding to the 'outer-sphere' molecular environment) one cannot account for the state of each of the modes. Instead, it is typically justifiable in this case to assume that these environmental vibrational modes are thermalised at all times. In this context, it is also useful to define the so-called spectral density which describes the strength of the system-bath coupling weighted by the phonon density of states [50]:

$$\mathcal{J}(\omega) = \sum_q |g_q|^2 \, \delta(\omega - \omega_q) \ . \tag{2.42}$$

The absolute strength of this coupling can be quantified by the reorganisation energy λ (which, as we shall demonstrate in Chapter 7, corresponds to the well-known Marcus reorganisation energy) given by:

$$\lambda = \sum_q \frac{|g_q|^2}{\omega_q} = \int_0^\infty \mathrm{d}\omega \, \frac{\mathcal{J}(\omega)}{\omega} \ . \tag{2.43}$$

We shall make extensive use of these definitions throughout this thesis. The exact choice of $\mathcal{J}(\omega)$ will depend on the investigated system and it may, in principle, account for both intramolecular vibrations as well as the device substrate/adjacent environment, see Chapters 6, 7 and 8.

2.4 Density matrix formalism

Throughout this thesis, we will extensively make use of the density matrix formalism which is introduced in this section. Let us assume that the quantum state of the system of interest is in the state $|\Psi(t)\rangle$ (where $|\Psi(t)\rangle$ can be generally represented by a vector). We can then define the corresponding density matrix as the outer product of this state vector:

$$\rho(t) = |\Psi(t)\rangle\langle\Psi(t)| \ . \tag{2.44}$$

The power of the density-matrix formalism stems from its ability to easily go beyond the pure-state description of quantum systems. More generally, the density matrix of a mixed system can be written as:

$$\rho(t) = \sum_j p_j \, |\Psi_j(t)\rangle\langle\Psi_j(t)| \ , \tag{2.45}$$

where the coefficients p_j are all non-negative and $\sum_j p_j = 1$. The density matrix possesses the following quantities:

1. It is Hermitian: $\rho^\dagger = \rho$;
2. It has a trace of one: $\mathrm{Tr}[\rho] = \sum_j \rho_{jj} = 1$;
3. It is positive: $\rho \geq 0$
4. For pure states: $\rho^2 = \rho$.

The expectation value of an operator A can be obtained via:

$$\langle A \rangle = \sum_j p_j \, \langle \Psi_j(t)|A|\Psi_j(t)\rangle = \mathrm{Tr}[A\rho] \; . \tag{2.46}$$

Finally, we determine the equation for the time-evolution of the density matrix. For pure states this is given by the Schrödinger equation which describes the time-evolution of the quantum state $|\Psi(t)\rangle$:

$$\frac{\mathrm{d}|\Psi(t)\rangle}{\mathrm{d}t} = -\mathrm{i}H \, |\Psi(t)\rangle \; , \tag{2.47}$$

where we have set $\hbar = 1$. Using the definition of the density matrix in Eq. (2.44), it can be trivially shown that in the density-matrix formalism it becomes:

$$\frac{\mathrm{d}\rho(t)}{\mathrm{d}t} = -\mathrm{i} \, [H, \rho(t)] \; , \tag{2.48}$$

which is known as the Liouville-von Neumann equation.

2.5 Quantum master equations

In this section, we derive the second-order quantum master equation following closely Ref. [50]. We begin by noting that broadly speaking the entire relevant Hilbert space can be divided into the 'system' and 'environment' parts, as schematically shown in Figure 2.4. The system and its environment interact with each other so that the internal dynamics of the former is affected by the interaction with the latter (and *vice versa*). While the dynamics of all of the (system and environment) degrees of freedom is typically too complex to be determined, one is typically interested solely in the dynamics of the system (which generally determines some observables of interest).

In light of the above discussion, we split the overall (time-independent) Hamiltonian into a system (H_S), environment (H_E), and system-environment interaction (H_I)

Hamiltonians:

$$H = H_{\mathrm{S}} + H_{\mathrm{E}} + H_{\mathrm{I}} \ . \tag{2.49}$$

Working in the interaction picture of $H_0 = H_{\mathrm{S}} + H_{\mathrm{E}}$, we consider the Liouville-von Neumann equation for the total (system and environment) density matrix:

$$\frac{\mathrm{d}\tilde{\sigma}(t)}{\mathrm{d}t} = -\mathrm{i}\,[\tilde{H}_{\mathrm{I}}(t), \tilde{\sigma}(t)] \ , \tag{2.50}$$

where $\tilde{\sigma}(t) = e^{\mathrm{i}H_0 t}\sigma(t)e^{-\mathrm{i}H_0 t}$, and $\tilde{H}_{\mathrm{I}}(t) = e^{\mathrm{i}H_0 t}H_{\mathrm{I}}e^{-\mathrm{i}H_0 t}$.
The general solution to Eq. (2.50) is:

$$\tilde{\sigma}(t) = \tilde{\sigma}(0) - \mathrm{i}\int_0^t \mathrm{d}\tau\,[\tilde{H}_{\mathrm{I}}(\tau), \tilde{\sigma}(\tau)] \ , \tag{2.51}$$

which can be inserted back into the Eq. (2.50), yielding:

$$\frac{\mathrm{d}\tilde{\sigma}(t)}{\mathrm{d}t} = -\mathrm{i}\,[\tilde{H}_{\mathrm{I}}(t), \tilde{\sigma}(0)] - \int_0^t \mathrm{d}\tau\,[\tilde{H}_{\mathrm{I}}(t), [\tilde{H}_{\mathrm{I}}(\tau), \tilde{\sigma}(\tau)]] \ . \tag{2.52}$$

Since we are interested solely in the behaviour of the system, we proceed to trace out the environmental degrees of freedom

$$\frac{\mathrm{d}\tilde{\rho}(t)}{\mathrm{d}t} = -\mathrm{i}\,\mathrm{Tr}_{\mathrm{E}}\,[\tilde{H}_{\mathrm{I}}(t), \tilde{\sigma}(0)] - \int_0^t \mathrm{d}\tau\,\mathrm{Tr}_{\mathrm{E}}\,[\tilde{H}_{\mathrm{I}}(t), [\tilde{H}_{\mathrm{I}}(\tau), \tilde{\sigma}(\tau)]] \ , \tag{2.53}$$

where $\rho(t)$ is the density matrix of the system: $\rho(t) = \mathrm{Tr}_{\mathrm{E}}[\sigma(t)]$ (and equivalently in the interaction picture). At this point, Eq. (2.53) is still exact (and as difficult to solve as the original Liouville-von Neumann equation). We now proceed to make a number of assumptions. Firstly, we assume the so-called separable initial conditions approximation, namely that at $t = 0$, there exist no correlations between the system and its environment. Therefore $\sigma(0)$ becomes: $\sigma(0) = \rho(0) \otimes \rho_{\mathrm{E}}(0)$ where $\rho_{\mathrm{E}}(0)$ is the environment density matrix. We then set the first term on the left-hand-side of Eq. (2.53) to zero. The validity of this operation can always be ensured by an appropriate definition of the interaction Hamiltonian.

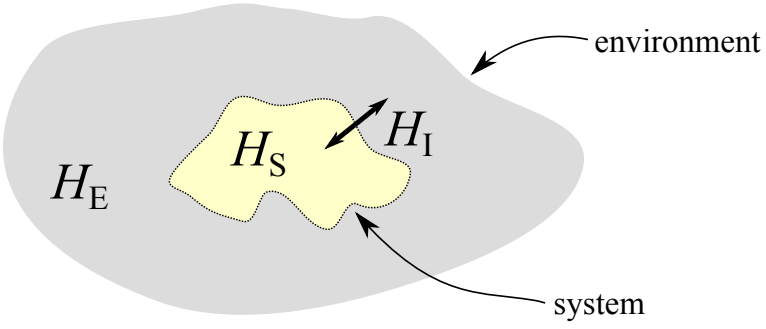


Figure 2.4: Schematic illustration of an open quantum system – a small quantum system interacting with much larger (typically thermalised) environment.

We now make the so-called *Born approximation* which assumes that the overall density matrix can be factorised into a system and environment parts at all times:

$$\sigma(t) \approx \rho(t) \otimes \rho_{\mathrm{E}} \ , \tag{2.54}$$

where the environmental density matrix is assumed to be stationary ($\rho_{\mathrm{E}}(t) = \text{const.}$). The environment is clearly assumed here to be unaffected by its coupling to the system, and no system-environment correlations are created during the system's time evolution. The Born approximation is therefore valid only in the limit of weak system-environment interactions. We shall make use of the Born approximation in large parts of this thesis, although the limitations of this approach will be addressed in Chapter 7. Eq. (2.53) is now given by:

$$\frac{\mathrm{d}\tilde{\rho}(t)}{\mathrm{d}t} = -\int_0^t \mathrm{d}\tau \, \mathrm{Tr}_{\mathrm{E}} \left[\tilde{H}_{\mathrm{I}}(t), [\tilde{H}_{\mathrm{I}}(\tau), \tilde{\rho}(\tau)\rho_{\mathrm{E}}]\right] \ . \tag{2.55}$$

While considerably simpler than the original Eq. (2.50) [due to factorisation of $\sigma(\tau)$], the above equation is still non-local in time as the time-evolution of the density matrix depends on its history. We therefore proceed to make the *Markov approximation* and replace $\tilde{\rho}(\tau)$ with $\tilde{\rho}(t)$. This assumption is once again valid in the case of weak system-environment interactions (where the environment is largely unaffected by its interaction with the system), when the environment memory time (the time over which the environment retains the information about the system) is much shorter than the timescale of the system evolution. Finally, we replace τ with $t - \tau$ and extend the

integration limit to infinity yielding:

$$\frac{\mathrm{d}\tilde{\rho}(t)}{\mathrm{d}t} = -\int_0^\infty \mathrm{d}\tau \ \mathrm{Tr}_\mathrm{E}\left[\tilde{H}_\mathrm{I}(t), [\tilde{H}_\mathrm{I}(t-\tau), \tilde{\rho}(t)\rho_\mathrm{E}]\right] . \tag{2.56}$$

Returning to the Schrödinger picture gives

$$\frac{\mathrm{d}\rho(t)}{\mathrm{d}t} = -\mathrm{i}[H_\mathrm{S}, \rho(t)] - \int_0^\infty \mathrm{d}\tau \ \mathrm{Tr}_\mathrm{E}\left[H_\mathrm{I}, [\tilde{H}_\mathrm{I}(-\tau), \rho(t)\rho_\mathrm{E}]\right] , \tag{2.57}$$

which is the *second-order Born-Markov quantum master equation*. Eq. (2.57) is the main result of this section and will be extensively used throughout this thesis.

Generally speaking, the interaction Hamiltonian has the form:

$$H_\mathrm{I} = \sum_\alpha A_\alpha \otimes B_\alpha \ , \tag{2.58}$$

where the operators A_α and B_α act exclusively on the system or the environment subspace of the Hilbert space, respectively. In the interaction picture of H_0, the interaction Hamiltonian therefore becomes:

$$\tilde{H}_\mathrm{I}(t) = \sum_\alpha \tilde{A}_\alpha(t) \otimes \tilde{B}_\alpha(t) \ , \tag{2.59}$$

where $\tilde{A}_\alpha(t) = e^{\mathrm{i}H_\mathrm{S}t} A_\alpha e^{-\mathrm{i}H_\mathrm{S}t}$ and $\tilde{B}_\alpha(t) = e^{\mathrm{i}H_\mathrm{E}t} B_\alpha e^{-\mathrm{i}H_\mathrm{E}t}$. Eqs. (2.58) and (2.55) can be inserted into the Born-Markov quantum master equation, which after the expansion of the commutators becomes:

$$\frac{\mathrm{d}\rho(t)}{\mathrm{d}t} = -\mathrm{i}[H_\mathrm{S}, \rho(t)] - \sum_{\alpha,\beta} \int_0^\infty \mathrm{d}\tau \left(C_{\alpha\beta}(\tau)[A_\alpha, \tilde{A}_\beta(-\tau)\rho(t)] + C_{\beta\alpha}(-\tau)[\rho(t)\tilde{A}_\beta(-\tau), A_\alpha] \right) , \tag{2.60}$$

where $C_{\alpha\beta}(\tau)$ denotes the correlation function:

$$C_{\alpha\beta}(\tau) = \mathrm{Tr}\left[\tilde{B}_\alpha(\tau) B_\beta \rho_\mathrm{E}\right] . \tag{2.61}$$

As we shall see, the dissipative terms to second-order in the molecule-lead coupling correspond to the sequential electron transfers between the molecular structure and the leads. The Born-Markov quantum master equation can therefore be used to describe the resonant transport regime (the main focus of this thesis). Unfortunately, this approach does not capture the phenomenon of lifetime broadening (or higher-order tunnelling processes). We shall focus on addressing some of these shortcomings in Chapter 7.

2.6 Observables & Full counting statistics

2.6.1 Steady-state

The quantum master equation for the evolution of the density matrix can be generally written as

$$\frac{\mathrm{d}\rho(t)}{\mathrm{d}t} = \mathcal{L}\rho(t) \ , \tag{2.62}$$

where $\mathcal{L}$ is the Liouvillian superoperator accounting for both the unitary and dissipative dynamics of the considered system. Throughout this thesis we will be interested in the steady-state values of various observables (which correspond to the experimentally-measurable quantities). Determining those involves first finding the steady-state solution of the relevant quantum master equation:

$$\frac{\mathrm{d}\rho(t)}{\mathrm{d}t} = 0 \ , \tag{2.63}$$

which yields the stationary density matrix ρ_{stat} which, in turn, satisfies

$$\mathcal{L}\rho_{\mathrm{stat}} = 0 \ . \tag{2.64}$$

In simple cases (see for instance Chapter 7), it will be possible to determine ρ_{stat} analytically. Typically, however, one will have to resort to finding the solution to Eq. (2.64) numerically by means of singular value decomposition [51] (performed in

the Liouville space).

2.6.2 Observables

Our primary observable of interest in this work will be the steady-state value of current flowing through the junction. We will formally define it as:

$$I = \langle I_{\mathrm{R}} \rangle = \frac{\mathrm{d}}{\mathrm{d}t} \langle Q_{\mathrm{R}}(t) \rangle \Big|_{t \to \infty} \tag{2.65}$$

where $\langle I_{\mathrm{R}} \rangle$ is the mean current at the right molecule-lead interface and $\langle Q_{\mathrm{R}}(t) \rangle$ denotes the average amount of charge collected in the right electrode between time 0 and t.

The electric current is most easily found by considering the electron flow at either one of the two molecule-lead interfaces. We note that in the steady state the electron flows at the left (L) and right (R) interface are equal and opposite: $I_{\mathrm{L}} = -I_{\mathrm{R}}$. Generally speaking, the value of the electric current flowing through the $l = \mathrm{L}, \mathrm{R}$ interface is given by the expectation value of the appropriate current operator $\mathcal{I}_l$ evaluated in the steady-state limit:

$$I_l = e \, \mathrm{Tr} \left[\mathcal{I}_l \rho_{\mathrm{stat}} \right] \ . \tag{2.66}$$

The current operators can be identified relatively easily as the part of the quantum master equation (which was used to find the stationary density matrix, ρ_{stat}) which describes the population transfer between the molecular system and the lead l as shall be discussed in Section 2.6.3, see Chapter 4 for a concrete example. We will find the expression given in Eq. (2.66) to be of a paramount importance throughout this thesis. Its rigorous derivation (making use of full counting statistics) will be therefore presented in Section 2.6.3.

In this thesis, we will also be interested in the average populations of molecular sites/orbitals. They are simply given by the diagonal elements of (the electronic subspace of) the stationary density matrix, ρ_{stat}, in an appropriate basis.

Lastly, we will also briefly consider zero-frequency current noise, $S(0)$. Similarly to

what has been done in Eq. (2.65), it can be formally defined as [52–54]:

$$S_{\mathrm{R}}(0) = \frac{\mathrm{d}}{\mathrm{d}t}\left[\langle Q_{\mathrm{R}}^2(t)\rangle - \langle Q_{\mathrm{R}}(t)\rangle^2\right]\Big|_{t\to\infty} . \tag{2.67}$$

It can also be shown that in the steady-state limit, $S_{\mathrm{R}}(0) = S_{\mathrm{L}}(0) \equiv S(0)$, similarly to what holds for the electric current [55].

Naturally, the magnitude of the observed (zero-frequency) current noise will depend on the magnitude of the electric current. It is therefore useful to define the dimensionless Fano factor F as the ratio

$$F = \frac{S(0)}{e|I|} . \tag{2.68}$$

The physical meaning of the above can be understood by noting that the denominator in Eq. (2.68) corresponds to the 'white noise' of a Poissonian process (where $S(0) = e|I|$).[4] The transport through the junction can be therefore described as a Poissonian process for $F = 1$, a super-Poissonian one for $F > 1$, and a sub-Poissonian one if $F < 1$.

We finish this section by noting that the populations of the molecular electronic states are invariant under the polaron transformation,

$$\langle \bar{a}_i^\dagger \bar{a}_i\rangle = \langle a_i^\dagger a_i\rangle . \tag{2.69}$$

Consequently, none of the results from this section are affected by the polaron transformation which will used extensively throughout this thesis.

2.6.3 Full counting statistics

Here, using full counting statistics [23, 56], we derive the previously-stated Eq. (2.66) for the electric current through the junction and present a similar expression for the

[4] A Poissonian process is one in which events are statistically independent of each other. That means that the distribution function $P_n(t)$ which describes the probability of collecting n electrons during an interval t is a Poisson distribution. An example of a Poissonian transport process is, for instance, electron tunnelling through a single barrier [23].

zero-frequency current noise.

Let us consider a quantum master equation of the general form:

$$\frac{\mathrm{d}\rho(t)}{\mathrm{d}t} = \mathcal{L}\rho(t) \ , \tag{2.70}$$

where $\mathcal{L}$ is the relevant (time-independent) Liouvillian. We introduce the n-resolved density matrix, $\rho^{(n)}(t)$, where n is the number of electrons transferred between the molecule and one of the leads (here we shall consider the right lead, R) by the time t such that at any time t,

$$\sum_n \rho^{(n)}(t) = \rho(t) \ . \tag{2.71}$$

The n-resolved quantum master equation is then given by:

$$\frac{\mathrm{d}\rho^{(n)}(t)}{\mathrm{d}t} = \left(\mathcal{L} - \mathcal{I}_{\mathrm{R}}^{+} - \mathcal{I}_{\mathrm{R}}^{-}\right)\rho^{(n)}(t) + \mathcal{I}_{\mathrm{R}}^{+}\rho^{(n-1)}(t) + \mathcal{I}_{\mathrm{R}}^{-}\rho^{(n+1)}(t) \ . \tag{2.72}$$

Here, $\mathcal{I}_{\mathrm{R}}^{+}$ ($\mathcal{I}_{\mathrm{R}}^{-}$) is a superoperator which describes tunnelling out of (into) the molecular system at the interface with the right electrode.

Next, let us define the cumulant generating function [57]:

$$e^{Z(\chi,t)} = \sum_n P_n(t) e^{\chi n} = \mathrm{Tr}\left[\sum_n \rho^{(n)}(t)\ e^{\chi n}\right] \ , \tag{2.73}$$

where $P_n(t)$ is the probability of n electrons being collected in the right electrode by the time t. Cumulants of the charge distribution can then be obtained by considering derivatives of $Z(\chi, t)$ with respect to the counting field χ at $\chi = 0$:

$$\langle\langle n^{(m)} \rangle\rangle(t) = \left.\frac{\partial^m Z(\chi,t)}{\partial \chi^m}\right|_{\chi=0} \ . \tag{2.74}$$

The average (steady-state) electric current, I, can be therefore found by considering the first cumulant:

$$I = e\,\frac{\mathrm{d}\langle\langle n \rangle\rangle(t)}{\mathrm{d}t} = e\,\frac{\mathrm{d}}{\mathrm{d}t}\left.\frac{\partial Z(\chi,t)}{\partial \chi}\right|_{\chi=0} \quad \text{at } t \to \infty \ . \tag{2.75}$$

In order to evaluate this expression, let us consider the time dependence of $\rho_\chi(t)$,

$$\rho_\chi(t) = \sum_n \rho^{(n)}(t)\, e^{\chi n} \ . \tag{2.76}$$

From Eq. (2.72), it is given by:

$$\dot{\rho}_\chi(t) = \left(\mathcal{L} - (1-e^{\chi})\mathcal{I}_{\rm R}^{+} - (1-e^{-\chi})\mathcal{I}_{\rm R}^{-}\right)\rho_\chi(t) = \mathcal{L}_\chi \rho_\chi(t) \ , \tag{2.77}$$

with a solution $\rho_\chi(t) = \exp(\mathcal{L}_\chi t)\ \rho_\chi(0)$, and $e^{Z(\chi,t)} = \mathrm{Tr}\left[\rho_\chi\right]$. This yields:

$$I = e\ \mathrm{Tr}\left[\left.\frac{\partial \mathcal{L}_\chi}{\partial \chi}\right|_{\chi=0} \rho_{\rm stat}\right] = e\ \mathrm{Tr}\left[\mathcal{I}_{\rm R}\rho_{\rm stat}\right] \ , \tag{2.78}$$

where $\mathcal{I}_{\rm R} = \mathcal{I}_{\rm R}^{+} - \mathcal{I}_{\rm R}^{-}$ is the current superoperator. This completes the derivation of Eq. (2.66).[5]

Similar ideas can be used to find an expression for the zero-frequency current noise. Considering again the quantum master equation (2.70), the zero-frequency current noise can be determined using the expression of Flindt, Novotný and Jauho [56, 58]:

$$S(0)/e^2 = \mathrm{Tr}\left[\left(\mathcal{I}_j^{+} + \mathcal{I}_j^{-}\right)\rho_{\rm stat}\right] - 2\ \mathrm{Tr}\left[\left(\mathcal{I}_j^{+} - \mathcal{I}_j^{-}\right)\mathcal{R}\left(\mathcal{I}_j^{+} - \mathcal{I}_j^{-}\right)\rho_{\rm stat}\right] \ , \tag{2.79}$$

where $\mathcal{I}_j^{\pm}$ are again the superoperators describing electron hopping on/off the interface with j-lead. Furthermore, $\mathcal{R} = (1-\mathcal{P})\mathcal{L}^{-1}(1-\mathcal{P})$ is the Moore-Penrose pseudoinverse of $\mathcal{L}$ where $\mathcal{P}$ is the projection operator formed as an outer product of identity and $\rho_{\rm stat}$ vectors. The derivation of Eq. (2.79) can be found for instance in Refs. [54, 56]. We shall make use of this result in Chapter 6.

[5] Naturally, $I_{\rm L}$ and $\mathcal{I}_{\rm L}$ can be obtained analogously.

Chapter 3

Experimental studies on single-molecule junctions

I was not good at putting things together with my fingers.

— Philip W. Anderson

In this chapter, we review the experimental techniques commonly used to fabricate and study charge transport through single-molecule junctions. We further discuss the general transport properties of these systems and experimental signatures of electron-vibrational coupling placing a special emphasis on the resonant transport regime.

The field of single-molecule electronics has undergone rapid development in the last twenty years and a great amount of theoretical knowledge and experimental evidence regarding transport properties of molecular junctions has been accumulated. Consequently, this chapter will provide us only with a brief glimpse at the rich tapestry of vibrational effects in single-molecule devices. Nonetheless, it will let us better understand the basic role of electron-vibrational coupling in molecular junctions and will form the conceptual foundations for the rest of this work. Importantly, in this chapter, we will discuss examples of physical phenomena that can be observed experimentally and which will be of interest in the remainder of this thesis.

3.1 Overview of experimental techniques

Fabrication of single-molecule junctions involves first assembling a pair of metallic contacts, acting as the source and drain electrodes, separated by a nanometer-sized gap able to fit a desired molecule. As discussed in the previous chapter, the presence of another (gate) electrode enables electrostatic control of the investigated system, that is, the ability to shift the energy levels of the molecule within the gap.

Various approaches, depending on the nature of these metallic contacts, have been developed over the years. Ideally, the experimental technique of choice should allow for [12, 59]:

1. Reproducibly forming single-molecule bridges;
2. Electrostatic gating control;
3. Fabrication of multiple molecular devices;
4. Control of the gap-size to accommodate any molecule of interest;
5. Integration of the junction into larger electronic circuits.

Unfortunately, none of the methods developed to-date has fully fulfilled all of the above criteria. In what follows, we will briefly discuss some of the commonly used techniques, together with their drawbacks and advantages.

3.1.1 Scanning Tunnelling Microscopy

Perhaps the most commonly used (and historically most relevant) approach is based on the Scanning Tunnelling Microscope (STM) [17, 35, 60–71]. The STM setup can be used to repeatedly form Au–molecule–Au junctions by moving an STM gold tip near a gold surface covered with molecules of interest [72], as schematically shown in Figure 3.1(a). The number of molecules bridging the tip-substrate gap can be changed by accurately controlling the movement of the tip [73]. STM-based techniques allow for

recording the current-voltage characteristics but they are typically unable to include the gate electrode and are therefore mostly limited to the off-resonant transport regime (see discussion in Section 3.2). In recent years, however, methods utilising electrolytic gating of STM molecular junctions have also been developed [74, 75]. Molecular conductance is also commonly measured as a function of the tip displacement as it is pulled away from the gold surface yielding the information regarding the nature of the molecule-tip contact. The studied molecules usually bind to the gold electrodes

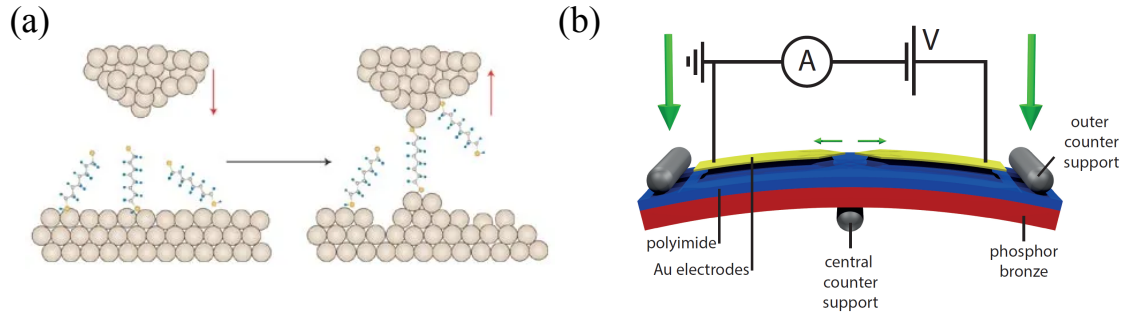


Figure 3.1: Schematic illustrations of various single-molecule junctions. (a) STM-based junction formed by approaching the gold surface covered with the desired molecules with an STM tip. Reprinted by permission from Ref. [76]. (b) Mechanically-controllable break junction: the size of the nanogap can be controlled by exerting the force as shown in the figure. Reprinted by permission from Ref. [77].

by forming covalent Au-S, Au-N or Au-P bonds [78, 79]. The use of appropriately functionalised molecular species is therefore necessary.

3.1.2 Mechanically-Controllable Break Junctions

The Mechanically-Controllable Break Junctions (MCBJ) constitute another method commonly used to investigate single-molecule charge transport [13, 80–88]. Fabricating a break junction typically starts with fixing a metallic (typically gold) wire onto a flexible substrate. Bending the substrate upon an exerted force causes an elongation and ultimately breaking of the wire thus producing a gap, the size of which can be carefully controlled, as schematically shown in Figure 3.1(b). MCBJs can be relatively easily incorporated into larger setups and exhibit high mechanical stability [89, 90]. Furthermore, the method benefits from lack of chemical contamination of the gap since the

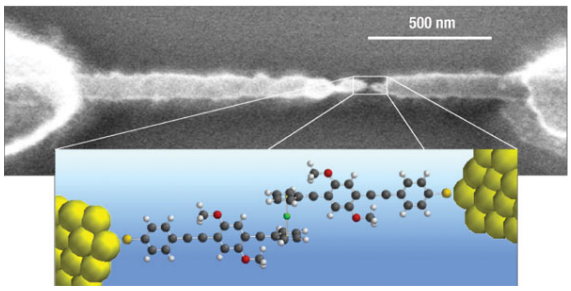


Figure 3.2: Scanning electron micrograph and a schematic of a molecular electromigration break junction. Figure reprinted by permission from Ref. [95].

breaking of the gold bridge takes place directly before the molecular deposition. More recently, van der Zant *et al.* have also developed a method of including an electrostatic gate in the MCBJ setup [77, 91]. All of this makes mechanically controllable break junctions a very attractive tool for investigating charge transport through single molecules.

3.1.3 Electromigration Break Junctions

One of the problems encountered when utilising gold electrodes used in the methods described above is the electromigration (transport) of gold atoms upon the applied bias voltage. The same effect, however, can be also utilised to produce nanogapped gold electrodes known as Electromigrated Break Junctions [14, 92–94], see Figure 3.2. These systems are usually fabricated as follows. After fabrication of a constriction in a gold wire (as shown in Figure 3.2), high voltage is applied across the device. Electromigration predominantly takes place in the region of the largest current density. The width of the constriction decreases until two separate electrodes are formed. One naturally cannot alter the width of the formed gap, however fabrication of a large number of devices is typically possible. Molecules can be deposited onto the electrodes either before [96] or after [97] the breaking process takes place. The gate electrode can be easily included in the device architecture. Controlling the size of the nanogap is, however, not trivial. Additionally, unintentional debris is often created during the fabrication process and it may sometimes exhibit characteristics similar to those of molecular systems [12].

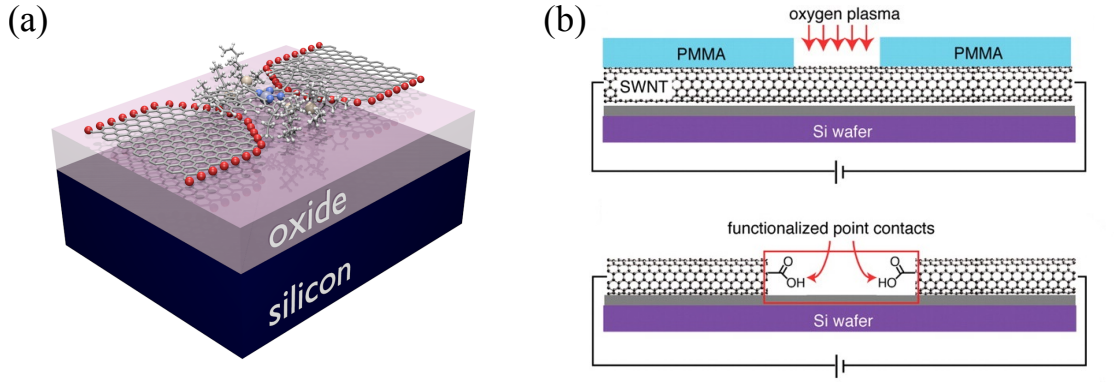


Figure 3.3: (a) Schematics of single-molecule junctions utilising graphene electrodes formed by electroburning. The Si substrate can be used as the gate electrode. Figure reproduced from Ref. [101]. (b) Schematic illustration of the process in which a pair of CNT electrodes is formed by opening of a nanotube using oxygen plasma from Ref. [105]. Reprinted with permission from AAAS. The edges of the nanotube are functionalised and can covalently bond to a desired molecule.

3.1.4 Carbon-based methods

More recently, techniques utilising carbon-based electrodes have also been developed, following the phenomenal growth of interest in graphene, carbon nanotube, and fullerene materials over the last decade.

Graphene nanogaps (with a gap-size of 1-2 nm) can be formed by the method of feedback-controlled electroburning [98–100], analogous to the electromigration described in the previous section. The deposited molecule can then bind to the electrodes via the π-stacking mechanism [6, 99, 101] or covalent amide coupling [102, 103]. The substrate (below the insulator layer) on which the graphene is deposited can be utilised as the gate electrode, as schematically shown in Figure 3.3(a). The method suffers from similar disadvantages to the electromigrated break junction technique. It allows, however, for more efficient gating control of the molecule as well as for applying much greater potential difference between the leads due the large stability of the graphene electrodes. Recently, it has been shown that single-molecule junctions utilising graphene electrodes exhibit striking similarities to those based on gold electrodes [104]. A more exhaustive description of this method is given in Chapter 8 where the experimental data obtained using this technique is analysed in some detail.

Carbon nanotubes also offer an interesting alternative, as demonstrated in a pioneering study by Guo *et al.* [105]. Once oxidatively opened (using electron-beam litography), the nanotube forms two contacts to which the molecule can covalently bind via an amide bond, as schematically illustrated in Figure 3.3(b). This technique benefits from the atomic reproducibility of the electrode-molecule contact and mechanical robustness of the fabricated devices.

Many other methods and variations on those described above have also been developed in recent years. They include atomic force microscopy (AFM) [106–108], Electrochemical Deposition [109–111], and Surface-Diffusion-Mediated Deposition Junctions [112, 113] and have recently been reviewed in detail in Refs. [12, 114].

3.2 Transport properties of molecular junctions

The device geometries discussed above can be broadly divided into two groups depending on whether or not they feature a gate electrode. If the gate electrode is present within the device geometry, one can relatively easily access the resonant transport regime. Figure 3.4 shows an example of a stability diagram (map of electric current as a function of the bias and gate voltage) reported in Ref. [42] for an electroburnt-graphene junction comprising a functionalised fullerene molecule. Coulomb diamonds (regions of suppressed current, as discussed in Chapter 2) corresponding to a number of different charge states are clearly visible. From the heights of these Coulomb diamonds, one can estimate the addition energy for each of those charge states, as shown in Figure 3.4. Typically, and as indeed can be seen in Figure 3.4, an E_{add} on the order of a few hundred meV is observed [6, 42, 101, 115–118]. The experimentally reported values of addition energy are usually significantly smaller than those calculated (or measured) for the corresponding molecular systems in the gas phase. This reduction in E_{add} is typically explained by the polarisation-induced renormalisation of molecu-

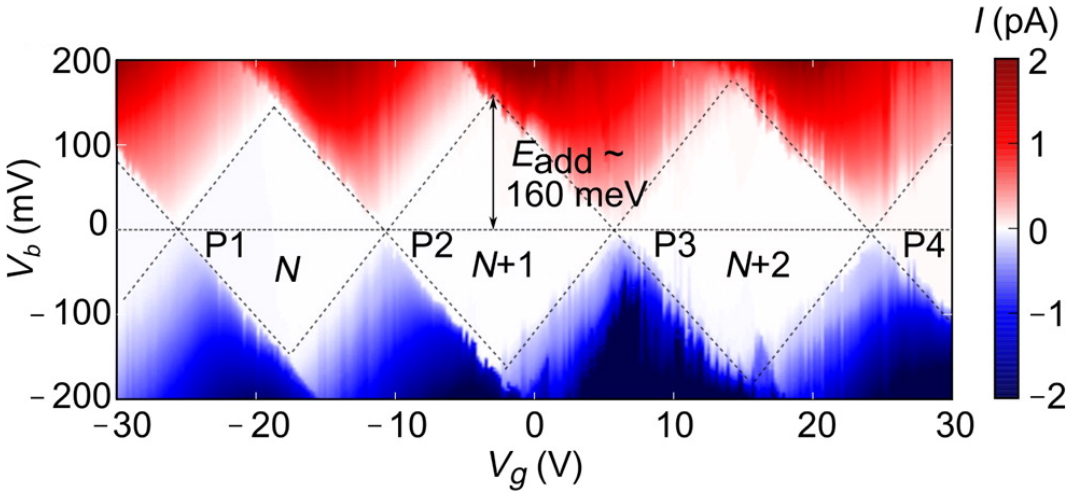


Figure 3.4: Stability diagram (map of electric current I as a function of the bias V_b and gate voltage V_g) for a functionalised-C_{60} molecular junction in an electro-burnt graphene junction. Reprinted with permission from Ref. [42]. Copyright 2015 American Chemical Society.

lar energy levels in the three-terminal junction setting [119]. Nonetheless, Coulomb blockade in molecular junctions is routinely observed at liquid-nitrogen temperature and can sometimes be witnessed even at room temperature [101].

In the absence of electrostatic gating control, one is typically limited to the off-resonant transport regime ('zero-gate behaviour', *c.f.* Figure 3.4) where the molecular energy levels lie outside of the bias window. The resonant regime can, however, sometimes be reached at higher bias voltage [13, 120]. Experimental studies of the off-resonant transport typically focus on correlating the values of electronic conductance (averaged over a large number of individual junctions) with details of the molecular structure or the nature of the molecule-lead contact. Vibrational effects, on the other hand, typically play a relatively modest role in this regime. Investigation of these phenomena is the domain of Inelastic Electron Tunnelling Spectroscopy (IETS), which is briefly discussed in Section 3.3. By contrast, as we shall discuss in Section 3.4, electron-vibrational coupling can have an enormous impact on the molecular transport properties in the resonant transport regime.

3.3 Vibrational effects in off-resonant regime

Although the main focus of this thesis is vibrational effects in the resonant transport regime, let us begin by discussing the off-resonant regime. There, the molecular electronic levels lie outside of the bias window and the charge transport through the molecule can then only take place via the cotunnelling mechanism, as discussed in the previous chapter. In the absence of electron-vibrational coupling, the current increases (approximately) linearly with bias voltage as the number of electrons that can directly tunnel through the molecular energy level increases linearly with the applied potential difference. This results from the almost linear increase in the number of electrons that can tunnel from the source to the drain with increasing bias [121].

In the presence of coupling of the molecular energy level to a vibrational mode (with frequency ω_0), an additional conduction channel opens whenever $eV_\mathrm{b} = n\omega_0$ (n is an integer): as the energy difference between the source and the drain increases beyond that of the vibrational mode, electrons can (inelastically) tunnel through the junction inducing a vibrational excitation in the molecular system [122, 123]. This manifests itself as a step in the differential conductance $\mathrm{d}I/\mathrm{d}V_\mathrm{b}$ and a peak in the second derivative $\mathrm{d}^2I/\mathrm{d}V_\mathrm{b}^2$, as shown in Figure 3.5 [124]. The magnitude of the above conductance steps depends on the strength of electron-vibrational coupling [126]. In presence of coupling to more than one vibrational mode, one can typically observe overlapping features corresponding to each of the modes as well as, to a lesser extent, peaks corresponding to simultaneous excitation of more than one vibrational mode [127]. Such features have been observed in a variety of molecular junctions in what is known as Inelastic Electron Tunnelling Spectroscopy [44, 67, 128–133]. Two examples of typical IETS spectra are shown in Figure 3.5. Overall, however, the magnitude of these inelastic effects is relatively modest and therefore such phenomena are very often ignored in theoretical investigations of the off-resonant regime. Finally, we note that vibrational inelastic tunnelling is nowadays a rather well-understood phenomenon. In fact, it is now commonly used as a spectroscopic tool to confirm the presence of the

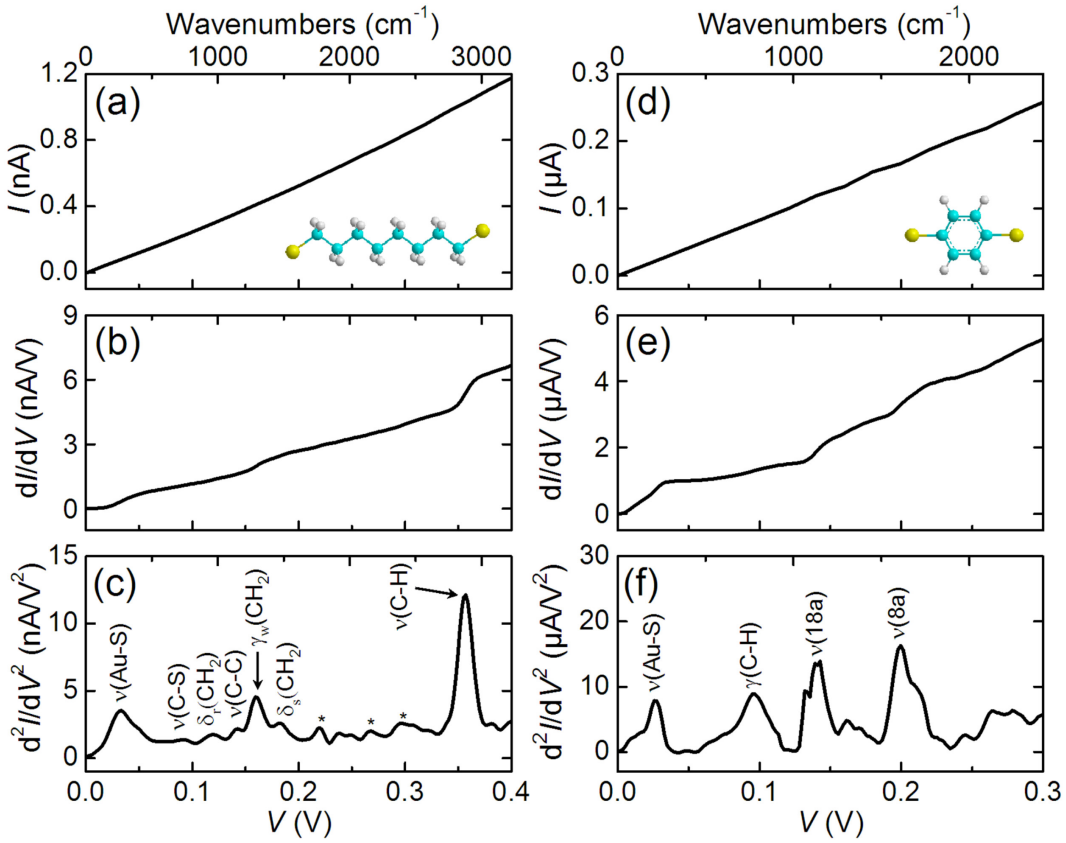


Figure 3.5: Experimental transport properties of 1,8-octanedithiol and 1,4-benzenedithiol junctions. (a,d) IV characteristics; (b,e) Differential conductance; (c,f) IETS spectrum. Reprinted from Ref. [125], with the permission of AIP Publishing. The peaks in panels (c,f) are assigned to specific molecular vibrational modes.

molecular system within the junction and to investigate the influence of the molecular environment on its structural and transport properties.

3.4 Vibrational effects in resonant regime

As we shall demonstrate, electron-vibrational interactions yield much richer behaviour in the resonant transport regime (when at least one of the molecular energy level lies within the bias window). We first return to the prototypical model system from Section 2.3.2 which comprises a single electronic energy level coupled with strength g to a vibrational mode with frequency ω_0. A simple rate-equation calculation of the IV characteristics for such a system predicts that the resonant current through the junction should increase in a step-wise manner (with step-width of $2\omega_0$ for symmetrically applied

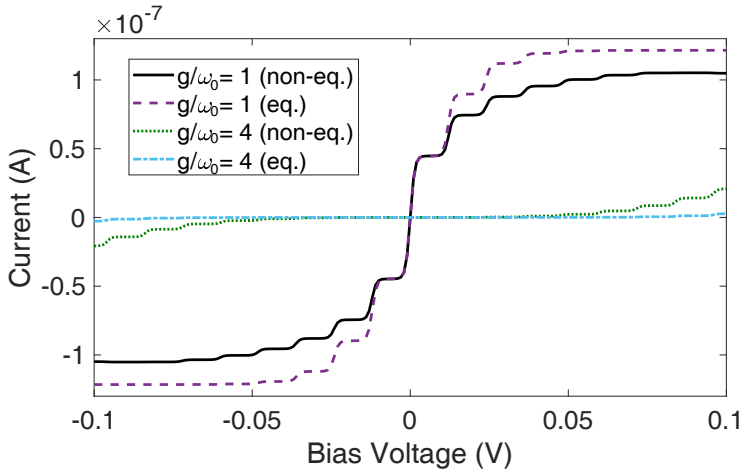


Figure 3.6: IV characteristics on resonance for the molecular system discussed in this section for different values of the electron-vibrational coupling strength and in the case of non-equilibrated (non-eq.) and equilibrated (eq.) vibrational mode, recalculated from Ref. [134].

bias voltage) as the consecutive vibrational levels fall into the bias window [134–136], see Figure 3.6.

In the case of a thermalised (equilibrated) vibrational mode and at a temperature such that $k_{\mathrm{B}}T \ll \omega_0$, the relative heights of the current steps can be correlated with the magnitude of $|\langle 0|X|v\rangle|^2$ matrix elements (accounting for the Franck-Condon overlap between the vibrational ground-state and the v^{th} vibrational excited state, see Section 2.3.1) and are thus determined by the dimensionless electron-vibrational coupling parameter $\Lambda = g/\omega_0$ [137]. At higher temperatures or in the presence of non-equilibrium vibrational dynamics, a number of phonon emission and absorption processes contribute to the conductance at each of the steps and so the heights of the respective steps cannot be *exactly* quantified by simply considering the $|X_{v,0}|^2$ Franck-Condon factors [138]. As shown in Figure 3.6, in case of $\Lambda = 1$ the current is substantially enhanced in case of equilibrated vibrational mode. For this choice of Λ, the transition between the neutral and charged molecular states is the most efficient if it occurs between the two vibrational ground states. Damping of the vibrational mode (following its excitation during a charging process) can thus increase the efficiency of the electron hopping on and off the molecule and, therefore, increase the electric current flowing through the junction.

Equally spaced steps in the IV characteristics (or equivalently peaks in the differential conductance) have been observed in a variety of molecular systems and are widely accepted as a signature of coupling to a single vibrational mode [35,42,94,117,139–141]. In the case of relatively weak electron-vibrational coupling, often only the first conductance peak can be resolved experimentally [41]. On the other hand, strong electron-phonon coupling can result in the suppression of current for a few initial steps. This is the so-called *Franck-Condon blockade* [134], which also has been observed experimentally [40, 42], and is discussed in detail in Section 3.4.1. Conversely, signatures of coupling to certain vibrational modes can also be used to confirm the presence of the desired molecule in the junction. Electronic degrees of freedom in the fullerene molecule, for instance, are known to couple to the lowest vibrational mode of C_{60} at around 33 meV. This feature is widely reproducible across various experiments and has been used to verify the presence of C_{60} within the junction [14, 142, 143].

3.4.1 Franck-Condon Blockade

As explained above, the relative heights of the steps in the IV characteristics at low temperatures can be accounted for by considering the magnitudes of the $|\langle 0|X|v\rangle|^2$ matrix elements. In the case of very strong vibrational coupling ($\Lambda \gg 1$), the magnitude of these matrix elements is nearly zero for small v. The current is therefore suppressed for the initial few steps in the IV characteristics, as shown in Figure 3.6. This phenomenon, known as Franck-Condon blockade, has been predicted by Koch and von Oppen in their seminal study in Refs. [134, 135]. First observed experimentally in a suspended GaAs/AlGaAs quantum dot (where the electronic degrees of freedom of the quantum dot couple to discrete phonon modes of the cavity) [31], it was later seen in carbon nanotube quantum dots [144] and more recently also in single-molecule junctions [40, 42]. In the case of strong electron-vibron coupling, charging of the molecule is the most efficient if it involves, for instance, a vibrational ground state of N charge state and one of the high vibrational levels in the $N+1$ state. Thus, as shown in Figure 3.6, the blockade is lifted at higher bias voltage where such transitions become energet-

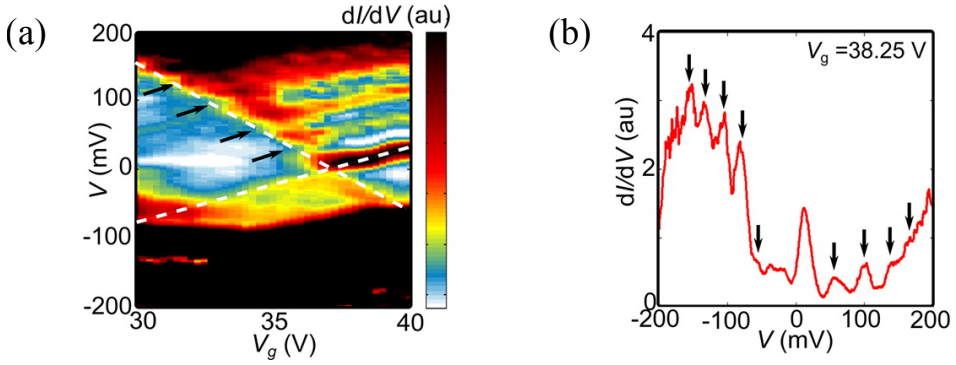


Figure 3.7: Transport characteristics of a curcominoid-based molecular junction studied in Ref. [41]. (a) Differential conductance map, and (b) differential conductance on resonance. The conductance map clearly shows a stepwise increase in the current through the system (peaks in $\mathrm{d}I/\mathrm{d}V$ curve). Each of the peaks marked by a black arrow was assigned to a specific molecular vibrational mode. Reprinted with permission from Ref. [41]. Copyright 2016 American Chemical Society.

ically possible. Furthermore, as also shown in Figure 3.6, vibrational relaxation (which brings the vibrational mode back to its ground state) leads to an overall decrease in current through the junction.

3.4.2 Beyond single-mode models

Typically, the molecular electronic degrees of freedom couple to more than one internal vibrational mode. Consequently, in the resonant IV characteristics one should observe a set of conductance peaks corresponding to the excitations of each of the vibrational modes. Such behaviour has indeed been observed in many experimental systems [65, 84, 143]. As previously stated, if the coupling to a given vibration is relatively weak, only the first conductance peak for each of the modes can be resolved. Such behaviour is shown in Figure 3.7, as observed recently by Burzuri *et al.* [41]. Occasionally, Raman and IR spectroscopy are used in order to confirm the vibrational origin of the conductance peaks in question [42, 145, 146], and by using *ab initio* methods the vibrational peaks can be assigned to particular modes within the molecule [41,140,147].

The presence of conductance peaks corresponding to a simultaneous excitation of more than one vibrational mode have also been predicted theoretically [127], but thus

far have not been unambiguously observed (such a simultaneous excitation of more than one vibrational mode should be expected to occur with significantly lower efficiency). Furthermore, in experimental measurements one can often observe that following a step in the current-voltage characteristics, the current continues to increase with increasing applied bias. This often happens despite the theoretical calculations predicting plateaus in the IV curves. In Ref. [148], it has been suggested that such behaviour may be a result of weak coupling between electronic degrees of freedom and a collection of internal vibrational modes. This gives rise to overlapping Franck-Condon staircases which can be individually hard to resolve but which, cumulatively, result in a substantial current increase across a wide range of bias voltage in the resonant transport regime.

The situation is further complicated by the presence of more than one energy level within, or in the vicinity of, the bias window (although the former typically occurs only at relatively high bias voltage). Charge transport through such vibrationally-coupled multi-level systems has been investigated in a number of theoretical studies [30,149–152] which have demonstrated a wealth of physical behaviour that can be observed in these systems, especially in the case of slow vibrational relaxation.

The effects of vibrational anharmonicity in the molecular-junction setting were investigated theoretically by Koch and von Oppen in Ref. [153]. They have found that it plays only a rather trivial role in the overall transport behaviour as it predominantly gives rise to non-equally spaced differential conductance peaks.

3.5 Current noise

Although throughout this thesis we focus predominantly on the electric current and electronic conductance, we will also briefly investigate the zero-frequency current noise in single-molecule junctions, see discussion in Chapter 2.

Experimental investigations of the higher moments of current in single-molecule junctions are, to date, very limited. Almost all studies of zero-frequency current noise were performed within the off-resonant transport regime [154–157] where, as previ-

ously discussed, vibrational effects play only a minor role in the transport characteristics. On the other hand, the role of vibrational effects in zero-frequency current noise in the resonant transport regime has received a fair amount of theoretical attention [53, 54, 134, 158, 159] (and will also be discussed in Chapter 6). In their aforementioned seminal work, Koch and von Oppen also predicted giant Fano factors (i.e. high levels of zero-frequency current noise) in the Franck-Condon blocked region in case of weak vibrational relaxation [134] (although a similar effect was in parallel discussed by Takei *et al.* [160]). This behaviour was attributed to an *avalanche mechanism* of the charge transport. In the Franck-Condon blocked region, at low bias, occasionally a charge transfer event excites the molecule to a higher vibrational state, the system then experiences an avalanche of charge transfer events until the vibrational mode in question finally relaxes back to its ground state. Indeed, Fano factors of the order of 10^3 were observed experimentally in a Franck-Condon blocked single-molecule devices [42]. More recently, to account for the experimental observation of Secker *et al.* [148], Schinabeck *et al.* demonstrated that equally large levels of current noise can also be present in the case of relatively weak coupling to a multitude of vibrational modes [54].

Experimental studies of (zero-frequency) current noise in molecular junctions unfortunately remain very challenging, especially in the resonant tunnelling regime. Consequently, despite growing theoretical interest [3, 161, 162], experimental progress in this area has been disappointingly slow.

Chapter 4

Double quantum dot: non-equilibrium vibrational effects

...and when he said, "Oh no, they pay you to do this", I said, "You must be kidding!"

— William H. Miller

The simplest theoretical model which can be used to study vibrational effects in molecular junctions comprises a single molecular energy level coupled to a single vibrational mode (as well as the source and drain electrodes). This model, sometimes referred to as the Anderson-Holstein model, has been the focus of multiple theoretical studies and its general behaviour was discussed in Chapters 2 and 3. A natural next step is to consider a two-site molecular system. Here, in the first research chapter of this thesis, we therefore examine the effects of electron-vibrational coupling on transport properties of such a molecular double quantum dot. As we shall demonstrate, this system is of a fundamental interest since its transport properties are affected both by the phenomena occurring at the molecule-lead interfaces as well as by intra-molecular dynamics. Special emphasis in this chapter will be placed on the effects of non-equilibrium vibrational dynamics arising in the steady-state charge transport in the resonant regime.

4.1 Theoretical model

As discussed above, here we consider a double quantum dot or, equivalently, a molecular dimer system. Since the two molecular sites are covalently linked, we shall assume that they are both coupled to a single vibrational (phonon) mode. Each of the sites, hereafter denoted as left (L) and right (R), is also coupled to a respective lead (fermionic reservoir), as schematically depicted in Figure 4.1. The model used here can be used to describe certain types of molecular junctions (see detailed discussion in Chapter 6) although it may also form an appropriate description of carbon nanotube double quantum dots [46, 163–165].

4.1.1 Hamiltonian

Based on the discussion above, the total Hamiltonian for this system is given by:

$$H = H_0 + H_{\rm C} + H_{\rm T} + H_{\rm V} \ , \tag{4.1}$$

where it is convenient to define the Hamiltonian H_0,

$$H_0 = H_{\rm M} + H_{\rm B} + H_{\rm E} \ , \tag{4.2}$$

which accounts for the molecular site energy levels $\varepsilon_{\rm L}$ and $\varepsilon_{\rm R}$ ($H_{\rm M}$), the vibrational mode (a harmonic oscillator) of frequency ω_0 ($H_{\rm B}$), and the source and drain electrodes ($H_{\rm E}$):

$$H_{\rm M} = \varepsilon_{\rm L}\, a_{\rm L}^{\dagger} a_{\rm L} + \varepsilon_{\rm R}\, a_{\rm R}^{\dagger} a_{\rm R} \ ; \tag{4.3}$$

$$H_{\rm B} = \omega_0\, b^{\dagger} b \ ; \tag{4.4}$$

$$H_{\rm E} = \sum_{j={\rm L,R}} \sum_{k_j} \epsilon_{k_j} c_{k_j}^{\dagger} c_{k_j} \ . \tag{4.5}$$

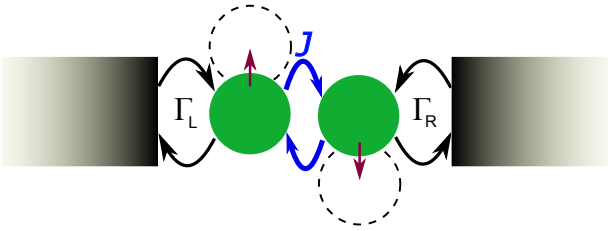


Figure 4.1: Schematic illustration of the system studied in this chapter. The two sites are coupled to each other with the strength J, and to the left and right electrodes with the strengths Γ_{L} and Γ_{R}, respectively.

In the above, $a_j^\dagger$ (a_j) and $c_{k_j}^\dagger$ (c_{k_j}) are the creation (annihilation) operators for an electron in state $|j\rangle$ on the site j on the double quantum dot and in state $|k_j\rangle$ on the left or right lead, respectively. Finally, the $b^\dagger$ (b) operator is the phononic creation (annihilation) operator of the vibrational mode.

The two sites (dots) are coupled to each other with the strength J (via the H_{T} Hamiltonian) and to the vibrational mode with strengths g_{L} and g_{R} for the left and right site, respectively (H_{C}):

$$H_{\mathrm{T}} = J(a_{\mathrm{L}}^\dagger a_{\mathrm{R}} + a_{\mathrm{R}}^\dagger a_{\mathrm{L}}) \ ; \tag{4.6}$$

$$H_{\mathrm{C}} = a_{\mathrm{L}}^\dagger a_{\mathrm{L}}(g_{\mathrm{L}}\, b^\dagger + g_{\mathrm{L}}^* b) + a_{\mathrm{R}}^\dagger a_{\mathrm{R}}(g_{\mathrm{R}}\, b^\dagger + g_{\mathrm{R}}^* b) \ . \tag{4.7}$$

Since the two spatially distinct sites are coupled to a 'shared' vibrational mode, it is important to account for the fact that the electron-phonon coupling constants, g_{L} and g_{R}, have a position-dependent phase [166–169]. Taking the position in the middle of the dots as the origin,[1] these can be defined as $g_{\mathrm{L}} = |g_{\mathrm{L}}|e^{-i\mathbf{q}\cdot\mathbf{d}/2}$ and $g_{\mathrm{R}} = |g_{\mathrm{R}}|e^{i\mathbf{q}\cdot\mathbf{d}/2}$ where $\mathbf{q}$ is the wavevector of the phonon mode and $\mathbf{d}$ is the separation between the two dots. Henceforth, the difference in phases of electron-phonon coupling will be denoted as $\xi = \mathbf{q}\cdot\mathbf{d}$.

Finally, the operator H_{V} accounts for the tunnel coupling between the sites and respective leads:

$$H_{\mathrm{V}} = \sum_{j=\mathrm{L,R}} \sum_{k_j} (V_{k_j} c_{k_j}^\dagger a_j + V_{k_j}^* a_j^\dagger c_{k_j}) \ . \tag{4.8}$$

[1] This choice is, naturally, inconsequential, as the only quantity of interest will be the phase difference between the electron-phonon couplings on the two sites.

The assumption that the leads are coupled to distinct sites (rather than to entire delocalized molecular orbitals) is well justified for tunnel coupling due to an exponential distance dependence of the tunnelling efficiency.

The electron-phonon coupling term can be eliminated from the above Hamiltonian by performing the polaron (Lang-Firsov) transformation introduced in Chapter 2,

$$\bar{H} = e^{S} H \, e^{-S} \ , \tag{4.9}$$

where $S = a_{\mathrm{L}}^{\dagger} a_{\mathrm{L}} \, \omega_0^{-1} (g_{\mathrm{L}} b^{\dagger} - g_{\mathrm{L}}^{*} b) + a_{\mathrm{R}}^{\dagger} a_{\mathrm{R}} \, \omega_0^{-1} (g_{\mathrm{R}} b^{\dagger} - g_{\mathrm{R}}^{*} b)$. The transformed Hamiltonian becomes:

$$H = \bar{H}_{\mathrm{M}} + H_{\mathrm{B}} + H_{\mathrm{E}} + \bar{H}_{\mathrm{T}} + \bar{H}_{\mathrm{V}} \ ; \tag{4.10}$$

$$\bar{H}_{\mathrm{M}} = \bar{\varepsilon}_{\mathrm{L}} a_{\mathrm{L}}^{\dagger} a_{\mathrm{L}} + \bar{\varepsilon}_{\mathrm{R}} a_{\mathrm{R}}^{\dagger} a_{\mathrm{R}} \ ; \tag{4.11}$$

$$\bar{H}_{\mathrm{T}} = J (X_{\mathrm{L}}^{\dagger} X_{\mathrm{R}} a_{\mathrm{L}}^{\dagger} a_{\mathrm{R}} + X_{\mathrm{R}}^{\dagger} X_{\mathrm{L}} a_{\mathrm{R}}^{\dagger} a_{\mathrm{L}}) \ ; \tag{4.12}$$

$$\bar{H}_{\mathrm{V}} = \sum_{j=\mathrm{L,R}} \sum_{k_j} (V_{k_j} X_j c_{k_j}^{\dagger} a_j + V_{k_j}^{*} X_j^{\dagger} a_j^{\dagger} c_{k_j}) \ . \tag{4.13}$$

Similarly to what we have discussed in Chapter 2, the energy levels of the two sites are now renormalized (polaron-shifted) such that $\bar{\varepsilon}_j = \varepsilon_j - \dfrac{|g_j|^2}{\omega_0}$ and the factors $X_j^{\dagger}$ (X_j) are the displacement operators:

$$X_j^{\dagger} = \exp \left(\frac{g_j}{\omega_0} \, b^{\dagger} - \frac{g_j^{*}}{\omega_0} \, b \right) \ , \tag{4.14}$$

which can be evaluated explicitly in the vibrational basis [49], see Appendix A. Importantly, they have been introduced both into the Hamiltonian describing molecule-lead coupling (as discussed in Chapter 2) as well as the one accounting for the coupling between the left and right site.

4.1.2 Phase difference in electron-phonon couplings

Since the effect of the difference in phases between electron-phonon couplings of the two sites will turn out to be of crucial importance, here we attempt to clarify their origin and experimental relevance. Generically, the Hamiltonian accounting for coupling between vibrational modes and charge carriers can be written as [36]:

$$H_{\mathrm{e-ph}} = \sum_{\mathbf{q}} M_{\mathbf{q}}\, \varrho(\mathbf{q})\, (b_{\mathbf{q}} + b^{\dagger}_{-\mathbf{q}}) \ , \tag{4.15}$$

where $M_{\mathbf{q}}$ is a coupling element characterising the nature of the interaction. In a typical solid state setting, this can be obtained from first principles (see Ref. [36] for bulk piezoelectric and deformation potential coupling, or Ref. [46] for the case of carbon nanotubes). The dependence of the electron-phonon coupling on the microscopic details of the latter can be absorbed into the effective coupling constants in the Hamiltonian (4.15) [170], as verified by a number of experimental studies [46,144,171]. By contrast, in a molecular setting ab-initio methods such as DFT might provide an informed choice [33], or one may resort to an effective coupling strength extracted from experimental data.

Since we only need to consider additional transport electrons (charge carriers), the charge density operator in Eq. (4.15), $\varrho(\mathbf{q})$, is given by:

$$\varrho(\mathbf{q}) = \sum_{j} a^{\dagger}_{j} a_{j} \int \mathrm{d}\mathbf{r}\, e^{-\mathrm{i}\mathbf{q}\cdot\mathbf{r}} \Psi_{j}(\mathbf{r})^{\dagger}\, \Psi_{j}(\mathbf{r}) \ , \tag{4.16}$$

where $a^{\dagger}_{j}$ (a_{j}) is the creation (annihilation) operator for a charge carrier on site j. Here, we have assumed that the wavefunctions are orthogonal, $\langle \Psi_{i}(\mathbf{r}) | \Psi_{j}(\mathbf{r}) \rangle = \delta_{ij}$.

In the case of a double quantum dot, the electron-phonon interaction Hamiltonian can then be written as:

$$H_{\mathrm{e-ph}} = \sum_{\mathbf{q}} (g_{L,\mathbf{q}}\, a^{\dagger}_{\mathrm{L}} a_{\mathrm{L}} + g_{R,\mathbf{q}}\, a^{\dagger}_{\mathrm{R}} a_{\mathrm{R}})(b_{\mathbf{q}} + b^{\dagger}_{\mathbf{-q}}) \ , \tag{4.17}$$

where the coupling elements are given by $M_{j,\mathbf{q}}$ multiplied by the Fourier transform of the electron density on the site j:

$$g_{j,\mathbf{q}} = M_{j,\mathbf{q}}\,\mathcal{P}[\Psi_j(\mathbf{r})]\ . \tag{4.18}$$

If the wavefunctions Ψ_{R} and Ψ_{L} are identical but centred at $\pm\mathbf{d}/2$, respectively, the coupling elements become, by the shift property of the Fourier transform [172]:

$$g_{L,\mathbf{q}} = e^{-\mathrm{i}\mathbf{q}\cdot\mathbf{d}/2} M_{j,\mathbf{q}}\,\mathcal{P}[\Psi(\mathbf{r})]\ , \tag{4.19}$$

$$g_{R,\mathbf{q}} = e^{\mathrm{i}\mathbf{q}\cdot\mathbf{d}/2} M_{j,\mathbf{q}}\,\mathcal{P}[\Psi(\mathbf{r})]\ , \tag{4.20}$$

and in the case of symmetric electron-phonon coupling $|g_{L,\mathbf{q}}| = |g_{R,\mathbf{q}}| = g_{\mathbf{q}}$ as:

$$g_{L,\mathbf{q}} = e^{-\mathrm{i}\mathbf{q}\cdot\mathbf{d}/2} g_{\mathbf{q}}\ , \tag{4.21}$$

$$g_{R,\mathbf{q}} = e^{\mathrm{i}\mathbf{q}\cdot\mathbf{d}/2} g_{\mathbf{q}}\ . \tag{4.22}$$

Finally, since the summation in Eq. (4.17) runs across the entire Brillouin zone, the coupling Hamiltonian can be more compactly written as:

$$H_{\mathrm{e-ph}} = \sum_{j,\mathbf{q}} a_j^\dagger a_j\,(g_{j,\mathbf{q}}^* b_{\mathbf{q}} + g_{j,\mathbf{q}} b_{\mathbf{q}}^\dagger)\ . \tag{4.23}$$

Under the assumption that the electronic degrees of freedom predominantly couple to a single phonon mode, as it is often the case in molecular systems, the Hamiltonian (4.23) reduces to the one in Eq. (4.7). Since the choice of origin is arbitrary, the important quantity in the transport through the considered double quantum dot is not the phase of the electron-phonon coupling itself, but rather the phase difference between the two sites. Consider for example a longitudinal mode propagating through a carbon nanotube. The difference in phases is given by $\xi = \mathbf{q}\cdot\mathbf{d}$ which in this case reduces to:

$$\xi = |\mathbf{q}| \times |\mathbf{d}| = \frac{2\pi d}{L}, \tag{4.24}$$

where L is the wavelength of the relevant phonon. Thus, what determines the value of ξ is the separation between the two sites in relation to L. In the case of carbon nanotube double quantum dots, it may be possible to change the value of ξ by shifting the relative positions of the two dots by using different electrostatic gate electrodes. Changing the distance between the two sites (with respect to the phonon mode) is not possible in single-molecule junctions. There, ξ is an immutable property of a given vibrational mode.

4.1.3 Quantum master equation

In this section, we derive a second-order quantum master equation within the Born-Markov approximation (as discussed in Chapter 2), describing the dynamics of the studied system. The first choice we must make is that of the interaction picture in which the quantum master equation will be derived. This choice is generally non-trivial [173–175], and here we will work in the 'local' interaction picture of $\bar{H}_0 = \bar{H}_{\mathrm{M}} + H_{\mathrm{B}} + H_{\mathrm{E}}$. In this interaction picture, the Liouville-von Neumann equation for the evolution of the total density matrix becomes:

$$\frac{\mathrm{d}\tilde{\sigma}(t)}{\mathrm{d}t} = -\mathrm{i}[\tilde{H}_{\mathrm{V}}(t) + \tilde{H}_{\mathrm{T}}(t), \tilde{\sigma}(t)] \ , \tag{4.25}$$

where

$$\tilde{H}_{\mathrm{V}}(t) = e^{\mathrm{i}\bar{H}_0 t}\bar{H}_{\mathrm{V}}e^{-\mathrm{i}\bar{H}_0 t} = \sum_{j,k_j}\left(V_{k_j}c_{k_j}^{\dagger}e^{\mathrm{i}(\epsilon_{k_j}-\bar{\varepsilon}_j)t}a_j\tilde{X}_j(t) + \mathrm{H.c.}\right) \ , \tag{4.26}$$

and similarly

$$\tilde{H}_{\mathrm{T}}(t) = e^{\mathrm{i}\bar{H}_0 t}\bar{H}_{\mathrm{T}}e^{-\mathrm{i}\bar{H}_0 t} \ ; \tag{4.27}$$

$$\tilde{X}_j(t) = e^{\mathrm{i}\bar{H}_0 t}X_j e^{-\mathrm{i}\bar{H}_0 t} \ . \tag{4.28}$$

Integrating Eq. (4.25) and substituting the solution into the second commutator,

one obtains:

$$\frac{\mathrm{d}\tilde{\sigma}(t)}{\mathrm{d}t} \;=\; -\mathrm{i}[\tilde{H}_{\mathrm{T}}(t),\tilde{\sigma}(t)] - \mathrm{i}[\tilde{H}_{\mathrm{V}}(t),\tilde{\sigma}(0)] - \int_0^t \mathrm{d}s\; [\tilde{H}_{\mathrm{V}}(t),[\tilde{H}_{\mathrm{V}}(s)+\tilde{H}_{\mathrm{T}}(s),\tilde{\sigma}(s)]] \;. \tag{4.29}$$

We now proceed to make the Born-Markov approximation and extend the integration limit in Eq. (4.29) to infinity, as discussed in Chapter 2. Then, we can expand the commutators and evaluate the resulting integrals using the Cauchy relation:

$$\int_0^\infty \mathrm{d}s\; e^{\pm\mathrm{i}\Omega s} = \pi\delta(\Omega) \pm \mathrm{i}\frac{\mathcal{P}}{\Omega}\;, \tag{4.30}$$

where $\mathcal{P}$ denotes Cauchy principal value (although in what follows we shall disregard the imaginary components). Moving back to the Schrödinger picture gives the following master equation description for the (joint) dynamics of the double quantum dot and the vibrational mode:

$$\begin{aligned}\frac{\mathrm{d}\bar{\rho}(t)}{\mathrm{d}t} &= -\mathrm{i}\left[\bar{H}_{\mathrm{S}},\bar{\rho}(t)\right] \\ &\quad + \sum_j \frac{\Gamma_j}{2}\left(a_j^\dagger W_j^\dagger \bar{\rho}(t) a_j X_j + a_j^\dagger X_j^\dagger \bar{\rho}(t) a_j W_j - a_j X_j a_j^\dagger W_j^\dagger \bar{\rho}(t) - \bar{\rho}(t) a_j W_j a_j^\dagger X_j^\dagger\right) \\ &+ \sum_j \frac{\Gamma_j}{2}\left(a_j Y_j \bar{\rho}(t) a_j^\dagger X_j^\dagger + a_j X_j \bar{\rho}(t) a_j^\dagger Y_j^\dagger - a_j^\dagger X_j^\dagger a_j Y_j \bar{\rho}(t) - \bar{\rho}(t) a_j^\dagger Y_j^\dagger a_j X_j\right)\;,\end{aligned} \tag{4.31}$$

where $\bar{H}_{\mathrm{S}} = \bar{H}_{\mathrm{M}} + H_{\mathrm{B}} + \bar{H}_{\mathrm{T}}$. The first term describes the coherent evolution within the double quantum dot while the subsequent terms account for the incoherent hopping on and off the double quantum dot with the rates $\Gamma_j = 2\pi|V_j|^2\varrho_j$ (modulated by the relevant Franck-Condon factors) where ϱ_j is the constant density of states in the lead j. The matrix elements of the W_j and Y_j operators in the vibrational basis are given by: $\langle v_m|W_j|v_p\rangle = f_j(\bar{\epsilon}_j + \omega_0(v_m - v_p))\langle v_m|X_j|v_p\rangle$ and $\langle v_m|Y_j|v_p\rangle = (1 - f_j(\bar{\epsilon}_j + \omega_0(v_m - v_p)))\langle v_m|X_j|v_p\rangle$. Here, $f_j(\epsilon)$ denotes the Fermi distribution function for the j-lead, $f_j(\epsilon) = 1/(e^{(\epsilon-\mu_j)/k_{\mathrm{B}}T}+1)$ and the chemical potential of the leads is determined by the (symmetrically) applied bias voltage V_{b}: $\mu_{\mathrm{L}} = +V_{\mathrm{b}}/2$ and $\mu_{\mathrm{R}} = -V_{\mathrm{b}}/2$, respectively.

We assume that only one additional electron can be found on the double quantum dot at any given time due to strong electron-electron repulsion (Coulomb blockade regime). Instead of including an explicit electron-electron interaction term in the Hamiltonian in Eq. (4.1), this is ensured by excluding the doubly-populated state from the electronic Hilbert space, and the fact that the quantum master equation (4.31) is trace-preserving, $\mathrm{Tr}[\bar{\rho}(t)] = 1$. The Hilbert space for the electronic degrees of freedom spans, therefore, three states ($|\mathrm{L}\rangle$, $|\mathrm{R}\rangle$, and $|\mathrm{E}\rangle$) corresponding to an electron occupying left or right dot, and the double quantum dot being empty, respectively.

To determine the value of the stationary electric current flowing through the system, we proceed in the way described in Chapter 2 and solve the quantum master equation (4.31) in the steady-state limit:

$$\frac{\mathrm{d}\bar{\rho}(t)}{\mathrm{d}t} = 0 \ , \tag{4.32}$$

and then compute the electric current as the expectation value of the current operator in the stationary state:

$$I = \langle I_j \rangle_{\mathrm{stat}} = \mathrm{Tr}(I_j \bar{\rho}_{\mathrm{stat}}). \tag{4.33}$$

Here, I_j are the operators describing the current flowing through the j-interface which can be inferred from the quantum master equation (4.31):

$$I_j \bar{\rho} = \frac{\Gamma_j}{2} \left(a_j^\dagger W_j^\dagger \bar{\rho}(t) a_j X_j + a_j^\dagger X_j^\dagger \bar{\rho}(t) a_j W_j - a_j Y_j \bar{\rho}(t) a_j^\dagger X_j^\dagger - a_j X_j \bar{\rho}(t) a_j^\dagger Y_j^\dagger \right) \ . \tag{4.34}$$

4.2 Results and Discussion

The time-evolution of the studied system has to be described in a truncated Hilbert space of the molecular vibrational mode. In this chapter, we shall include $n = 100$ vibrational states, which yields sufficient numerical convergence. Eq. (4.32) is therefore given here in a Hilbert space of dimension $3n \times 3n$. It will be solved using Krylov-subspace techniques in a way analogous to the one described by Flindt *et al.* [56]. The method amounts to solving Eq. (4.32) in a subspace with reduced dimension $9n^2 \times p$

(p is typically around 50) by means of Arnoldi iteration, avoiding an explicit evaluation of the Liouvillian [51, 176]. Generally, preconditioning is required to produce correct results. The outcomes of these calculations will then be tested against increasing the dimension of the Krylov subspace (p) and by comparing them to the results obtained using a direct method (direct singular value decomposition) in smaller vibrational Hilbert spaces.

In what follows, we distinguish between two different parameter regimes depending on the relative magnitudes of dot-lead ($\Gamma_{\mathrm{L}}, \Gamma_{\mathrm{R}}$) and inter-dot couplings (J). First, a strong inter-dot coupling regime where the coupling between the sites is much stronger than between the dots and the leads ($J \gg \Gamma_{\mathrm{L}}, \Gamma_{\mathrm{R}}$) and second, a weak inter-dot coupling regime where the opposite is true ($\Gamma_{\mathrm{L}}, \Gamma_{\mathrm{R}} > J$). We will describe the transport properties in both these regimes in the following subsections.

4.2.1 Strong inter-dot coupling regime

In this section, we study a double quantum dot system that is weakly coupled to the source and drain electrodes (as compared to the inter-dot coupling, J). Figure 4.2(a) shows the IV characteristics for such a system. For simplicity, we consider a completely symmetric case such that $\bar{\varepsilon}_{\mathrm{L}} = \bar{\varepsilon}_{\mathrm{R}}$, $|g_{\mathrm{L}}| = |g_{\mathrm{R}}|$ and $\Gamma_{\mathrm{L}} = \Gamma_{\mathrm{R}}$. As expected, the system with strong inter-dot coupling behaves similarly to a single quantum dot (single-site molecular junction) coupled to a vibrational mode. The onset in the IV trace occurs when the chemical potential of the source electrode is equal to the polaron-shifted energy of the left dot $\bar{\varepsilon}_{\mathrm{L}}$. The current through the system then increases in a stepwise manner as consecutive vibrational levels fall within the bias window. The peaks in the differential conductance are separated by $2\omega_0$ and the relative heights of these steps can be explained qualitatively by considering the values of the $|\langle v_m|X|0\rangle|^2$ elements (accounting for the Franck-Condon overlap between the vibrational groundstate and the m^{th} vibrational excited state) [134, 137, 177]. Unlike for a single-site molecule, however, the phase difference in the electron-phonon coupling strengths between the

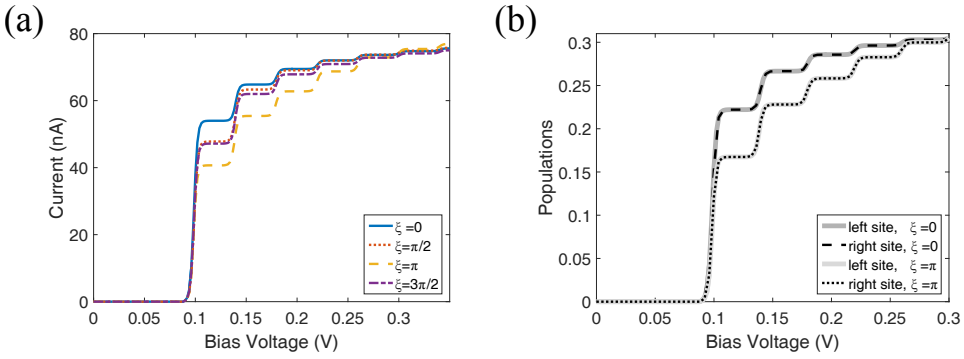


Figure 4.2: (a) Current-voltage characteristics and (b) Voltage-dependent populations of the sites in a strongly coupled two-site molecular system. The calculation was performed for a symmetric system: $\bar{\varepsilon}_{\mathrm{L}} = \bar{\varepsilon}_{\mathrm{R}} = 50$ meV. The energy of the vibrational mode was taken to be $\omega_0 = 0.2$ eV, the electron-phonon coupling constants $|g_{\mathrm{L}}| = |g_{\mathrm{R}}| = 0.18$ eV, the coupling between the sites $J = -0.3$ eV and between the sites and the leads as $\Gamma_{\mathrm{L}} = \Gamma_{\mathrm{R}} = 1$ meV. The temperature was assumed to be 10 K, leading to appreciable thermal broadening.

sites can result in an overall current suppression, especially for low vibrational levels, as shown in Figure 4.2(a). It is important to stress that the incoherent hopping (on and off the leads) is independent of the phase of the electron-phonon coupling. The reason the transport is retarded in the presence of a phase difference in electron-phonon coupling between the sites can be explained as follows: when the two sites couple to the vibrational mode with the same phase (so that $\xi = 2\pi$ or a multiple thereof) the factor $X_{\mathrm{L}}^{\dagger} X_{\mathrm{R}}$ in the inter-dot coupling Hamiltonian $\bar{H}_{\mathrm{T}}$ [see Eq. (4.12)] becomes an identity operator on the vibrational space, $X_{\mathrm{L}}^{\dagger} X_{\mathrm{R}} = \mathbb{1}$. This means that the coherent transition between the sites takes place without any vibrational excitations. However, if the sites couple to the vibrational mode with different phases this is no longer the case and the coherent evolution within the double quantum dot will be accompanied by a phonon emission. Higher vibrational states produced in such a way will then be less efficient in tunnelling out to the leads due to poorer Franck-Condon overlap leading to an overall suppression of the current. As shown in Figure 4.2(b), the charge populations on the two sites are equal independently of the applied bias and of phase difference in the electron-phonon coupling. This should come as no surprise given that the two sites are strongly coupled and the system is entirely symmetric.

In order to confirm the non-equilibrium origin of the observed effects, we proceed to

study the transport properties of the considered double quantum dot in the presence of damping of the vibrational mode. Now, the quantum master equation has the form [50, 135]:

$$\frac{\mathrm{d}\bar{\rho}(t)}{\mathrm{d}t} = \text{left-hand side of Eq. (4.31)}$$
$$+\gamma_{\mathrm{d}}\left(N+1\right)\left[b\bar{\rho}(t)b^{\dagger}-\frac{1}{2}b^{\dagger}b\bar{\rho}(t)-\frac{1}{2}\bar{\rho}(t)b^{\dagger}b\right]+\gamma_{\mathrm{d}}N\left[b^{\dagger}\bar{\rho}(t)b-\frac{1}{2}bb^{\dagger}\bar{\rho}(t)-\frac{1}{2}\bar{\rho}(t)bb^{\dagger}\right], \tag{4.35}$$

where γ_{d} is the phenomenological damping rate, and $N = [\exp(\omega_0/k_{\mathrm{B}}T) - 1]^{-1}$ is the mean number of the vibrational quanta in a thermalised mode with frequency ω_0, as given by the Bose-Einstein distribution. At the low temperatures considered here, in thermal equilibrium, the considered vibrational mode is found almost entirely in its ground-state. (We note that vibrational relaxation times in carbon nanotube quantum dots and molecular junctions can be, however, quite long, as has been observed experimentally [42, 178].)

In Figure 4.3(a), we show the IV characteristics for $\xi = \{0, \pi\}$ calculated while allowing full for the non-equilibrium dynamics of the vibrational mode ($\gamma_{\mathrm{d}} = 0$, as in Figure 4.2), and introducing very fast damping of the mode in question ($1/\gamma_{\mathrm{d}} \to 0$). In the case of very fast damping, the current suppression discussed above is indeed washed away, and furthermore, the transport characteristics are independent of ξ, as expected.

Let us now consider the dependence of the current through the molecule (at the bias voltage $V_{\mathrm{b}} = 2\bar{\varepsilon}_{\mathrm{L}} + \omega_0$ and for $\gamma_{\mathrm{d}} = 0$) on the strength of inter-site coupling J in the limit $J \gg \Gamma_{\mathrm{L}}, \Gamma_{\mathrm{R}}$. In the case of $\xi = 0$, the transport is virtually independent of J as it is limited by incoherent hopping rates Γ_j, as demonstrated in Figure 4.3(b). However, as discussed above, when ξ is non-zero, the internal dynamics of the system becomes relevant. Now, for $\xi = \pi/2$ and $\xi = \pi$, increasing the strength of the inter-site coupling J leads to a suppression of current. This surprising result can be understood by recalling that for non-zero ξ the coherent transition between the sites 'produces'

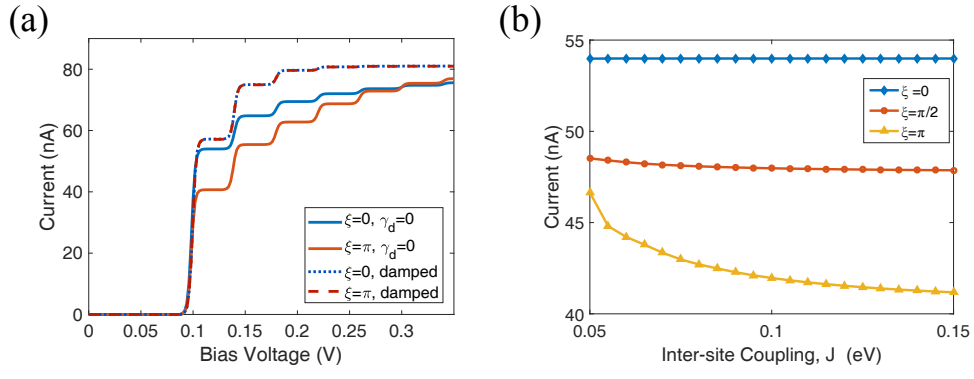


Figure 4.3: (a) Current-voltage characteristics and (b) Current at bias voltage $V_{\mathrm{b}} = 2\bar{\varepsilon}_{\mathrm{L}} + \omega_0$ (first step in the current-voltage characteristics). The calculations were performed for a symmetric system: $\bar{\varepsilon}_{\mathrm{L}} = \bar{\varepsilon}_{\mathrm{R}} = 50$ meV. The energy of the vibrational mode was taken to be $\omega_0 = 0.02$ eV, the electron-phonon coupling constants $|g_{\mathrm{L}}| = |g_{\mathrm{R}}| = 0.018$ eV, the coupling between the sites and the leads is $\Gamma_{\mathrm{L}} = \Gamma_{\mathrm{R}} = 1$ meV and the temperature was assumed to be 10 K.

higher vibrational states which then give rise to the observed current suppression. The stronger the coupling J, the greater vibrational excitation can accumulate before the electron tunnels out into the leads.

Finally, let us stress that one should expect this parameter regime (where inter-dot coupling J is stronger than the coupling to the leads) to be appropriate in the case of most single-molecule junctions. The strength of the electron-phonon coupling in these systems is often estimated experimentally by considering the relative heights of the Franck-Condon steps [42, 144]. As shown above, one has to be careful in using the same approach in two- (or multiple-)site systems where phase difference in electron-phonon coupling becomes relevant. Another surprising conclusion from the presented results is that the intramolecular dynamics can quite significantly affect the transport properties of the studied system in this parameter regime despite the fact that the transport efficiency is limited by the rates of electron transfer at the molecule-lead interfaces.

4.2.2 Weak inter-dot coupling regime

Let us now consider the reverse situation, that is, when the two sites (dots) are weakly coupled to each other but interact with the electrodes more strongly.[2] As we will show here, this case delivers somewhat richer set of physical phenomena. Once again, we shall first focus on a symmetric system.

As before, when there is no phase difference in the vibrational coupling between the sites ($\xi = 0$), one can observe a stepwise increase in the current through the system, see Figure 4.4(a). This, once again, can be explained by vibrational effects in tunnel coupling between the sites and the leads. Even though the bottleneck in the overall transport is now the coherent hopping between the sites, the vibrational effects in incoherent hopping on the molecule will play an important role as long as the hopping rates Γ_j and inter-site coupling J are comparable.

Moving on to the case of non-zero ξ, we can see that once again difference in phases of electron-phonon coupling induces a current suppression. In addition, unlike in the previous section, the non-zero phase difference leads to negative differential conductance – a decrease in current with increasing bias voltage. As we stated before, in this parameter regime, it is the inter-site transition that limits the overall transport rate. Hence, the vibrational excitations occurring in the case of non-zero ξ are not as important. What is crucial now is how the phase difference in electron-phonon couplings affects the $|L\rangle \leftrightarrow |R\rangle$ transition. As we shall demonstrate below, it turns out that this transition is suppressed for non-zero ξ (resulting in the observed current suppression) and is even less efficient for higher vibrational states, giving rise to the negative differential conductance shown in Figure 4.4(a).

Since it is the coherent hopping between the sites that is the rate-limiting step in the overall charge transport, the populations of the two sites are no longer equal, see Figure 4.4(b). In the case of $\xi = 0$, populations of the two sites increase with

[2]Since our focus lies again in the resonant regime of transport, we may again make use of the second-order quantum master equation. It should be remembered, however, that the quantum master equation (4.31) is perturbative with respect to the molecule-leads coupling.

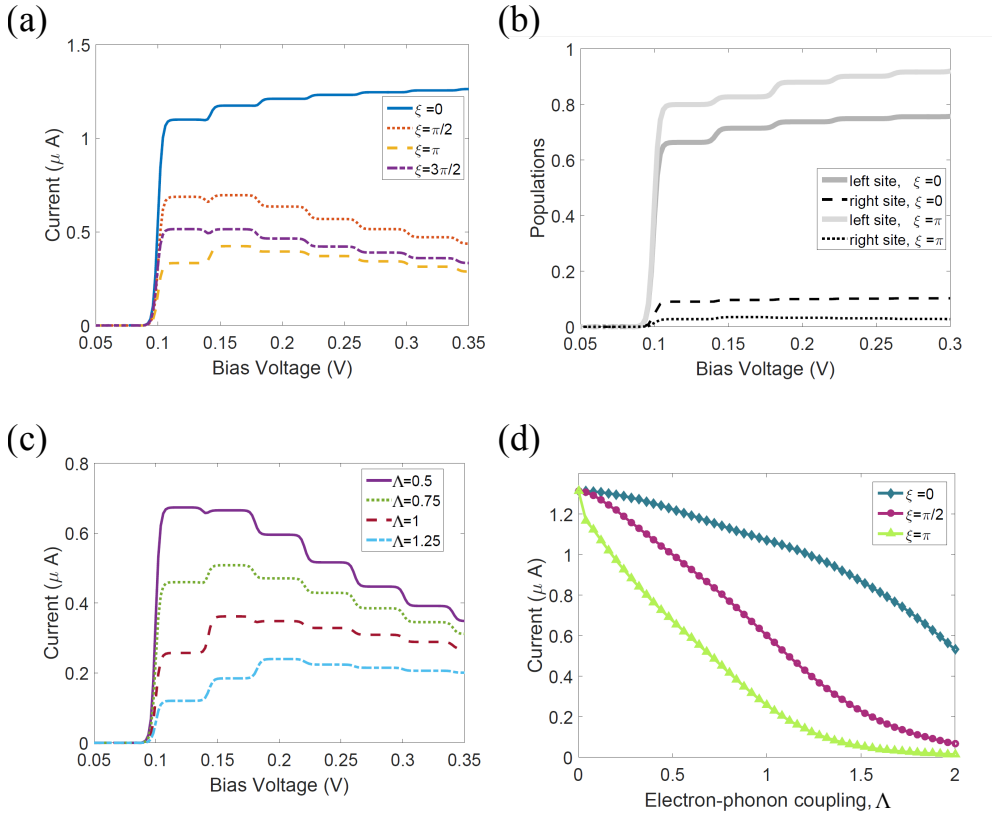


Figure 4.4: (a) Current-voltage characteristics and (b) Voltage-dependent populations of the sites in a strongly coupled two-site molecular system. The model is identical to the one used in Figure 4.2 except for the coupling between the sites, $J = -0.01$ eV, and between the sites and the leads: $\Gamma_{\rm L} = \Gamma_{\rm R} = 0.05$ eV. (c) Current-voltage characteristics and (d) Current at bias voltage $V_{\rm b} = 2\bar{\varepsilon}_{\rm L} + \omega_0$ for a symmetric DQD: $\bar{\varepsilon}_{\rm L} = \bar{\varepsilon}_{\rm R} = 0.3$. The energy of the vibrational mode was taken to be $\omega_0 = 0.2$ eV, the electron-phonon coupling constants $|g_{\rm L}| = |g_{\rm R}| = \Lambda\omega_0$, the inter-site coupling, $J = 0.01$ eV and between the sites and the leads, $\gamma_{\rm L} = \gamma_{\rm R} = 0.05$ eV, $T = 10$ K.

the applied bias voltage. However, if the sites couple to the vibrational mode with different phases, an increase in $V_{\rm b}$ is accompanied by a decrease in the population of the right site (correlating with the current through the double quantum dot). This demonstrates a rather different physical origin of observed effects as compared with the ones reported in Section 4.2.1, *c.f.* Figure 4.2(b).

To understand the origin of the observed negative differential conductance in more detail, let us now consider transport through the two-site system for different values of the electron-phonon constant. Current-voltage characteristics for different values of the dimensionless electron-phonon coupling parameter $\Lambda = |g|/\omega_0$ are shown in Figure 4.4(c). The position of the maximum value of the current shifts depending on the value

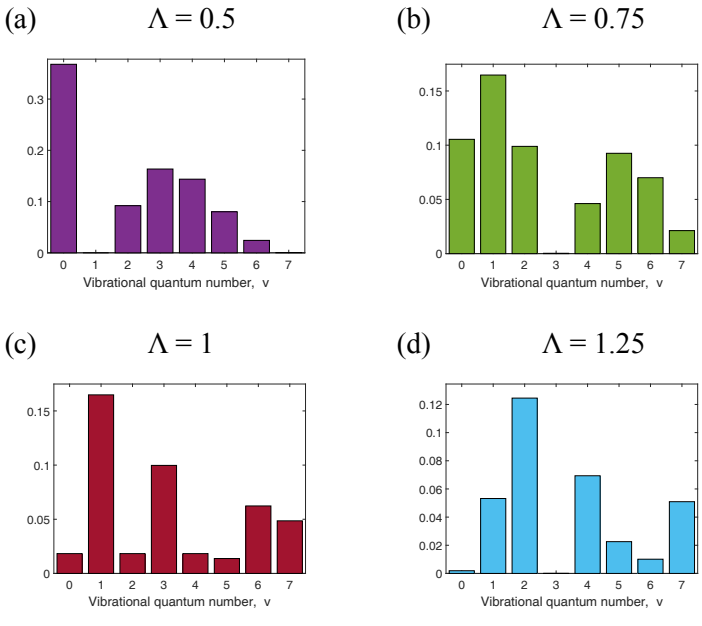


Figure 4.5: Square-moduli of diagonal matrix elements of $X_{\mathrm{L}}^{\dagger}X_{\mathrm{R}}$ operators for different values of Λ as used in Figure 4.4(c).

of Λ. This can be qualitatively related to the magnitudes of the diagonal elements of the $X_{\mathrm{L}}^{\dagger}X_{\mathrm{R}}$ operator, see Figure 4.5, and explained as follows. As can be seen in Eq. (4.12), the displacement operators affect the overall efficiency of the coherent hopping between the sites. In particular, the $X_{\mathrm{L}}^{\dagger}X_{\mathrm{R}}$ and $X_{\mathrm{R}}^{\dagger}X_{\mathrm{L}}$ operators can be written as [49]:

$$X_{\mathrm{L}}^{\dagger}X_{\mathrm{R}} = \exp\left[\left(\frac{g_{\mathrm{L}} - g_{\mathrm{R}}}{\omega}\right) b^{\dagger} - \left(\frac{g_{\mathrm{L}}^{*} - g_{\mathrm{R}}^{*}}{\omega}\right) b\right] \tag{4.36}$$

(disregarding the inconsequential $\exp[\mathrm{i}\,\mathrm{Im}(g_{\mathrm{L}}g_{\mathrm{R}}^{*}/\omega_0^2)]$ factor) and its Hermitian conjugate, accordingly. For the symmetric case studied in this chapter, $g_{\mathrm{L}} = ge^{-\mathrm{i}\xi/2}$ and $g_{\mathrm{R}} = ge^{\mathrm{i}\xi/2}$ so that:

$$X_{\mathrm{L}}^{\dagger}X_{\mathrm{R}} = \exp(\alpha\, b^{\dagger} - \alpha^{*} b)\ , \tag{4.37}$$

where $\alpha = 2i\dfrac{g}{\omega_0}\sin(\xi/2)$. The diagonal elements in the vibrational basis of this operator are given by [49]:

$$\langle v|X_{\mathrm{L}}^{\dagger}X_{\mathrm{R}}|v\rangle = \exp(-|\alpha|^2/2)\ L_v(|\alpha|^2)\ , \tag{4.38}$$

where v is a vibrational quantum number and L_v is a Laguerre polynomial of order v.

From this it can be seen that although the magnitude of $\langle v|X_{\mathrm{L}}^{\dagger}X_{\mathrm{R}}|v\rangle$ varies non-trivially with v, due to the exponential term in Eq. (4.38), the diagonal elements of the $X_{\mathrm{L}}^{\dagger}X_{\mathrm{R}}$ ($X_{\mathrm{R}}^{\dagger}X_{\mathrm{L}}$) operator should be maximum at $\xi = 0$ and decrease towards $\xi = \pi$. Similarly, for a given ξ, their magnitude should also decrease with increasing Λ. One can see that these trends correlate well with the conductance of the double quantum dot, as shown in Figure 4.4. In Figure 4.5, we also consider the square-moduli of diagonal matrix elements of $X_{\mathrm{L}}^{\dagger}X_{\mathrm{R}}$ operators for different values of Λ, as used in calculation in Figure 4.4(c). One can notice that the maximum current in Figure 4.4(c) occurs at bias voltage for which the vibrational level v, corresponding to the largest $|\langle v|X_{\mathrm{R}}^{\dagger}X_{\mathrm{L}}|v\rangle|^2$ matrix element enters the bias window: compare Figure 4.4(c) and Figure 4.5. However, the relative magnitudes of the steps in the current-voltage characteristics cannot be as easily correlated with values of $\langle v|X_{\mathrm{R}}^{\dagger}X_{\mathrm{L}}|v\rangle$. The observed values of electric current result from a rather complex interplay between vibrational effects during hopping on and off the double quantum dot and the dynamics within the system. Finally, similarly to what has been done in Section 4.2.1, it can be demonstrated that damping of the vibrational mode lifts the observed negative differential conductance.

It is also interesting to consider the value of current at the first step of the IV trace (at $V_{\mathrm{b}} = 2\bar{\varepsilon}_{\mathrm{L}} + \omega_0$) as a function of Λ and ξ, see Figure 4.4(d). One can observe two overlapping effects. Firstly, a decrease in transport efficiency as the electron-phonon coupling (Λ) increases – this is fundamentally an example of the Franck - Condon blockade [134,135]. Secondly, the current declines as the difference in phases of electron-phonon coupling ξ deviates from 0 (or 2π) – the effect described and explained above.

We have hitherto considered charge transport through a degenerate double quantum dot, i.e. when $\bar{\varepsilon}_{\mathrm{L}} = \bar{\varepsilon}_{\mathrm{R}}$. Let us finish this section by briefly considering a case in which the energy levels of the two sites are detuned (for example due to an asymmetric structure of the molecule [85]). Current-voltage characteristics for this situation are shown in Figure 4.6. Firstly, introducing an energy gap between the sites decreases the current through the double quantum dot as it retards the efficiency of $|L\rangle \leftrightarrow$

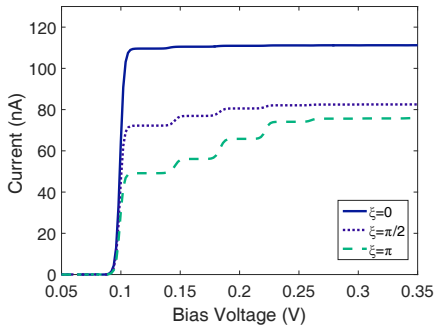


Figure 4.6: Current-voltage characteristics for a detuned double quantum dot: $\bar{\varepsilon}_{\mathrm{L}} = 0.05$ eV, $\bar{\varepsilon}_{\mathrm{R}} = 0.15$ eV. The energy of the vibrational mode was taken to be $\omega_0 = 0.02$ eV, the electron-phonon coupling constants $|g_{\mathrm{L}}| = |g_{\mathrm{R}}| = 0.018$ eV, the inter-site coupling, $J = -0.01$ eV and between the sites and the leads, $\gamma_{\mathrm{L}} = \gamma_{\mathrm{R}} = 0.05$ eV, $T = 10$ K.

$|R\rangle$ transition. Moreover, for a considerable detuning between the sites, the negative differential conductance (observed in $\bar{\varepsilon}_{\mathrm{L}} = \bar{\varepsilon}_{\mathrm{R}}$ case) is lifted. Now, higher vibrational states (on the left site) are in fact more efficient in tunnelling from the left to right site, especially into lower vibrational states (on the right site). Thus, increasing the bias voltage (resulting in an increase in the populations of higher vibrational levels) leads to an overall increase in the current through the double quantum dot.

4.3 Conclusions

In this chapter, we have derived a quantum master equation that can describe charge transport through a two-site molecular system (or a carbon nanotube double quantum dot) in which both of the sites (quantum dots) are coupled to a single shared vibrational mode. The method used here relies on a (perturbative) Born-Markov approximation with respect to lead-dot coupling but, unlike most previous studies of similar model systems (with the notable exception of Ref. [179]), treats electron-phonon interactions exactly (by incorporating the vibrational degrees of freedom in the considered Hilbert space). Using this method we have demonstrated that, depending on the phase difference in electron-phonon couplings ξ, one can observe current suppression and/or negative differential conductance in transport through the studied system.

Even the symmetric double quantum dot system which we have focused on here (in which $\Gamma_{\mathrm{L}} = \Gamma_{\mathrm{R}}$, $|g_{\mathrm{L}}| = |g_{\mathrm{R}}|$) exhibits a wealth of physical behaviour. Rather than focusing on the details of the charge transport characteristics in these systems, it is therefore important to stress here the critical conclusion of this chapter: Transport properties of extended molecular systems (or their carbon nanotube quantum dot equivalents) can be significantly affected by intramolecular vibrational dynamics stemming from coupling of the sites to a shared vibrational environment. These effects will be especially important in the presence of slow vibrational relaxation when large non-equilibrium phononic populations can be generated in the steady-state limit.

Chapter 5

Pariser-Parr-Pople-based approach

I decided this was a good
opportunity. It turned out well.

— John A. Pople

The molecular systems discussed in this thesis were hitherto described in a phenomenological manner: as a 'site' or a collection thereof. From a perspective of a chemist, this is rather unsatisfactory. Furthermore, it is not always clear how to best phenomenologically describe a given molecular structure. Consequently, the site models of the type discussed in the previous chapters, by their very construction, can only describe the phenomena that they were designed to capture – effectively providing an *a posteriori* modelling platform. On the other hand, the commonly used *ab initio* or DFT-based models are typically computationally expensive, often cannot adequately capture the crucial electron-electron correlations, and their complexity can often obscure the physical mechanisms at play. One solution to the above problem, which will be adopted here, is to rely on the semi-empirical Pariser-Parr-Pople (PPP) Hamiltonian. As described in Section 5.1, it captures the structural details of the molecular systems (also on a quantitative level) while simultaneously accounting for the many-body effects present in the studied structures.

Here, we will use the PPP Hamiltonian to describe charge transport through a prototypical junction comprising a spiro-conjugated molecular system (hitherto not con-

sidered in the transport setting in the literature). With this approach we shall uncover the unusual transport properties of the considered structure. As we will demonstrate, its peculiar behaviour originates from quantum interference between spatially degenerate electronic energy levels. However, populating these levels results in Jahn-Teller distortion (which is a phenomenon of a vibronic origin). We will therefore proceed to demonstrate how the electron-vibrational interactions can be incorporated into the semi-empirical framework used here, and study the interplay between the quantum-interference and vibrational effects present in the considered spiro-conjugated molecular junction.

5.1 Pariser-Parr-Pople Hamiltonian

The celebrated PPP model [180–182] can be most simply viewed as a many-body extension of the well-known Hückel (or tight-binding) model. In general, we are interested in describing the π-electronic structure of an aromatic molecule consisting of M sp^2 carbon centres. Similarly to the Hückel Hamiltonian, we work in the basis of M carbon sites (in the simplest picture the p_z orbitals), each with energy ε_i. The carbon sites i and j are coupled to each other through the kinetic part of the Hamiltonian with the strength t_{ij}, which therefore reflects the structure of the molecule. Unlike the Hückel treatment, however, the PPP model also accounts for the on-site electron-electron interactions (repulsion between two electrons of opposite spin occupying the same carbon site), as well as the long-range repulsion (between electrons occupying different sites). In the second-quantisation formalism, the PPP Hamiltonian can be written as:

$$H_{\mathrm{PPP}} = \sum_{i}^{M} \varepsilon_i \, n_i + \sum_{\sigma=\{\uparrow,\downarrow\}} \sum_{<i,j>} t_{ij}(a_{i\sigma}^{\dagger} a_{j\sigma} + a_{j\sigma}^{\dagger} a_{i\sigma}) + \sum_{i}^{M} U(n_{i\uparrow} - \frac{1}{2})(n_{i\downarrow} - \frac{1}{2}) + \sum_{i \neq j} \frac{V_{ij}}{2}(n_i - 1)(n_j - 1) \ , \quad (5.1)$$

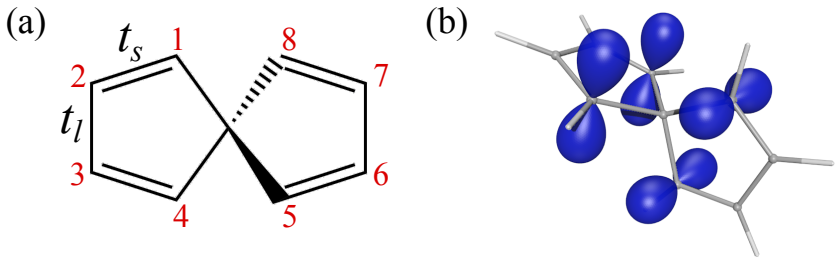


Figure 5.1: (a) Structure of the spiro[4.4]nonatetraene molecule. (b) Schematic of the SNT molecule showing the alignment of the p_z orbitals around the spiro-link.

where $a_{i\sigma}$ ($a^\dagger_{i\sigma}$) is the fermionic annihilation (creation) operator for an electron on site i with spin $\sigma = \{\uparrow, \downarrow\}$, $n_{i\sigma} = a^\dagger_{i\sigma} a_{i\sigma}$, and $n_i = n_{i\uparrow} + n_{i\downarrow}$. Furthermore, U is the on-site, and V_{ij} the inter-site electrostatic repulsion. We follow the usual convention and describe the latter using the Ohno parametrisation: $V_{ij} = U/\sqrt{1 + r_{ij}^2 U^2/207.3\text{eV}^2}$, where r_{ij} is the distance between the two p_z orbitals (in Å) [183]. Additionally, since the PPP model can successfully yield quantitative predictions [184], it is important to correlate the values of the hopping integrals t_{ij} with the appropriate molecular bond-lengths, as will be done in Section 5.2.

5.2 The case study: Spiro[4.4]nonatetraene

Here, as a case study, we shall consider a junction incorporating a spiro[4.4]nonateraene (SNT) molecule, a prototypical spiro-conjugated molecular system, pictured in Figure 5.1(a). Spiro-conjugated molecules comprise conjugated moieties connected via a saturated link in such a way that the π-units are orthogonal [185,186]. Due to this peculiar geometry, the π-units interact with each other across the spiro-link, as shown in Figure 5.1(b), giving rise to an unusual electronic structure [185–187]. We wish to describe this system (first in the absence of the metallic electrodes) with the PPP Hamiltonian given in Eq. (5.1). We will assume that the values of the hopping integrals within each of the π sub-units are given by: $t_{ij} = t[1 - \delta(r_{ij} - r_0)]$ where $\delta = 1.22$ Å^{-1} and $r_0 = 1.40$ Å [188,189] while the coupling across the spiro-link will be described using the Hansson-Stafström parametrisation [190, 191], see Appendix B. We will include only $M = 8$ carbon sites, as numbered in Figure 5.1(a) – we ignore the saturated sp^3 carbon

site in the centre of the structure in Figure 5.1. Nonetheless, as we shall show below, Hamiltonian (5.1) can very well describe the π-electronic structure of the molecule. Let us note that the irreducible symmetry of the SNT molecule is D_{2d}, and that this system is not bipartite. As a result of the latter, the Coulson–Rushbrooke pairing theorem is violated [192], and the Hamiltonian does not exhibit the electron–hole symmetry.

Since the PPP Hamiltonian is typically only used to describe fully-conjugated molecules [184], we begin here by validating its use in the present case by reproducing the experimental (gas-phase) excitation spectrum of the SNT molecule from Ref. [193]. We start by determining the equilibrium geometry of the SNT molecule using the B3LYP functional and 6-31G(d,p) basis set in Gaussian09 [194, 195].[1] This fully determines the PPP Hamiltonian as a function of two parameters: t and U. We proceed to diagonalise the Hamiltonian for the half-filled state (for $N_\uparrow = N_\downarrow = 4$ where N_σ is the number of π electrons with spin σ). The energies of the many-body states (with respect to the totally symmetric 8-particle ground-state) obtained in this way correspond to the experimentally measurable excitation energies.

We first briefly discuss here how the character of the calculated electronic transitions is determined. To do so we need to consider the eigenvalues (or equivalently the expectation values) of the total-spin and spatial-symmetry operators (to determine the singlet/triplet and symmetry character of the transition, respectively). The total-spin operator is given simply by:

$$S^2 = S_x^2 + S_y^2 + S_z^2 \ , \tag{5.2}$$

with $S_q^2 = \left[\sum_i^M S_q^{(i)}\right]^2$, where $S_q^{(i)}$ are the Pauli matrices for the site i. The many-body symmetry operators are somewhat less trivial, perhaps with the exception of the identity operator which we shall denote as $\mathbb{1}$. In general, they are constructed from the 'flip' (F_i) and 'exchange' (X_{ij}) operators. The former are given by:

$$F_i = \prod_\sigma (\mathbb{1} - 2n_{i\sigma}) \ , \tag{5.3}$$

[1]The geometry optimisation performed using the dispersion corrected B3LYP-D3 functional or 6-311+G(d) basis set yields virtually identical results – see SI of Ref. [2] for a detailed comparison.

State	Experimental [193]	CASPT2 [193]	PPP (stand.)	PPP (opt.)
$1\ ^3E$	2.98	2.86	2.70	2.91
$1\ ^1E$	4.46	4.35	5.22	4.47
$1\ ^3B_2$	4.48	4.64	4.17	4.51
$1\ ^3A_1$	4.52	4.83	4.20	4.54
$2\ ^3E$	4.90	5.10	6.52	5.71
$1\ ^1B_2$	–	5.55	5.37	5.57
$2\ ^1E$	5.78	5.40	6.56	5.78
$2\ ^1A_1$	–	5.67	5.38	5.59
$3\ ^1A_1$	–	5.78	5.39	5.79

Table 5.1: Comparison between the experimental and theoretical values of excitation energies of the SNT molecule.

and correspond to an inversion of the p_z orbital on site i around the centre of an atom. The latter correspond to an exchange of two sites (i and j) under a given symmetry operation:

$$X_{ij} = \prod_{\sigma} \left(\mathbb{1} - n_{i\sigma} n_{j\sigma} + a^{\dagger}_{i\sigma} a_{j\sigma} + a^{\dagger}_{j\sigma} a_{i\sigma} \right) \ . \tag{5.4}$$

The symmetry operators (acting on the entire Fock space) can be then constructed by inspection. For instance, for the SNT molecule, the operators describing reflections in the xz and yz planes are given by:

$$\sigma_d^{(xz)} = X_{58}\, X_{67}\, F_1\, F_2\, F_3\, F_4 \ , \tag{5.5}$$

$$\sigma_d^{(yz)} = X_{14}\, X_{23}\, F_5\, F_6\, F_7\, F_8 \ , \tag{5.6}$$

respectively. The $C_2(z)$ operator can by found by exploiting the group property: $C_2(z) = \sigma_d^{(xz)} \sigma_d^{(yz)}$. Other symmetry operators can be constructed accordingly.

We compute the electronic excitation energies by first using the standard values of $t = -2.4$ eV and $U = 11.26$ eV [196]. As shown in Table 5.1, this yields a reasonable qualitative agreement with the experimental data from Ref. [193] but, generally speaking, the singlet excitation energies are significantly overestimated whereas those corresponding to triplet transitions are underestimated.

As is commonly done [184, 188], we therefore proceed to optimise the values of t and U by fitting the experimental excitation spectrum. This yields: $t = -2.36$ eV and

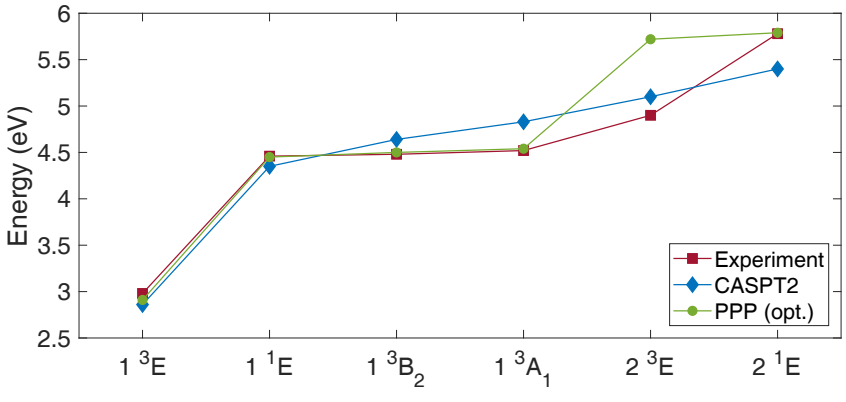


Figure 5.2: Graphical comparison of the experimental, CASPT2, and optimised PPP excitation energies.

$U = 9.31$ eV. While the optimised value of t is very close to the standard value of (-2.4 eV), the optimised value of U is significantly smaller than the typically used 11.26 eV. This is, however, a common conclusion: see, for instance, Refs. [188, 197].

Figure 5.2 shows a graphical comparison of the experimental, CASPT2 (also from Ref. [193]), and PPP excitation energies. The optimised PPP results significantly outperform the CASPT2 results for all but the high-energy triplet ($2\ ^3E$) transitions.[2] The significantly worse match for this particular transition may be a result of excluding the sp^3 carbon centre from the present analysis. Nonetheless, an impressive agreement between the experimental and PPP values has been reached (complete qualitative agreement in terms of the degeneracies and the singlet/triplet character of the transitions with an average relative quantitative error of 3.4%.).

Throughout the remainder of this chapter, we will continue to use the values of the t and U parameters extracted here, although we note that the electron-electron interactions may be renormalised and the molecule structure may distort after its deposition into a junction.

[2]In fact, this transition has not been included in the optimisation procedure. Doing so results in a significantly better agreement for the remaining excitation energies as well as yields a higher (closer to the typically used) value of the parameter U.

5.3 Electronic transport properties

Having validated the use of the PPP Hamiltonian in spiro-conjugated molecules, we proceed to first study the purely electronic transport properties of the prototypical SNT-based junction, schematically pictured in the inset in Figure 5.3. We shall consider transport through an unfunctionalised SNT structure. Experimental studies would probably require functionalising the SNT core with the so-called anchor groups, which bind to the source and drain electrodes, although a direct connection of organic molecules to metallic electrodes is also possible [157, 198]. Nonetheless, much can be learnt by considering transport through prototypical molecular systems as has been previously shown in both the off-resonant [199–201] and resonant [202–204] regimes. Consequences of functionalization and the resulting symmetry breaking will be discussed in Section 5.5.

We assume that the molecular system is coupled to two fermionic reservoirs (modelled as non-interacting reservoirs: $H_{\mathrm{E}} = \sum_{l=L,R}\sum_{k_l,\sigma}\epsilon_{k_l}c^{\dagger}_{k_l\sigma}c_{k_l\sigma}$) by the usual tunnelling Hamiltonian:

$$H_{\mathrm{MLC}} = \sum_{l=\mathrm{L,R}}\sum_{k_l,\sigma} V_{k_l}a^{\dagger}_{l\sigma}c_{k_l\sigma} + \mathrm{H.c.}\ , \tag{5.7}$$

where we set $a_{\mathrm{L}\sigma} := a_{2\sigma}$, and $a_{\mathrm{R}\sigma} := a_{6\sigma}$, as pictured in Figure 5.3, and for simplicity set the on-site energy at zero gate voltage to zero, $\varepsilon_i = -|e|V_{\mathrm{g}}$. Throughout this chapter, we will assume symmetric molecule-lead coupling $\gamma_{\mathrm{L}} = \gamma_{\mathrm{R}} = \gamma$ where $\gamma_l = 2\pi|V_l|^2$.

Similarly to what has been done in the Chapter 4, we describe this problem with the second-order quantum master equation within the Born-Markov approximation (see Chapter 2) which in the present case takes the form:

$$\frac{\mathrm{d}\rho(\tau)}{\mathrm{d}\tau} = -\mathrm{i}[H_{\mathrm{PPP}},\rho(\tau)] - \int_0^{\infty}\mathrm{d}s\ \mathrm{Tr}_E\left[H_{\mathrm{MLC}},\left[\tilde{H}_{\mathrm{MLC}}(-s),\rho(\tau)\rho_E\right]\right]\ , \tag{5.8}$$

where ρ_E accounts for the thermalised fermionic environment (leads), and $\tilde{}$ denotes an interaction picture of H_{PPP}. We proceed by expanding the commutators above and noting that $\mathrm{Tr}_E[c^{\dagger}_{k_l}c_{k_l}\rho_E] = \langle c^{\dagger}_{k_l}c_{k_l}\rangle = f_l(\epsilon_{k_l})$ where $f_l(\epsilon_{k_l}) = 1/(1+\exp[(\epsilon_{k_l}-\mu_l)/kT])$,

and using the anticommutation property of the fermionic operators $\langle c_{k_l} c_{k_l}^\dagger \rangle = 1 - f_l(\epsilon_{k_l})$; $\langle c_{k_l} c_{k_l} \rangle = \langle c_{k_l}^\dagger c_{k_l}^\dagger \rangle = 0$. This yields:

$$\begin{aligned}\frac{\mathrm{d}\rho(\tau)}{\mathrm{d}\tau} = -\mathrm{i}[H_{\mathrm{PPP}}, \rho(\tau)] - \sum_\sigma \sum_{l,k_l} |V_{k_l}|^2 \int_0^\infty \mathrm{d}s \, \{ \\ [1 - f_l(\epsilon_{k_l})]\, e^{-\mathrm{i}\epsilon_{k_l} s} \left(a_{l\sigma}^\dagger \tilde{a}_{l\sigma}(-s)\rho(\tau) - \tilde{a}_{l\sigma}(-s)\rho(\tau) a_{l\sigma}^\dagger \right) \\ + f_l(\epsilon_{k_l})\, e^{+\mathrm{i}\epsilon_{k_l} s} \left(a_{l\sigma} \tilde{a}_{l\sigma}^\dagger(-s)\rho(\tau) - \tilde{a}_{l\sigma}^\dagger(-s)\rho(\tau) a_{l\sigma} \right) \\ + f_l(\epsilon_{k_l})\, e^{-\mathrm{i}\epsilon_{k_l} s} \left(\rho(\tau) \tilde{a}_{l\sigma}(-s) a_{l\sigma}^\dagger - a_{l\sigma}^\dagger \rho(\tau) \tilde{a}_{l\sigma}(-s) \right) \\ + [1 - f_l(\epsilon_{k_l})]\, e^{+\mathrm{i}\epsilon_{k_l} s} \left(\rho(\tau) \tilde{a}_{l\sigma}^\dagger(-s) a_{l\sigma} - a_{l\sigma} \rho(\tau) \tilde{a}_{l\sigma}^\dagger(-s) \right) \Big\} \ . \end{aligned} \tag{5.9}$$

It is most convenient to work in the frame of molecular eigenstates (where H_{PPP} is diagonal). The annihilation (and, equivalently, the creation) operators can be written as:

$$\tilde{a}_l(s) = \sum_{N,p,q} \xi_{p,q}^{(N-1,N)} \ e^{\mathrm{i}(E_q^{(N-1)} - E_p^{(N)})s} \ |\Psi_q^{(N-1)}\rangle\langle\Psi_p^{(N)}| \ , \tag{5.10}$$

where N denotes a charge state, p, q are the quantum numbers of the respective states, and the coefficients $\xi_{p,q}^{(N)}$ depend on the details of the Hamiltonian. The integrals over s can now be performed using the Cauchy relation given in Eq. (4.30) [50]. We then replace the sum over energy levels k_l with an integral,

$$\sum_{k_l} \to \int_{-\infty}^{\infty} \mathrm{d}\epsilon_{k_l} \varrho_l \ , \tag{5.11}$$

where ϱ_l is the constant density of states in lead l (wide-band approximation, WBA). The rates for the processes in the quantum master equation (5.9) are then of the form:

$$\pi |V_l|^2 \varrho_l \int_{-\infty}^{\infty} \mathrm{d}\epsilon_{k_l} \ f_l(\epsilon_{k_l}) \delta(\Omega) = \pi |V_l|^2 \varrho_l f_l(\Omega) \ , \tag{5.12}$$

and so forth. In Eq. (5.12) we have disregarded the principal value terms which yield small renormalisation of the system Hamiltonian, but which can be significantly overestimated within the WBA.

The size of the Fock space for the molecular Hamiltonian in Eq. (5.1) is 65,536. To make our calculation tractable, we therefore proceed to: ignore coherences between molecular states with different numbers of $\{N_\uparrow, N_\downarrow\}$ electrons (not an additional approximation) and between energy levels spaced more than 10γ apart [205]; and finally, consider only low-lying states (here, all states lying within at least $2eV_\mathrm{b}$ of the ground state at any particular gate voltage). All of the above simplifications were benchmarked on smaller molecular systems and were shown not to affect the outcome of the calculation.

Figure 5.3(a) shows the resulting stability diagram. Two unusual features quickly become apparent. We observe current blockade (non-closing Coulomb diamonds) at positive gate voltage, as well as a number of regions of negative differential conductance at negative V_g. As we shall see, both of these phenomena stem from destructive quantum interference between the degenerate E states of the SNT molecule. Let us consider the charge transport in the basis of eigenstates of H_PPP. There, it is possible to diagonalise the molecular Hamiltonian in such a way that each of the E states is localised on either moiety and therefore coupled only to a single (left or right) electrode. The charge transport through the considered system is therefore blocked at the spiro-link. Alternatively, one may diagonalise the Hamiltonian in a way in which both of the degenerate E are coupled to both of the electrodes but they do so with opposite phases – this results in a complete destructive (inter-orbital) quantum interference in the resonant transport regime. This behaviour is a consequence of the unusual geometry of the spiro-conjugated systems in which the interaction between the two moieties mixes only states of certain symmetry [185,186]: such complete destructive interference (in the resonant transport regime) cannot be observed, for instance, in meta-connected benzene and similar structures [202, 204, 206, 207].

To understand the observed current blockade and negative differential conductance in detail, we study more closely the IV characteristics at $V_\mathrm{g} = \pm 4$ eV. In both cases the molecular system is found in the (neutral) $8A_1$ state at $V_\mathrm{b} = 0$ V. For negative gate voltage, as the bias is increased, the transitions to $7A_2$ and $7B_1$ states become

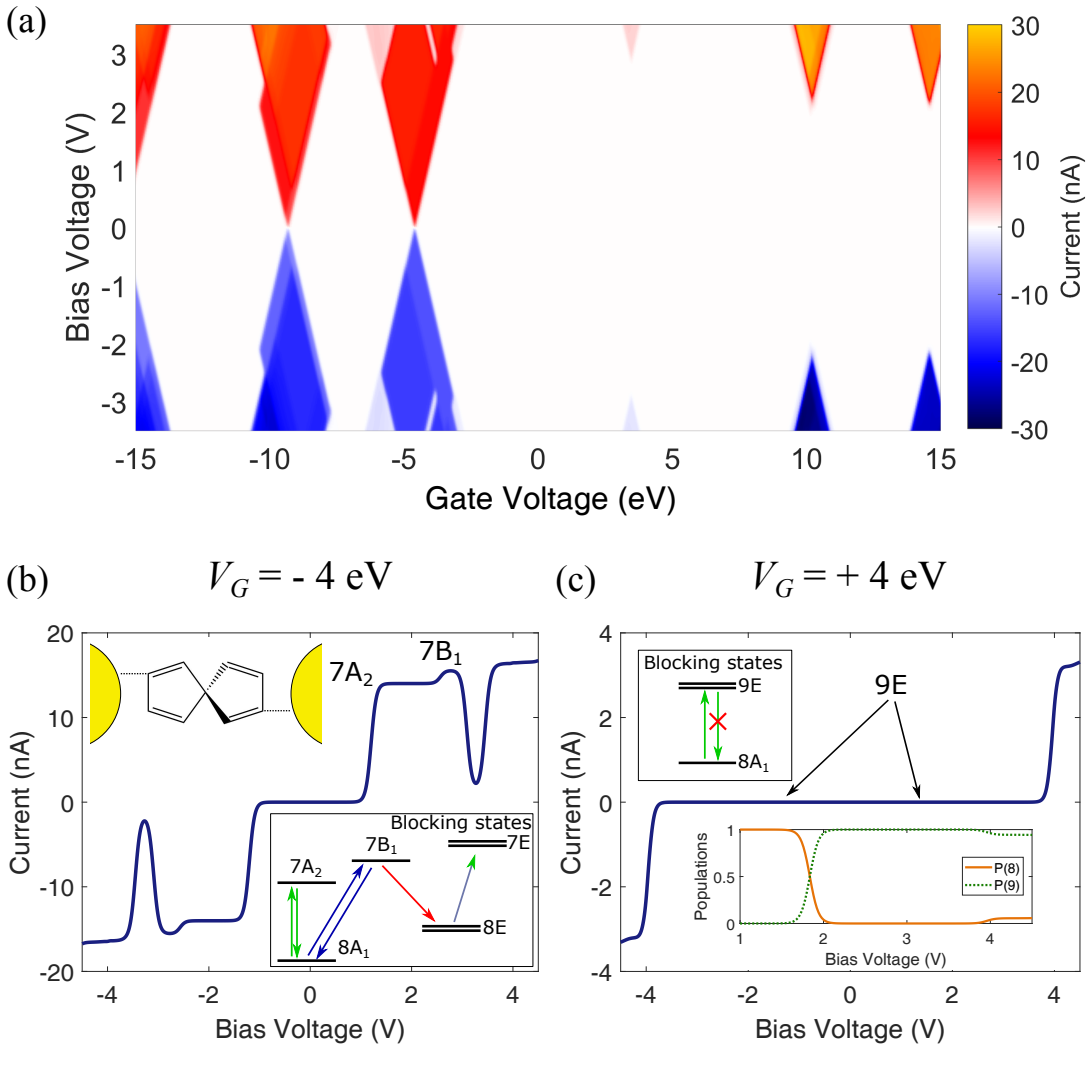


Figure 5.3: (a) Stability diagram (map of current as a function of the gate and bias voltage) of a prototypical spiro-conjugated molecular junction. (b,c) IV characteristics at $V_g = \pm 4$ eV. $\gamma = 1$ meV, $T = 300$ K throughout. Inset at the bottom of panel (c) shows the charge state populations as a function of the bias voltage. Additional insets in panels (b) and (c) show schematic energy level diagrams relevant for charge transport at the considered values of V_g.

possible, each of which results in a step-wise increase in current, see Figure 5.3(b). At higher bias, through a sequence of events schematically plotted in the inset in Figure 5.3(b), the degenerate $7E$ states become populated. As discussed above, they interfere destructively and consequently the transport through these states is blocked. Due to strong electron-electron repulsion [208], further electron transfers onto the molecule cannot take place, giving rise to negative differential conductance. At $V_g = +4$ eV, the states of E symmetry are the lowest-lying 9-particle states. As the bias is increased,

they become populated and this, again due to destructive quantum interference, results in a current blockade. In transport through the E states, a complete destructive interference occurs at the 'spiro'-link which localises the propagating charge density on either of the moieties (depending on the sign of V_{b}). While the negative differential conductance is a feature characteristic of systems with degenerate energy levels [204, 205, 209], the full current blockade observed here is a consequence of the peculiar geometry of spiro-conjugated systems.

5.4 Jahn–Teller distortion

The phenomena discussed above arise from quantum interference between two spatially-degenerate energy levels. Populating degenerate electronic states, however, typically results in Jahn-Teller (JT) distortion [210]. This is also the case in the SNT molecule where, upon charging, the symmetry reduces from D_{2d} to D_2 as the two conjugated moieties undergo a twist away from the 90° angle (b_1-type distortion) [193]. As shown in Figure 5.4(a), upon such twisting, couplings across the spiro-link are no longer antisymmetric ($t_{15} \neq -t_{18}$ and so on). This distortion lifts the degeneracy of the 9-particle ground state (effectively reducing the overall energy of the system) and will thus have a deleterious effect on the destructive QI phenomena discussed above.

5.4.1 Static perspective

We first approach this problem from a static perspective. In Figure 5.4(b) we calculate the IV characteristics at $V_{\mathrm{g}} = +4$ eV for different values of θ – the angle between the two moieties (we manually rotate one of the moieties and evaluate a new PPP Hamiltonian for each value of θ).

As the angle between the two moieties is twisted away from $\pi/2$, the two orbitals cease to interfere destructively and the current blockade is lifted. Figure 5.4(c) is showing the values of high voltage ($V_{\mathrm{b}} = 3$ V) current as a function of θ. In the case of stronger molecule-lead coupling, destructive quantum interference survives at

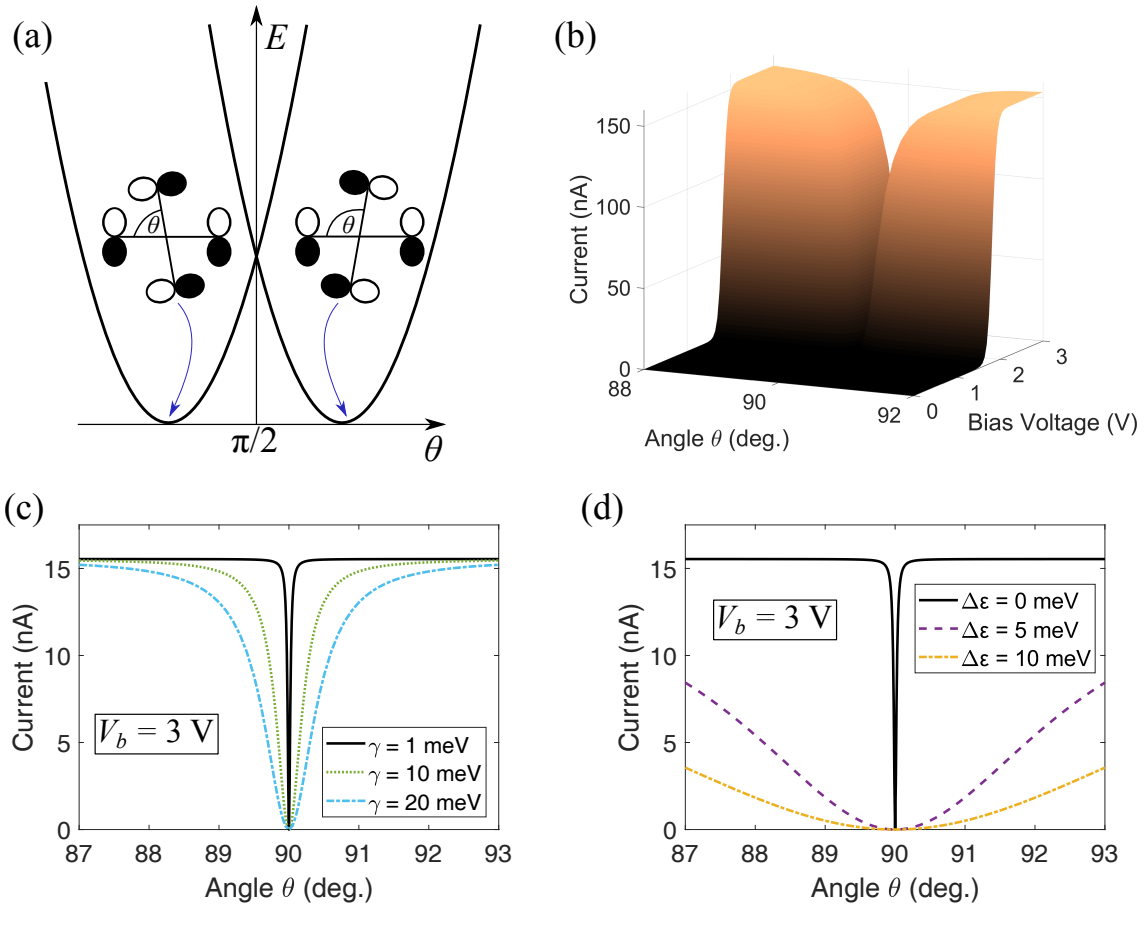


Figure 5.4: (a) Schematic energy diagram of the $9E$ states as a function of θ. (b) IV characteristics at $V_{\mathrm{g}} = 4$ eV, $\gamma = 10$ meV for different values of θ. (c) Values of current at $V_{\mathrm{g}} = 4$ eV, $V_{\mathrm{b}} = 3$ V for different values of θ and γ; curves for $\gamma = 10$ and 20 meV were re-scaled by factors of 10 and 20 respectively. (d) Values of current at $V_{\mathrm{g}} = 4$ eV, $V_{\mathrm{b}} = 3$ V for different values of θ in the presence of energetic detuning between the two moieties. We shift the site energies on the two moieties by $\pm\Delta\varepsilon$, $\gamma = 1$ meV.

significantly larger twist angles. For sufficiently strong molecule-lead coupling, Jahn-Teller distortion can be expected to have little effect on the current blockade, whereas in the case of very weak coupling the blockade is lifted even by a modest JT distortion.

It is also interesting to consider the effect of the twisting in the presence of an energetic detuning between the moieties due to capacitive coupling of the molecule to the source and drain electrodes, *c.f.* Chapter 6. It localises the otherwise degenerate states on either of the two moieties and thus stabilises the current blockade, see Figure 5.4(d). We can therefore infer that the current blockade can be stabilised by the applied bias voltage. Similar stabilisation of the current blockade can be obtained by a geometric distortion of a b_2-type (i.e. one that reduces the molecular symmetry to C_{2v}

and localises the otherwise degenerate states on either of the two moieties). Curiously, certain types of symmetry breaking (for instance the ones inducing a transition from D_{2d} to D_2 point group) can lift the observed quantum-interference effects, whereas other (for instance, the ones inducing a transition from D_{2d} to C_{2v} point group) appear to reinforce such phenomena.

5.4.2 Dynamic perspective: vibrational effects

Microscopically, Jahn-Teller distortion is a dynamic phenomenon whose origins can be traced to electron-vibrational coupling between the degenerate electronic E states and vibrational modes that break their degeneracy [210, 211]. In the case of the SNT molecule, the E states are most strongly coupled to a low-frequency twisting mode of b_1 symmetry (JT distortion of $E \otimes b_1$ type), schematically pictured in Figure 5.5(a).

As discussed at the beginning of this chapter, we must therefore incorporate the electron-vibrational interactions into the PPP-based framework considered so far. We focus on the dynamics at the gate voltage of $V_{\mathrm{g}} = +4$ eV, and consequently we need to retain only 5 electronic states: the totally symmetric 8-particle ground state ($8A_1$) and four (doubly spatially and spin-degenerate) 9-particle ($9E$) states. Then, the relevant Hamiltonian can be written as [210, 212]:

$$H_{\mathrm{JT}} = \varepsilon'(n_\alpha + n_\beta) + \omega b^\dagger b + g(b^\dagger + b)(n_\alpha - n_\beta) + \sum_{l,k_l,\sigma} \epsilon_{k_l} c^\dagger_{k_l\sigma} c_{k_l\sigma} + \sum_{l,k_l,\sigma} V_l d^\dagger_{l\sigma} c_{k_l\sigma} + \mathrm{H.c.}\ , \tag{5.13}$$

where $n_\alpha = \sum_\sigma n_{\alpha\sigma}$, ε' is the energy difference between the $8A_1$ and $9E$ states, g is the electron-phonon coupling constant, and ω is the frequency of the b_1 mode in question with raising (lowering) operator $b^\dagger$ (b). The operator $d^\dagger_{l\sigma}$ ($d_{l\sigma}$) accounts for (de-)charging of the molecule at the contact $l = \mathrm{L}, \mathrm{R}$ and can be written as $d^\dagger_{l\sigma} = \zeta_{l\alpha} a^\dagger_{\alpha\sigma} + \zeta_{l\beta} a^\dagger_{\beta\sigma}$ where the coefficients $\zeta_{l\alpha}$ and $\zeta_{l\beta}$ are obtained using the PPP Hamiltonian. Since there are infinitely many ways in which a Hamiltonian with degenerate energy levels can be diagonalised, the crucial issue is now determining the α and β states which couple to the b_1 mode in a way described above. It can be seen from Hamiltonian

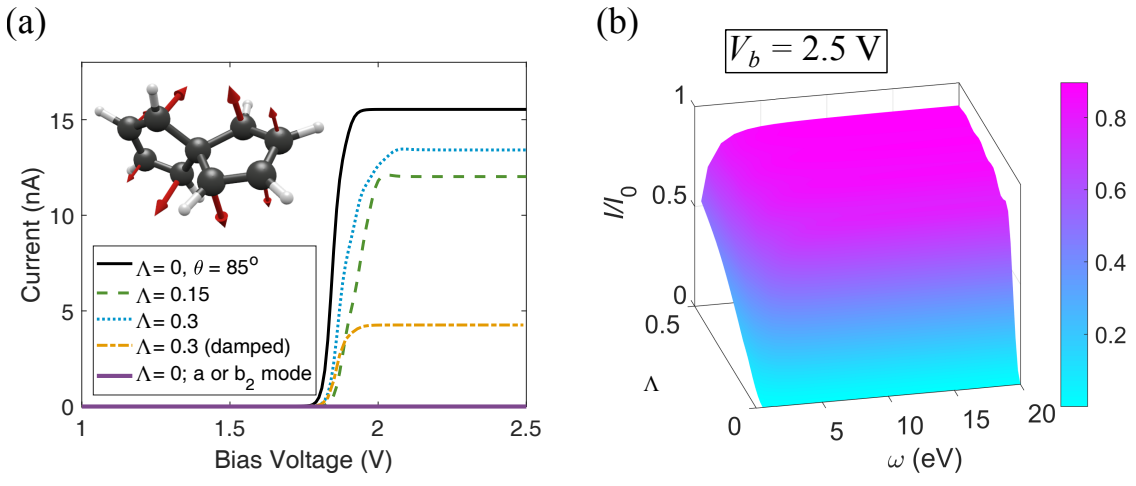


Figure 5.5: (a) IV characteristics for different values of the electron-phonon coupling parameter λ for $\omega = 27$ meV and hopping rate: $\gamma = 1$ meV. The damping rate is taken to be $\gamma_d = 0.1$ meV where appropriate, $T = 77$ K. (b) Values of current at $V_\mathrm{b} = 2.5$ V as a function of λ and ω renormalised by I_0 - value of current for $\lambda = 0$ and $\theta = 85°$. The molecule-lead rate is $\gamma = 20$ meV, $T = 300$ K. 50 vibrational levels were included in both calculations.

(5.13) that the α and β states do not change with the vibrational coordinate (although crucially their energies do). We therefore obtain the α and β states by diagonalising the full PPP Hamiltonian at $\theta = \pi/2 + \delta\theta$ where $\delta\theta \to 0$. We now proceed to describe this problem in a way analogous to what has been done in Chapter 4 – with a second-order quantum master equation within the Born-Markov approximation in a polaron-transformed frame. The stationary density matrix is found by solving the above QME in the steady-state limit. We allow for fully non-equilibrium dynamics of the vibrational mode unless specified otherwise (where the damping of the vibrational mode is introduced phenomenologically as in Section 4.4).

Figure 5.5(a) shows the IV characteristics at $V_\mathrm{g} = +4$ eV obtained for different values of the dimensionless electron-phonon coupling parameter, $\Lambda = g/\omega$. Firstly, we note that coupling to the mode of b_1 symmetry lifts the current blockade with the electric current increasing with increasing Λ. The latter can be contrasted with what occurs typically in a simple single-level case where the inclusion of vibrational interactions leads to a suppression of current in the resonant transport regime [134]. While full non-equilibrium dynamics of the b_1 mode can rather efficiently lift the current blockade, even very slow damping can significantly reduce the current flowing through

the system. In Figure 5.5(b) we consider values of current at high bias ($V_\mathrm{b} = 2.5$ V) as a function of ω and Λ.[3] Once again, increasing Λ yields higher values of current. Curiously, the electric current decreases with decreasing ω. This can be explained as follows. Within the Franck-Condon principle, the electron hopping on and off the molecule occurs within a rigid nuclear framework. For $\omega \ll \gamma$, when the relevant nuclear dynamics is much slower then the (de-)charging of the molecule, this unitary evolution of the vibrational mode will become the bottleneck of the overall electron transport.

In contrast to the above, distortions induced by a_1 and a_2 vibrational modes do not split the $9E$ states and are therefore incapable of lifting the current blockade, see Figure 5.5(a). Coupling to vibrational modes of b_2 symmetry similarly cannot do that despite also resulting in Jahn-Teller distortion (to C_{2v} symmetry). This situation can be described by a Hamiltonian equivalent to (5.13) but with (redefined) α and β localised on either of the two conjugated moieties.

5.5 Symmetry breaking

The above phenomena result from the fact that the SNT molecule exhibits degenerate energy levels. In practice, one may expect some degree of symmetry breaking to occur, motivating a more detailed discussion of this issue.

There are essentially two ways in which molecular symmetry can be broken in the junction setting:

1. via binding of the symmetric molecule either directly to the metallic electrodes or to the anchor groups which then bind to the electrodes;

2. via the applied bias potential inducing a voltage drop within the molecule.

[3]Both of these parameters can be modified by functionalisation of the SNT core. The frequency of the b_1 vibrational mode in question, for instance, can be modified by functionalising the SNT core with side-groups which do not break the symmetry but decrease the frequency of the twisting mode, see the Supporting Information of Ref. [2].

With regards to the first issue, we consider functionalising the SNT molecule with thiol groups, as shown in Figure 5.6. Such a functionalisation breaks the symmetry of the system (structure in Figure 5.6 belongs to C_2 point group), and therefore results in the splitting of the otherwise degenerate levels. The degree of splitting between

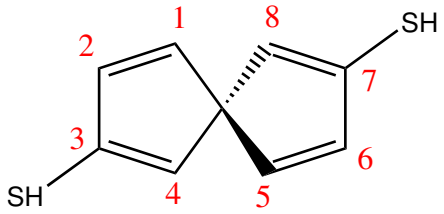


Figure 5.6: Spiro[4.4]nonatetraene molecule functionalised with thiol groups.

the LUMO and LUMO+1 levels (which are degenerate in the case of unfunctionalised SNT) can be estimated using DFT calculations [194]: the LUMO/LUMO+1 gap is roughly equal to 9 meV.[4] This means that the two levels can still interfere destructively for sufficiently, but realistically, strong molecule-lead hopping rate. The functionalisation considered here is by far the simplest one and it may be possible to functionalise the spiro-conjugated core in a way which will give rise to a significantly smaller LUMO/LUMO+1 splitting. Furthermore, as discussed above, the SNT molecule undergoes a Jahn-Teller distortion upon charging. Similarly, the structure in Figure 5.6 undergoes a pseudo-Jahn-Teller distortion once negatively charged and, similar to the SNT molecule, this distortion also involves twisting of the angle between the π-moieties. The angle between the two moieties of the molecule in Figure 5.6 (defined as the angle between 2-3 and 7-6 carbon bonds) is equal to roughly 90.02° in the neutral state and is reduced to 79.63° in the anionic state.[5] In other words, this system behaves analogously to the unfunctionalised SNT molecule and should exhibit very similar transport behaviour. Binding of the unfunctionalised SNT molecule to the metallic electrodes will result in qualitatively analogous behaviour as the binding

[4]We obtain roughly 9.25 meV using 6-31G(d) and 6-31+G(d,p) basis sets; and 9.5 meV using 6-311+G(d,p) basis set - all calculated using B3LYP functional in Gaussian09.

[5]Both results obtained in Gaussian09 using B3LYP functional and 6-31G(d) basis set [213]. Although DFT calculations performed on anionic species should ideally be performed using diffuse basis functions, in the present case they provoke convergence problems, and as was previously shown they generally have relatively small effect in PAH anions [214].

to the anchor groups discussed above. Its effects will, however, vary depending on the kind of connection made and may be of a significantly smaller magnitude.

As discussed above, the symmetry of the studied molecular system can also be broken by the applied bias voltage which can energetically detune the carbon sites of the molecular system. The degree of this symmetry breaking will naturally depend on the applied bias and may be disregarded for small V_{b}. The effects for larger applied bias on the transport characteristics were considered in Section 5.4.1.

5.6 Conclusions

In this chapter, we have studied charge transport through a prototypical spiro-conjugated molecular junction. Unlike in the previous (and forthcoming) chapters, we have described the molecular system within the junction with a semi-empirical (and experimentally validated) Pariser-Parr-Pople Hamiltonian. It was first shown here that the unusual geometry of the SNT system considered above gives rise to a current blockade and negative differential conductance in the resonant transport regime. These phenomena stem from destructive quantum interference between the spatially degenerate E states. However, populating these doubly-degenerate electronic levels also gives rise to Jahn-Teller distortion which removes the electronic degeneracy and, as we have shown, is therefore capable of lifting the aforementioned phenomena. The overall transport behaviour is thus determined by the interplay between the two effects. In order to describe the dynamics of the Jahn-Teller effect in the transport setting, we have shown how vibrational interactions can be incorporated into to the PPP-based theoretical framework. We predict that the signatures of destructive quantum interference (current blockade and negative differential conductance) can survive in the limit of relatively strong molecule-lead coupling, as well as in the case of slow nuclear dynamics. The possibility to control destructive quantum interference can turn molecular systems like the one studied here into attractive components when designing functional molecular circuits.

Chapter 6

Environment-assisted quantum transport

Well, one just goes on.

— Roald Hoffmann

Here, we return to a two-site molecular system akin to the one considered in Chapter 4, but we instead study its transport properties in the case of coupling to a collection of thermalised vibrational modes (a phonon bath). These phonon baths correspond to the broader junction environment (the substrate on which the molecule is deposited [140, 215] or the solution in which it is immersed [75, 216–220]), although in principle they can also account for a collection of weakly-coupled damped molecular modes.

We will demonstrate how such interactions can be incorporated into the theoretical description of the molecular junctions. Furthermore, we will show that they can significantly enhance the current flowing through the junction in analogy to the phenomenon of environment-assisted quantum transport postulated in the context of energy transport in photosynthetic complexes [221, 222]. We shall also take this opportunity to study the performance of different theoretical approaches which can be used in this context, and predict behaviour that ought to be expected in experimental transport studies on such two-site systems.

6.1 Theoretical model

In this chapter, we consider a two-site molecular junction, schematically pictured in Figure 6.1(a), where each of the sites [left (L) and right (R)] is coupled to an independent phonon bath and either the source or the drain electrode. The two-site character of the molecule can most easily be achieved by breaking the conjugation within the system (introducing regions of low π-electron density). The model used here is inspired by the experimental studies of Perrin *et al.* [83, 85] who studied the molecular system pictured in Figure 6.1(b), although several other structures of this type have recently also been investigated in the transport setting [70, 83, 85, 223, 224].

Our system is governed by the following Hamiltonian ($\hbar = 1$ and $e = 1$ throughout):

$$H = H_{\mathrm{M}} + H_{\mathrm{B}} + H_{\mathrm{C}} + H_{\mathrm{V}} + H_{\mathrm{E}} \ . \tag{6.1}$$

Here, H_{M} denotes the molecular tight-binding Hamiltonian:

$$H_{\mathrm{M}} = \sum_{j=\mathrm{L,R}} \varepsilon_j \, a_j^\dagger a_j + J(a_{\mathrm{L}}^\dagger a_{\mathrm{R}} + \mathrm{H.c.}) \ , \tag{6.2}$$

where $a_j^\dagger$ (a_j) is the usual raising (lowering) operator which creates (annihilates) an electron on site j with energy ε_j, and J is the strength of the tunnel coupling between the neighbouring sites. As the two site-orbitals $|\mathrm{L}\rangle$ and $|\mathrm{R}\rangle$ are not eigenstates of the molecular Hamiltonian, they hybridise into two linear (bonding and antibonding) combinations – or molecular orbitals (MO):

$$|\Psi_+\rangle = \cos\theta \, |\mathrm{L}\rangle + \sin\theta \, |\mathrm{R}\rangle \ ; \tag{6.3}$$

$$|\Psi_-\rangle = \sin\theta \, |\mathrm{L}\rangle - \cos\theta \, |\mathrm{R}\rangle \ . \tag{6.4}$$

Here, the mixing angle θ is given by $\tan 2\theta = -2J/\Delta\varepsilon$, where $\Delta\varepsilon = \varepsilon_R - \varepsilon_L$. The

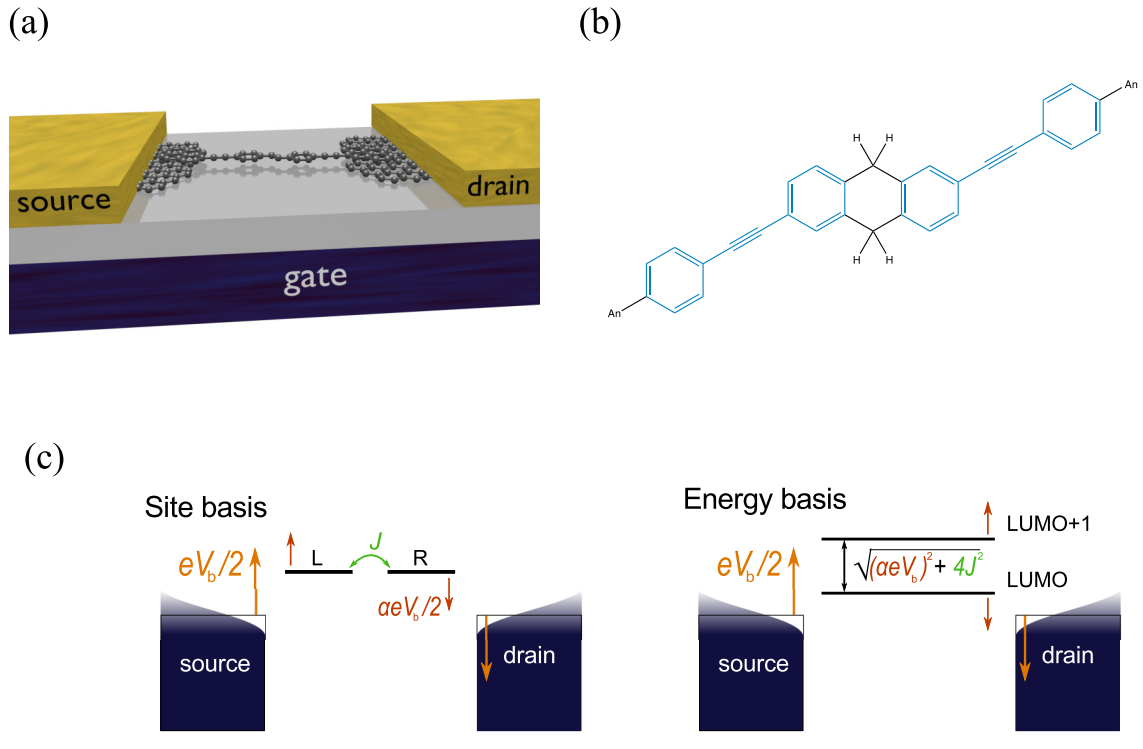


Figure 6.1: (a) Schematic depiction of the considered junction. (b) Schematic of a molecular system considered in this chapter; 'An' denotes an anchor group which binds to the electrodes. (c) Level structure in site and energy basis; arrows indicate energy shifts under an applied bias voltage V_b.

energies of these bonding and antibonding states are:[1]

$$\varepsilon_\pm = \frac{\varepsilon_\mathrm{L} + \varepsilon_\mathrm{R}}{2} \mp \frac{\sqrt{\Delta\varepsilon^2 + 4J^2}}{2} \,. \tag{6.5}$$

Alternatively, one may begin the above considerations with a pair of closely spaced molecular orbitals, $|\Psi_+\rangle$ and $|\Psi_-\rangle$, of a bonding and antibonding character (in the case of molecular system studied by Perrin *et al.* in Ref. [83], both the HOMO/HOMO-1 and LUMO/LUMO+1 pairs satisfy this condition [225]). Then, the $|\mathrm{L}\rangle$ and $|\mathrm{R}\rangle$ states can be obtained directly from Eqs. (6.3) and (6.4).

As has been demonstrated experimentally, the molecular site energies (ε_L and ε_R) in such systems are sensitive to an applied bias voltage [83, 85]. We will focus on a symmetric molecular structure in which the sites capacitively couple to the source or

[1]For $J < 0$, as used here, the bonding orbital $|\Psi_+\rangle$ is lower in energy.

drain electrode as follows: $\varepsilon_{\rm L} = \varepsilon_0 + \alpha V_{\rm b}/2$ and $\varepsilon_{\rm R} = \varepsilon_0 - \alpha V_{\rm b}/2$ for an applied bias of $V_{\rm b}$, so that $\alpha V_{\rm b}$ is the voltage drop within the molecule.

We treat the environment as bosonic baths of (thermalised) vibrational modes of frequencies ω_{q_j}. Since in this chapter we are predominantly interested in the effects of the broader environment, we assume that each of the sites is coupled to an independent phonon bath. Therefore, given the raising (lowering) operators $b^\dagger_{q_j}$ (b_{q_j}), the bath Hamiltonian reads:

$$H_{\rm B} = \sum_{j={\rm L,R}} \sum_{q_j} \omega_{q_j} b^\dagger_{q_j} b_{q_j} \ , \tag{6.6}$$

and the modes couple to the electronic degrees of freedom within the molecular wire with strength g_{q_j} via:

$$H_{\rm C} = \sum_{j={\rm L,R}} \sum_{q_j} g_{q_j} a^\dagger_j a_j (b^\dagger_{q_j} + b_{q_j}) \ . \tag{6.7}$$

We shall make use of the usual definition of the spectral density [Eq. (2.42)] to characterise the environmental coupling: $\mathcal{J}_j(\omega) = \sum_{q_j} |g_{q_j}|^2 \ \delta(\omega - \omega_{q_j})$. Finally, the fermionic reservoirs (leads) and their couplings to the molecular sites are governed by the Hamiltonians:

$$H_{\rm E} = \sum_{j={\rm L,R}} \sum_{k_j} \epsilon_{k_j} c^\dagger_{k_j} c_{k_j} \ , \tag{6.8}$$

$$H_{\rm V} = \sum_{k_{\rm L},k_{\rm R}} V_{k_{\rm L}} c^\dagger_{k_{\rm L}} a_{\rm L} + V_{k_{\rm R}} c^\dagger_{k_{\rm R}} a_{\rm R} + {\rm H.c.} \ , \tag{6.9}$$

where $c^\dagger_{k_j}$ (c_{k_j}) creates (annihilates) an electron in the lead level k_j.

We focus on the sequential tunnelling regime of transport, assuming that due to the strong Coulomb interactions only one additional (transport) electron can be found on the molecular wire at any given time. This assumption is typically well justified for molecular systems at moderate bias voltage, as verified by a number of experimental studies (see Chapter 3). Hence, the tight-binding basis used here comprises only three electronic states corresponding to the additional charge density occupying either of the two sites and the vacuum state (molecule in the neutral charge state).

6.2 Quantum master equations

In this chapter, we will describe the charge transport through the considered molecular wire using three different theoretical approaches: the pure-dephasing, Redfield, and polaron methods. In what follows, we will use these approaches to derive the quantum master equations that will describe the dynamics of the molecular junction.

6.2.1 Pure-dephasing & Redfield approaches

We begin by considering the second-order quantum master equation from Chapter 2:

$$\frac{\mathrm{d}\rho(t)}{\mathrm{d}t} = -\mathrm{i}[H_{\mathrm{S}}, \rho(t)] - \int_0^t \mathrm{d}\tau \ \mathrm{Tr}_E \left[H_{\mathrm{I}}, \left[\tilde{H}_{\mathrm{I}}(-\tau), \rho(t)\rho_{\mathrm{E}}\right]\right] \ , \tag{6.10}$$

where H_{S} and H_{I} are the system and the interaction Hamiltonians, respectively, ρ_{E} denotes the density matrix of the thermalised environment (comprising two fermionic reservoirs and two phonon baths), and $\tilde{A}$ denotes operator A in the interaction picture of $H_{\mathrm{S}} + H_{\mathrm{B}} + H_{\mathrm{E}}$. In the case of the system considered here, $H_{\mathrm{S}} \equiv H_{\mathrm{M}}$ and $H_{\mathrm{I}} \equiv H_{\mathrm{C}} + H_{\mathrm{V}}$. Since (within the Born approximation) terms linear in H_{V} vanish, the intra-molecular phenomena and those at the molecule-lead interfaces can be separated. The quantum master equation can be therefore written as:

$$\frac{\mathrm{d}\rho(t)}{\mathrm{d}t} = -\mathrm{i}[H_{\mathrm{M}}, \rho(t)] + \mathcal{L}_{leads}\rho(t) + \mathcal{L}_{ph}\rho(t) \ , \tag{6.11}$$

where the superoperators in Eq. (6.11) are:

$$\mathcal{L}_{leads}\rho(t) = -\int_0^\infty \mathrm{d}\tau \ \mathrm{Tr}_{\mathrm{E}} \left[H_{\mathrm{V}}, [\tilde{H}_{\mathrm{V}}(-\tau), \rho(t)\rho_{\mathrm{E}}]\right] \ ; \tag{6.12}$$

$$\mathcal{L}_{ph}\rho(t) = -\int_0^\infty \mathrm{d}\tau \ \mathrm{Tr}_{\mathrm{E}} \left[H_{\mathrm{C}}, [\tilde{H}_{\mathrm{C}}(-\tau), \rho(t)\rho_{\mathrm{E}}]\right] \ . \tag{6.13}$$

In the above, anticipating that our interest will lie in the steady-state dynamics, we have extended the integration limit to infinity. We note here that in charge transport

through nanoscopic systems, non-Markovian effects generally only have a small effect on the values of steady-state (average) electric current [226, 227].

The superoperator $\mathcal{L}_{leads}\rho(t)$ is evaluated simply by expanding the commutators in Eq. (6.12) yielding:

$$\begin{aligned}\mathcal{L}_{leads}\rho(t) = -\sum_{j,k_j}\int_0^\infty \mathrm{d}\tau \Big[& h_{k_j}(\tau)\left(a_j\tilde{a}_j^\dagger(-\tau)\rho(t) - \tilde{a}_j^\dagger(-\tau)\rho(t)a_j\right) \\ & + \bar{h}_{k_j}(-\tau)\left(a_j^\dagger\tilde{a}_j(-\tau)\rho(t) - \tilde{a}_j(-\tau)\rho(t)a_j^\dagger\right) \\ & + h_{k_j}(-\tau)\left(\rho(t)\tilde{a}_j(-\tau)a_j^\dagger - a_j^\dagger\rho(t)\tilde{a}_j(-\tau)\right) \\ & + \bar{h}_{k_j}(\tau)\left(\rho(t)\tilde{a}_j^\dagger(-\tau)a_j - a_j\rho(t)\tilde{a}_j^\dagger(-\tau)\right)\Big] \ .\end{aligned} \tag{6.14}$$

Here, $h_{k_j}(\tau) \equiv |V_{k_j}|^2\, f_j(\epsilon_{k_j})\, e^{\mathrm{i}\epsilon_{k_j}\tau}$, $\bar{h}_{k_j}(\tau) \equiv |V_{k_j}|^2\,[1 - f_j(\epsilon_{k_j})]\, e^{\mathrm{i}\epsilon_{k_j}\tau}$ with the Fermi distribution given by: $f_j(\epsilon_{k_j}) = \mathrm{Tr}_{\mathrm{E}}(\rho_{\mathrm{E}}c_{k_j}^\dagger c_{k_j}) = 1/(e^{(\epsilon_{k_j}-\mu_j)/kT}+1)$, and μ_j is the chemical potential of the lead $j = \mathrm{L}, \mathrm{R}$.

Fourier decomposition $\left[\tilde{A}(\tau) = \sum_\zeta e^{-\mathrm{i}\zeta\tau}A(\zeta)\right]$ of the creation and annihilation operators in Eq. (6.14) reveals that they oscillate only at the frequencies corresponding to molecular orbital energies,

$$\tilde{a}_L(\tau) = \left(\frac{\Delta\varepsilon+\eta}{2\eta}a_L - \frac{J}{\eta}a_R\right)e^{-\mathrm{i}\varepsilon_+\tau} + \left(\frac{-\Delta\varepsilon+\eta}{2\eta}a_L + \frac{J}{\eta}a_R\right)e^{-\mathrm{i}\varepsilon_-\tau} \ , \tag{6.15}$$

$$\tilde{a}_R(\tau) = \left(-\frac{J}{\eta}a_L - \frac{\Delta\varepsilon-\eta}{2\eta}a_R\right)e^{-\mathrm{i}\varepsilon_+\tau} + \left(\frac{J}{\eta}a_L + \frac{\Delta\varepsilon+\eta}{2\eta}a_R\right)e^{-\mathrm{i}\varepsilon_-\tau} \ , \tag{6.16}$$

where $\Delta\varepsilon = \varepsilon_R - \varepsilon_L$ and $\eta = \sqrt{\Delta\varepsilon^2 + 4J^2}$. Analogous expressions can be found for $\tilde{a}_L^\dagger(\tau)$ and $\tilde{a}_R^\dagger(\tau)$, and we can also confirm that for each of these operators $\sum_\zeta A(\zeta) = A$. The integral over τ in Eq. (6.14) can be evaluated again using the relation (4.30) (where we will ignore the imaginary part which generally introduces small renormalisations to the system Hamiltonian, but does not converge within the wide-band approximation). Finally, the sum over the energy levels k_j in the leads can be replaced by an integral and evaluated, assuming a constant density of states ϱ_j in each of the leads and $V_{k_j} = V_j$ for all k_j, similar to what has been done in the previous chapters. The dissipator $\mathcal{L}_{leads}\rho(t)$

becomes:

$$\begin{aligned}\mathcal{L}_{leads}\rho(t) = -\frac{1}{2}\sum_{j}\sum_{\zeta=\varepsilon_+,\varepsilon_-}\Gamma_j\Big\{ & f_j(\zeta)\left(a_j a_j^\dagger(\zeta)\rho(t) - a_j^\dagger(\zeta)\rho(t)a_j\right) \\ & +[1-f_j(\zeta)]\left(a_j^\dagger a_j(\zeta)\rho(t) - a_j(\zeta)\rho(t)a_j^\dagger\right) \\ & +f_j(\zeta)\left(\rho(t)a_j(\zeta)a_j^\dagger - a_j^\dagger\rho(t)a_j(\zeta)\right) \\ & +[1-f_j(\zeta)]\left(\rho(t)a_j^\dagger(\zeta)a_j - a_j\rho(t)a_j^\dagger(\zeta)\right)\Big\}\,,\end{aligned} \tag{6.17}$$

where $\Gamma_j = 2\pi|V_j|^2\varrho_j$. It is clear that (to second order in the molecule-lead coupling) vibrational coupling does not affect the phenomena at the molecule-lead interfaces. This should be contrasted with the polaron approach which is also derived to the second-order with respect to the molecule-lead coupling, albeit in the polaron-transformed frame (*vide infra*).

6.2.1.1 Pure-dephasing approach

The differences between the pure-dephasing and Redfield approaches lie in the evaluation of the phononic dissipator in Eq. (6.11). The pure-dephasing approach involves replacing the superoperator $\mathcal{L}_{ph}$ with $\mathcal{L}_{deph}$:

$$\mathcal{L}_{deph}\rho(t) = \Gamma_D\sum_{j=L,R}\frac{1}{2}\left(2n_j\rho(t)n_j - n_j\rho(t) - \rho(t)n_j\right)\,, \tag{6.18}$$

where $n_j = a_j^\dagger a_j$ [50, 221, 228, 229]. This Lindbladian superoperator describes an exponential decay of coherences [off-diagonal elements of $\rho(t)$] in the site basis at the rate Γ_D. The phenomenological dissipator in Eq. (6.18) can be motivated by the form of the electron-phonon coupling Hamiltonian H_C, which acts as the number operator on the electronic subspace. While the simplicity of $\mathcal{L}_{deph}$ is indeed very appealing, it is important to bear in mind here that the pure-dephasing approach displays infinite-temperature characteristics (*vide infra*). Its limitations in the context of our model will be discussed in Section 6.3.4.

6.2.1.2 Redfield approach

By contrast, the Redfield approach will involve evaluating the phononic dissipator in Eq. (6.13) [50, 230–232]. It takes the form:

$$\begin{aligned}\mathcal{L}_{ph}\rho(t) = -\sum_{j=L,R}\int_0^\infty \mathrm{d}\tau \left[C_j^R(\tau)\left(n_j\tilde{n}_j(-\tau)\rho(t) - \tilde{n}_j(-\tau)\rho(t)n_j\right)\right. \\ \left. + C_j^R(-\tau)\left(\rho(t)\tilde{n}_j(-\tau)n_j - n_j\rho(t)\tilde{n}_j(-\tau)\right)\right] ,\end{aligned} \tag{6.19}$$

where we have once again utilised the Markovian approximation. As in the case of the pure-dephasing approach, the vibrational effects occurring at the two sites are separated due to the assumption that each of the sites is coupled to an independent phonon bath. The correlation functions in Eq. (6.19) are given by:

$$C_j^R(\tau) = \mathrm{Tr}_\mathrm{E}[D_j(\tau)D_j(0)\rho_\mathrm{E}] , \tag{6.20}$$

where $D_j(\tau) = \sum_{q_j} g_{q_j}(b_{q_j}^\dagger e^{\mathrm{i}\omega_{q_j}\tau} + b_{q_j}e^{-\mathrm{i}\omega_{q_j}\tau})$. Tracing out the bosonic degrees of freedom, the Redfield correlation function becomes (see Appendix C):

$$C_j^R(\tau) = \int_0^\infty \mathrm{d}\omega\, \mathcal{J}_j(\omega)\left[\cos(\omega\tau)\coth(\beta\omega/2) - \mathrm{i}\sin(\omega\tau)\right] , \tag{6.21}$$

where β is the inverse temperature: $\beta = 1/k_\mathrm{B}T$. Similarly to what has been done in Eqs. (6.15, 6.16), one can perform a Fourier decomposition of the $\tilde{n}_j(\tau)$ operator which yields:

$$\tilde{n}_j(\tau) = \sum_\zeta n_j(\zeta)\, e^{-\mathrm{i}\zeta\tau} , \tag{6.22}$$

where $\zeta = \Big\{0, (\varepsilon_+ - \varepsilon_-), (\varepsilon_- - \varepsilon_+)\Big\}$.
The Redfield dissipator in Eq. (6.19) therefore becomes:

$$\mathcal{L}_{ph}\rho(t) = \sum_{j=\mathrm{L,R}}\sum_\zeta \gamma_{r+}^{(\zeta)}\left[n_j(\zeta)\rho(t)n_j - n_jn_j(\zeta)\rho(t)\right] + \gamma_{r-}^{(\zeta)}\left[n_j\rho(t)n_j(\zeta) - \rho(t)n_j(\zeta)n_j\right] , \tag{6.23}$$

where the rates in the above are given by:

$$\gamma_{r\pm}^{(\zeta)} = \int_0^\infty \mathrm{d}\tau \, C_j^R(\pm\tau) \, e^{-\mathrm{i}\zeta\tau} \ . \tag{6.24}$$

The dissipator in Eq. (6.23) induces transitions between the eigenstates of the molecular Hamiltonian with rates determined by the value of the phononic correlation function (6.21) at the frequency corresponding to the energy gap between the relevant molecular eigenstates.

We note here that the Redfield dissipator given above cannot normally be recast into a Lindblad form, and consequently the Redfield quantum master equation is not guaranteed to preserve the positivity of the density matrix (unlike, for instance, the pure-dephasing approach) [50]. Following the computation of the stationary density matrix, one must always therefore verify its physical character.

6.2.2 Polaron approach

6.2.2.1 Polaron transformation

The first step in the derivation of the quantum master equation in the polaron frame is the polaron (Lang-Firsov) transformation [47], already introduced in Chapter 2, which eliminates the electron-phonon coupling Hamiltonian (H_C). In the present case, it is given by:

$$\bar{H} = e^S H e^{-S} \ , \tag{6.25}$$

where

$$S = \sum_{j=\mathrm{L,R}} \sum_{q_j} g_{q_j} a_j^\dagger a_j (b_{q_j}^\dagger - b_{q_j}) \ . \tag{6.26}$$

This leads to the transformed Hamiltonian: $\bar{H} = \bar{H}_\mathrm{M} + H_\mathrm{B} + \bar{H}_\mathrm{V} + H_\mathrm{R}$, where

$$\bar{H}_\mathrm{M} = \sum_{j=\mathrm{L,R}} \bar{\varepsilon}_j a_j^\dagger a_j + J \left(X_L^\dagger X_R \, a_L^\dagger a_R + \mathrm{H.c.} \right) \ , \tag{6.27}$$

and

$$\bar{H}_{\mathrm{V}} = \sum_{j=\mathrm{L,R}} \sum_{k_j} V_{k_L} c_{k_j}^{\dagger} X_j a_j + \mathrm{H.c.}\ . \tag{6.28}$$

Here, $\bar{\varepsilon}_j$ denotes the renormalised site energy $\bar{\varepsilon}_j = \varepsilon_j - \sum_{q_j} g_{q_j}^2/\omega_{q_j}$ (for consistency with the other approaches this renormalisation will be ignored – it changes the position of the levels with respect to the Fermi energy and only has a trivial effect on the dynamics of the system). Finally, X_j are the usual displacement operators:

$$X_j = \exp\left[-\sum_{q_j} \frac{g_{q_j}}{\omega_{q_j}} (b_{q_j}^{\dagger} - b_{q_j}) \right] \ , \tag{6.29}$$

which were introduced into the molecule-lead as well as the inter-site coupling terms.

6.2.2.2 Quantum Master Equation

In this section, we derive a quantum master equation describing the dynamics of the considered model system in the polaron frame. We begin by redefining the Hamiltonian in terms of the system ($\bar{H}_{\mathrm{S}}$), the environment ($H_E = H_{\mathrm{R}} + H_{\mathrm{B}}$), and the interaction Hamiltonian ($\bar{H}_{\mathrm{I}}$). The system Hamiltonian is (dropping the renormalisation of the site energies) given by:

$$\bar{H}_{\mathrm{S}} = \sum_{j=\mathrm{L,R}} \varepsilon_j a_j^{\dagger} a_j + J \langle X_{\mathrm{LR}} \rangle \left(a_{\mathrm{L}}^{\dagger} a_{\mathrm{R}} + \mathrm{H.c.} \right) \ . \tag{6.30}$$

It accounts for the site energies, as well as the coupling between the sites. The latter is renormalised by $\langle X_{\mathrm{LR}} \rangle = \langle X_{\mathrm{L}} \rangle \langle X_{\mathrm{R}} \rangle$, where $\langle ... \rangle$ denotes an average with respect to the thermal equilibrium and

$$\langle X_j \rangle = \langle X_j^{\dagger} \rangle = \exp\left(-\frac{1}{2} \int_0^{\infty} \mathrm{d}\omega \frac{\mathcal{J}_j(\omega)}{\omega^2} \coth(\beta\omega/2) \right) \ . \tag{6.31}$$

The interaction Hamiltonian is now defined as $\bar{H}_{\mathrm{I}} = \bar{H}_{\mathrm{V}} + \bar{H}_{\mathrm{P}}$ where:

$$\bar{H}_{\mathrm{P}} = J \left[\left(X_L^{\dagger} X_{\mathrm{R}} - \langle X_{\mathrm{LR}} \rangle \right) a_{\mathrm{L}}^{\dagger} a_{\mathrm{R}} + \mathrm{H.c.} \right] \ , \tag{6.32}$$

and $\bar{H}_{\mathrm{V}}$ is defined in Eq. (6.28) [230, 233, 234]. Since terms linear in c_{k_j} (or $c^{\dagger}_{k_j}$) again vanish when tracing out the fermionic degrees of freedom, the quantum master equation can be written in the form:

$$\frac{\mathrm{d}\bar{\rho}(t)}{\mathrm{d}t} = -\mathrm{i}[\bar{H}_{\mathrm{S}}, \bar{\rho}(t)] - \int_0^{\infty} \mathrm{d}\tau \ \mathrm{Tr}_{\mathrm{E}} \left[\bar{H}_{\mathrm{V}}, [\tilde{H}_{\mathrm{V}}(-\tau), \bar{\rho}(t)\bar{\rho}_{\mathrm{E}}]\right] - \int_0^{\infty} \mathrm{d}\tau \ \mathrm{Tr}_{\mathrm{E}} \left[\bar{H}_{\mathrm{P}}, [\tilde{H}_{\mathrm{P}}(-\tau), \bar{\rho}(t)\bar{\rho}_{\mathrm{E}}]\right] \ , \quad (6.33)$$

or simply

$$\frac{\mathrm{d}\bar{\rho}(t)}{\mathrm{d}t} = -\mathrm{i}[\bar{H}_{\mathrm{S}}, \bar{\rho}(t)] + \mathcal{L}_{\mathrm{leads}}\bar{\rho}(t) + \mathcal{L}_{\mathrm{pol}}\bar{\rho}(t) \ . \quad (6.34)$$

6.2.2.3 Molecule-lead terms

Let us first evaluate the $\mathcal{L}_{\mathrm{leads}}\bar{\rho}$ term given by:

$$\mathcal{L}_{\mathrm{leads}}\bar{\rho}(t) = -\int_0^{\infty} \mathrm{d}\tau \ \mathrm{Tr}_{\mathrm{E}} \left[\bar{H}_{\mathrm{V}}, [\tilde{H}_{\mathrm{V}}(-\tau), \bar{\rho}(t)\bar{\rho}_{\mathrm{E}}]\right] \ . \quad (6.35)$$

Similarly to what has been done in Section 6.2.1, expanding the commutator and tracing out the environmental degrees of freedom yields:

$$\begin{aligned} \mathcal{L}_{leads}\bar{\rho}(t) = -\sum_j \sum_{\zeta=\varepsilon_+,\varepsilon_-} & \gamma_j^{(\zeta)} \left(a_j \tilde{a}_j^{\dagger}(\zeta)\bar{\rho}(t) - \tilde{a}_j^{\dagger}(\zeta)\bar{\rho}(t)a_j\right) \\ & + \bar{\gamma}_j^{(\zeta)} \left(a_j^{\dagger}\tilde{a}_j(\zeta)\bar{\rho}(t) - \tilde{a}_j(\zeta)\bar{\rho}(t)a_j^{\dagger}\right) \\ & + \left[\gamma_j^{(\zeta)}\right]^* \left(\bar{\rho}(t)\tilde{a}_j(\zeta)a_j^{\dagger} - a_j^{\dagger}\bar{\rho}(t)\tilde{a}_j(\zeta)\right) \\ & + \left[\bar{\gamma}_j^{(\zeta)}\right]^* \left(\bar{\rho}(t)\tilde{a}_j^{\dagger}(\zeta)a_j - a_j\bar{\rho}(t)\tilde{a}_j^{\dagger}(\zeta)\right) \ . \end{aligned} \quad (6.36)$$

Once again, we have replaced the sum over the lead energy levels with an integral, assumed a wide-band approximation and $V_{k_j} = V_j = \mathrm{const}$.

The electron hopping rates in Eq. (6.36) are therefore given by:

$$\gamma_j^{(\zeta)} = \Gamma_j \int_{-\infty}^{\infty} \frac{\mathrm{d}\epsilon}{2\pi} f_j(\epsilon) \int_0^{\infty} \mathrm{d}\tau \, C_j^P(\tau) e^{\mathrm{i}(\epsilon-\zeta)\tau} \; ; \tag{6.37}$$

$$\bar{\gamma}_j^{(\zeta)} = \Gamma_j \int_{-\infty}^{\infty} \frac{\mathrm{d}\epsilon}{2\pi} [1 - f_j(\epsilon)] \int_0^{\infty} \mathrm{d}\tau \, C_j^P(\tau) e^{-\mathrm{i}(\epsilon-\zeta)\tau} \; , \tag{6.38}$$

where the phononic correlation functions $C_j^P(\tau) \equiv \langle X_j(\tau) X_j^\dagger \rangle = \langle X_j^\dagger(\tau) X_j \rangle$ can be evaluated as follows (see Appendix C):

$$C_j^P(\tau) = \langle X_j \rangle^2 \exp\left[\int_0^{\infty} \mathrm{d}\omega \, \frac{\mathcal{J}_j(\omega)}{\omega^2} \left(\cos\omega\tau \coth\left(\frac{\beta\omega}{2}\right) - \mathrm{i}\sin\omega\tau \right) \right] \; . \tag{6.39}$$

Once again, we will ignore the imaginary parts of Eqs. (6.37, 6.38). We note that, unlike in the Redfield and pure-dephasing approaches, the superoperator (6.36) captures the vibrational effects at the molecule-lead interfaces (through the presence of the phononic correlation functions).

6.2.2.4 Intra-molecular terms

Finally, similar approximations will be made in evaluating the next term in Eq. (6.33). Expanding the commutators yields:

$$\begin{aligned}
\mathcal{L}_{\mathrm{pol}}\bar{\rho}(t) = -|J|^2 \int_0^{\infty} \mathrm{d}\tau \Big\{ & \\
& C_-^P(\tau) \left(s\tilde{s}(-\tau)\rho(t) - \tilde{s}(-\tau)\rho(t)s \right) + C_+^P(\tau) \left(s\tilde{s}^\dagger(-\tau)\rho(t) - \tilde{s}^\dagger(-\tau)\rho(t)s \right) \\
& + C_+^P(\tau) \left(s^\dagger\tilde{s}(-\tau)\rho(t) - \tilde{s}(-\tau)\rho(t)s^\dagger \right) + C_-^P(\tau) \left(s^\dagger\tilde{s}^\dagger(-\tau)\rho(t) - \tilde{s}^\dagger(-\tau)\rho(t)s^\dagger \right) \\
& + C_-^P(-\tau) \left(\rho(t)\tilde{s}(-\tau)s - s\rho(t)\tilde{s}(-\tau) \right) + C_+^P(-\tau) \left(\rho(t)\tilde{s}^\dagger(-\tau)s - s\rho(t)\tilde{s}^\dagger(-\tau) \right) \\
& + C_+^P(-\tau) \left(\rho(t)\tilde{s}(-\tau)s^\dagger - s^\dagger\rho(t)\tilde{s}(-\tau) \right) + C_-^P(-\tau) \left(\rho(t)\tilde{s}^\dagger(-\tau)s^\dagger - s^\dagger\rho(t)\tilde{s}^\dagger(-\tau) \right) \Big\} \; .
\end{aligned} \tag{6.40}$$

Here, for brevity, $s \equiv a_{\mathrm{L}}^\dagger a_{\mathrm{R}}$. Furthermore, $\tilde{s}(\tau) = \tilde{a}_{\mathrm{L}}^\dagger(\tau)\tilde{a}_{\mathrm{R}}(\tau)$ and equivalently for $\tilde{s}^\dagger(\tau)$, and the correlation functions present in Eq. (6.40) take the form:

$$C_+^P(t) = \langle X_{\mathrm{L}}^\dagger(\tau) X_{\mathrm{R}}(\tau) X_{\mathrm{L}} X_{\mathrm{R}}^\dagger \rangle - \langle X_{\mathrm{L}} \rangle^2 \langle X_{\mathrm{R}} \rangle^2 \; , \tag{6.41}$$

and

$$C_{-}^{P}(t) = \langle X_{\mathrm{L}}^{\dagger}(\tau) X_{\mathrm{R}}(\tau) X_{\mathrm{L}}^{\dagger} X_{\mathrm{R}} \rangle - \langle X_{\mathrm{L}} \rangle^2 \langle X_{\mathrm{R}} \rangle^2 \ . \tag{6.42}$$

Using the relations given in Appendix C, they become:

$$C_{+}^{P}(\tau) = \prod_{j=\mathrm{L,R}} \langle X_j \rangle^2 \exp\left[\int_0^{\infty} \mathrm{d}\omega \, \frac{\mathcal{J}_j(\omega)}{\omega^2} \left(\cos\omega\tau \coth\left(\frac{\beta\omega}{2}\right) - \mathrm{i}\sin\omega\tau \right) \right] - \langle X_{\mathrm{L}} \rangle^2 \langle X_{\mathrm{R}} \rangle^2 \ , \tag{6.43}$$

$$C_{-}^{P}(\tau) = \prod_{j=\mathrm{L,R}} \langle X_j \rangle^2 \exp\left[- \int_0^{\infty} \mathrm{d}\omega \, \frac{\mathcal{J}_j(\omega)}{\omega^2} \left(\cos\omega\tau \coth\left(\frac{\beta\omega}{2}\right) - \mathrm{i}\sin\omega\tau \right) \right] - \langle X_{\mathrm{L}} \rangle^2 \langle X_{\mathrm{R}} \rangle^2 \ . \tag{6.44}$$

The dissipator in Eq. (6.40) becomes:

$$\begin{aligned} \mathcal{L}_{\mathrm{pol}} \bar{\rho}(t) = \sum_{\zeta=0,\Delta\varepsilon,-\Delta\varepsilon} & \gamma_{P-}^{(\zeta)} \left(\tilde{s}(\zeta)\rho(t)s - s\tilde{s}(\zeta)\rho(t) \right) + \gamma_{P+}^{(\zeta)} \left(\tilde{s}^{\dagger}(\zeta)\rho(t)s - s\tilde{s}^{\dagger}(\zeta)\rho(t) \right) \\ & + \gamma_{P+}^{(\zeta)} \left(\tilde{s}(\zeta)\rho(t)s^{\dagger} - s^{\dagger}\tilde{s}(\zeta)\rho(t) \right) + \gamma_{P-}^{(\zeta)} \left(\tilde{s}^{\dagger}(\zeta)\rho(t)s^{\dagger} - s^{\dagger}\tilde{s}^{\dagger}(\zeta)\rho(t) \right) \\ & + \left[\gamma_{P-}^{(\zeta)} \right]^{*} \left(s\rho(t)\tilde{s}(\zeta) - \rho(t)\tilde{s}(\zeta)s \right) + \left[\gamma_{P+}^{(\zeta)} \right]^{*} \left(s\rho(t)\tilde{s}^{\dagger}(\zeta) - \rho(t)\tilde{s}^{\dagger}(\zeta)s \right) \\ & + \left[\gamma_{P+}^{(\zeta)} \right]^{*} \left(s^{\dagger}\rho(t)\tilde{s}(\zeta) - \rho(t)\tilde{s}(\zeta)s^{\dagger} \right) + \left[\gamma_{P-}^{(\zeta)} \right]^{*} \left(s^{\dagger}\rho(t)\tilde{s}^{\dagger}(\zeta) - \rho(t)\tilde{s}^{\dagger}(\zeta)s^{\dagger} \right) \ , \end{aligned} \tag{6.45}$$

with the rates given by:

$$\gamma_{P\pm}^{(\zeta)} = |J|^2 \int_0^{\infty} \mathrm{d}\tau \, C_{\pm}^{P}(\tau) \, e^{-\mathrm{i}\zeta\tau} \ . \tag{6.46}$$

Within the polaron approach, the vibrational coupling affects the transport differently than in the Redfield and pure-dephasing approaches. In the Redfield and pure-dephasing approaches, the electron-vibrational interactions induce incoherent transitions which disrupt the otherwise coherent dynamics. Within the polaron approach, the impact of the vibrational coupling is two-fold: it renormalises the coherent coupling as well as induces direct transitions between the two sites, as can be seen in Eq. (6.40).

For all of the above approaches (i.e. the pure-dephasing, Redfield, and polaron), the respective quantum master equations will be solved in the steady-state limit, $\mathrm{d}\rho(t)/\mathrm{d}t =$

0. The observables of interest (site populations, electric current and zero-frequency noise) will be extracted from the resulting stationary density matrix in the same way as described in Chapter 2.

6.3 Results

Throughout this chapter we set the position of the site energy levels (at $V_g = 0$) with respect to the Fermi energies of the unbiased leads to $\varepsilon_0 = 27$ meV, the inter-site coupling $J = -24$ meV, and $\Gamma_L = \Gamma_R = 1$ meV. In principle, $\alpha \in [0, 1]$, however, as values between 0.48 and 0.74 have been reported in experimental and DFT studies [83, 85, 235], we shall adopt $\alpha = 0.6$ unless stated otherwise. For this choice of ε_0 and J, the bonding and antibonding MOs both lie above the Fermi energy and will henceforth be referred to as the LUMO and LUMO+1, respectively.[2]

6.3.1 Purely electronic transport

Before proceeding to examine the effects of vibrational coupling on transport through the considered system, we first study its transport properties in the absence of electron-vibrational interactions.

The IV characteristics for this case are shown in Figure 6.2(a) for different values of α. The presence of two current steps (for $\alpha = 0$) reveals the existence of two transport channels: one for each of the molecular orbitals (MOs) included in our model. The first plateau spans bias voltage range at which only the LUMO level is located within the bias window (its width corresponds to twice the energy gap between LUMO and LUMO+1). As discussed above, for non-zero α an applied bias energetically detunes the two site orbitals. As a result, the efficiency of transport through each of the channels (as quantified by the electric current) decreases with increasing bias leading to Negative Differential Conductance (NDC) [208]. This effect has been observed

[2]Here, we consider a pair of MOs lying above the Fermi energy of the leads. At zero bias, they are hence the two lowest unoccupied MOs of the molecular system even though they do not necessarily have to correspond to the vacuum LUMO and LUMO+1 levels.

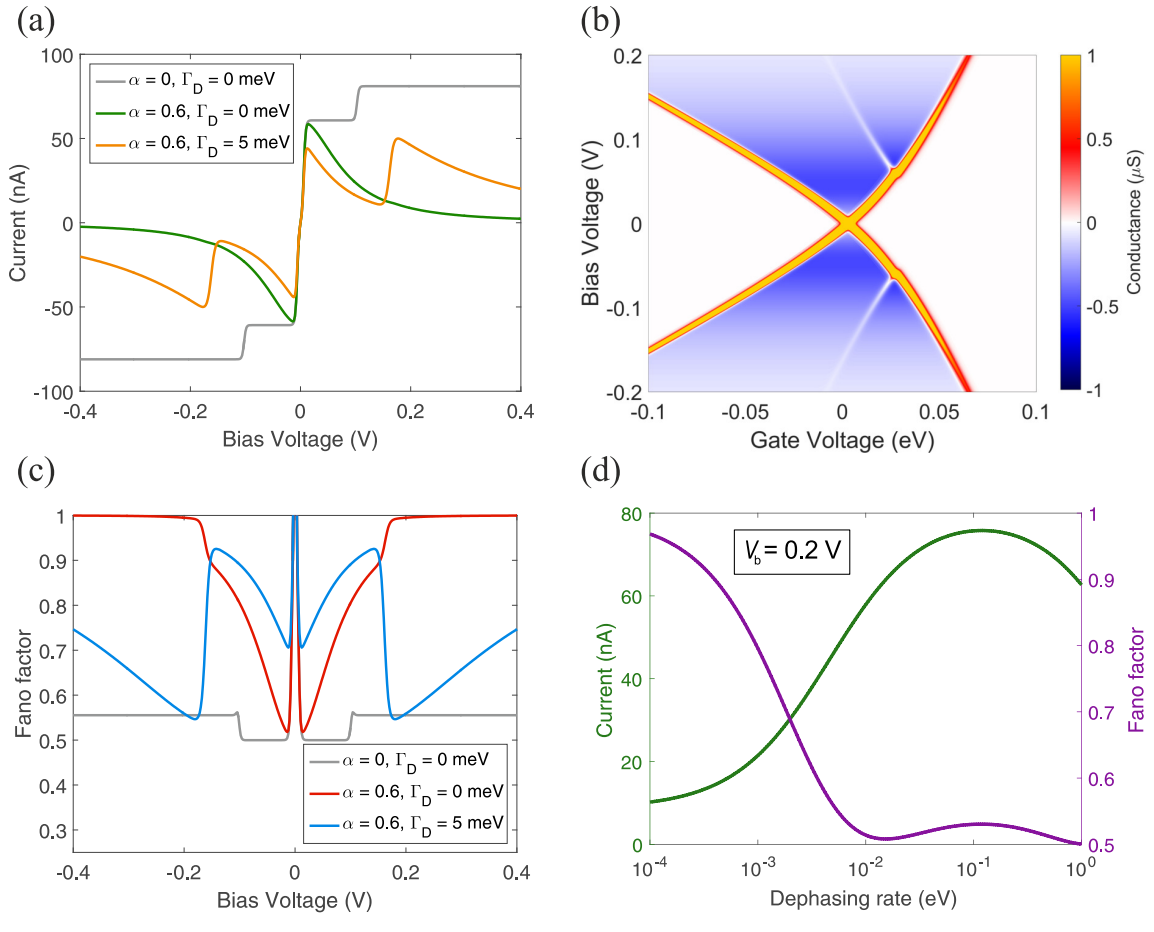


Figure 6.2: (a) IV characteristics; (b) Conductance map for $\alpha = 0.6$ in the absence of environmental coupling; (c) Fano factors as a function of V_b; (d) Current values, and Fano factor at $V_\mathrm{b} = 0.2$ eV as a function of Γ_D. The temperature in the leads: $T = 10$ K.

experimentally and discussed by Perrin *et al.* [83]. Note that the capacitive coupling shifts the position of the LUMO/LUMO+1 levels and hence the position of the steps in the IV characteristics. A calculated conductance map (differential conductance as a function of the bias and gate voltage) for the studied molecular system is shown in Figure 6.2(b). Therein, for simplicity, we have taken $\varepsilon_\mathrm{L/R} = \varepsilon_0 \pm \alpha V_\mathrm{b}/2 - V_\mathrm{g}$, where V_g is the back-gate potential. Similarly to Figure 6.2(a), it demonstrates the existence of two transport channels showing pronounced NDC features. Importantly, the edges of the Coulomb diamonds and the lines corresponding to the higher excited state are curved (in the opposite directions for the LUMO and LUMO+1 levels) due to the capacitive coupling of the sites to the source and drain electrodes.

In the limit of low temperature, the value of current (when only the LUMO, and

both the LUMO and LUMO+1 levels are within the bias window) can be evaluated analytically by solving the QME from Section 6.2. At low bias (i.e. when only the LUMO level lies within the bias window) the current is given by:

$$I = \frac{4J^2\Gamma_L\Gamma_R}{8J^2(\Gamma_L+\Gamma_R)+2\eta(\varepsilon_R-\varepsilon_L)(\Gamma_L-\Gamma_R)+\Gamma_L\Gamma_R^2+2(\Gamma_L+\Gamma_R)(\varepsilon_L-\varepsilon_R)^2} \ . \quad (6.47)$$

Besides being limited to low temperature, the above expression relies on the assumption of weak molecule-lead couplings (for which treating H_{V} as a perturbation is justified). By contrast, for the case of high bias voltages, we recover the well-known result for the current flowing through a double quantum dot structure [236, 237]:

$$I = \frac{4J^2\Gamma_L\Gamma_R}{4J^2\Gamma_R^2+4\Gamma_L\left((\varepsilon_R-\varepsilon_L)^2+2J^2\right)(\Gamma_L-\Gamma_R)+\Gamma_L\Gamma_R^2} \ . \quad (6.48)$$

We also take this opportunity to study the zero-frequency noise, discussed in Chapters 2 and 3. Figure 6.2(c) shows the Fano factor as a function of the bias voltage. For $\alpha = 0$ and at low bias the Fano factor takes the value of roughly $1/2$ (characteristic of a single transport channel), whereas at high bias it approaches $F \approx 5/9$ (the expected infinite-bias value for a strongly coupled resonant double quantum dot) [55, 238, 239]. Energetic detuning of the sites results in an increase of the Fano factor, tending towards unity in the high bias limit.[3]

6.3.2 Pure-dephasing model

We now consider the role of vibrational coupling, initially by employing pure dephasing as the simplest, albeit widely used, way of capturing environmental interactions. As discussed before, the role of environmental coupling in this approach is reduced to an exponential decay of the off-diagonal elements of the density matrix in the site basis. The result of introducing phenomenological dephasing (at rate Γ_{D}) is shown in

[3]This can be conceptually understood by noting that at high bias, the two MOs are localised on either of the sites and the therefore the overall transport resembles tunnelling through a single barrier (between the two sites) which a Poissonian process.

Figure 6.2(a). Firstly, the electric current through the LUMO orbital is significantly suppressed. Introducing pure dephasing results in a population transfer between the LUMO and LUMO+1 orbitals. Since at low bias the LUMO+1 level lies outside of the bias window, charge density transferred into this level drains into both leads. This results in a decrease in net current flowing through the system. This effect – dephasing-driven population transfer between LUMO and LUMO+1 – is shown in Figure 6.3 where we plot the populations of the LUMO and LUMO+1 levels as a function of bias in the absence of pure dephasing, and for $\Gamma_{\mathrm{D}} = 1$ meV. The LUMO+1 level is significantly populated at low bias in the presence of pure dephasing whilst remaining virtually unoccupied for $\Gamma_{\mathrm{D}} = 0$.

Secondly, the current flowing through both MOs (at V_{b} above ~ 0.17 V when $V_{\mathrm{b}}/2 = \varepsilon_{-}$) significantly increases with Γ_{D}. This is essentially an example of an environment-assisted quantum transport (ENAQT) phenomenon [221, 229, 240, 241].[4] At high bias voltage there exists a large energy gap between the two site-orbitals rendering the unitary $|\mathrm{L}\rangle \leftrightarrow |\mathrm{R}\rangle$ transition highly inefficient. The presence of dephasing projects population onto specific sites and thus helps to overcome this energy step. The values of current at $V_{\mathrm{b}} = 0.2$ V as a function of the dephasing rate are shown in Figure 6.2(d). The efficiency of transport through the molecule increases with Γ_{D} as long as it does not considerably exceed the system's characteristic frequency (the energy difference between the MOs, here ~ 0.13 eV). Beyond that point I decreases with the dephasing rate eventually reaching the Quantum Zeno limit [229]. The conditions necessary to observe environment-assisted transport effects in our model system can be summarised as follows: firstly, the dephasing rate must be at least comparable to the molecule-lead coupling strengths, and secondly, the bias-induced energy gap between the sites (here αV_{b}) should be greater than the strength of the inter-site coupling J. This regime should apply to a wide range of molecular multi-site structures, especially if studied in an appropriate device geometry (in which weak molecule-lead coupling can be achieved,

[4] This phenomenon has attracted a great deal of attention in the nascent field of quantum biology. In particular, it has been argued that Nature exploits the subtle interplay between the quantum and dissipative phenomena to optimise the energy transport *in vivo*.

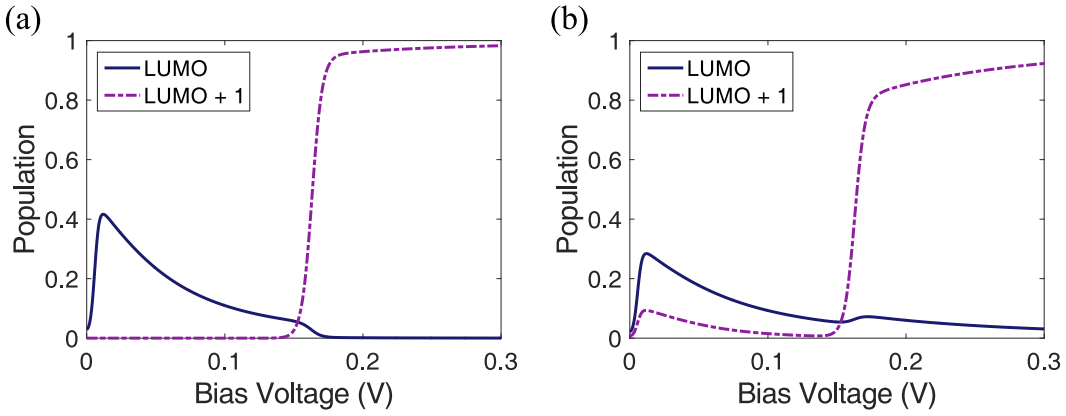


Figure 6.3: Populations of LUMO and LUMO+1 levels in the (a) absence [$\Gamma_{\mathrm{D}} = 0$ meV], and (b) presence of pure dephasing [$\Gamma_{\mathrm{D}} = 1$ meV]. All other parameters as in Figure 6.2(a).

and in which the measurements can be performed at relatively high temperatures).

We now return to the issue of current noise in the studied junction. As shown in Figure 6.2(c), for transport occurring solely through the LUMO, F increases in the presence of pure dephasing which is again attributable to environment-induced population transfer between the molecular levels. In contrast, by assisting the inter-site charge transition, pure dephasing decreases F at high bias in accordance with studies on resonant tunnelling diodes [238], see Figure 6.2(d).

6.3.3 Redfield and Polaron approaches

In this section, we will use the Redfield and Polaron approaches derived in Section 6.2. Treating environmental effects more rigorously than in the previous section requires making certain assumptions about the nature of the vibrational coupling. In this chapter, for simplicity, we assume that the electronic degrees of freedom interact with an unstructured environment and use a superohmic SD with an exponential cut-off:

$$\mathcal{J}(\omega) = \frac{\lambda}{2} \frac{\omega^3}{\omega_{\mathrm{c}}^3} e^{-\omega/\omega_{\mathrm{c}}} , \tag{6.49}$$

where λ is the reorganisation energy and ω_{c} is the cut-off frequency.

The IV characteristics calculated using the Redfield and Polaron approaches (for

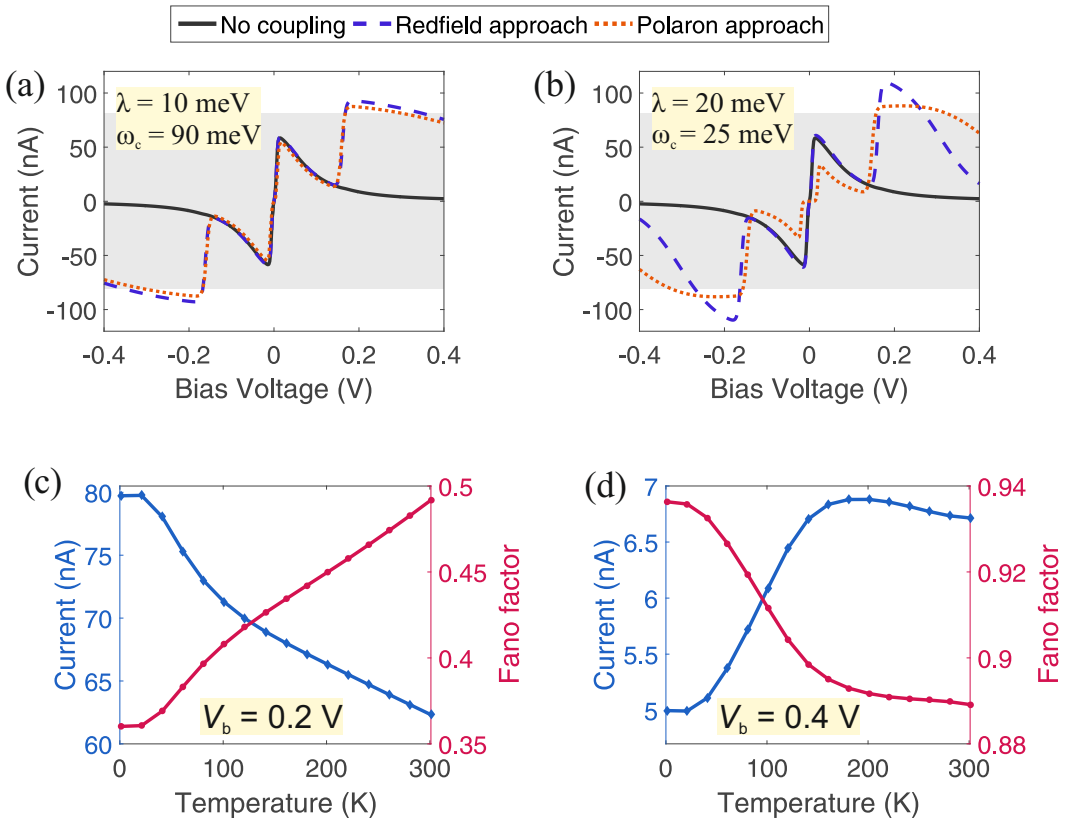


Figure 6.4: (a,b) IV characteristics in the absence of environmental coupling, and presence of coupling to superohmic phonon baths for different values of the λ and ω_c at $T = 10$ K. (c,d) Values of steady-state current and the Fano factor as a function of temperature in the case of coupling to phonon baths with $\lambda = 10$ meV, $\omega_c = 15$ meV obtained using the Polaron method.

the same electronic parameters as in Figure 6.2) are presented in Figure 6.4. Firstly, we also note a significant qualitative resemblance with the results obtained using the pure-dephasing model: the electron-vibrational interactions again lead to a significant enhancement of electric current at high bias. Furthermore, the Redfield and polaron methods yield closely coinciding results for relatively weak vibrational coupling. The small differences between the two approaches in this parameter regime stem predominantly from vibrational effects on molecule-lead interfaces that are not captured by the Redfield method. By contrast, in the strong coupling regime the two methods deliver markedly different results, see Figure 6.4(b). We attribute this partially to considerable vibrational effects on the molecule-lead interfaces (not captured by the Redfield approach), and partially to a failure of the perturbative Redfield technique in

the stronger coupling regime.

Employing these more sophisticated methods (as opposed to the phenomenological pure dephasing) also allows us to properly account for the temperature dependence of the observables of interest. Figure 6.4(c) shows the values of current and the Fano factor as a function of temperature for different values of the bias voltage calculated using the Polaron method. At lower bias, $V_\mathrm{b} = 0.2$ V, the current decreases with temperature as it is dominated by effects occurring at the molecule-lead interfaces: both the vibrational effects and the broadening of the Fermi distributions in the leads. The opposite trend is present at high bias $V_\mathrm{b} = 0.4$ V, see Figure 6.2(d). There, transport is largely insensitive to interfacial effects and an increase in temperature augments intramolecular electron hopping. (Even there, however, Fermi and phonon broadening will eventually lead to a decrease in current at high enough T.) In both cases the Fano factor displays a temperature dependence that is anti-correlated with that of the steady-state current. We conclude that in realistic systems the response of the current as well as Fano factor to increasing temperature will *qualitatively* depend on the bias voltage at which it was measured, even within the resonant tunnelling regime.

We return to Figure 6.4(a) and (b) and focus on the magnitude of the current maxima: surprisingly, environmental coupling paired with non-zero α (i.e. detuned sites) lets the LUMO+1 current peaks exceed the large-bias plateau of the resonant $\alpha = 0$ case (in the absence of environmental interactions). This bound is indicated by the grey background shading in Figures 6.4(a,b). A common interpretation of ENAQT is that it regains (some of) the efficiency lost due to the energetic network disorder [229]. Here, a combination of detuning and environmental coupling unlocks transport efficiency which *exceeds* what is available from an idealised quantum channel [242] (i.e. a noiseless degenerate chain). In the limit of $J \gg \Gamma$, i.e. for comparatively weak molecule-lead coupling, a quasi-equilibrium is established following an electron jump from the source onto the molecule before the electron exits into the drain. In the degenerate case, the additional charge density populates equally both of the sites. On the other

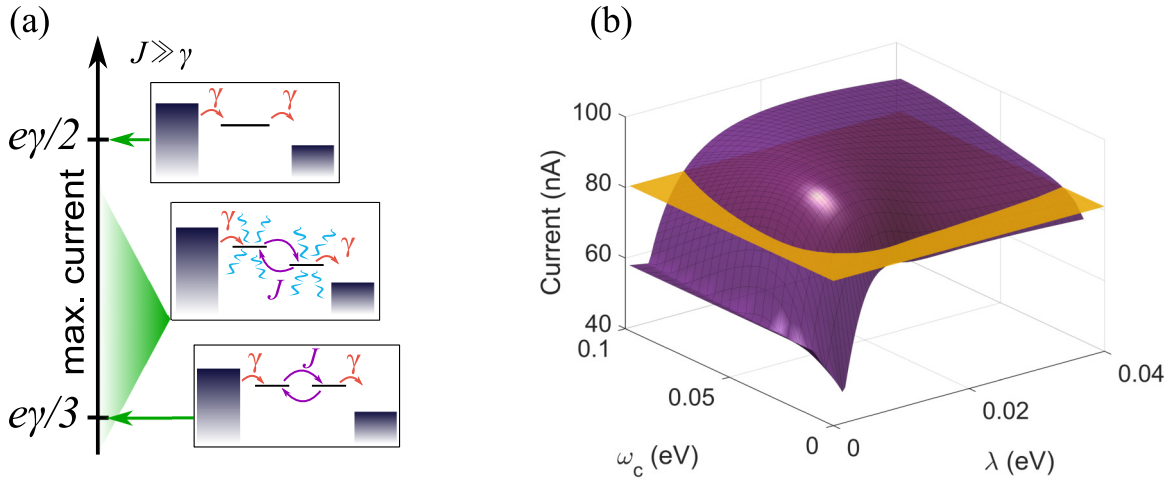


Figure 6.5: (a) Schematic illustration, showing the available current maxima for different scenarios with $J \gg \Gamma$ where $\Gamma = \Gamma_{\mathrm{L}} = \Gamma_{\mathrm{R}}$. (b) Overall maximum value of the current as a function of λ and ω_{c} at $T = 10$ K (Polaron method). The orange plane corresponds to maximum current for $\alpha = 0$ and $\lambda = 0$.

hand, energetic detuning together with environmental coupling favours localisation of the charge density on the site with lower energy thus enhancing the steady-state transport efficiency. However, we note that the current through a two-site system can never surpass that of an equivalent single-site system, Figure 6.5(a).[5]

This phenomenon is depicted more clearly in Figure 6.5(b) which shows the overall maximum value of current as a function of the reorganisation energy and the cut-off frequency of the phonon baths as compared to the value for $\alpha = 0$ and $\lambda = 0$ (orange plane). We note that qualitatively similar behaviour occurs for weaker coupling and that the magnitude of the effect depends on the environmental coupling strength [*c.f.* Figure 6.4(a)]. The agreement between the Redfield and the Polaron approach, which are justified in complementary parameter regimes [233], demonstrates that this effect is not just an artefact arising from the approximations involved in the derivation of a particular model.

[5]For a single-site system, if $\Gamma_{\mathrm{L}} = \Gamma_{\mathrm{R}} = \Gamma$, the steady-state population of the additional charge density on the molecule is $\frac{1}{2}$. This gives an average current of $e\Gamma/2$. For a two-site system, where $\Gamma \ll J$, the steady-state population on each of the sites is $\frac{1}{3}$ which yields an average current of $e\Gamma/3$.

6.3.4 Limitations of the pure-dephasing approach

We finish this chapter with a discussion of limitations of the pure-dephasing model. While this approach possesses the appeal of simplicity, its phenomenological nature and infinite-temperature character can lead to (unphysical) behaviour which differs substantially from that predicted by its microscopically-founded alternatives.

The central idea of the pure-dephasing approach is to assume that the phononic dissipator in the QME is given by Eq. (6.18) which describes an exponential decay of inter-site coherences. As stated above, the pure dephasing approach effectively yields infinite-temperature behaviour since the upward and downward transitions between the molecular eigenstates occur with equal rates. This means that, for instance, in a simple donor-acceptor system in the steady-state limit, the additional charge density will be equally likely found on the donor and the acceptor, irrespective of the energy difference between them.

This has several implications in the case of our model. The upper bound on the current (in the presence of dephasing) is given by the value of current in the absence of environmental interactions, and for $\alpha = 0$ [grey line in Figure 6.2(a)]. Such a bound does not hold – and can be violated (see Figure 6.5) – when using more rigorous microscopically derived approaches. It is also interesting to consider a case of a different energetic alignment of the molecular orbitals than the one studied in the previous sections. First, we set $\varepsilon_0 = 10$ meV. That means the one of the considered MOs is above and one is below the Fermi energy (and so in what follows we will refer to them as HOMO and LUMO levels, respectively), as schematically shown in Figure 6.6.

The IV characteristics for this case are calculated in the absence and presence of pure dephasing, see Figure 6.6(b). At low bias (and in the absence of dephasing), the HOMO level is fully occupied, the LUMO level is empty. No (resonant) current flows through the system since neither of the levels lies within the bias window. As we increase the bias voltage, we see the usual NDC behaviour (grey curve). Introducing pure dephasing [using Eq. (6.18)] leads to a surprising behaviour: electric current at

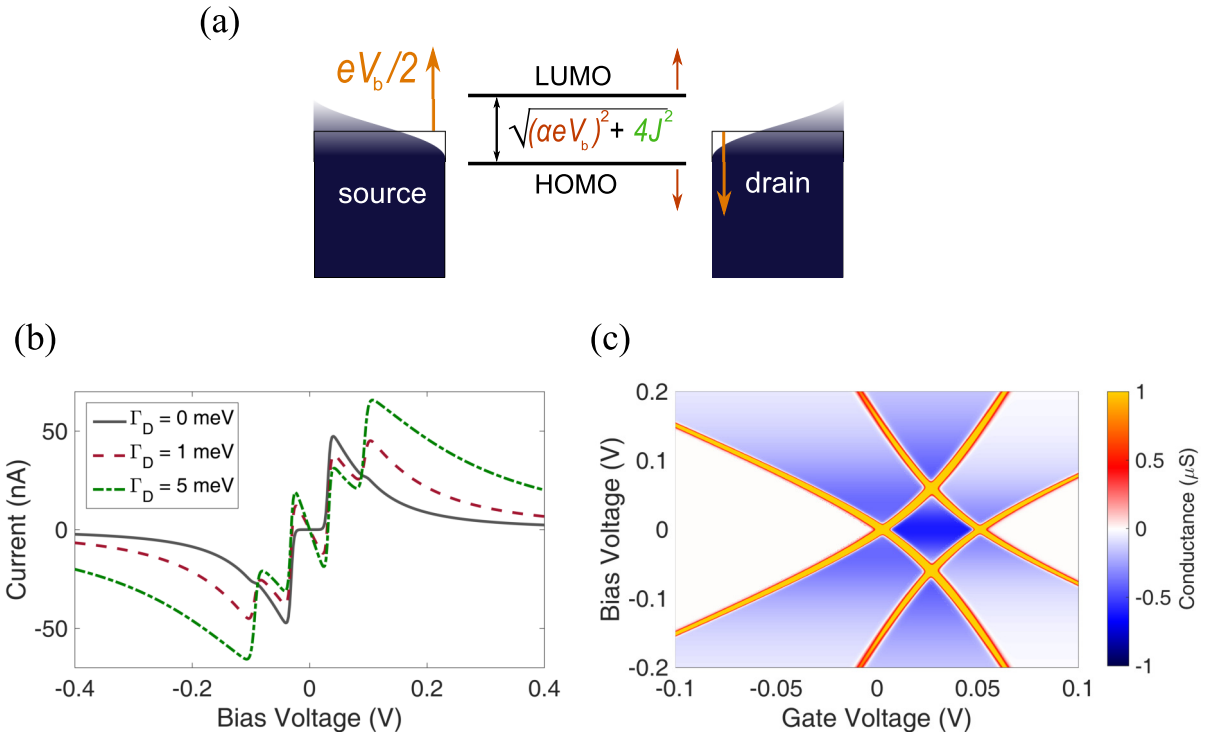


Figure 6.6: (a) Schematic energy diagram (in the energy basis) for the system discussed in this section. (b) IV characteristics of a two-site system in the presence of dephasing at the rate Γ_{D}. (c) Conductance map with $\Gamma_{\mathrm{D}} = 1$ meV. In both figures $\varepsilon_0 = 10$ meV, $\alpha = 0.6$, and $T_{\mathrm{e}} = 10$ K.

low bias flows in the opposite direction to the applied bias. Pure dephasing results in population transfer from HOMO to LUMO, and since the LUMO level lies outside of the bias window, this charge density can tunnel out into both of the leads. Because of the energetic detuning present within our model, at positive bias the LUMO level is predominantly centred on the left site. Consequently, the charge density predominantly tunnels out into the source electrode – leading to negative current at positive bias and *vice versa*. This is clearly an example of a *qualitative* failure of the pure dephasing model.[6] We can, similarly to what has been done in Section 6.3.1, calculate a conductance map for our system, this time in the presence of pure dephasing, see Figure 6.6(c). It clearly shows the effect described above. Besides giving rise to the unphysical negative differential conductance at low positive gate voltages, pure dephasing is also capable of lifting the Coulomb blockade for positive gate potentials [*c.f.* Figure 6.2(b)].

[6]Such seemingly paradoxical behaviour can, in fact, also be obtained within the Redfield approach (for an ohmic spectral density) at high temperature. This requires, however, to artificially separate the phononic and electronic temperatures, and keep the latter close to zero.

In conclusion, due to its infinite-temperature character, the pure-dephasing approach can give rise to a number of artefacts in the molecular transport characteristics. This suggests that while the pure-dephasing approach is attractive due to its inherent simplicity, even qualitative predictions obtained using this method should be treated with caution.

6.4 Conclusions

In this chapter, we have studied the effects of collective vibrational coupling on the charge transport properties of a molecular two-site system. This problem was approached using three different theoretical approaches in which the environmental interactions were described using: (i) the phenomenological pure-dephasing approach; (ii) the perturbative Redfield theory; and (iii) the polaron approach.

We have demonstrated that the two-site systems considered here can exhibit certain unusual transport properties: large regions of negative differential conductance and curved edges of the Coulomb diamonds. Secondly, we have shown that the environmental interactions can significantly enhance the efficiency of charge transport through such systems by assisting the inter-site transition. This effect was predicted by all of the considered theoretical approaches and is an example of an environment quantum transport phenomenon. We have also demonstrated that a combination of the environmental dissipative effects and energetic disorder can be used to achieve transport efficiency which exceeds that of an idealised transport channel. Furthermore, we have also taken this opportunity to examine the limitations of the pure-dephasing approach. We have shown that it can give rise to a number of artefacts stemming from its infinite-temperature character. Finally, as we have demonstrated throughout this chapter, systems of the type considered here constitute a promising platform which can be used experimentally to study the intra-molecular vibrational effects in single-molecule junctions.

Chapter 7

Collective vibrational effects: Theory

For computation, I had a little calculator which had been captured from the German army.

— Noel S. Hush

In this chapter, we return to a single-site system briefly discussed in Chapter 3. The work described here is partially motivated by the detailed experimental measurements of transport through zinc-porphyrin molecular junctions which will be discussed and analysed in the next chapter. They will illustrate a common difficulty encountered in the field of molecular electronics – the apparent variability of transport behaviour between different junctions comprising the same molecular structures. This problem stems mainly from differences in the microscopic structure of the leads, the molecule-lead contacts, and geometric distortions of the deposited molecular systems. As the result, however, there currently exists a dissonance between the theoretical modelling of (inelastic) resonant transport and the majority of experimental studies on the topic. The analysis in the latter is often limited to qualitatively identifying the vibrational features [35,41,94,139,243], as reproducing the full IV characteristics has often proven to be problematic. This is clearly unsatisfactory and there thus exists a need for

a theoretical approach which captures all the relevant transport phenomena at the minimal required level of complexity.

Here, we develop a theoretical framework describing the charge transport through a single-molecule junction modelled as a single electronic level coupled to two fermionic reservoirs, as well as a collection of thermalised vibrational modes. Such a model system has been extensively studied in the past, but the existing theoretical approaches are, for various reasons, inadequate for the problem at hand. They are either: (i) perturbative in the molecule-lead coupling (and therefore do not capture lifetime broadening) [1, 134, 135, 244], (ii) based on scattering approaches that do not account for charge occupation of the molecular system (see Section 7.3) [245–248], or (iii) computationally expensive/cannot be easily extended beyond the single-mode case (and hence cannot be readily used to explain or fit the experimental data) [249–253]. Our first objective, therefore, is to arrive at an expression for the steady-state electric current in the resonant transport regime which will capture the effects of electron-vibrational interactions and lifetime broadening as well as account for the charge occupation of the molecular system. This will be achieved using a Generalised Quantum Master Equation (GQME) in a polaron-transformed frame. The second goal of this chapter is to derive a number of high-temperature approximations to the GQME result which can be very easily computed or even fitted to the empirical data. The methodology derived here will be applied to examples building on phenomenological as well as microscopically-motivated electron-vibrational coupling. In the subsequent chapter, the framework developed here will also be used to explain and model the experimentally-observed transport behaviour.

7.1 Model

The theoretical model studied here is schematically pictured in Figure 7.1, and described by the following Hamiltonian ($\hbar = 1$ and $e = 1$ throughout): $H = H_S + H_{SE} + H_E + H_{SB} + H_B$. We assume that the molecule possesses only a single electronic energy

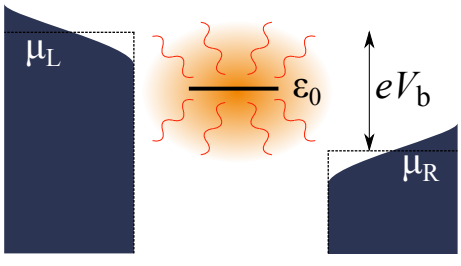


Figure 7.1: A schematic illustration of the system studied in this chapter. The molecular junction is modelled as a single electronic level coupled to a collection of thermalised vibrational modes, as well as the left (L) and right (R) electrode. V_b denotes the bias potential, μ_L and μ_R are the chemical potentials of the left and right electrode, respectively.

level with the creation (annihilation) operator $a_0^\dagger$ (a_0) and energy ε_0:

$$H_S = \varepsilon_0 \, a_0^\dagger a_0 \ . \tag{7.1}$$

The position of the energy level in question, with respect to the Fermi energies of the unbiased electrodes, can be altered by applying the gate potential V_g: $\varepsilon_0 = \varepsilon_{00} - V_\mathrm{g}$ where ε_{00} is the position of the electronic energy level at $V_\mathrm{g} = 0$. The left (L) and right (R) electrodes are described by

$$H_E = \sum_{l=\mathrm{L,R}} \sum_{k_l} \epsilon_{k_l} c_{k_l}^\dagger c_{k_l} \ , \tag{7.2}$$

where $c_{k_l}^\dagger$ (c_{k_l}) is the creation (annihilation) operator for the electron in the level k_l with energy ϵ_{k_l} in the lead l. The molecule-lead coupling is described by the usual tunnelling Hamiltonian:

$$H_{SE} = \sum_{l=\mathrm{L,R}} \sum_{k_l} V_{k_l} a_0^\dagger c_{k_l} + V_{k_l}^* c_{k_l}^\dagger a_0 \ , \tag{7.3}$$

where V_{k_l} is the coupling strength. Furthermore, the molecular electronic energy level is also coupled to a collection of thermalised vibrational modes (a phonon bath) which are modelled as harmonic oscillators with frequencies ω_q and raising (lowering) operators

$b_q^\dagger$ (b_q):

$$H_B = \sum_q \omega_q b_q^\dagger b_q \ . \tag{7.4}$$

The electronic-vibrational coupling has the familiar linear form:

$$H_{SB} = \sum_q g_q \, a_0^\dagger a_0 (b_q^\dagger + b_q) \ , \tag{7.5}$$

where g_q is the electron-vibrational coupling constant. In general, the electronic degrees of freedom in molecular junctions can couple both to the intra-molecular as well as environmental vibrational modes, the latter originating from the solvent [75, 216–220] or the surface on which the molecule is deposited [140, 215]. In what follows we will disregard any non-equilibrium dynamics of the considered vibrational modes (*c.f.* Chapters 4 and 5), and shall treat all the vibrational interactions on an equal footing through the previously encountered spectral density: $\mathcal{J}(\omega) = \sum_q |g_q|^2 \delta(\omega - \omega_q)$, which describes the distribution of the vibrational modes weighted by the strength of the electronic-vibrational coupling.

7.2 Derivation

We first perform the polaron (Lang-Firsov) transformation which eliminates the H_{SB} term from the Hamiltonian: $\bar{H} = e^G H e^{-G}$, where $G = \sum_q (g_q/\omega_q) \, a_0^\dagger a_0 (b_q^\dagger - b_q)$ [36, 47]. This yields the Hamiltonian in the polaron-transformed frame:

$$\bar{H} = \bar{H}_S + \bar{H}_{SE} + H_E + H_B \ ; \tag{7.6}$$

$$\bar{H}_S = \left(\varepsilon_0 - \sum_q \frac{|g_q|^2}{\omega_q} \right) \, a_0^\dagger a_0 \equiv \bar{\varepsilon}_0 \, a_0^\dagger a_0 \ ; \tag{7.7}$$

$$\bar{H}_{SE} = \sum_{l,k_l} V_{k_l} X^\dagger a_0^\dagger c_{k_l} + V_{k_l}^* c_{k_l}^\dagger X a_0 \ . \tag{7.8}$$

As can be seen above, the position of the molecular electronic energy level has been renormalised. Furthermore, the usual displacement operators X and $X^\dagger$ have been

introduced into the molecule-lead coupling Hamiltonian:

$$X = \exp\left[-\sum_q \frac{g_q}{\omega_q}(b_q^\dagger - b_q)\right] \ . \tag{7.9}$$

Physically, their presence in Eq. (7.8) accounts for the fact that the charging of the molecule is accompanied by a displacement of the vibrational modes coupled to this molecular level. Their properties were extensively discussed in Chapter 2.

Working in the polaron-transformed frame, we begin with a second-order quantum master equation within the Born approximation. It will prove useful to express it in the form given by Yan [254]:

$$\frac{\mathrm{d}\rho(t)}{\mathrm{d}t} = -\mathrm{i}\mathcal{L}\rho(t) - \int_0^t \mathrm{d}\tau \langle \mathcal{L}'(t)\mathcal{G}(t,\tau)\mathcal{L}'(\tau)\mathcal{G}^\dagger(t,\tau)\rangle \rho(t) \ . \tag{7.10}$$

The super-operators in the above are defined as: $\mathcal{L}\bullet \equiv [\bar{H}_S, \bullet]$, $\mathcal{L}'\bullet \equiv [\bar{H}_{SE}, \bullet]$, and $\langle \ldots \rangle$ denotes the trace over all (phononic and fermionic) environmental degrees of freedom. $\mathcal{G}(t,\tau)$ is the (free) system propagator: $\mathcal{G}(t,\tau) \equiv e^{-\mathrm{i}\mathcal{L}(t-\tau)}$. It can be defined in Hilbert space, as acting on an arbitrary operator A, by:

$$\mathcal{G}(t)[A] = e^{-\mathrm{i}\bar{H}_S t} A e^{\mathrm{i}\bar{H}_S t} \ . \tag{7.11}$$

In order to go beyond the second-order Born approximation (and similar to what is done within the self-consistent Born approximation [255, 256]), we shall replace the free system propagator $\mathcal{G}(t,\tau)$ in Eq. (7.10) with an effective one, $\mathcal{U}(t,\tau)$. When deriving the second-order molecule-lead hopping rates, this as-yet-unknown effective propagator will account for the fact that the unitary evolution of the relevant system operators is influenced by the system-environment coupling and allow us to incorporate the otherwise missing lifetime broadening into our description.

Let us first expand the commutators in Eq. (7.10) and then replace the free prop-

agator with $\mathcal{U}(t,\tau) = \mathcal{U}(t-\tau)$. This yields:

$$\frac{\mathrm{d}\rho(t)}{\mathrm{d}t} = -\mathrm{i}[\bar{H}_S, \rho(t)] - \sum_l \sum_{k_l} \int_0^t \mathrm{d}\tau \Big\{$$
$$C^+_{k_l}(t-\tau)B(t-\tau)a_0\,\mathcal{U}(t-\tau)\left[a_0^\dagger\right]\rho(t) - C^{-*}_{k_l}(t-\tau)B^*(t-\tau)a_0\,\rho(t)\mathcal{U}(t-\tau)\left[a_0^\dagger\right]$$
$$+C^-_{k_l}(t-\tau)B(t-\tau)a_0^\dagger\,\mathcal{U}(t-\tau)\left[a_0\right]\rho(t) \; - C^{+*}_{k_l}(t-\tau)B^*(t-\tau)a_0^\dagger\,\rho(t)\mathcal{U}(t-\tau)\left[a_0\right]$$
$$+C^{-*}_{k_l}(t-\tau)B^*(t-\tau)\,\rho(t)\mathcal{U}(t-\tau)\left[a_0^\dagger\right]a_0 - C^+_{k_l}(t-\tau)B(t-\tau)\,\mathcal{U}(t-\tau)\left[a_0^\dagger\right]\rho(t)a_0$$
$$+C^{+*}_{k_l}(t-\tau)B^*(t-\tau)\,\rho(t)\mathcal{U}(t-\tau)\left[a_0\right]a_0^\dagger \; - C^-_{k_l}(t-\tau)B(t-\tau)\,\mathcal{U}(t-\tau)\left[a_0\right]\rho(t)a_0^\dagger\Big\}\,. \tag{7.12}$$

In the equation above, we denoted $C^+_{k_l}(t-\tau) = |V_{k_l}|^2\langle c^\dagger_{k_l}(t)c_{k_l}(\tau)\rangle$ and $C^-_{k_l}(t-\tau) = |V_{k_l}|^2\langle c_{k_l}(t)c^\dagger_{k_l}(\tau)\rangle$. These fermionic correlation functions can be written as:

$$\sum_{k_l} C^\pm_{k_l}(t) = \int_{-\infty}^{\infty} \frac{\mathrm{d}\epsilon}{2\pi}\,\Gamma^\pm_l(\epsilon)\,e^{\pm\mathrm{i}\epsilon t}\,, \tag{7.13}$$

where $\Gamma^+_l(\epsilon) = \Gamma_l(\epsilon)f_l(\epsilon)$ and $\Gamma^-_l(\epsilon) = \Gamma_l(\epsilon)[1-f_l(\epsilon)]$. Here, $\Gamma_l(\epsilon) = 2\pi\sum_{k_l}|V_{k_l}|^2\delta(\epsilon - \epsilon_{k_l})$ is the spectral density for the lead l. The Fermi distributions in each of the leads are given by: $f_l(\epsilon) = (\exp[(\epsilon-\mu_l)/k_\mathrm{B}T]+1)^{-1}$, where μ_l is the chemical potential of the lead l. Furthermore, $B(t-\tau)$ is the phononic correlation function defined as:

$$B(t-\tau) = \langle X(t)X^\dagger(\tau)\rangle = \mathrm{Tr}\Big[X(t)X^\dagger(\tau)\rho_B\Big]\,, \tag{7.14}$$

where ρ_B is the density matrix of the phonon bath. As shown in Appendix C, for thermalised vibrational modes it is given by:

$$B(t) = \exp\left[\int_0^\infty \mathrm{d}\omega \frac{\mathcal{J}(\omega)}{\omega^2}\left(\coth\left(\frac{\beta\omega}{2}\right)\times\big(\cos\omega t - 1\big) - \mathrm{i}\sin\omega t\right)\right]. \tag{7.15}$$

In Eq. (7.12), we next substitute $t' = t-\tau$ and, anticipating that our interest will lie in the steady-state limit, extend the integration limit to infinity and replace $\rho(t)$ with the stationary density matrix ρ_st such that: $\mathrm{d}\rho_\mathrm{st}/\mathrm{d}t = 0$. The quantum master equation

now takes the form:

$$0 = -\mathrm{i}\mathcal{L}\rho_{\mathrm{st}} - \sum_{l}\int_{-\infty}^{\infty}\frac{\mathrm{d}\epsilon}{2\pi}\Big\{\int_{0}^{\infty}\mathrm{d}t'\;\Gamma_{l}^{+}(\epsilon)e^{+\mathrm{i}\epsilon t'}B(t')a_0\,\mathcal{U}(t')\left[a_0^{\dagger}\right]\rho_{\mathrm{st}} - ...\Big\}\;, \qquad (7.16)$$

and similarly for the rest of the terms. The solution to the above QME is the stationary density matrix, ρ_{st}, which shall be used to calculate the current flowing through the junction.

7.2.1 The effective propagator

Before we determine the effective propagator required in Eq. (7.16), let us briefly discuss the free propagator present in Eq. (7.10). It is defined in Eq. (7.11) which in the present case yields: $\mathcal{G}(t)[a_0] = a_0 e^{\mathrm{i}\bar{\varepsilon}_0 t}$, and $\mathcal{G}(t)[a_0^{\dagger}] = a_0^{\dagger}e^{-\mathrm{i}\bar{\varepsilon}_0 t}$. One can easily see the origin of the problem encountered within the standard Born approximation. Since, in the second-order QME (7.10), it is assumed that the evolution of the creation (annihilation) operator is unaffected by the molecule-lead coupling, the electron hopping described by this dissipator will not account for lifetime broadening. Therefore, we replace the free propagator with:

$$\mathcal{U}(t)[A] = \mathrm{Tr}\left[e^{-\mathrm{i}\bar{H}t}Ae^{\mathrm{i}\bar{H}t}\right]\;, \qquad (7.17)$$

where $A = \{a_0, a_0^{\dagger}\}$, *c.f.* Ref. [152].

In order to determine $\mathcal{U}(t)[a_0]$, let us consider the equations of motion for $a_0(t) \equiv \exp\left(-\mathrm{i}\bar{H}t\right)a_0\exp\left(\mathrm{i}\bar{H}t\right)$, and $c_{k_l}(t) \equiv \exp\left(-\mathrm{i}\bar{H}t\right)c_{k_l}\exp\left(\mathrm{i}\bar{H}t\right)$ operators in the polaron-transformed frame:

$$\dot{a}_0(t) = \mathrm{i}\bar{\varepsilon}_0 a_0(t) - \mathrm{i}\sum_{l,k_l}V_{k_l}X^{\dagger}(t)c_{k_l}(t)\;; \qquad (7.18)$$

$$\dot{c}_{k_l}(t) = \mathrm{i}\epsilon_{k_l}c_{k_l}(t) - \mathrm{i}\,V_{k_l}^{*}X(t)a_0(t)\;. \qquad (7.19)$$

Using the Laplace transform, $a_0(z) = \int_0^{\infty}\mathrm{d}t e^{-zt}a_0(t)$, we can turn this set of differential

equations into an algebraic one:

$$z a_0(z) - a_0(0) = \mathrm{i}\bar{\varepsilon}_0 a_0(z) - \mathrm{i}\sum_{l,k_l} V_{k_l} X^\dagger(z) c_{k_l}(z) \ ; \tag{7.20}$$

$$z c_{k_l}(z) - c_{k_l}(0) = \mathrm{i}\epsilon_{k_l} c_{k_l}(z) - \mathrm{i}\ V_{k_l}^* X(z) a_0(z) \ . \tag{7.21}$$

Eliminating the fermionic reservoir modes gives:

$$[z - \mathrm{i}\bar{\varepsilon}_0]\ a_0(z) = a_0(0) - \sum_{l,k_l} \frac{|V_{k_l}|^2}{z - \mathrm{i}\epsilon_{k_l}} a_0(z) - \mathrm{i}\sum_{l,k_l} \frac{V_{k_l} X^\dagger(z)}{z - \mathrm{i}\epsilon_{k_l}} c_{k_l}(0) \ . \tag{7.22}$$

Crucially, the displacement operators have cancelled in the second term on the right-hand-side of Eq. (7.22). We disregard the final term (which vanishes when tracing out the fermionic reservoirs) and assuming a continuum of states in the leads, replace the sum in the second term of Eq. (7.22) with an integral:

$$\sum_{k_l} \frac{|V_{k_l}|^2}{z - \mathrm{i}\epsilon_{k_l}} \ \rightarrow \ \int_{-\infty}^{\infty} \frac{\mathrm{d}\epsilon_l}{2\pi} \ \frac{\Gamma_l(\epsilon_l)}{z - \mathrm{i}\epsilon_l} \ . \tag{7.23}$$

We will assume that $\Gamma_l(\epsilon_l)$ is a Lorentzian: $\Gamma_l(\epsilon_l) = \dfrac{\Gamma_l\ \delta_l^2}{\epsilon_l^2 + \delta_l^2}$, and to obtain the wide-band approximation, set $\delta_l \rightarrow \infty$ [173]. Consequently,

$$a_0(z) = \frac{1}{z - \mathrm{i}\bar{\varepsilon}_0 + (\Gamma_\mathrm{L} + \Gamma_\mathrm{R})/2} \ a_0(0) \ . \tag{7.24}$$

Moving back to the time domain and defining $\Gamma = (\Gamma_\mathrm{L} + \Gamma_\mathrm{R})/2$, yields:

$$\mathcal{U}(t)\,[a_0] = a_0 e^{+\mathrm{i}\bar{\varepsilon}_0 t - \Gamma t} \ , \tag{7.25}$$

and similarly, for $a_0^\dagger$, we obtain: $\mathcal{U}(t)\left[a_0^\dagger\right] = a_0^\dagger e^{-\mathrm{i}\bar{\varepsilon}_0 t - \Gamma t}$. We note that the simplicity of the correction to the Born approximation ($e^{-\Gamma t}$) is only possible due to the (not immediately obvious) cancellation of the displacement operators in Eq. (7.22).

7.2.2 Back to the quantum master equation

Once again, we will take $V_{k_l} = V_l = \text{const.}$ and assume the wide-band approximation. Then, $\Gamma_l(\epsilon)$ in Eq. (7.13) becomes $\Gamma_l = 2\pi|V_l|^2\varrho_l$ where ϱ_l is the constant density of states in lead l. Inserting $\mathcal{U}(t)\left[a_0\right]$ and $\mathcal{U}(t)\left[a_0^\dagger\right]$ into the quantum master equation allows us to express it in a surprisingly simple form:

$$0 = -\mathrm{i}[\bar{H}_S, \rho_{\mathrm{st}}] + \sum_l \Big\{ \upsilon_l \left(a_0^\dagger \rho_{\mathrm{st}} a_0 - a_0 a_0^\dagger \rho_{\mathrm{st}} \right) + \upsilon_l^* \left(a_0^\dagger \rho_{\mathrm{st}} a_0 - \rho_{\mathrm{st}} a_0 a_0^\dagger \right) + \bar{\upsilon}_l \left(a_0 \rho_{\mathrm{st}} a_0^\dagger - a_0^\dagger a_0 \rho_{\mathrm{st}} \right) + \bar{\upsilon}_l^* \left(a_0 \rho_{\mathrm{st}} a_0^\dagger - \rho_{\mathrm{st}} a_0^\dagger a_0 \right) \Big\} , \quad (7.26)$$

where the rates υ_l and $\bar{\upsilon}_l$ can be inferred from Eq. (7.16).

The solution to the Eq. (7.26), in the basis of the neutral and charged molecular states ($\{|N\rangle,\ |N+1\rangle\}$), can be written as:

$$\rho_{\mathrm{st}} = \begin{pmatrix} \dfrac{\bar{\gamma}_L + \bar{\gamma}_R}{\gamma_{\mathrm{L}} + \gamma_{\mathrm{R}} + \bar{\gamma}_L + \bar{\gamma}_R} & 0 \\ 0 & \dfrac{\gamma_{\mathrm{L}} + \gamma_{\mathrm{R}}}{\gamma_{\mathrm{L}} + \gamma_{\mathrm{R}} + \bar{\gamma}_L + \bar{\gamma}_R} \end{pmatrix} , \quad (7.27)$$

where the electron hopping rates in the above are defined as $\gamma_l = 2\mathrm{Re}[\upsilon_l]$, $\bar{\gamma}_l = 2\mathrm{Re}[\bar{\upsilon}_l]$, and given by:

$$\gamma_l = 2\ \mathrm{Re}\left[\Gamma_l \int_{-\infty}^{\infty} \frac{\mathrm{d}\epsilon}{2\pi} f_l(\epsilon) \int_0^{\infty} \mathrm{d}\tau\ e^{+\mathrm{i}(\epsilon - \bar{\varepsilon}_0)\tau} e^{-\Gamma\tau} B(\tau) \right] ; \quad (7.28)$$

$$\bar{\gamma}_l = 2\ \mathrm{Re}\left[\Gamma_l \int_{-\infty}^{\infty} \frac{\mathrm{d}\epsilon}{2\pi} [1 - f_l(\epsilon)] \int_0^{\infty} \mathrm{d}\tau\ e^{-\mathrm{i}(\epsilon - \bar{\varepsilon}_0)\tau} e^{-\Gamma\tau} B(\tau) \right] . \quad (7.29)$$

We note that coherences between the two charge states vanish (and are generally decoupled from the electronic populations). This is, in fact, universally true and is not a consequence of the approximations made herein [257]. The quantum master equation (7.26) has a secular form and consequently we only need to consider the real parts of the response functions, as shown above.

In the steady-state, the electric current through the molecule at the left and right

contacts is equal and opposite. Let us consider the right contact where it can be expressed (again, in units of e and $\hbar$) simply as: $I = (\ \gamma_{\mathrm{R}}\rho_{N,N,\mathrm{st}} - \bar{\gamma}_R\rho_{N+1,N+1,\mathrm{st}})$, see Section 2.5.2. Together with Eq. (7.27) this gives the generic expression for the electric current:

$$I = \frac{\gamma_{\mathrm{L}}\bar{\gamma}_R - \gamma_{\mathrm{R}}\bar{\gamma}_L}{\gamma_{\mathrm{L}} + \gamma_{\mathrm{R}} + \bar{\gamma}_L + \bar{\gamma}_R} \ . \tag{7.30}$$

The above, together with Eqs. (7.28,7.29), constitutes the GQME approach and satisfies the first objective of this chapter. Therein, the lifetime broadening is captured by the inclusion of the $e^{-\Gamma\tau}$ correction to the usual Born approximation, the $B(\tau)$ term describes the vibrational effects in electron tunnelling on and off the molecule, while the charge state of the molecule is accounted for by the steady-state density matrix (7.27), and consequently also by Eq. (7.30).

7.3 Comparison with NEGF

How does our result compare to the well-established non-equilibrium Green's function (NEGF) approaches? Let us first consider the limit of no vibrational coupling: $\mathcal{J}(\omega) = 0$. Then, the hopping-on rate becomes:

$$\gamma_l = 2\ \mathrm{Re}\ \Gamma_l \int_{-\infty}^{\infty} \frac{\mathrm{d}\epsilon}{2\pi} f_l(\epsilon) \int_0^{\infty} \mathrm{d}\tau e^{\mathrm{i}(\epsilon-\varepsilon_0)\tau} e^{-\Gamma\tau} \ , \tag{7.31}$$

and equivalently for $\bar{\gamma}_l$. The one-sided Fourier transform can be easily evaluated:

$$\Psi(\epsilon) = \mathrm{Re} \int_0^{\infty} \mathrm{d}\tau \exp\left[(+\mathrm{i}(\epsilon-\varepsilon_0) - \Gamma)\,\tau\right] = \frac{\Gamma}{\Gamma^2 + (\epsilon-\varepsilon_0)^2} \ , \tag{7.32}$$

and therefore the numerator in Eq. (7.30) is given by:

$$\gamma_{\mathrm{L}}\bar{\gamma}_R - \gamma_{\mathrm{R}}\bar{\gamma}_L = 2\Gamma_{\mathrm{L}}\Gamma_{\mathrm{R}} \int_{-\infty}^{\infty} \frac{\mathrm{d}\epsilon}{2\pi} [f_L(\epsilon) - f_R(\epsilon)]\Psi(\epsilon) \ , \tag{7.33}$$

and the denominator simplifies to:

$$\sum_{l=L,R} \gamma_l + \bar{\gamma}_l = \sum_{l=L,R} 2\ \Gamma_l \int_{-\infty}^{\infty} \frac{\mathrm{d}\epsilon}{2\pi} \Psi(\epsilon) = \sum_{l=L,R} \Gamma_l\ . \tag{7.34}$$

This yields the following expression for the electric current:

$$I = \int_{-\infty}^{\infty} \frac{\mathrm{d}\epsilon}{2\pi} [f_L(\epsilon) - f_R(\epsilon)] \frac{\Gamma_\mathrm{L}\Gamma_\mathrm{R}}{(\epsilon - \varepsilon_0)^2 + \Gamma^2}\ , \tag{7.35}$$

which, reassuringly, is the usual Landauer-Büttiker expression for current through a single non-interacting level [247, 258].

Returning to the case of non-zero vibrational coupling, the problem at hand has been approached using NEGF methods by a number of authors [245–248, 252, 253]. Here, we will compare our result to the one derived by Jauho *et al.* [247]. Therein, the electric current was found to be given by:

$$I = \frac{\Gamma_\mathrm{L}\Gamma_\mathrm{R}}{\Gamma_\mathrm{L} + \Gamma_\mathrm{R}} \int_{-\infty}^{\infty} \frac{\mathrm{d}\epsilon}{2\pi} [f_L(\epsilon) - f_R(\epsilon)] \int_{-\infty}^{\infty} \mathrm{d}\tau e^{\mathrm{i}\epsilon\tau} a(\tau)\ , \tag{7.36}$$

where $a(\tau) = \mathrm{i}[G^r(\tau) - G^a(\tau)]$, and the retarded Green function is given by: $G^r(\tau) = -\mathrm{i}\theta(\tau) e^{-\mathrm{i}\tau\bar{\varepsilon}_0} e^{-\Gamma\tau} B(\tau)$, where $\theta(\tau)$ is the Heaviside step function, and $G^a(\tau) = [G^r(-\tau)]^\dagger$.

The difference between the result derived here and that of Jauho *et al.* stems from the fact that in the former the current was found by first determining the steady-state populations of the molecular charge states whereas the latter was derived assuming that the molecular system is always found in the N charge state [246]. As we shall demonstrate, this may result in qualitative differences between the two methods. This is perhaps best seen with a numerical example.

In what follows, the bias voltage is applied symmetrically: $\mu_l = \pm V_\mathrm{b}/2$. For simplicity, it is assumed that the electronic level considered here is coupled to a phonon bath with a structureless super-ohmic spectral density:

$$\mathcal{J}(\omega) = \frac{\lambda}{2} \left(\frac{\omega}{\Omega_c}\right)^3 e^{-\omega/\Omega_c}\ , \tag{7.37}$$

where λ is the reorganisation energy and Ω_c is the cut-off frequency. We begin, in Figure 7.2(a), by showing the IV characteristics calculated for the case of symmetric molecule-lead coupling ($\Gamma_\mathrm{L} = \Gamma_\mathrm{R}$) and the molecular energy level being on resonance ($\bar{\varepsilon}_0 = 0$). The GQME and NEGF techniques give rise to identical IV characteristics, and it can generally be shown that, for the special case of $\bar{\varepsilon}_0 = 0$, Eqs. (7.30) and (7.36) are equivalent.

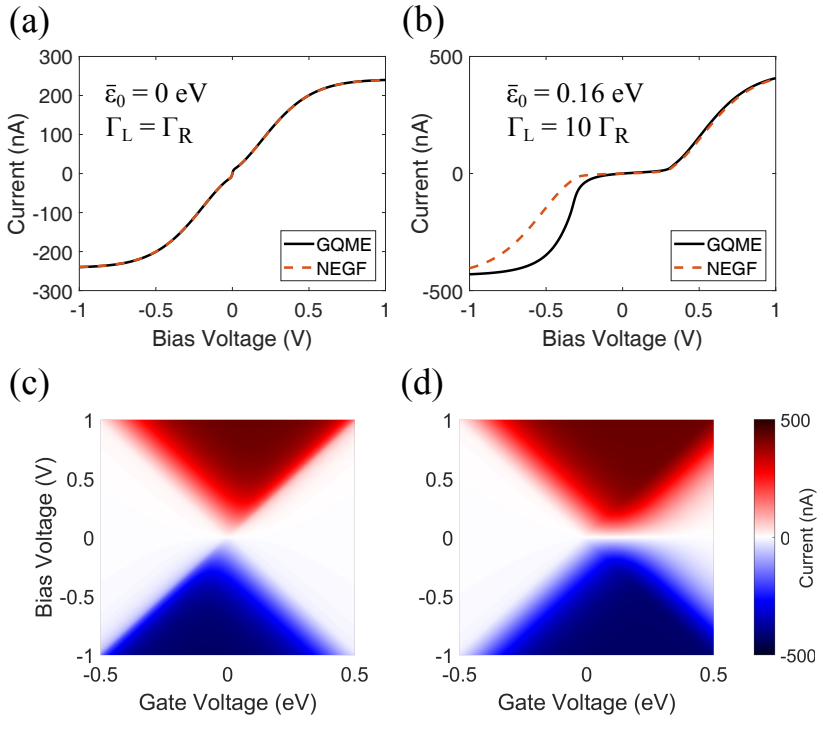


Figure 7.2: Transport characteristics for an electronic level coupled to a super-ohmic phonon bath with $\lambda = 150$ meV and $\Omega_c = 25$ meV. (a) IV characteristics on resonance: $\bar{\varepsilon}_0 = 0$ meV. (b) IV characteristics off resonance with $\bar{\varepsilon}_0 = 160$ meV. (c, d) Stability diagrams calculated for the case asymmetric coupling $\Gamma_\mathrm{L} = 10\Gamma_\mathrm{R}$ using (c) GQME, and (d) NEGF approach. $T = 10$ K and $\Gamma_\mathrm{R} = 2$ meV throughout.

We now move on to the more interesting case: one of non-zero $\bar{\varepsilon}_0$ and asymmetric molecule-lead coupling ($\Gamma_\mathrm{L} \neq \Gamma_\mathrm{R}$). If one of the molecule-lead coupling strengths is much greater than the other, the molecular energy level is almost always found empty or occupied, depending on the sign of V_b. That means that depending on the direction of the applied bias voltage, different inelastic processes (coinciding with electron hopping either on or off the molecule) form the overall bottleneck in the charge transport. This gives rise to a certain degree of current rectification – asymmetric IV

characteristics despite the symmetrically applied bias voltage [177]. This effect has been observed experimentally (for the most compelling evidence see Ref. [42]) and, as shown in Figure 7.2(b), is captured by the GQME approach derived here. In contrast, the NEGF result remains entirely symmetric with respect to the sign of V_{b}, as can also be inferred directly from Eq. (7.36). This is further shown in Figures 7.2(c,d) which contain the stability diagrams (maps of current as a function of the bias and gate voltages) obtained using the GQME and NEGF methods with the parameters as in Figure 7.2(b).

In summary, the GQME result is in a complete agreement with the NEGF result on resonance, as well as for vanishing electron-vibrational coupling. In the case of asymmetric molecule-lead coupling, it can also account for current rectification – an effect not captured by the NEGF approach considered here.

7.4 Microscopically-motivated coupling

Before proceeding to the high-temperature transport behaviour, we first take this opportunity to study the low-temperature transport characteristics for a microscopically-motivated (i.e. non-phenomenological) electron-vibrational coupling. The model junction we shall consider here incorporates a curcuminoid-based molecule, see inset in Figure 7.3(a), a system that was recently studied experimentally by Burzurí and coworkers [41] (some of their experimental results are shown in Figure 3.7). Therein, the authors have estimated the electron-vibrational coupling strength (of the anionic charge state) for each of the molecular vibrational modes using the method described in Ref. [259] as follows: Firstly, one performs the geometry optimisation of the neutral and charged (here anionic) structure. By comparing the two geometries, the so-called Duschinsky shift vector can be obtained from which the dimensionless g_q/ω_q quantity can be easily determined for each of the molecular vibrational modes [260, 261]. The result of this calculation (from Ref. [41]) is for convenience shown in Figure 7.3(a).

At this point there are two ways in which one can proceed. We can either (i)

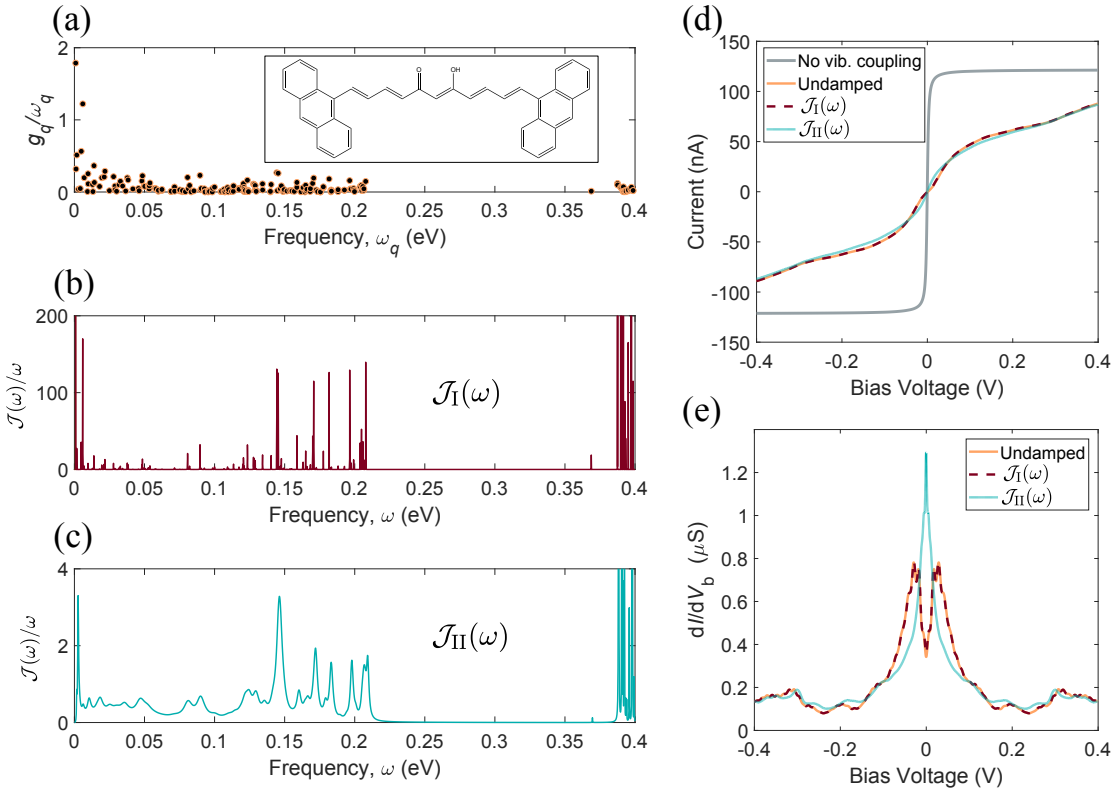


Figure 7.3: (a) Dimensionless electron-phonon coupling parameters as a function of the vibrational frequencies ω_q, from Ref. [41]. Inset: the molecular structure of the curcuminoid molecule considered therein. (b,c) Continuous spectral densities obtained from the above coupling parameters with (b) $\eta = 1$ meV, $\Lambda_0 = 50$ meV, and (c) $\eta = 50$ meV, $\Lambda_0 = 60$ meV. (d) IV characteristics, and (e) Differential conductance ($\mathrm{d}I/\mathrm{d}V_\mathrm{b}$) obtained for transport through the 9ALCccmoid-based junction. $\Gamma_\mathrm{L} = \Gamma_\mathrm{R} = 1$ meV, $\bar{\varepsilon}_0 = 0$, and $T = 4$ K in both instances.

assume the molecular vibrational modes are infinitely long-lived, or (ii) introduce a small amount of damping and combine all these electron-vibrational couplings into a single smooth spectral density. In both instances the total spectral density can be obtained simply as a sum:

$$\mathcal{J}_{\rm tot}(\omega) = \sum_q \mathcal{J}_q(\omega) \ , \tag{7.38}$$

where $\mathcal{J}_q(\omega)$ is a spectral density for the vibrational mode q. For the the infinitely long-lived (undamped) modes, these are simply: $\mathcal{J}_q(\omega) = |g_q|^2 \delta(\omega - \omega_q)$. In the damped case, we shall assume that $\mathcal{J}_q(\omega)$ takes the form given by Roden *et al.* [262]:

$$\mathcal{J}_q(\omega) = \frac{(g_q/\omega_q)^2 \ \eta \ \omega^3 \ e^{-\omega/\Lambda_0}\Theta(\omega)}{\pi^2\eta^2\omega^2 e^{-2\omega/\Lambda_0} + (\omega - \omega_q + \eta\Lambda_0 - \eta\omega e^{-\omega/\Lambda_0}\mathrm{Ei}(\omega/\Lambda_0))^2} \ , \tag{7.39}$$

where $\Theta(\omega)$ is the unit step function, and $\mathrm{Ei}(x)$ denotes the exponential integral. The above expression was obtained by assuming that the vibrational mode in question is coupled to a secondary ohmic phonon bath (with a cut-off frequency Λ_0 and a reorganisation energy $\eta\Lambda_0$). Figures 7.3(b,c) show two damped spectral densities obtained in this way from the DFT vibrational coupling strengths plotted in Figure 7.3(a) for illustrative values of η and Λ_0.

Figure 7.3(d) shows the IV characteristics on resonance at $T = 4$ K for the case of coupling to the undamped vibrational modes, the continuous spectral densities from Figures 7.3(b,c), as well as the case of no vibrational coupling (the Landauer-Büttiker limit). Coupling to the undamped and only slightly damped [$\mathcal{J}_{\mathrm{I}}(\omega)$, Figure 7.3(b)] vibrational modes reassuringly delivers virtually identical behaviour. Significantly different characteristics can be observed in the case of much greater damping [$\mathcal{J}_{\mathrm{II}}(\omega)$, Figure 7.3(c)]. These differences are clearly visible in the plot of differential conductance ($\mathrm{d}I/\mathrm{d}V_{\mathrm{b}}$) in Figure 7.3(e). At zero bias, the junction is markedly less conductive in the case of coupling to the undamped molecular modes. This can be explained by significant damping of the low-frequency vibrational modes in $\mathcal{J}_{\mathrm{II}}(\omega)$ which, as the result, leads to a smaller degree of a Franck-Condon-type suppression at low bias voltage.

Somewhat surprisingly, the structure of the transport characteristics [peaks in the differential conductance, Figure 7.3(e)] even in the undamped case cannot be easily correlated with the individual molecular vibrational modes. This is a worrisome observation since these features are universally regarded as signatures of coupling to the molecular vibrational modes (the frequencies of which can be inferred from positions of the aforementioned peaks), see Chapter 3.

The origin of this unexpected behaviour can be traced back to the two low-frequency vibrational modes that are strongly coupled (with $g_q/\omega_q > 1$) to the electronic energy level, see Figure 7.3(a). To understand this effect, let us consider transport through an electronic level coupled to a vibrational mode with frequency ω_Q (with an intermediate coupling strength, $g_q/\omega_q < 1$). In the absence of strong coupling to any low-frequency modes, one would expect to observe a peak in the differential conductance for bias

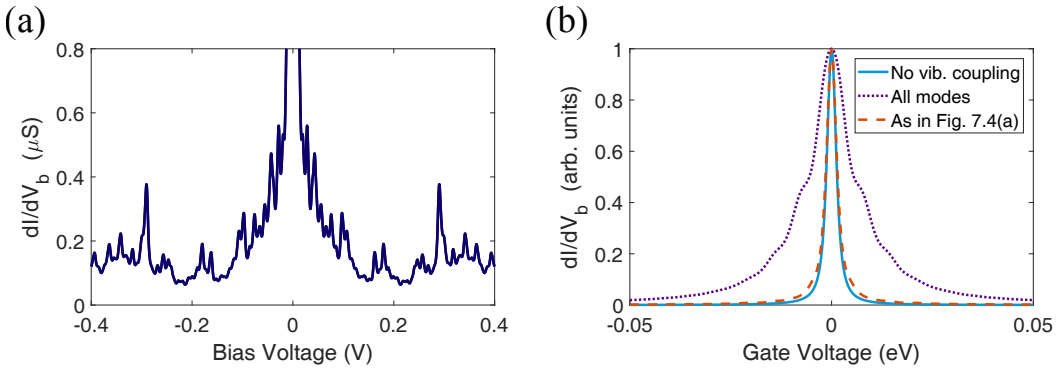


Figure 7.4: (a) Differential conductance on resonance ($\bar{\varepsilon}_0 = 0$) assuming coupling to the undamped modes in Figure 7.3(a) with the exception of the two strongly-coupled, low-frequency modes. (b) Renormalised zero-bias conductance as a function of the gate voltage in the case of coupling to undamped vibrational modes: $\bar{\varepsilon}_0 = -V_\mathrm{g}$. The molecule-lead coupling: $\Gamma_\mathrm{L} = \Gamma_\mathrm{R} = 1$ meV; $T = 4$ K.

voltage such that $eV_\mathrm{b} = 2\omega_Q$ (for symmetrically applied bias, and on resonance). This corresponds to an excitation of the vibrational mode in question and a simultaneous ground-state-to-ground-state transition for all the remaining vibrational modes. However, when the molecular electronic level in question is also strongly coupled to a certain low-frequency mode (with frequency ω_P), the aforementioned transition is no longer efficient due to the poor Franck-Condon overlap for the ground-state-to-ground-state transition of the mode P. Instead, the visible peaks in the differential conductance (corresponding to efficient inelastic transitions) occur for the simultaneous excitation of both the Q and P modes, and therefore at $eV_\mathrm{b} = 2(\omega_Q + n\omega_P)$ where n is a positive integer. The situation is further complicated when, as is the case here, ω_P is smaller than the lifetime broadening Γ. Then, the off-set of the original peak is no longer simply an integer amount of ω_P since the individual excitations of mode P can no longer be resolved. Figure 7.4(a) shows the differential conductance calculated for parameters as in Figure 7.3(e) but ignoring the two strongly coupled low-frequency modes. Disregarding coupling to these modes recovers the expected behaviour – the differential conductance now features a set of peaks which can easily be correlated with specific vibrational excitations.

Finally, we also demonstrate the effect of these low-frequency modes on the zero-bias conductance. In Figure 7.4(b), we plot $\mathrm{d}I(V_\mathrm{b} = 0)/\mathrm{d}V_\mathrm{b}$ as a function of the

gate voltage. As can be seen therein, the coupling to the low-frequency modes can significantly affect the width of the conductance peak which is often used to extract the lifetime broadening Γ. As we demonstrate here, the values extracted in such a way should be treated with caution. In fact, a significantly smaller value of Γ than extracted in Ref. [41] was used throughout this Section. Using the value extracted from the conductance peak by Burzurí *et al.* (10 meV) washes away the vibrational features reported in Ref. [41].

To conclude, it was shown here how our GQME framework can be applied to the case of microscopically-motivated vibrational coupling. Furthermore, using this approach we found that (for realistic, *ab initio* parameters) coupling to low-frequency modes can have an unexpectedly large effect on the molecular transport properties. As discussed here, this observation may be of great importance in the experimental transport studies.

7.5 High(er)-temperature limits

In this section, we derive a number of approximations to Eqs. (7.28, 7.29) valid at increasing temperatures. This collection of results yields a tiered theoretical framework, schematically pictured in Figure 7.5. As we shall demonstrate, two different approximations need to be made within the generalised quantum master equation to arrive at the well-known Marcus theory – one regarding the phononic correlation function, and one regarding the $e^{-\Gamma\tau}$ correction. The order in which they ought to be made, and thus the pathway taken in Figure 7.5, depends on the relative magnitudes of the lifetime broadening Γ and the cut-off frequency of the phonon bath (describing the distribution of the vibrational modes).

7.5.1 Born-Markov approximation

Firstly, we recognise that the $e^{-\Gamma\tau}$ correction to the Born approximation will lead solely to broadening of the IV characteristics. Broadening of the Fermi distributions in the

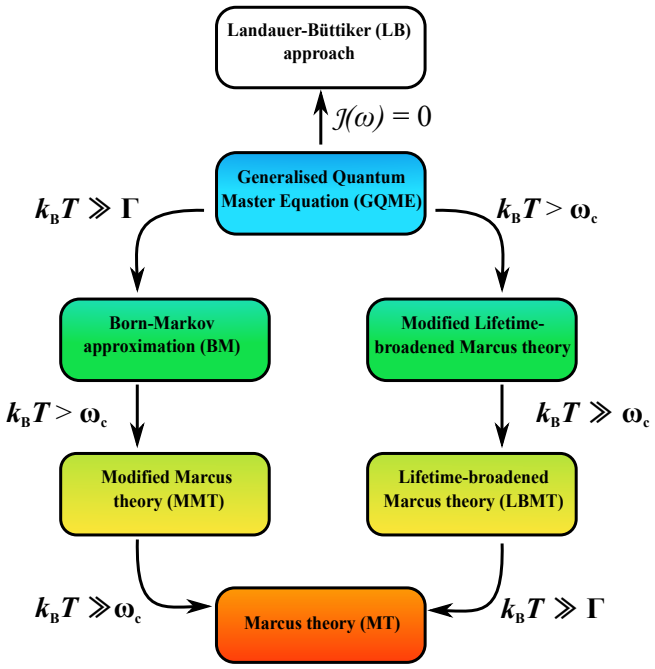


Figure 7.5: Schematic illustration of the main conceptual result of this chapter: a tiered theoretical framework describing vibrational effects in the resonant transport regime.

leads (at non-zero T) will have the same effect and so the aforementioned correction can be ignored in the limit of $k_{\mathrm{B}}T \gg \Gamma$. This trivially recovers the result obtained within the usual second order Born-Markov approximation with respect to the leads in the polaron-transformed frame (*c.f.* Chapter 6):

$$\gamma_l^{\mathrm{BM}} = 2\ \mathrm{Re}\left[\Gamma_l \int_{-\infty}^{\infty} \frac{\mathrm{d}\epsilon}{2\pi} f_l(\epsilon) \int_0^{\infty} \mathrm{d}\tau\ e^{+\mathrm{i}(\epsilon-\bar{\varepsilon}_0)\tau} B(\tau)\right]\ ; \tag{7.40}$$

$$\bar{\gamma}_l^{\mathrm{BM}} = 2\ \mathrm{Re}\left[\Gamma_l \int_{-\infty}^{\infty} \frac{\mathrm{d}\epsilon}{2\pi} [1 - f_l(\epsilon)] \int_0^{\infty} \mathrm{d}\tau\ e^{-\mathrm{i}(\epsilon-\bar{\varepsilon}_0)\tau} B(\tau)\right]\ . \tag{7.41}$$

7.5.2 Marcus theory

Let us now take the high-temperature limit in Eqs. (7.40, 7.41) and assume a slowly fluctuating (low-frequency) environment [263]. For the phononic correlation function this allows us to approximate: $\coth(\beta\omega/2) \approx 2/\beta\omega$, $\cos(\omega t) - 1 \approx -\omega^2 t^2/2$, and $\sin(\omega t) \approx \omega t$. This simplifies Eq. (7.15) to:

$$B(t) \approx \exp\left(-\lambda t^2/\beta - \mathrm{i}\lambda t\right)\ , \tag{7.42}$$

where λ is the (Marcus) reorganisation energy, formally defined as:

$$\lambda = \int_0^\infty \mathrm{d}\omega \, \frac{\mathcal{J}(\omega)}{\omega} = \sum_q \frac{|g_q|^2}{\omega_q} \, . \tag{7.43}$$

Performing the one-sided Fourier transform leads to:

$$\gamma_l^{\mathrm{MT}} = 2 \, \Gamma_l \int_{-\infty}^{\infty} \frac{\mathrm{d}\epsilon}{2\pi} f_l(\epsilon) \sqrt{\frac{\pi}{4\lambda k_{\mathrm{B}} T}} \exp\left(-\frac{[\lambda - (\epsilon - \bar{\varepsilon}_0)]^2}{4\lambda k_{\mathrm{B}} T} \right) \, ; \tag{7.44}$$

$$\bar{\gamma}_l^{\mathrm{MT}} = 2 \, \Gamma_l \int_{-\infty}^{\infty} \frac{\mathrm{d}\epsilon}{2\pi} [1 - f_l(\epsilon)] \sqrt{\frac{\pi}{4\lambda k_{\mathrm{B}} T}} \exp\left(-\frac{[\lambda + (\epsilon - \bar{\varepsilon}_0)]^2}{4\lambda k_{\mathrm{B}} T} \right) \, . \tag{7.45}$$

These are the well-known expressions for the rates of the electron hopping between a metallic electrode and a molecular energy level, as described by Marcus theory (MT) [264, 265] (in the field of electrochemistry it is sometimes referred to as Marcus-DOS or Marcus-Hush-Chidsey theory [266–269]). These expressions are commonly used to study the charge transport through redox molecular junctions [103, 270–276]. However, as we shall demonstrate below, MT is often insufficient for describing molecular transport characteristics and gives rise to a number of artefacts, especially at lower temperatures.

7.5.3 Modified Marcus theory

The main advantage of Marcus theory, besides its apparent simplicity, is the fact that the entire complexity of the phononic spectral density (which is often unknown in molecular systems) is reduced to a single parameter: the reorganisation energy, λ. This is especially important in the context of experimental studies where λ can act as a fitting parameter. However, as we shall show here (also see Chapter 8), MT often inadequately describes the low-temperature behaviour of molecular junctions: it severely overestimates vibrational effects at low frequencies and underestimates them at high frequencies [which is a clear consequence of approximations made to arrive at Eq. (7.42)]. Our goal here is to develop an extension of Marcus theory which will, at least partially, rectify those shortcomings.

In deriving Marcus theory, we approximated $\coth(\beta\omega/2)$ as $2/\beta\omega$. Here, let us simply expand this term to the second order: $\coth(\beta\omega/2) \approx 2/\beta\omega + \beta\omega/6$. Following the same procedure as in the previous section yields an equally simple result:

$$\gamma_l^{\mathrm{MMT}} = 2\,\Gamma_l \int_{-\infty}^{\infty} \frac{\mathrm{d}\epsilon}{2\pi} f_l(\epsilon) \sqrt{\frac{\pi}{4\lambda k_{\mathrm{B}}T + \chi/3k_{\mathrm{B}}T}} \exp\left(-\frac{[\lambda - (\epsilon - \bar{\varepsilon}_0)]^2}{4\lambda k_{\mathrm{B}}T + \chi/3k_{\mathrm{B}}T}\right) \; ; \tag{7.46}$$

$$\bar{\gamma}_l^{\mathrm{MMT}} = 2\,\Gamma_l \int_{-\infty}^{\infty} \frac{\mathrm{d}\epsilon}{2\pi} [1 - f_l(\epsilon)] \sqrt{\frac{\pi}{4\lambda k_{\mathrm{B}}T + \chi/3k_{\mathrm{B}}T}} \exp\left(-\frac{[\lambda + (\epsilon - \bar{\varepsilon}_0)]^2}{4\lambda k_{\mathrm{B}}T + \chi/3k_{\mathrm{B}}T}\right) \; . \tag{7.47}$$

In the above, a new parameter describing the electron-phonon coupling (χ) has been introduced. It is formally defined as:

$$\chi = \int_0^{\infty} \mathrm{d}\omega \; \omega \times \mathcal{J}(\omega) = \sum_q |g_q|^2 \omega_q \; . \tag{7.48}$$

The rates in Eqs. (7.46, 7.47) constitute what we shall in the following refer to as the *Modified Marcus theory* (MMT). It is clear that $\chi/3k_{\mathrm{B}}T$ acts as a low-temperature correction to the usual Marcus theory. As it will be demonstrated (*vide infra*), the Modified Marcus theory removes some of the artefacts of MT while retaining most of its mathematical simplicity.

What is the physical meaning of the parameter χ? It accounts for the coupling to higher frequency vibrational modes for which the high-temperature assumption of MT is not justified. The correction in Eqs. (7.46, 7.47) thus vanishes if the vibrational modes have frequencies much lower than $k_{\mathrm{B}}T$. It is also clear that the hopping rates derived above do not have the typical Arrhenius form although it is recovered at high temperatures.

We shall now demonstrate the effectiveness of the Modified Marcus theory on a numerical example. We will again assume that the electron-phonon coupling can be described by the spectral density given in Eq. (7.37) and consider a case of coupling to relatively high-frequency vibrational modes. In Figure 7.6, we plot the IV characteristics obtained using various theoretical approaches for increasing temperature

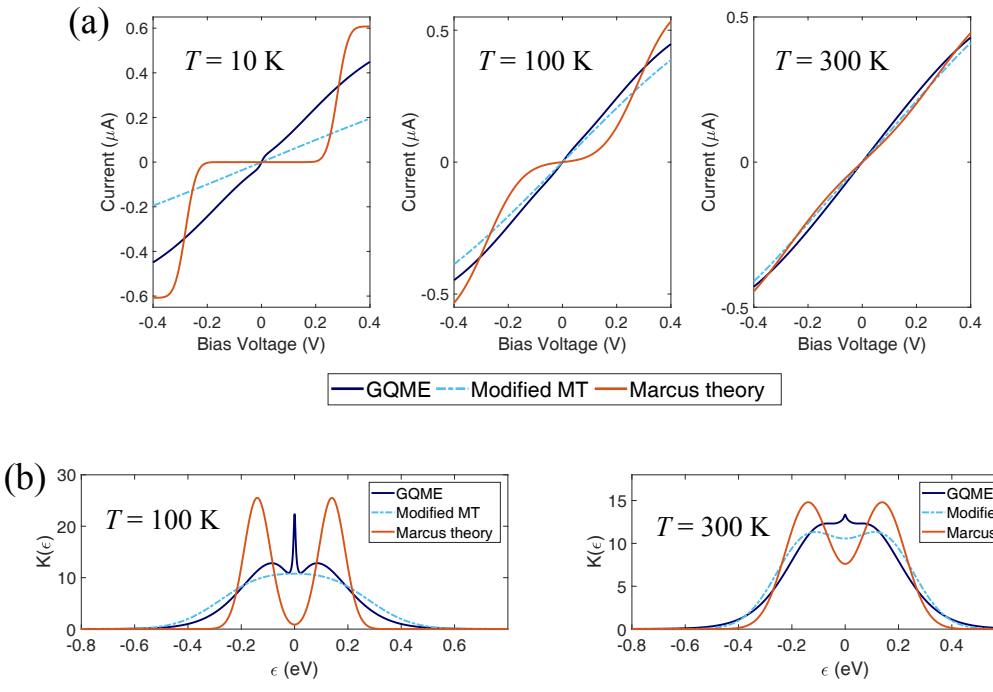


Figure 7.6: (a) IV characteristics on resonance ($\bar{\varepsilon}_0 = 0$ eV) at different temperatures. The molecular energy level is coupled to a vibrational environment with SD of Eq. (7.37) with $\lambda = 140$ meV and $\Omega_c = 25$ meV ($\chi = 0.0011$ eV^3); $\Gamma_\mathrm{L} = \Gamma_\mathrm{R} = 5$ meV. (b) Plots of $K(\epsilon)$, sum of the energy-dependent hopping rates, for parameters as in (a).

(left-hand-side of diagram in Figure 7.5). Due to relatively small lifetime broadening, the GQME and BM approaches yield very similar results and we shall omit the latter for clarity. Marcus approach gives rise to certain artefacts at lower temperatures: current suppression at low bias voltage (effectively a spurious Franck–Condon blockade), and current plateaus at artificially low V_b. The origin of these features can be directly traced back to the assumptions made in the derivation of Marcus theory (Section 7.5.2). As can be seen in Figure 7.6, the Modified Marcus theory can successfully rectify these shortcomings at intermediate temperatures. It performs best in the regime where the $\chi/3k_\mathrm{B}T$ correction is smaller than the $4\lambda k_\mathrm{B}T$ factor giving rise to the criterion: $\chi/\lambda < 12(k_\mathrm{B}T)^2$. In the case of the super-ohmic SD used here, this condition becomes simply $k_\mathrm{B}T > \Omega_c$. At lower temperatures, the correction at hand leads to an underestimation of the current in the resonant transport regime (see Figure 7.6) and its overestimation off resonance. This can be explained as follows. The energy-dependent hopping rates in the GQME (or the Born-Markov) approach are not symmetric around

$\epsilon = \bar{\varepsilon}_0 \pm \lambda$. Meanwhile, the $\chi/3k_{\mathrm{B}}T$ correction introduced in the Modified Marcus theory induces a symmetric broadening of the Gaussian rates (predicted by MT). For very low temperature, this additional broadening gives rise to the effects discussed above.

To further investigate the Modified Marcus approach, we plot the quantity $K(\epsilon) = K^{+}(\epsilon) + K^{-}(\epsilon)$, where $K^{\pm}(\epsilon)$ are given by:

$$K^{\pm}(\epsilon) = \mathrm{Re} \int_0^{\infty} \mathrm{d}\tau \, e^{\pm \mathrm{i}\epsilon\tau - \Gamma\tau} B(\tau), \tag{7.49}$$

and are directly proportional to the energy-dependent hopping rates present in Eqs. (7.28, 7.29). As discussed in Section 7.3, on resonance, $K(\epsilon)$ directly determines the transport characteristics. Figure 7.6(b) shows $K(\epsilon)$ obtained using the phononic correlation functions as present in the GQME and the Marcus approaches at different temperatures (the lifetime broadening Γ is artificially set to zero in both of the Marcus approaches). Several aspects of transport characteristics plotted in Figure 7.6(a) become clearer. Firstly, we notice the presence of a peak at $\epsilon = 0$ in the GQME result. It corresponds to an elastic (ground-state-to-ground-state) electron hopping and is naturally missing in both of the Marcus approaches which, as the result, significantly underestimate the zero-bias conductance. Secondly, within the Marcus approach $K^{\pm}(\epsilon)$ are Gaussian functions centred at $\epsilon = \pm\lambda$. At a given temperature, their width is determined solely by the reorganisation energy. This may give rise to artefacts visible in the IV characteristics in Figure 7.6(a). On the other hand, within the Modified Marcus approach, the width of these Gaussian functions is also influenced by the additional parameter, χ, which at intermediate temperatures, removes the spurious effects present in the usual Marcus treatment.

Can the (Modified) Marcus theory be applied to the curcuminoid-based junction from Section 7.4? Firstly, the Marcus approaches cannot capture the effects of the structure of the spectral density on the transport characteristics. On a qualitative level, they can therefore only be valid at temperatures at which the structure of the IV characteristics is washed away by the thermal broadening of the Fermi distributions

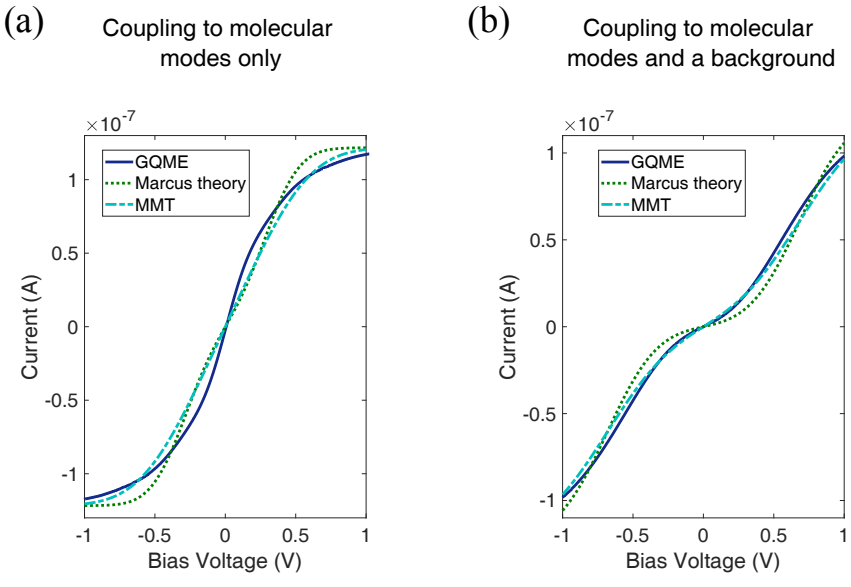


Figure 7.7: IV characteristics on resonance ($\bar{\varepsilon}_0 = 0$) at $T = 300$ K with $\Gamma_{\mathrm{L}} = \Gamma_{\mathrm{R}} = 1$ meV. The molecular energy level is coupled to: (a) the molecular modes from Figure 7.3(a); (b) the molecular modes as well as a super-ohmic background accounted for by Eq. (7.37) with $\lambda = 200$ meV and $\omega_{\mathrm{c}} = 15$ meV. The high-frequency molecular modes of around 400 meV (C-H stretches) were ignored when calculating the χ parameter.

in the leads. Secondly, the collection of the molecular vibrational modes considered in Section 7.4 is predominantly of very high frequency – ω_q is much larger than $k_{\mathrm{B}}T$ at 300 K for most of the modes. Consequently, the high-temperature assumption of MT will only be satisfied well above room temperature. Similarly, the criterion for the applicability of the Modified MT yields the temperature of over 600 K. As the result, the IV characteristics obtained using the GQME approach at room temperature differ from those obtained using the (Modified) Marcus theory, see Figure 7.7(a).

The molecular system deposited in the junction, however, can be also coupled to environmental low-frequency modes (of the substrate or the solution in which the junction is immersed). If this coupling dominates, the room-temperature validity of (M)MT is recovered, as shown in Figure 7.7(b). Furthermore, as can be seen therein, the Modified Marcus approach once again significantly outperforms the conventional Marcus theory.

7.5.4 Lifetime-broadened Marcus theory

We now return to Eqs. (7.28, 7.29) and assume that the molecular level is more strongly coupled to the leads (Γ comparable $k_{\mathrm{B}}T$), and interacts predominantly with low-frequency vibrational modes. We can then take the same limits as in Section 7.5.2 (but retaining the lifetime broadening) to yield:

$$\gamma_l^{\mathrm{LBMT}} = 2\ \Gamma_l \int_{-\infty}^{\infty} \frac{\mathrm{d}\epsilon}{2\pi} f_l(\epsilon)\ \mathrm{Re}\left[\sqrt{\frac{\pi}{4\lambda k_{\mathrm{B}}T}}\exp\left(\frac{(\Gamma - \mathrm{i}\nu_+)^2}{4\lambda k_{\mathrm{B}}T}\right)\mathrm{erfc}\left(\frac{\Gamma - \mathrm{i}\nu_+}{\sqrt{4\lambda k_{\mathrm{B}}T}}\right)\right]\ ; \tag{7.50}$$

$$\bar{\gamma}_l^{\mathrm{LBMT}} = 2\ \Gamma_l \int_{-\infty}^{\infty} \frac{\mathrm{d}\epsilon}{2\pi} [1 - f_l(\epsilon)] \mathrm{Re}\left[\sqrt{\frac{\pi}{4\lambda k_{\mathrm{B}}T}}\exp\left(\frac{(\Gamma - \mathrm{i}\nu_-)^2}{4\lambda k_{\mathrm{B}}T}\right)\mathrm{erfc}\left(\frac{\Gamma - \mathrm{i}\nu_-}{\sqrt{4\lambda k_{\mathrm{B}}T}}\right)\right]\ , \tag{7.51}$$

where, for brevity, $\nu_\pm = \lambda \mp (\epsilon - \bar{\varepsilon}_0)$, and $\mathrm{erfc}(x)$ denotes the complementary error function. Eqs. (7.50, 7.51) form the basis of what we refer to as the *Lifetime-broadened Marcus theory* (LBMT).

Naturally, ignoring the lifetime broadening, by setting $\Gamma = 0$ in Eqs. (7.50, 7.51), again gives the Marcus theory. On the other hand, by taking the limit $\lambda \to 0$, one can recover the Landauer-Büttiker expression for transport through a single non-interacting level (in a way analogous to what has been done in Section 7.3).

What happens for comparable λ and Γ? Off resonance ($eV_{\mathrm{b}}/2 < \bar{\varepsilon}_0$), the Lifetime-broadened Marcus transport interpolates between the results obtained using the Marcus theory and the LB formalism, as shown in Figure 7.8(a). In other words, the otherwise elastic Landauer-Büttiker transport is suppressed by the vibrational coupling, or conversely, the incoherent Marcus transport is enhanced in the presence of lifetime broadening. Let us also note here that, in the off-resonant regime, transport occurring solely through the hopping mechanism (as described by the Marcus theory) yields lower values of current than the purely elastic transport (for given Γ_{L} and Γ_{R}). We believe this to be generally the case for the single-site model studied here. With the molecular energy level within the bias window ($eV_{\mathrm{b}}/2 > \bar{\varepsilon}_0$), the lifetime-broadened

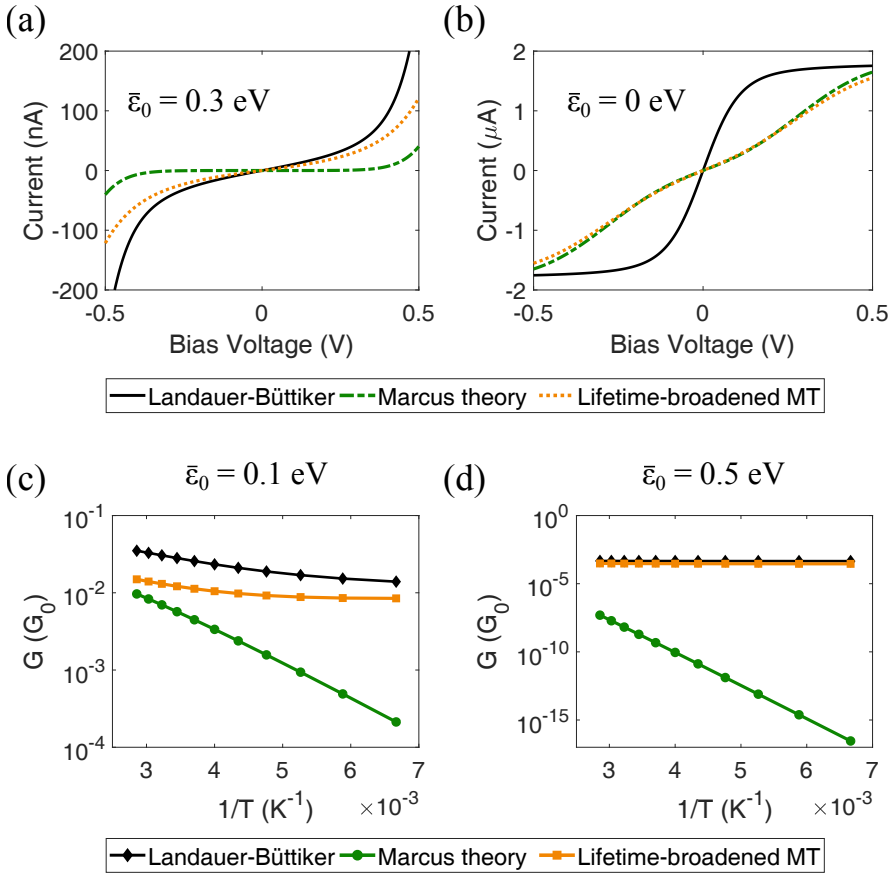


Figure 7.8: (a,b) IV characteristics obtained using the Landauer-Büttiker formalism, Marcus theory and the Lifetime-broadened MT for $T = 240$ K, and symmetric molecule-lead coupling: $\Gamma_{\mathrm{L}} = \Gamma_{\mathrm{R}} = 15$ meV. (c,d) Zero-bias conductance in units of G_0. The reorganisation energy in MT and Lifetime-broadened MT was set to $\lambda = 0.14$ eV. The position of the energy level: (a) $\bar{\varepsilon}_0 = 0.3$ eV; (b) $\bar{\varepsilon}_0 = 0$ eV; (c) $\bar{\varepsilon}_0 = 0.1$ eV; (d) $\bar{\varepsilon}_0 = 0.5$ eV. For consistency the same (renormalised) position of the energy level was used within the Landauer-Büttiker approach.

Marcus theory yields lower values of current than the remaining transport mechanisms since it includes all sources of broadening of the IV characteristics (lifetime, phonon, and thermal broadening of the Fermi distributions), see Figure 7.8(b).

It is also interesting to consider the temperature dependence of the zero-bias conductance, which is often used to identify the transport mechanism. We consider two cases with the molecular energy level lying $\bar{\varepsilon}_0 = 0.1$ eV and 0.5 eV above the Fermi energy of the unbiased leads in the temperature range between 150 and 350 K. In both cases, the elastic LB transport exhibits a weak temperature dependence (although much more pronounced closer to the resonance) stemming from the thermal broad-

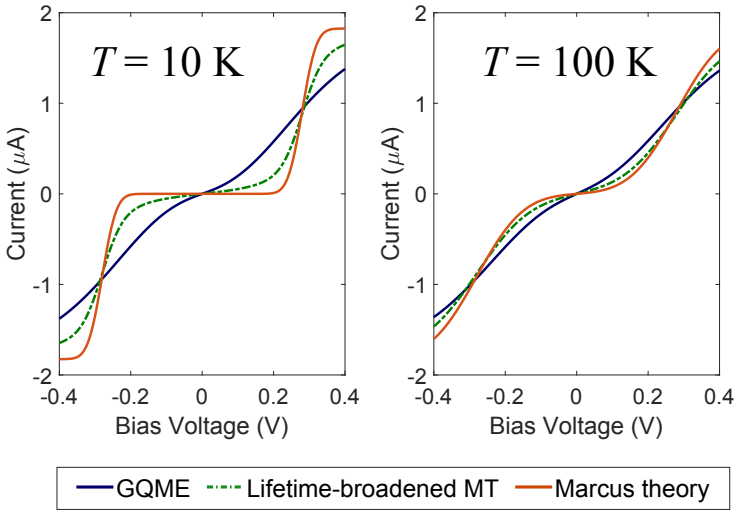


Figure 7.9: IV characteristics on resonance ($\bar{\varepsilon}_0 = 0$ eV) at different temperatures. The molecular energy level is coupled to a vibrational environment with SD of Eq. (7.37) with $\lambda = 140$ meV and $\Omega_c = 12$ meV; $\Gamma_{\rm L} = \Gamma_{\rm R} = 15$ meV.

ening of the Fermi distributions in the leads. The temperature dependence of the Marcus hopping is dominated by the Arrhenius character of the MT rates giving rise to almost linear dependence of $\log(G/G_0)$ on inverse temperature (G_0 is the conductance quantum), see Figures 7.8(c,d). Perhaps surprisingly, the Lifetime-broadened Marcus transport does not manifest such linear behaviour. As mentioned above, in the off-resonant regime the elastic (LB) transport through a single-site junction is always more efficient than the incoherent Marcus hopping. As the result, even a modest amount of lifetime broadening (as incorporated in LBMT) will have a profound effect on the off-resonant conductance.

We now repeat the calculation from Figure 7.6(a) for the case of larger Γ and lower cut-off frequency Ω_c, and analyse the performance of Lifetime-broadened MT. As can be seen in Figure 7.9, MT gives rise to the same artefacts as in Section 7.5.3. Incorporating lifetime broadening (as is done in LBMT) yields a much better agreement with the GQME result, especially at lower temperatures.

We also consider the off-resonant transport regime at high temperature, see Figure 7.10. Therein, the lifetime-broadened MT is in an excellent agreement with the GQME result. On the other hand, the usual Marcus theory greatly underestimates the molec-

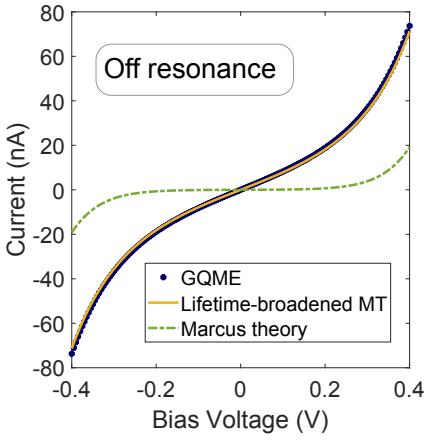


Figure 7.10: Transport characteristics in the off-resonant regime at $T = 300$ K, $\bar{\varepsilon}_0 = 0.3$ eV. Other parameters as in Figure 7.9.

ular conductance. As shown here, lifetime broadening appears to be a vital part of the transport description off resonance, even at temperatures significantly exceeding Γ.

Typically, the coherent resonant transport (as described by the Landauer-Büttiker formalism) and the semi-classical electron hopping (Marcus theory) are regarded as two distinct transport mechanisms, see for instance discussion in Ref. [103]. As shown here, it is possible to capture both of these phenomena in a simple unifying expression. It is also apparent that the elastic (Landauer-Büttiker) transport and Marcus hopping cannot be considered independently (the total conductance is clearly not a sum of these two contributions). Furthermore, let us also stress that while MT may describe the resonant transport regime reasonably well, its use in the off-resonant case is highly questionable.

Finally, analogously to what has been done in Section 7.5.3, in deriving Eqs. (7.50, 7.51) one may keep the higher-order term in the expansion of $\coth(\beta\omega/2)$. This results in expressions equivalent to Eqs. (7.50, 7.51) but with $4\lambda k_{\mathrm{B}}T$ terms replaced by $4\lambda k_{\mathrm{B}}T + \chi/3k_{\mathrm{B}}T$ giving rise to what we refer to in Figure 7.5 as *Modified Lifetime-broadened Marcus Theory*.

7.6 Conclusions

Several important results were derived in this chapter. Firstly, we have arrived at a relatively compact expression for the electric current flowing through the junction which captures the inelastic vibrational effects and lifetime broadening as well as accounts for the charge population of the molecular system. Furthermore, and perhaps more importantly, by taking various high-temperature limits we have obtained a tiered theoretical framework schematically pictured in Figure 7.5. It allows for a theoretical description of the charge transport at the minimal required level of complexity and should therefore prove immensely useful in interpreting experimental measurements on single-molecule junctions. In the limit of very high temperature, we recover the well-known Marcus theory, and in the absence of electron-phonon coupling, the GQME result reduces to the Landauer-Büttiker approach (for the case of a single electronic level). Furthermore, we have obtained various extensions of Marcus theory containing: a low-temperature correction to the semi-classical hopping rates (Modified Marcus theory, Section 7.5.3); lifetime broadening (Lifetime-broadened Marcus theory, Section 7.5.4); and both of the above (Modified Lifetime-broadened Marcus theory, also in Section 7.5.4). The Lifetime-broadened Marcus theory is of particular importance as it bridges the two approaches most commonly used to account for charge transport through molecular junctions, and may prove to be valuable in a range of practical applications. The effectiveness of the framework derived herein will be further demonstrated in the forthcoming chapter.

Chapter 8

Collective vibrational effects: Experimental evidence

Yes, that works actually pretty well.

— Freeman J. Dyson

Here, equipped with the theoretical framework derived in the previous chapter, we proceed to analyse the experimental charge transport through zinc-porphyrin molecular junctions. We first briefly describe the fabrication procedure and the details of the studied devices. Then, we demonstrate that resonant transport through these single-molecule transistors cannot be described using the usual Landauer-Büttiker approach as the inclusion of the inelastic vibrational effects turns out to be necessary, and we proceed to model the experimental transport behaviour using the theoretical approach from Chapter 7. We show that transport at liquid-nitrogen temperature can be very well accounted for by the Modified Marcus theory, and extract the values of parameters controlling the transport behaviour of these molecular junctions. On the other hand, at lower temperatures, lifetime broadening and the structure of the phononic spectral density begin to play an important role in determining the charge transport characteristics. This prompts the use of the full GQME result from Section 7.2.2, which successfully reproduces the results of experimental transport studies considered herein.

8.1 Zinc-porphyrin molecular junctions

The molecular junctions investigated here are based on functionalised zinc-porphyrin molecules, schematically shown in Figure 8.1. The core of this structure (in black) is connected to two anchor groups (in pink) which are designed to bind to the graphene electrodes, as well as the bulky side groups (green) which additionally prevent molecular aggregation. The mechanical binding to the graphene electrodes occurs due to a combination of π-π stacking of the pyrene units onto the graphene surface, and the attractive interactions between the graphene sheets and the -$OC_{12}H_{25}$ alkyl chains, see Figure 8.1. This binding mechanism has been demonstrated to result in relatively large fabrication yields [116], and is expected to give rise to a greater device-to-device reproducibility than alternative approaches [277].

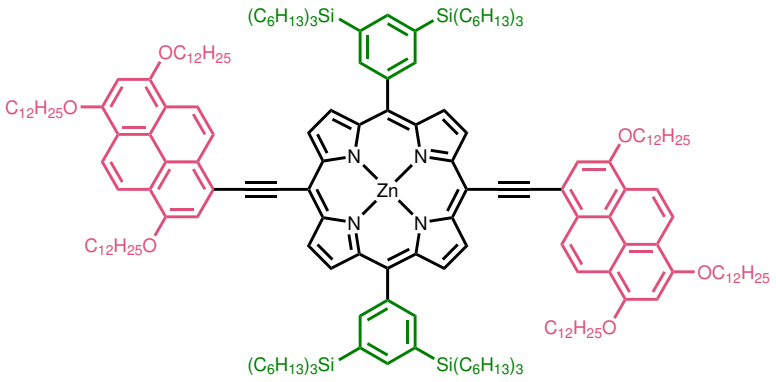


Figure 8.1: Schematic of the functionalised zinc-porphyrin compound used to fabricate single-molecule junctions employed in the experimental studies described here.

The first step in the fabrication of single-molecule devices is the preparation of an empty graphene nano-junction which is manufactured as follows. The process begins by transferring a sheet of graphene onto a silicon chip covered with 300 nm of SiO_2 on which the gold contacts are deposited. Next, graphene is etched into a two-dimensional ribbon between the gold contacts. A nano-gap in this graphene structure is formed by the process of electroburning, which is performed in air by applying a potential difference across the device. During this procedure, the voltage is gradually increased until a drop in the current through the ribbon is observed, at which point the voltage

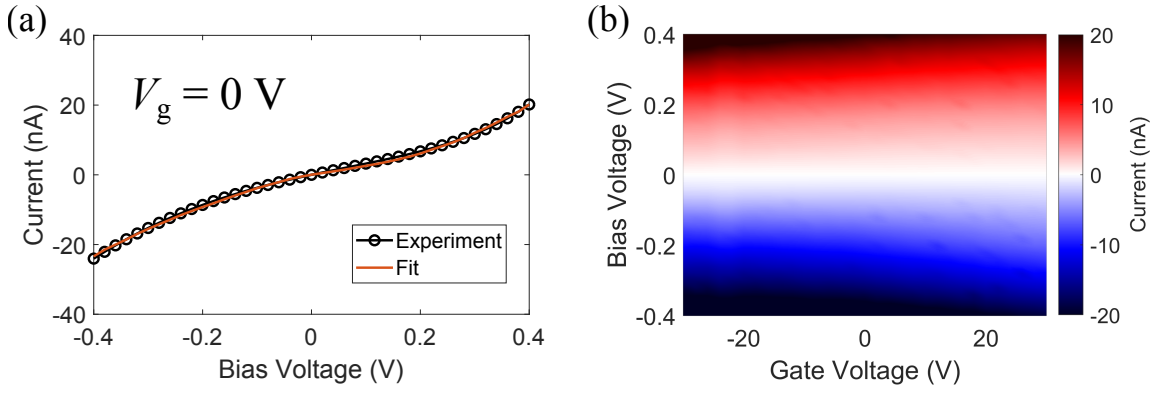


Figure 8.2: (a) Experimental IV characteristics and fit to the Simmons model. (b) Stability diagram for an empty graphene junction.

is swept back to zero and the whole process is repeated. Each time the constriction narrows and the conductance of the graphene ribbon decreases. The procedure stops when a predetermined resistance is reached [100].

Devices fabricated in such a way usually exhibit characteristics of an empty nano-gap with a typical IV characteristics shown in Figure 8.2(a). The transport through such a gap can usually be well accounted for using the standard Simmons model which describes charge transport through a square barrier between two metallic electrodes [100, 278] (fit shown in the figure). It can also be used to estimate the size of the gap - it typically turns out to be between 1 and 2 nm. Another distinctive feature of the successfully fabricated gaps is the minimal dependence of their transport properties on the applied gate voltage, see Figure 8.2(b). The final step of the fabrication process is the depositing of the porphyrin molecules into the gap. This is done simply by immersing the chip in a chloroform solution of the desired compound. If during the deposition a molecule bridges the gap, it significantly alters the transport characteristics of the junction. In particular, a successful deposition should lead to an overall increase in the electric current and induce a Coulomb blockade, commonly observed for single-electron transistors, see Section 8.2.

8.2 Deviation from the single-level model

Figure 8.3 shows an example of a stability diagram as well as the IV characteristics on resonance [at the charge degeneracy point, yellow line in Figure 8.3(b)] for a porphyrin molecular junction fabricated in the way described above (device **A**). Somewhat surprisingly, the resonant transport characteristics of this junctions cannot be accounted for using the single-level model Landauer-Büttiker model, Eq. (7.35), which predicts symmetric IV characteristics that plateau within a few tens of meV of applied bias, see Figure 8.3(a). This conclusion holds for all eight junctions comprising the molecular structure from Figure 8.1 (as well as over twenty junctions based on zinc-porphyrin molecules with different anchor groups studied in Ref. [116]). The natural question is therefore: how can we explain and model this behaviour? One can imagine four possible reasons for this striking breakdown of the single-level model:

1. Voltage dependence of the molecule-lead couplings;

2. Non-uniform density of states in the leads (breakdown of the wide-band approximation);

3. Presence of additional low-lying molecular electronic states;

4. Relatively strong electron-vibrational coupling.

The voltage dependence of the molecule-lead coupling strengths can stem from the distortions (geometric shifts) of the molecular orbital wavefunction due to the electric field applied across the junction. However, this effect should lead to an increase of the coupling to the left lead and a decrease in coupling to right one, or *vice versa* depending on the sign of V_{b}. It should thus create a transport bottleneck at one of these interfaces, as it has been confirmed in recent *ab initio* studies [279], and eventually give rise to negative differential conductance (not observed here). This mechanism can therefore be excluded from further considerations.

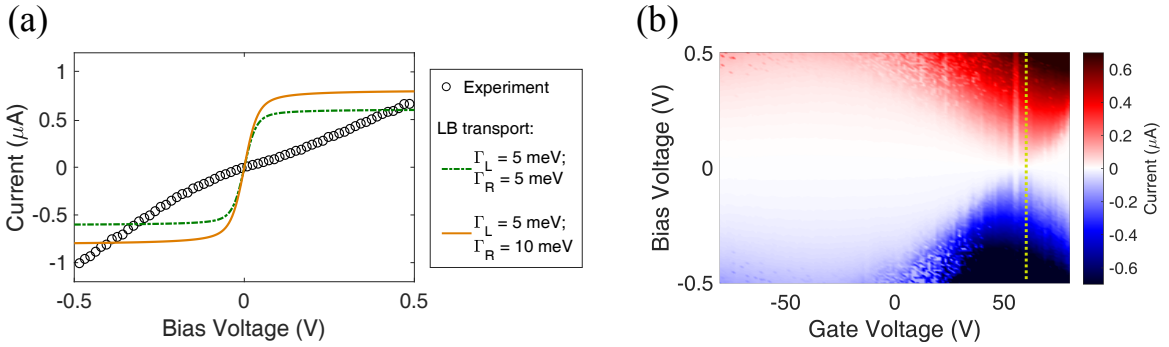


Figure 8.3: Transport characteristics of device **A** at $T = 77$ K: (a) Experimental and theoretical (Landauer-Büttiker) IV characteristics on resonance, and (b) Stability diagram.

Regarding the second point, one should perhaps expect to observe the breakdown of the wide-band approximation in the case of graphene leads since graphene is a zero-gap semiconductor. During the fabrication procedure, however, the leads are heavily p-doped, effectively becoming metallic. One should also bear in mind that random disorder in the microscopic structure of graphene can induce small density of states (DOS) fluctuations in the leads. As we have previously shown in Ref. [6], they can influence the effective tunnelling rates in single-molecule transistors and even give rise to structure in the transport characteristics. Such DOS fluctuations, however, typically occur on the energy scale of roughly 1 meV and are gated to a different extent than the molecular energy levels, giving rise to features not observed herein (*vide infra*).

Next, the existence of low-lying electronic states only a few tens of meV above the ground state (at least a handful of which would be required to account for the observed behaviour) is inconsistent with what can be inferred about the used zinc-porphyrin compound from both the spectroscopic studies and DFT calculations [280]. In what follows, we shall thus assume the presence of only one electronic energy level in each of the relevant charge states.

Let us therefore move to the final point on the above list: the electron-vibrational coupling. It is known that the vibrational interactions can significantly affect the charge transport in various organic materials including molecular junctions (see Chapter 3). As we shall show in the case of devices studied here, the collective electron-vibrational

coupling can indeed give rise to the observed behaviour for realistic values of vibrational coupling strengths. In what follows, we proceed to model the molecular system within the junction as a single energy level coupled to a collection of thermalised vibrational modes.

In order to explain the experimental measurements it will also be necessary to account for the (spin) degeneracies of the relevant levels electronic energy levels. For instance, in the case of a doubly spin-degenerate $N+1$ charge state (that is when N is even), the electronic Hamiltonian in Eq. (7.1) should be replaced with:

$$H_S = \sum_{\sigma=\uparrow,\downarrow} \varepsilon_0 a_{0\sigma}^\dagger a_{0\sigma} + U a_{0\uparrow}^\dagger a_{0\uparrow} a_{0\downarrow}^\dagger a_{0\downarrow} \ . \tag{8.1}$$

We note, however, that the double occupancy of molecular energy levels is generally not possible at low-bias conditions considered herein. We thus set $U \to \infty$, and simply exclude the doubly-populated state from the Hilbert space. We shall further ignore this repulsive term from the equations of motion used to determine the effective propagator in Section 7.2.1. Consequently, only a very simple correction to the Eq. (7.30) needs to be made. We replace it with:

$$I = n_N n_{N+1} \frac{\gamma_{\mathrm{L}} \bar{\gamma}_R - \gamma_{\mathrm{R}} \bar{\gamma}_L}{n_{N+1}(\gamma_{\mathrm{L}} + \gamma_{\mathrm{R}}) + n_N(\bar{\gamma}_L + \bar{\gamma}_R)} \ . \tag{8.2}$$

where n_N and n_{N+1} are the degeneracies of the N and $N+1$ charge states, respectively. Assuming a lack of spatial degeneracy (the molecular structure in Figure 8.1 belongs to the C_2 point group), $n_N = 1$ for an even N (a charge state with an even number of electrons), and $n_N = 2$ otherwise.

What is the physical meaning of this degeneracy factors in Eq. (8.2)? Let us consider a system which (for a given V_{g}) is found in an even-N charge state at zero bias. As V_{b} is increased, the resonant transport (charging and de-charging of the molecule) becomes possible. Since the $N+1$ charge state is doubly degenerate (it possesses an odd number of electrons), the electron hopping onto the molecule is twice as likely as it would have

been in the absence of this degeneracy – both spin-up and spin-down electrons can charge the molecule. The efficiency of the electron hopping off the molecule, on the other hand, is not affected since the N charge state is singly-degenerate. The opposite is true for an odd N. In the case of asymmetric molecule-lead couplings, the above can lead to current rectification (asymmetric IV characteristics with rectification ratios up to 2) even on resonance, *c.f.* Figure 7.2(a).

8.3 Inelastic resonant charge transport

8.3.1 Liquid-nitrogen temperature

The bulk of the transport measurements on the zinc-porphyrin junctions considered here were performed at the liquid-nitrogen temperature of 77 K. One might anticipate that, at least on a qualitative level, the transport behaviour under these conditions can be described by Marcus or Modified Marcus theory derived in the previous chapter. The former model features only three free parameters: two molecule-lead coupling strengths, $\Gamma_{\mathrm{L}}/\Gamma_{\mathrm{R}}$, and the reorganisation energy, λ. The Modified MT also contains the parameter χ, which accounts for the coupling to the high-frequency vibrational modes. Since the binding of the molecules to the graphene electrodes is a stochastic process, Γ_{L} and Γ_{R} can be expected to take markedly different values for every studied device. In fact, it has been recently demonstrated that in the device geometry considered here, Γ_{L} and Γ_{R} can vary across over three orders of magnitude [116]. Conversely, the values of the reorganisation energy (as well as those of χ) should more characteristic of the studied structure. It should be noted, however, that certain variability in λ (and χ) will almost certainly also be present. This can occur in part due to the possible geometric distortions of the deposited molecular structures, as well as due to the microscopic differences between the fabricated nano-junctions since, as remarked before, the molecular electronic degrees of freedom can generally also be coupled to the vibrational modes of the underlying substrate.

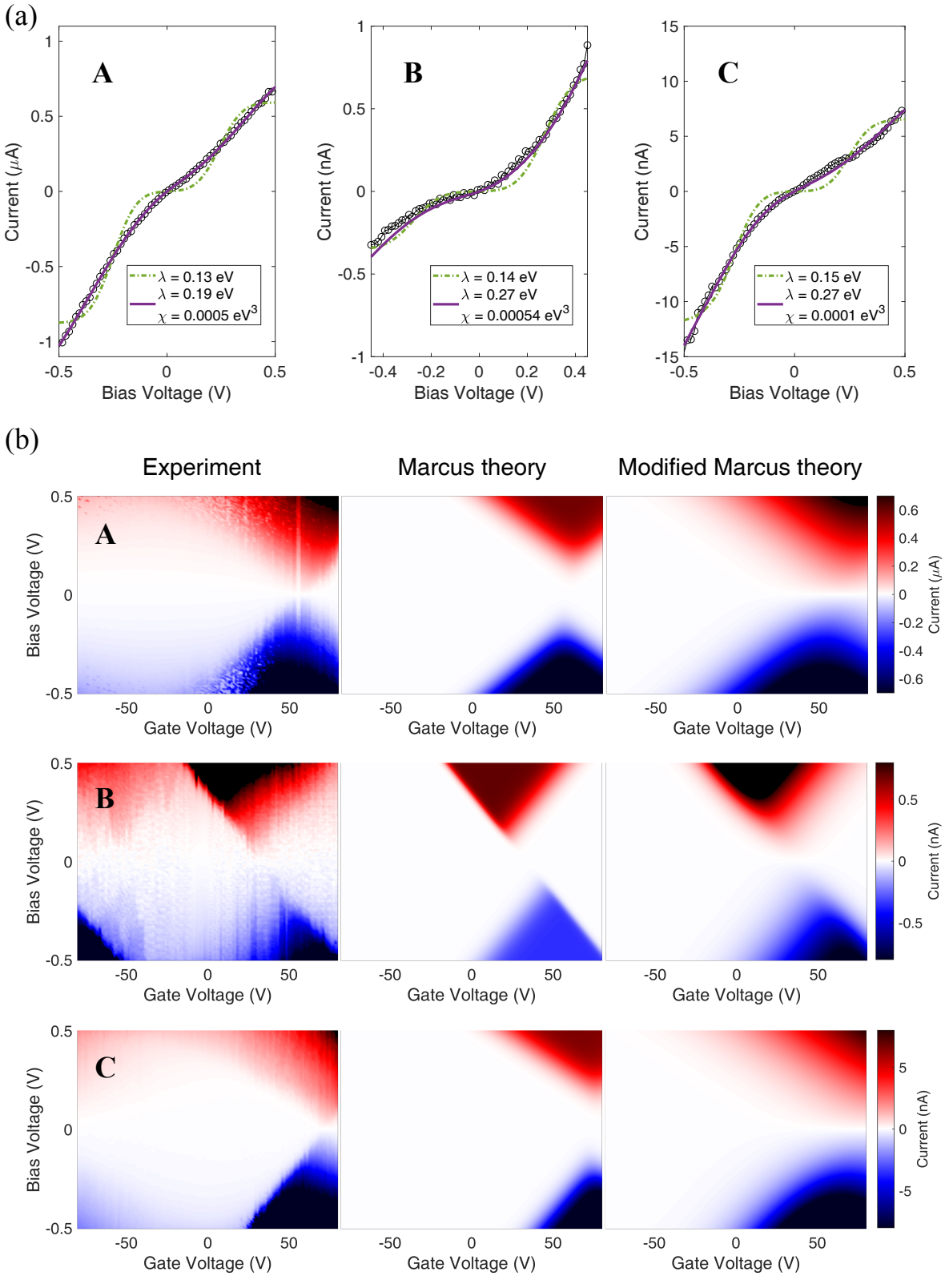


Figure 8.4: (a) Experimental IV characteristics on resonance (circles) together with fits to Marcus (dashed line), and Modified Marcus theory (solid line) for three devices. (b) Stability diagrams measured experimentally and calculated with the parameters from (a). All measurements were performed at $T = 77$ K.

	λ (Marcus theory)	λ (Modified MT)	χ (Modified MT)
Mean	100 meV	192 meV	3.8×10^{-4} eV^3
Std. deviation	47 meV	99 meV	2.5×10^{-4} eV^3

Table 8.1: The extracted values of the reorganisation energy and the parameter χ.

In Figure 8.4(a) we show the fits of the resonant IV characteristics to the Marcus and Modified Marcus approaches for three devices (**A**, **B** and **C**). On a qualitative level, both of the Marcus approaches can reproduce the experimental transport behaviour although the usual Marcus theory gives rise to the same artefacts as in Section 7.5.3: current suppression at low bias and early plateaus in the IV characteristics for higher V_b. The Modified Marcus theory, on the other hand, yields an excellent match to the experimental data. It can be argued, and rightly so, that the better fit of MMT is entirely due to the presence of another fitting parameter (χ). As discussed in Chapter 7, the fact that the electron-vibrational coupling within Marcus theory is reduced to a single parameter (λ) is perhaps its biggest strength as well as weakness. In practice, one often also needs to account for the structure or at least the energetic extent of the phononic spectral density. Modified Marcus theory is perhaps the simplest way of achieving that goal.

The values of the reorganisation energy and the χ parameter extracted from these fits (of eight molecular junctions) are tabulated in Table 8.1. As expected, considerable variations in the obtained λ and χ are observed. This is in line with the fact that the experimental reproducibility of results obtained for different junctions comprising the same molecular structures is a very common problem in the field of molecular electronics, and is inherent to single-molecule measurements. Nonetheless, all of the studied junctions can be very well described using the model at hand. We find that the molecule-lead coupling is strongly asymmetric ($\Gamma_\mathrm{L} \gg \Gamma_\mathrm{R}$, or *vice versa*) in all three devices shown here. This should be expected if the values of Γ_L and Γ_R indeed are stochastic and is thus consistent with the large variations in the conductance between the studied devices. Consequently, the resonant IV characteristics are strongly asymmetric with the rectification ratio (current ratio between the forward and backward

bias) approaching the value of 2. This confirms that one of the charge states involved is doubly (spin-)degenerate, as expected.

In Figure 8.4(b) we further plot the experimentally-measured and calculated stability diagrams (using the Marcus and Modified Marcus approaches with parameters obtained from the fits of the resonant IV characteristics).[1] Overall, a good agreement between the experimental results and the Modified Marcus approach can be reached, although, as already discussed in Section 7.5.3, MMT tends to marginally overestimate the electric current outside of the bias window. Particularly encouraging, however, is the fact that it both correctly captures the asymmetries of the stability diagrams (stemming solely from the asymmetric molecule-lead coupling) as well as quantitatively matches the observed values of current.

8.3.2 Vibrational coupling in zinc-porphyrins

Similar to what was done in Section 7.4, we now calculate the resonant transport properties of the zinc-porphyrin junction with the aid of DFT calculations. Figures 8.5(a,b) show the electron-phonon coupling parameters calculated for a molecular structure in Figure 8.1 deposited in a junction (details of this calculation are described in Ref. [5]) for the (a) N to $N-1$, and (b) $N-1$ to $N-2$ charge transitions (the N charge state corresponds to the neutral species). These calculations yield the (inner-sphere) reorganisation energies of $\lambda = 67$ meV for the former, and $\lambda = 149$ meV in the case of the latter transition. These values do not account for coupling to the low-frequency environmental vibrational modes (those of the substrate). It should be anticipated therefore that the overall reorganisation energy will be somewhat larger (and different for every device) than the above. The value of the reorganisation energy obtained for the N to $N-1$ transition is therefore consistent with the MMT fits at 77 K shown in Figure 8.4, see Table 8.1. In Figures 8.5(c,d), we calculate the IV characteristics

[1] Unlike in the previous chapters, here we do not simply apply the bias voltage symmetrically. Instead, we determine the capacitances between the molecule and the source, drain, and gate electrodes from the slopes of the Coulomb diamonds. We then gate the molecular energy level as described in Section 2.1.

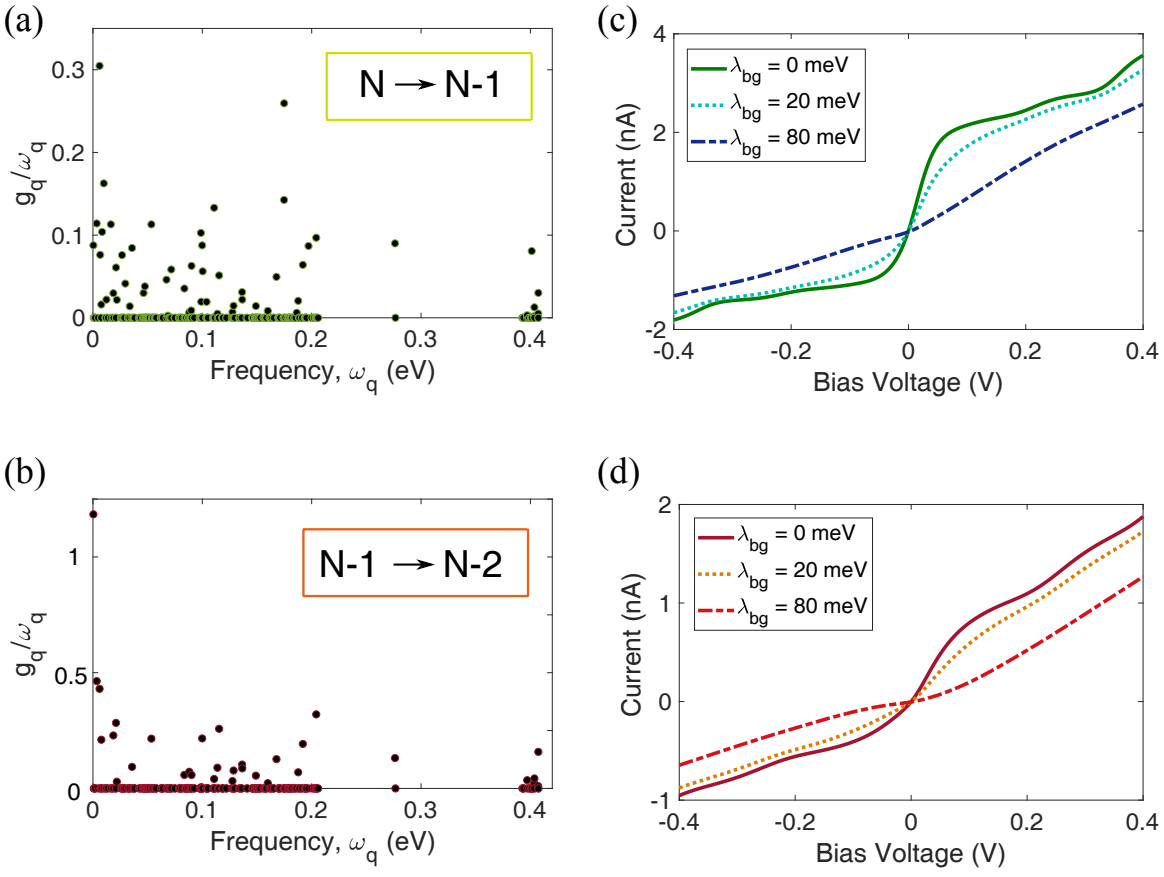


Figure 8.5: (a, b) Values of the dimensionless electron-phonon coupling parameters, g_q/ω_q, for the (a) $N \to N-1$, and (b) $N-1 \to N-2$ charge transitions. The calculations were performed in Gaussian09 with B3LYP functional and 6-31G(d) basis set [194], see SI of Ref. [5] for details. (c, d) Resonant IV characteristics ($\bar{\epsilon}_0 = 0$) at $T = 77$ K with $\Gamma_L = 1$ meV, $\Gamma_R = 10$ μeV, $\omega_{bg} = 15$ meV throughout.

on resonance using the DFT electron-phonon coupling parameters, and assuming that the molecular vibrational modes are infinitely long-lived (solid lines). We also plot the transport characteristics in the presence of additional coupling to the environmental vibrational modes (dashed lines) – once again represented by the super-ohmic spectral density of Eq. (7.37) with instructive values of λ_{bg} and ω_{bg}. As shown therein, the low-bias conductance is markedly overestimated (as compared to the experimental measurements) in the case of coupling solely to the molecular vibrational modes. The additional electron-vibrational interactions are necessary to qualitatively reproduce the observed behaviour.[2] This conclusion should not be surprising. As discussed

[2]In a recent AFM study, the authors investigated the electron-vibrational coupling between a naphthalocyanine molecule and the NaCl substrate, and calculated the overall reorganisation energy associated with charging of the considered structure ($\lambda \sim 0.8$ eV) [215]. The situation encountered here is however far more complex: the molecular system in Figure 8.1 is non-planar and deposited on

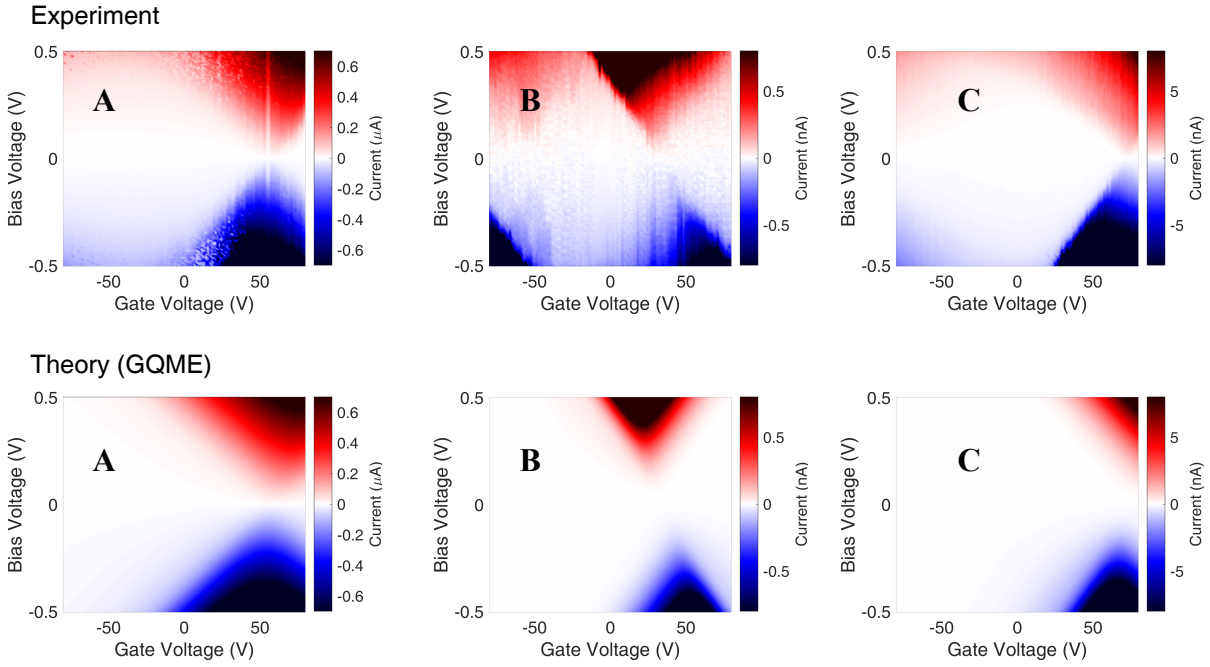


Figure 8.6: Stability diagrams measured experimentally and calculated using the GQME approach with parameters obtained using DFT calculations and through the fitting of the IV characteristics (see text).

in the previous chapter, low-frequency modes (such as those of the broader environment) have a disproportionately large effect on the transport characteristics – even relatively small $\lambda_{\rm bg}$ leads to a considerable suppression of the zero-bias conductance, see Figures 8.5(c,d). Furthermore, the presence of this environmental coupling also appears to wash away the structure of the transport characteristics, which is similarly not observed in the experiment.

Based on these encouraging results, we proceed to analyse the experimental transport data using the method described above, i.e. assuming that the phononic spectral density is given by:

$$\mathcal{J}(\omega) = \sum_q |g_q|^2 \, \delta(\omega - \omega_q) + \frac{\lambda_{\rm bg}}{2} \left(\frac{\omega}{\omega_{\rm bg}} \right)^3 e^{-\omega/\omega_{\rm bg}} \, . \tag{8.3}$$

The vibrational frequencies ω_q and the corresponding coupling strengths g_q are the values calculated for the N to $N-1$ charge transition [plotted in Figure 8.5(a)], while $\lambda_{\rm bg}$ and $\omega_{\rm bg}$ act as free fitting parameters. We shall once again fit the IV characteristics

a highly non-uniform surface, the microscopic details of which can only be hypothesised.

on resonance and reproduce the entire stability diagram from the resulting parameters. The results of these calculations (for devices **A**-**C**) are shown in Figure 8.6. Again, a good agreement between the theoretical results and the experimental data is reached. We further note that an overestimation of off-resonant current (present within the Modified Marcus theory) is not present within the more sophisticated (GQME) treatment used here. We obtain values of the outer-sphere reorganisation energy λ_{bg} of approximately 180, 240, and 220 meV for devices **A**-**C**, respectively.

8.3.3 Low-temperature measurements

To further confirm the vibrational origin of the observed behaviour, we have studied the charge transport through porphyrin molecular junctions at significantly lower temperatures. There, it should be possible to resolve at least some of the structure of the vibrational spectral density. Figures 8.7(a,b) show the IV characteristics and the differential conductance measured on resonance at $T = 5$ K for device **X**. The latter clearly features a set of roughly equidistant peaks – a signature of relatively strong coupling to a single molecular vibrational mode. Similarly, the conductance map shown in Figure 8.7(e) possesses a set of equidistant lines which, importantly, are parallel to the edges of the Coulomb diamond. This means that the states corresponding to the aforementioned features are gated to the same extent as the molecular electronic level involved in the transport. Consequently, they most likely correspond to molecular (here, vibrational) excited states, *c.f.* Ref. [6]. Reassuringly, the DFT calculations performed on the studied zinc-porphyrin structure for this charge transition ($N - 1 \rightarrow N - 2$), see Figure 8.5(b), predict the presence of a vibrational mode with frequency of roughly 6 meV (close to the observed $\omega_X \approx 5.3$ meV) that is relatively strongly coupled to the electronic degree of freedom (with the g_q/ω_q factor of 0.43).[3]

Importantly, however, the conductance in Figure 8.7(b) does not decay to zero in between of those peaks. This again suggests a presence of additional weak electron-

[3]While this agreement is indeed encouraging, it should be noted that the DFT calculations also predict relatively strong coupling to a handful of other molecular modes which seemingly cannot be resolved in our experiment.

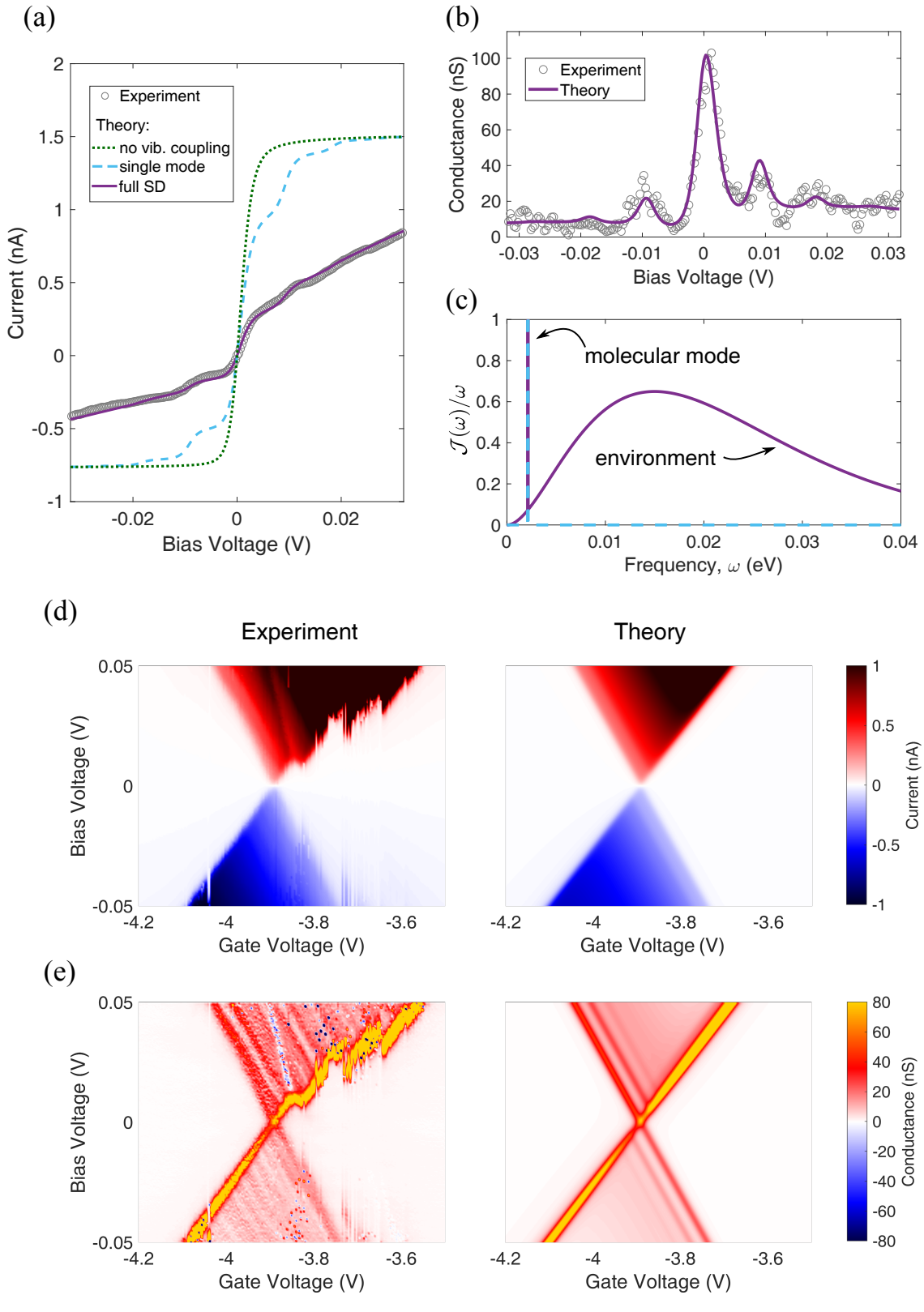


Figure 8.7: The low-bias transport characteristics of device **X**. (a) Experimental and theoretical IV characteristics measured at $T = 5$ K. (b) Differential conductance – derivative of (a). (c) Phononic spectral density used in the fit of the differential conductance. (d, e) Experimental and theoretical stability diagrams (d), and conductance maps (e), measured at $T = 7$ K.

Γ_{L}	Γ_{R}	λ_{bg}	ω_{bg}	g_X/ω_X
0.4 meV	3 μeV	18 meV	7.5 meV	0.65

Table 8.2: The values of parameters extracted from the fit of the low-bias differential conductance of device **X** shown in Figure 8.7(b).

vibrational coupling to environmental modes which cannot be resolved. We therefore proceed to fit the low-bias differential conductance in Figure 8.7(b) with the GQME-based model (see Chapter 7), assuming that coupling to the vibrational spectral density takes the form:

$$\mathcal{J}(\omega) = |g_X|^2 \, \delta(\omega - \omega_X) + \frac{\lambda_{\mathrm{bg}}}{2} \left(\frac{\omega}{\omega_{\mathrm{bg}}} \right)^3 e^{-\omega/\omega_{\mathrm{bg}}} \, , \tag{8.4}$$

and is pictured in Figure 8.7(c). It consists of a sharp peak which corresponds to the strongly-coupled molecular vibrational mode ω_X and a broad background which accounts for all the residual vibrational modes, and can be associated with both the molecular structure itself as well as the substrate on which the porphyrin molecule is deposited. In what follows we limit ourselves to five fitting parameters: two molecule-lead couplings Γ_{L} and Γ_{R}, the reorganisation energy λ_{bg} and the cut-off frequency ω_{bg} of the phononic background, and the electron-phonon coupling strength g_X for the strongly-coupled vibrational mode ω_X. The frequency of the mode in question has been inferred from the experimental differential conductance, and therefore does not need to act as a fitting parameter.

As shown in Figure 8.7(b), the result of this fit is in excellent agreement with the experimental resonant conductance.[4] The fitted parameters are shown in Table 8.2. In Figure 8.7(a) we also plot the IV characteristics obtained for the coupling parameters extracted above as well as (i) in the absence of electron-vibrational coupling, and (ii) in the presence of coupling solely to the molecular mode highlighted in Figure 8.7(c). As can be seen therein, neither of the latter approaches can qualitatively reproduce the experimental transport characteristics. Figures 8.7(d,e) further show the experimental

[4]The small differences between the experimental and fitted differential conductance for the first vibrational peak at $V_{\mathrm{b}} \sim \pm 0.01$ V stems likely from non-equilibrium vibrational dynamics (ignored here).

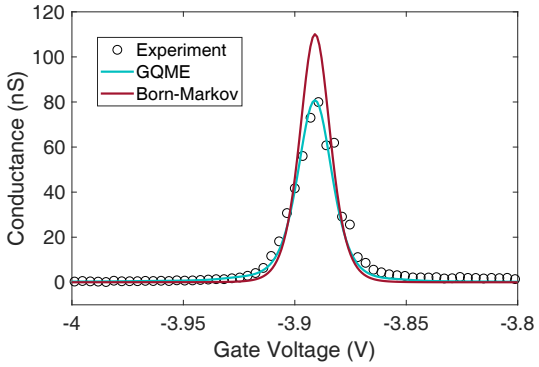


Figure 8.8: Experimental and theoretical zero-bias conductance of device **X** at $T = 7$ K. The theoretical values were calculated with the parameters from Table 8.2.

and theoretical stability diagrams and conductance maps (the latter calculated with the parameters from the fit described above). Once again, our results concur very well with the experiment.

We once again find that the molecule-lead bonding in this system is highly asymmetric, $\Gamma_{\mathrm{L}} \gg \Gamma_{\mathrm{R}}$, leading to asymmetric IV characteristics on resonance (with rectification ratio of ≈ 2). The lifetime broadening is therefore determined by Γ_{L}, while Γ_{R} controls the overall value of current flowing through the junction. Through the fitting procedure described above, we obtain lifetime broadening of $\Gamma \approx 0.2$ meV. In Figure 8.8 we compare the experimental and theoretical gate traces (zero-bias conductance as a function the gate voltage) with the theoretical ones calculated using the GQME and Born-Markov approaches (with and without lifetime broadening, respectively; see Chapter 7). Whilst Γ is significantly smaller than $k_{\mathrm{B}}T$ at 7 K (which corresponds to roughly 0.6 meV), we find that its inclusion is necessary to quantitatively capture the observed behaviour. As shown in Figure 8.8, the Born-Markov approach overestimates the zero-bias conductance by over 30 %.

8.3.4 From quantum to semi-classical transport behaviour

An interesting question to consider next is whether it is possible to observe a gradual transition from the quantum regime considered in the previous section (where one needs to treat the vibrational modes quantum-mechanically as well as include the lifetime

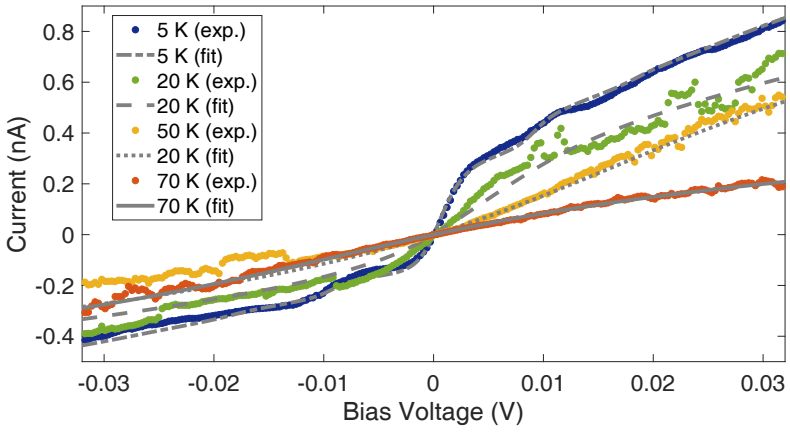


Figure 8.9: Resonant IV characteristics measured at different temperatures, grey lines show the fits of these IV characteristics to the GQME model with two free parameters: Γ_{L} and Γ_{R}. The electronic energy level is assumed to couple to the same spectral density as in Figure 8.7.

broadening in the transport description) to the semi-classical one considered in Section 8.3.1 (where Marcus approaches are applicable). To address this issue we have also studied the transport properties of the junction **X** for increasing temperature. The resulting IV characteristics (on resonance) are shown in Figure 8.9. Unfortunately, it appears that the molecule-lead couplings vary between measurements performed at different temperatures (some of the IV characteristics have different asymmetries). This may occur either due to a dislocation of the molecule during the warm-up procedure or due to small rearrangements in the microscopic structure of the leads which affect the local densities of states and therefore also the molecule-lead hopping rates. Nonetheless, all of the presented IV characteristics can be still very well described by our model with the vibrational coupling as in Figure 8.7, although with different Γ_{L}, Γ_{R} for every temperature. The relevant fits are shown in Figure 8.9; the extracted values of the molecule-lead couplings can be found in Table 8.3.

We limit ourselves here to several qualitative comments. Firstly, the structure of the IV characteristics is being washed away as the temperature is increased. The transport characteristics at 70 K no longer feature the Franck-Condon steps clearly visible at 5 K. Furthermore, at higher temperature the transport characteristics of device **X** become almost linear with V_{b} – in agreement with the low-bias behaviour of devices **A**, **B**, **C**.

T	Γ_{L}	Γ_{R}
5 K	0.4 meV	3.2 μeV
20 K	57 μeV	2.4 μeV
50 K	0.4 meV	2.2 μeV
70 K	1.9 μeV	5.2 μeV

Table 8.3: The values of parameters extracted from the fits of the IV characteristics of device **X** at various temperatures.

As already demonstrated in Figure 8.4, such behaviour can be successfully accounted for by the Marcus approaches used above.

8.4 Conclusions

In this chapter, we have used the theoretical approaches developed earlier in this thesis to understand and interpret the experimental charge transport measurements performed on zinc-porphyrin molecular junctions. We have demonstrated that the apparent breakdown of the usual (single-level) Landauer-Büttiker description can be rationalised by accounting for the electron-vibrational interactions. The transport behaviour of the studied molecular junctions at the liquid-nitrogen temperature can be very well described using our Modified Marcus approach (as well as the full GQME approach). Conversely, the conventional Marcus theory fails to successfully reproduce the experimental observations, and instead gives rise to a number of artefacts, as has been anticipated and discussed in Section 7.5.3. This breakdown of Marcus theory indicates the importance of nuclear tunnelling, not captured by MT, in charge transport through the considered junctions at 77 K. In order to describe the low-temperature measurements, we have resorted to the full GQME approach from Section 7.2.2 as the inclusion of lifetime broadening and the structure of the phononic spectral density turned out to be necessary.

To sum up, not only have we empirically demonstrated the validity and effectiveness of the theoretical framework derived in the previous chapter, but we have also explained and quantitatively reproduced the experimental behaviour of molecular junctions across a range of temperatures. This study has also uncovered the significance of coupling to

the broader environmental degrees of freedom in the device geometry used herein. The expected lack of such interactions in the case of suspended molecular break junctions could explain the more conventional shape of the resonant IV characteristics often encountered in those systems [148,243]. Furthermore, we have shown that the electron-vibrational coupling suppresses the resonant current through the studied junctions, and therefore has a detrimental effect on the on/off ratio of the studied molecular transistors. Such devices should thus perform best in the regime of small reorganisation energy.

Chapter 9

Conclusions

Well, who's going to take me?

— Rudolph A. Marcus

This thesis has examined the role of electron-vibrational coupling in charge transport through molecular junctions. Throughout this work, we have explored the breadth of phenomena that arise as a result of these interactions, predominantly in the resonant transport regime.

The first two research chapters focused on the effects of interactions between the electronic degrees of freedom and individual vibrational modes. Since, as discussed in Chapter 3, the simple single-site (Anderson-Holstein) model has been extensively studied in the literature and is rather well understood, we have focused on less-explored electronic model systems. In particular, we have examined the role of vibrational coupling in transport through extended molecular junctions on the example of two-site molecular system (Chapter 4), and through systems with degenerate electronic levels (Chapter 5). In both cases special emphasis was placed on non-equilibrium vibrational effects in the steady-state limit. In the case of the molecular double quantum dot considered in Chapter 4, we have shown that such effects can give rise to current suppression and negative differential conductance. In Chapter 5, we have demonstrated how vibrational effects can be incorporated into a PPP-based theoretical model. We

have applied this framework to a case-study of a spiro-conjugated molecular junction and demonstrated that the unusual electronic structure of this system gives rise to destructive quantum interference in charge transport through the degenerate electronic E states. We have further shown that, since populating these states gives rise to Jahn-Teller distortion (which lifts the aforementioned interference effects), the transport properties of such a junction are determined by an interplay between the two phenomena.

For the remainder of this thesis we have focused on collective vibrational effects. Chapter 6 discussed the role of such collective vibrational environment (thermalised phonon baths) in the case of a two-site molecular system. It was shown that interactions of this type can significantly enhance the efficiency of charge transport (as quantified by the electric current), analogous to the phenomenon of environment-assisted quantum transport. We also took that opportunity to examine and compare some of the theoretical approaches commonly used to study the effects of vibrational coupling in the transport setting. In Chapter 7 we then returned to a single-site model previously discussed in Chapters 2 and 3. Using a generalised quantum master equation, we have shown how one can go beyond the perturbative treatment of the molecule-lead interactions and derived a relatively simple approach which enables us to simultaneously account for electron-vibrational interactions, lifetime broadening, and the charge state of the molecular system within the junction. This chapter contains what is perhaps the most important conceptual result of this thesis: a theory which (at least in the single-level case considered here) unifies the Marcus and Landauer-Büttiker theories of charge transport – a long-standing problem in the field, see for instance discussion in Ref. [271]. The theoretical framework from Chapter 7 was then successfully applied in Chapter 8 to explain the experimental measurements of transport properties of zinc-porphyrin molecular junctions. We have demonstrated that the resonant charge transport in these systems is governed by an interplay between electron-vibrational and electron-electron interactions. We have further shown that, in order to explain the experimentally-observed behaviour, it is necessary to account for both the inner-

and outer-sphere vibrational coupling (molecular vibrational modes and the broader phononic environment, respectively). Overall, we have reached an agreement between the observed experimental transport behaviour and the results of theoretical calculations. This joint experimental-theoretical study has given us, for the first time, a complete understanding of the resonant charge regime in graphene-based single-molecule junctions.

As demonstrated in the final research chapter of this thesis, the issues hindering the further development of the field of molecular electronics are nowadays predominantly of a technical nature. While the transport behaviour of individual molecular junctions can be very well understood, it varies hugely between the studied molecular devices. The unsolved challenge to control the molecule-lead coupling and the wider junction environment severely hinders the technological development of the field.

That said, forty years ago, the idea of constructing functional single-molecule electronic devices seemed rather unattainable. Nowadays, molecular junctions are routinely fabricated and in a number of proof-of-principle studies were shown to indeed exhibit rectifying [85, 281], switching [6, 14, 101, 235] and thermoelectric behaviour [282–285].

What will the next forty years bring?

Appendix A

Displacement operators

In Chapter 2, we have introduced the displacement operators X and $X^\dagger$. Here, we shall briefly discuss their properties following mainly Ref. [49]. In general, for a single phonon mode, they take the form:

$$X(\alpha) = \exp\left(\alpha b^\dagger - \alpha^* b\right) \ ; \tag{A.1}$$

$$X^\dagger(\alpha) = \exp\left(-\alpha b^\dagger + \alpha^* b\right) \ , \tag{A.2}$$

where $b^\dagger$ and b are the phononic creation and annihilation operators, respectively. It therefore follows that

$$X(-\alpha) = X^\dagger(\alpha) \ , \tag{A.3}$$

and $X^\dagger(\alpha)X(\alpha) = \mathbb{1}$. Using the identity:

$$\exp\left[\theta(A+B)\right] = \exp(\theta A)\exp(\theta B)\exp\left\{-(\theta^2/2)[A,B]\right\} \ , \tag{A.4}$$

the displacement operator can be written as:

$$X(\alpha) = \exp(\alpha b^\dagger)\exp(-\alpha^* b)\exp\left(-|\alpha|^2/2\right) \tag{A.5}$$

It will be necessary in Chapters 4 and 5 to explicitly evaluate the displacement operator in the vibrational basis i.e. to find the matrix elements $\langle m|X(\alpha)|n\rangle$. First, let us evaluate the diagonal elements: $\langle n|X(\alpha)|n\rangle$. Using Eq. (A.5), they are given by:

$$\begin{aligned}
\langle n|X(\alpha)|n\rangle &= \langle n|\exp(\alpha b^\dagger)\exp(-\alpha^* b)|n\rangle \exp\left(-|\alpha|^2/2\right) \\
&= \sum_{l=0}^{\infty}\sum_{m=0}^{\infty} \frac{\alpha^l\,(-\alpha^*)^m}{l!\,m!}\,\langle n|b^{\dagger l}\,b^m|n\rangle \exp\left(-|\alpha|^2/2\right) \\
&= \sum_{l=0}^{n}\sum_{m=0}^{n} \frac{\alpha^l(-\alpha^*)^m}{l!\,m!}\langle n-l|\left(\frac{n!}{(n-l)!}\right)^{1/2}\left(\frac{n!}{(n-m)!}\right)^{1/2}|n-m\rangle \exp\left(-|\alpha|^2/2\right) \\
&= \sum_{m=0}^{n} \frac{(-|\alpha|^2)^m}{(m!)^2}\,\frac{n!}{(n-m)!}\exp\left(-|\alpha|^2/2\right) \\
&= L_n(|\alpha|^2)\exp\left(-|\alpha|^2/2\right)\ ,
\end{aligned} \tag{A.6}$$

where L_n is the Laguerre polynomial of order n.

The off-diagonal elements can be written as:

$$\begin{aligned}
\langle m|X(\alpha)|m-l\rangle &= \langle m|\exp(\alpha b^\dagger)\exp(-\alpha^* b)\,b^l|m\rangle \left(\frac{(m-l)!}{m!}\right)^{1/2}\exp\left(-|\alpha|^2/2\right) \\
&= \exp\left(-|\alpha|^2/2\right)\left(\frac{(m-l)!}{m!}\right)^{1/2}\left(-\frac{\partial}{\partial\alpha^*}\right)^l\langle m|\exp(\alpha b^\dagger)\exp(-\alpha^* b)|m\rangle \\
&= \exp\left(-|\alpha|^2/2\right)\left(\frac{(m-l)!}{m!}\right)^{1/2}(-\alpha)^l\left(-\frac{\partial}{\partial|\alpha|^2}\right)^l L_m(|\alpha|^2)\ .
\end{aligned} \tag{A.7}$$

Therefore, for $n < m$, the relevant matrix element is

$$\langle m|X(\alpha)|n\rangle = \exp\left(-|\alpha|^2/2\right)\left(\frac{n!}{m!}\right)^{1/2}(-\alpha)^{m-n}L_n^{m-n}(|\alpha|^2)\ , \tag{A.8}$$

and for $n > m$

$$\langle m|X(\alpha)|n\rangle = \exp\left(-|\alpha|^2/2\right)\left(\frac{m!}{n!}\right)^{1/2}(\alpha^*)^{n-m}L_n^{n-m}(|\alpha|^2)\ , \tag{A.9}$$

where L_n^{m-n} is an associated Laguerre polynomial.

Appendix B

Hansson-Stafström parametrisation

As described in Chapter 5, we account for the inter-site coupling across the spiro-link in the SNT molecule using the Hansson–Stafström parametrisation [190, 191]. For convenience, we briefly describe it below.

Firstly, it is assumed that the matrix hopping element between the sites i and j is proportional to the overlap between two p_z orbitals located on the sites i and j (this is known as the Mulliken approximation [286]):

$$t_{ij} = kS_{ij} \ , \tag{B.1}$$

with a proportionality constant k. The overlap S_{ij} is determined from the formulae of Mulliken *et al.* [287], and takes the form:

$$S_{ij} = \cos(\Phi_{ij})\cos(\Omega_{ij})\cos(\Theta_{ij})S_\pi - \sin(\Omega_{ij})\sin(\Theta_{ij})S_\sigma \ . \tag{B.2}$$

The angles in the equation above are:

$$\Phi_{ij} = \arccos(\mathbf{p}_i \cdot \mathbf{p}_j/|\mathbf{p}_i||\mathbf{p}_j|) \ , \tag{B.3}$$

$$\Omega_{ij} = \pi/2 - \arccos(\mathbf{p}_i \cdot \mathbf{r}_{ij}/|\mathbf{p}_i||\mathbf{r}_{ij}|) \ , \tag{B.4}$$

$$\Theta_{ij} = -\Omega_{ji} \ , \tag{B.5}$$

where $\mathbf{p}_i$ is a vector along the p_z orbital on site i, $\mathbf{r}_{ij}$ is a vector between the sites i and j and

$$S_\pi = e^{-\xi r}\left[1 + r\xi + \frac{2}{5}(r\xi)^2 + \frac{1}{15}(r\xi)^3\right] , \tag{B.6}$$

$$S_\sigma = e^{-\xi r}\left[-1 - r\xi - \frac{1}{5}(r\xi)^2 + \frac{2}{15}(r\xi)^3 + \frac{1}{15}(r\xi)^4\right] , \tag{B.7}$$

where r is the distance between the two sites and the orbital exponent ξ is given by $\xi = 3.07$ Å^{-1}. For consistency the value of parameter k was chosen such that for $\Theta_{ij} = \Omega_{ij} = \Phi_{ij} = 0$ and $r_{ij} = 1.40$ Å, $t_{ij} = t$ (where t is the parameter optimised by fitting the experimental excitation spectrum).

Appendix C

Phononic correlation functions

In this appendix, we justify the form of the phononic correlation functions used in Chapters 6 and 7. We begin with the Redfield correlation function given in Eq. (6.21). It has the form:

$$C^R(\tau) = \mathrm{Tr_E}[D(\tau)D(0)\rho_\mathrm{E}] \ , \tag{C.1}$$

where $D(\tau) = \sum_q g_q(b_q^\dagger e^{\mathrm{i}\omega_q\tau} + b_q e^{-\mathrm{i}\omega_q\tau})$. Since the terms linear in b_q ($b_q^\dagger$) vanish when tracing out the phonon baths, it can be written as:

$$C^R(\tau) = \mathrm{Tr_E}\left[\sum_q g_q^2(b_q^\dagger b_q e^{\mathrm{i}\omega_q\tau} + b_q b_q^\dagger e^{-\mathrm{i}\omega_q\tau})\rho_\mathrm{E}\right] \ . \tag{C.2}$$

Tracing out the phonon baths, it becomes:

$$C^R(\tau) = \sum_q g_q^2\left[(2N_q+1)\cos(\omega_q\tau) - \mathrm{i}\sin(\omega_q\tau)\right] \ , \tag{C.3}$$

where $N_q = (\exp(\omega_q/k_\mathrm{B}T) - 1)^{-1}$ is the average excitation of the mode q (given by the Bose-Einstein distribution). Using the definition of the spectral density from Eq. (2.42), the above can be written in the more convenient form:

$$C^R(\tau) = \int_0^\infty \mathrm{d}\omega\ \mathcal{J}(\omega)\left[\cos(\omega\tau)\coth(\beta\omega/2) - \mathrm{i}\sin(\omega\tau)\right] \ , \tag{C.4}$$

which is the result stated in Chapter 6.

We next proceed to consider the phononic correlation functions that are present within the polaron treatments in Chapter 6 and 7:

$$\langle X^{\dagger}(\tau)X\rangle = \mathrm{Tr}_{\mathrm{E}}[X^{\dagger}(\tau)X(0)\rho_{\mathrm{E}}] \; ; \tag{C.5}$$

$$\langle X(\tau)X\rangle = \mathrm{Tr}_{\mathrm{E}}[X(\tau)X(0)\rho_{\mathrm{E}}] \; , \tag{C.6}$$

where X and $X^{\dagger}$ are the displacement operators:

$$X(\tau) = \exp\left[-\sum_{q}\frac{g_q}{\omega_q}(b_q^{\dagger}e^{\mathrm{i}\omega_q\tau} - b_q e^{-\mathrm{i}\omega_q\tau})\right] \; , \tag{C.7}$$

and equivalently for $X^{\dagger}(\tau)$. The correlation functions given in Eqs. (C.5) and (C.6) can be found by carefully expanding the displacement operators (as relevant Taylor series), and evaluating the resulting traces over the phononic degrees of freedom. This rather tedious procedure gives:

$$\langle X^{\dagger}(\tau)X\rangle = \exp\left[-\sum_{q}\frac{g_q^2}{\omega_q^2}\big(N_q(1-e^{\mathrm{i}\omega_q t}) + (N_q+1)(1-e^{-\mathrm{i}\omega_q t})\big)\right] \; , \tag{C.8}$$

where $N_q = (e^{\omega_q\beta}-1)^{-1}$ is the average excitation of the mode q at . Again, using the definition of the phononic spectral density from Eq. (2.42), the above can be written in a more convenient form:

$$\langle X^{\dagger}(\tau)X\rangle = \exp\left[\int_0^{\infty}\mathrm{d}\omega\frac{\mathcal{J}(\omega)}{\omega^2}\left(\coth\left(\frac{\beta\omega}{2}\right)\big(\cos\omega\tau - 1\big) - \mathrm{i}\sin\omega\tau\right)\right] \; . \tag{C.9}$$

Analogously, we find that

$$\langle X(\tau)X\rangle = \exp\left[-\int_0^{\infty}\mathrm{d}\omega\frac{\mathcal{J}(\omega)}{\omega^2}\left(\coth\left(\frac{\beta\omega}{2}\right)\big(\cos\omega\tau + 1\big) - \mathrm{i}\sin\omega\tau\right)\right] \; . \tag{C.10}$$

We finish by noting that the above expressions for the phononic correlation functions can be also derived by making use of Glauber coherent states [288], see for instance Ref. [230].

Bibliography

[1] J. K. Sowa, J. A. Mol, G. A. D. Briggs, and E. M. Gauger. Vibrational effects in charge transport through a molecular double quantum dot. *Phys. Rev. B*, 95(8):085423, 2017.

[2] J. K. Sowa, J. A. Mol, G. A. D. Briggs, and E. M. Gauger. Spiro-conjugated molecular junctions: between Jahn–Teller distortion and destructive quantum interference. *J. Phys. Chem. Lett.*, 9(8):1859–1865, 2018.

[3] J. K. Sowa, J. A. Mol, G. A. D. Briggs, and E. M. Gauger. Environment-assisted quantum transport through single-molecule junctions. *Phys. Chem. Chem. Phys.*, 19(43):29534–29539, 2017.

[4] J. K. Sowa, J. A. Mol, G. A. D. Briggs, and E. M. Gauger. Beyond Marcus theory and the Landauer-Büttiker approach in molecular junctions: A unified framework. *J. Chem. Phys.*, 149(15):154112, 2018.

[5] J. O. Thomas, B. Limburg, J. K. Sowa, K. Willick, J. Baugh, E. M. Gauger, G. A. D. Briggs, H. L. Anderson, and J. A. Mol. Understanding resonant charge transport through single-molecule junctions. *(Submitted)*, 2019.

[6] P. Gehring, J. K. Sowa, J. Cremers, Q. Wu, H. Sadeghi, Y. Sheng, J. H. Warner, C. J. Lambert, G. A. D. Briggs, and J. A. Mol. Distinguishing lead and molecule states in graphene-based single-electron transistors. *ACS Nano*, 11(5):4739–4745, 2017.

[7] J. K. Sowa, J. A. Mol, and E. M. Gauger. Marcus theory of thermoelectricity in molecular junctions. *J. Phys. Chem. C*, 123(7):4103–4108, 2019.

[8] A. Harzheim, J. K. Sowa, J. Swett, G. A. D. Briggs, J. A. Mol, and P. Gehring. Thermoelectric characterisation of electroburnt graphene quantum dot. *Manuscript in preparation*, 2019.

[9] B. Limburg, J. O. Thomas, J. K. Sowa, K. Willick, J. Baugh, E. M. Gauger, G. A. D. Briggs, J. A. Mol, and H. L. Anderson. Charge-state assignment of nanoscale single-electron transistors from their current-voltage characteristics. *Manuscript in preparation*, 2019.

[10] A. Aviram and M. A. Ratner. Molecular rectifiers. *Chem. Phys. Lett.*, 29(2):277–283, 1974.

[11] L. A. Bumm, J. J. Arnold, M. T. Cygan, T. D. Dunbar, et al. Are single molecular wires conducting? *Science*, 271(5256):1705, 1996.

[12] D. Xiang, X. Wang, C. Jia, T. Lee, and X. Guo. Molecular-scale electronics: from concept to function. *Chem. Rev.*, 116(7):4318–4440, 2016.

[13] M. A. Reed, C. Zhou, C. J. Muller, T. P. Burgin, and J. M. Tour. Conductance of a molecular junction. *Science*, 278(5336):252–254, 1997.

[14] H. Park, J. Park, A. K. L. Lim, E. H. Anderson, A. P. Alivisatos, and P. L. McEuen. Nanomechanical oscillations in a single-C_{60} transistor. *Nature*, 407(6800):57–60, 2000.

[15] J. Park, A. N. Pasupathy, J. I. Goldsmith, C. Chang, Y. Yaish, J. R. Petta, M. Rinkoski, J. P. Sethna, H. D. Abruña, P. L. McEuen, et al. Coulomb blockade and the Kondo effect in single-atom transistors. *Nature*, 417(6890):722–725, 2002.

[16] W. Liang, M. P. Shores, M. Bockrath, J. R. Long, and H. Park. Kondo resonance in a single-molecule transistor. *Nature*, 417(6890):725, 2002.

[17] X. D. Cui, A. Primak, X. Zarate, J. Tomfohr, O. F. Sankey, A. L. Moore, T. A. Moore, D. Gust, G. Harris, and S. M. Lindsay. Reproducible measurement of single-molecule conductivity. *Science*, 294(5542):571–574, 2001.

[18] C. Kergueris, J.-P. Bourgoin, S. Palacin, D. Estève, C. Urbina, M. Magoga, and C. Joachim. Electron transport through a metal-molecule-metal junction. *Phys. Rev. B*, 59(19):12505, 1999.

[19] R. Hanson, L. P. Kouwenhoven, J. R. Petta, S. Tarucha, and L. M. K. Vandersypen. Spins in few-electron quantum dots. *Rev. Mod. Phys.*, 79(4):1217, 2007.

[20] C. W. J. Beenakker. Theory of Coulomb-blockade oscillations in the conductance of a quantum dot. *Phys. Rev. B*, 44(4):1646, 1991.

[21] K. K. Likharev. Correlated discrete transfer of single electrons in ultrasmall tunnel junctions. *IBM J. Res. Dev.*, 32(1):144–158, 1988.

[22] I. O. Kulik and R. I. Shekhter. Kinetic phenomena and charge-discreteness effects in granulated media. *Zh. Eksp. Teor. Fiz.*, 68(2):623–640, 1975.

[23] Y. V. Nazarov and Ya. M. Blanter. *Quantum transport: introduction to nanoscience*. Cambridge University Press, 2009.

[24] C. J. Gorter. A possible explanation of the increase of the electrical resistance of thin metal films at low temperatures and small field strengths. *Physica*, 17(8):777–780, 1951.

[25] P. W. Atkins and R. S. Friedman. *Molecular Quantum Mechanics*. Oxford University Press, 2011.

[26] L. S. Cederbaum and W. Domcke. On the vibrational structure in photoelectron spectra by the method of Green's functions. *J. Chem. Phys.*, 60(7):2878–2889, 1974.

[27] P. W. Anderson. Localized magnetic states in metals. *Phys. Rev.*, 124(1):41, 1961.

[28] M. Thoss and W. Domcke. Theory of vibrational relaxation processes in resonant collisions of low-energy electrons with large molecules. *J. Chem. Phys.*, 109(16):6577–6595, 1998.

[29] U. Weiss. *Quantum Dissipative Systems*, volume 13. World Scientific, 2012.

[30] R. Härtle, R. Volkovich, M. Thoss, and U. Peskin. Communication: Mode-selective vibrational excitation induced by nonequilibrium transport processes in single-molecule junctions. *J. Chem. Phys.*, 133(8):081102, 2010.

[31] E. M. Weig, R. H. Blick, T. Brandes, J. Kirschbaum, W. Wegscheider, M. Bichler, and J. P. Kotthaus. Single-electron-phonon interaction in a suspended quantum dot phonon cavity. *Phys. Rev. Lett.*, 92(4):046804, 2004.

[32] Y. Okazaki, I. Mahboob, K. Onomitsu, S. Sasaki, and H. Yamaguchi. Gate-controlled electromechanical backaction induced by a quantum dot. *Nat. Commun.*, 7, 2016.

[33] T. Frederiksen, M. Paulsson, M. Brandbyge, and A.-P. Jauho. Inelastic transport theory from first principles: Methodology and application to nanoscale devices. *Phys. Rev. B*, 75(20):205413, 2007.

[34] A. Erpenbeck, R. Härtle, and M. Thoss. Effect of nonadiabatic electronic-vibrational interactions on the transport properties of single-molecule junctions. *Phys. Rev. B*, 91(19):195418, 2015.

[35] J. Repp, P. Liljeroth, and G. Meyer. Coherent electron-nuclear coupling in oligothiophene molecular wires. *Nat. Phys.*, 6(12):975–979, 2010.

[36] G. D. Mahan. *Many-particle physics*. Plenum Press, New York, 1990.

[37] N. Sergueev, D. Roubtsov, and H. Guo. *Ab Initio* Analysis of Electron-Phonon Coupling in Molecular Devices. *Phys. Rev. Lett.*, 95:146803, 2005.

[38] C. T. Chang, J. P. Sethna, A. N. Pasupathy, J. Park, D. C. Ralph, and P. L. McEuen. Phonons and conduction in molecular quantum dots: Density functional calculations of Franck-Condon emission rates for bifullerenes in external fields. *Phys. Rev. B*, 76:045435, 2007.

[39] F. Giustino. Electron-phonon interactions from first principles. *Rev. Mod. Phys.*, 89(1):015003, 2017.

[40] E. Burzurí, Y. Yamamoto, M. Warnock, X. Zhong, K. Park, A. Cornia, and Herre S. J. van der Zant. Franck–Condon blockade in a single-molecule transistor. *Nano Lett.*, 14(6):3191–3196, 2014.

[41] E. Burzurí, J. O. Island, R. Díaz-Torres, A. Fursina, A. González-Campo, O. Roubeau, S. J. Teat, N. Aliaga-Alcalde, E. Ruiz, and H. S. J. van der Zant. Sequential Electron Transport and Vibrational Excitations in an Organic Molecule Coupled to Few-Layer Graphene Electrodes. *ACS Nano*, 10(2):2521–2527, 2016.

[42] C. S. Lau, H. Sadeghi, G. Rogers, S. Sangtarash, P. Dallas, K. Porfyrakis, J. Warner, C. J. Lambert, G. A. D. Briggs, and J. A. Mol. Redox-dependent Franck–Condon blockade and avalanche transport in a graphene–fullerene single-molecule transistor. *Nano Lett.*, 16(1):170–176, 2015.

[43] M. Paulsson, T. Frederiksen, and M. Brandbyge. Inelastic transport through molecules: Comparing first-principles calculations to experiments. *Nano Lett.*, 6(2):258–262, 2006.

[44] J. G. Kushmerick, J. Lazorcik, C. H. Patterson, R. Shashidhar, D. S. Seferos, and G. C. Bazan. Vibronic contributions to charge transport across molecular junctions. *Nano Lett.*, 4(4):639–642, 2004.

[45] R. C. Powell. *Symmetry, group theory, and the physical properties of crystals*, volume 824. Springer, 2010.

[46] A. Mavalankar, T. Pei, E. M. Gauger, J. H. Warner, G. A. D. Briggs, and E. A. Laird. Photon-assisted tunneling and charge dephasing in a carbon nanotube double quantum dot. *Phys. Rev. B*, 93:235428, 2016.

[47] I. G. Lang and Y. A. Firsov. Kinetic theory of semiconductors with low mobility. *J. Exptl. Theoret. Phys. (U.S.S.R.)*, 16:1301, 1963.

[48] T. Brandes. Coherent and collective quantum optical effects in mesoscopic systems. *Phys. Rep.*, 408(5-6):315–474, 2005.

[49] S. M. Barnett and P. M. Radmore. *Methods in theoretical quantum optics*, volume 15. Oxford University Press, 2002.

[50] H-P. Breuer and F. Petruccione. *The Theory of Open Quantum Systems*. Clarendon Press, Oxford, 2006.

[51] G. H. Golub and C. F. Van Loan. *Matrix computations*. Johns Hopkins University Press, Baltimore, MD, USA, 1996.

[52] D. K. C. MacDonald. Spontaneous fluctuations. *Rep. Prog. Phys.*, 12(1):56, 1949.

[53] C. Flindt, T. Novotnỳ, and A.-P. Jauho. Current noise spectrum of a quantum shuttle. *Phys. E*, 29(1):411–418, 2005.

[54] C. Schinabeck, R. Härtle, H. B. Weber, and M. Thoss. Current noise in single-molecule junctions induced by electronic-vibrational coupling. *Phys. Rev. B*, 90:075409, 2014.

[55] Y. M. Blanter and M. Büttiker. Shot noise in mesoscopic conductors. *Phys. Rep.*, 336(1):1–166, 2000.

[56] C. Flindt, T. Novotnỳ, and A.-P. Jauho. Full counting statistics of nano-electromechanical systems. *EPL*, 69(3):475, 2004.

[57] D. A. Bagrets and Yu. V. Nazarov. Full counting statistics of charge transfer in Coulomb blockade systems. *Phys. Rev. B*, 67(8):085316, 2003.

[58] C. Flindt, T. Novotnỳ, and A.-P. Jauho. Current noise in a vibrating quantum dot array. *Phys. Rev. B*, 70(20):205334, 2004.

[59] T. Li, W. Hu, and D. Zhu. Nanogap electrodes. *Adv. Mater.*, 22(2):286–300, 2010.

[60] L. Venkataraman, J. E. Klare, C. Nuckolls, M. S. Hybertsen, and M. L. Steigerwald. Dependence of single-molecule junction conductance on molecular conformation. *Nature*, 442(7105):904–907, 2006.

[61] S. W. Wu, G. V. Nazin, X. Chen, X. H. Qiu, and W. Ho. Control of relative tunneling rates in single molecule bipolar electron transport. *Phys. Rev. Lett.*, 93:236802, 2004.

[62] B. C. Stipe, M. A. Rezaei, and W. Ho. Single-molecule vibrational spectroscopy and microscopy. *Science*, 280(5370):1732–1735, 1998.

[63] Y. F. Wang, J. Kröger, R. Berndt, H. Vázquez, M. Brandbyge, and M. Paulsson. Atomic-Scale Control of Electron Transport through Single Molecules. *Phys. Rev. Lett.*, 104:176802, 2010.

[64] J. Gaudioso, L. J. Lauhon, and W. Ho. Vibrationally mediated negative differential resistance in a single molecule. *Phys. Rev. Lett.*, 85:1918–1921, 2000.

[65] J. Hihath, C. Bruot, and N. Tao. Electron-Phonon Interactions in Single Octanedithiol Molecular Junctions. *ACS Nano*, 4(7):3823–3830, 2010.

[66] F. Mohn, J. Repp, L. Gross, G. Meyer, M. S. Dyer, and M. Persson. Reversible bond formation in a gold-atom–organic-molecule complex as a molecular switch. *Phys. Rev. Lett.*, 105:266102, 2010.

[67] X. H. Qiu, G. V. Nazin, and W. Ho. Vibronic States in Single Molecule Electron Transport. *Phys. Rev. Lett.*, 92:206102, 2004.

[68] G. Sedghi, V. M. García-Suárez, L. J. Esdaile, H. L. Anderson, C. J. Lambert, S. Martín, D. Bethell, S. J. Higgins, M. Elliott, N. Bennett, et al. Long-range electron tunnelling in oligo-porphyrin molecular wires. *Nat. Nanotechnol.*, 6(8):517–523, 2011.

[69] G. Sedghi, K. Sawada, L. J. Esdaile, M. Hoffmann, H. L. Anderson, D. Bethell, W. Haiss, S. J. Higgins, and R. J. Nichols. Single molecule conductance of porphyrin wires with ultralow attenuation. *J. Am. Chem. Soc.*, 130(27):8582–8583, 2008.

[70] C. M. Guédon, H. Valkenier, T. Markussen, K. S. Thygesen, J. C. Hummelen, and S. J. van der Molen. Observation of quantum interference in molecular charge transport. *Nat. Nanotechnol.*, 7(5):305–309, 2012.

[71] N. Pavliček, I. Swart, J. Niedenführ, G. Meyer, and J. Repp. Symmetry Dependence of Vibration-Assisted Tunneling. *Phys. Rev. Lett.*, 110:136101, 2013.

[72] B. Xu and N. J. Tao. Measurement of single-molecule resistance by repeated formation of molecular junctions. *Science*, 301(5637):1221–1223, 2003.

[73] F. Chen, J. Hihath, Z. Huang, X. Li, and N. J. Tao. Measurement of single-molecule conductance. *Annu. Rev. Phys. Chem.*, 58:535–564, 2007.

[74] I. Díez-Pérez, Z. Li, S. Guo, C. Madden, H. Huang, Y. Che, X. Yang, L. Zang, and N. Tao. Ambipolar transport in an electrochemically gated single-molecule field-effect transistor. *ACS Nano*, 6(8):7044–7052, 2012.

[75] B. Capozzi, Q. Chen, P. Darancet, M. Kotiuga, M. Buzzeo, J. B. Neaton, C. Nuckolls, and L. Venkataraman. Tunable charge transport in single-molecule junctions via electrolytic gating. *Nano Lett.*, 14(3):1400–1404, 2014.

[76] N. J. Tao. Electron transport in molecular junctions. *Nat. Nanotechnol.*, 1(3):173–181, 2006.

[77] M. L. Perrin, C. J. O. Verzijl, C. A. Martin, A. J. Shaikh, R. Eelkema, J. H. van Esch, J. M. van Ruitenbeek, J. M. Thijssen, H. S. J. van der Zant, and D. Dulić. Large tunable image-charge effects in single-molecule junctions. *Nat. Nanotechnol.*, 8(4):282–287, 2013.

[78] Y. S. Park, A. C. Whalley, M. Kamenetska, M. L. Steigerwald, M. S. Hybertsen, C. Nuckolls, and L. Venkataraman. Contact chemistry and single-molecule conductance: a comparison of phosphines, methyl sulfides, and amines. *J. Am. Chem. Soc.*, 129(51):15768–15769, 2007.

[79] M. Kamenetska, S. Y. Quek, A. C. Whalley, M. L. Steigerwald, H. J. Choi, S. G. Louie, C. Nuckolls, M. S. Hybertsen, J. B. Neaton, and L. Venkataraman. Conductance and geometry of pyridine-linked single-molecule junctions. *J. Am. Chem. Soc.*, 132(19):6817–6821, 2010.

[80] C. J. Muller, B. J. Vleeming, M. A. Reed, J. J. S. Lamba, R. Hara, L. Jones II, and J. M. Tour. Atomic probes: a search for conduction through a single molecule. *Nanotechnology*, 7(4):409, 1996.

[81] D. Xiang, H. Jeong, T. Lee, and D. Mayer. Mechanically controllable break junctions for molecular electronics. *Adv. Mater.*, 25(35):4845–4867, 2013.

[82] D. Z. Manrique, C. Huang, M. Baghernejad, X. Zhao, O. A. Al-Owaedi, H. Sadeghi, V. Kaliginedi, W. Hong, M. Gulcur, T. Wandlowski, et al. A quantum circuit rule for interference effects in single-molecule electrical junctions. *Nat. Commun.*, 6, 2015.

[83] M. L. Perrin, R. Frisenda, M. Koole, J. S. Seldenthuis, J. A. C. Gil, H. Valkenier, J. C. Hummelen, Ni. Renaud, Fer. C. Grozema, J. M. Thijssen, et al. Large negative differential conductance in single-molecule break junctions. *Nat. Nanotechnol.*, 9(10):830–834, 2014.

[84] M. L. Perrin, C. A. Martin, F. Prins, A. J. Shaikh, R. Eelkema, J. H. van Esch, J. M. van Ruitenbeek, H. S. J. van der Zant, and D. Dulić. Charge transport in a zinc–porphyrin single-molecule junction. *Beilstein J. Nanotechnol.*, 2(1):714–719, 2011.

[85] M. L. Perrin, E. Galán, R. Eelkema, J. M. Thijssen, F. Grozema, and H. S. J. van der Zant. A gate-tunable single-molecule diode. *Nanoscale*, 8(16):8919–8923, 2016.

[86] Y. Li, S. Kaneko, S. Fujii, and M. Kiguchi. Symmetry of Single Hydrogen Molecular Junction with Au, Ag, and Cu Electrodes. *J. Phys. Chem. C*, 119(33):19143–19148, 2015.

[87] R. Frisenda, R. Gaudenzi, C. Franco, M. Mas-Torrent, C. Rovira, J. Veciana, I. Alcon, S. T. Bromley, E. Burzurí, and H. S. J. Van der Zant. Kondo effect in a neutral and stable all organic radical single molecule break junction. *Nano Lett.*, 15(5):3109–3114, 2015.

[88] T. Böhler, J. Grebing, A. Mayer-Gindner, H. v Löhneysen, and E. Scheer. Mechanically controllable break-junctions for use as electrodes for molecular electronics. *Nanotechnology*, 15(7):S465, 2004.

[89] J.-H. Tian, B. Liu, X. Li, Z.-L. Yang, B. Ren, S.-T. Wu, N. Tao, and Z.-Q. Tian. Study of molecular junctions with a combined surface-enhanced Raman and mechanically controllable break junction method. *J. Am. Chem. Soc.*, 128(46):14748–14749, 2006.

[90] V. Dubois, S. N. Raja, P. Gehring, S. Caneva, H. S. J. van der Zant, F. Niklaus, and G. Stemme. Massively parallel fabrication of crack-defined gold break junctions featuring sub-3 nm gaps for molecular devices. *Nat. Commun.*, 9(1):3433, 2018.

[91] C. A. Martin, J. M. van Ruitenbeek, and H. S. J. van der Zant. Sandwich-type gated mechanical break junctions. *Nanotechnology*, 21(26):265201, 2010.

[92] H. Park, A. K. L. Lim, A. P. Alivisatos, J. Park, and P. L. McEuen. Fabrication of metallic electrodes with nanometer separation by electromigration. *Appl. Phys. Lett.*, 75(2):301–303, 1999.

[93] H. S. J. van der Zant, Y.-V. Kervennic, M. Poot, K. ONeill, Z. de Groot, J. M. Thijssen, H. B. Heersche, N. Stuhr-Hansen, T. Bjørnholm, D. Vanmaekelbergh, et al. Molecular three-terminal devices: fabrication and measurements. *Farad. Discuss.*, 131:347–356, 2006.

[94] E. A. Osorio, M. Ruben, J. S. Seldenthuis, J. M. Lehn, and H. S. J. van der Zant. Conductance Switching and Vibrational Fine Structure of a [2 × 2] Co_4^{II} Gridlike Single Molecule Measured in a Three-Terminal Device. *Small*, 6(2):174–178, 2010.

[95] M. A. Reed. Molecular electronics: Back under control. *Nat. Mater.*, 3(5):286–287, 2004.

[96] H. Song, Y. Kim, Y. H. Jang, H. Jeong, M. A. Reed, and T. Lee. Observation of molecular orbital gating. *Nature*, 462(7276):1039–1043, 2009.

[97] H. S. J. van der Zant, E. A. Osorio, M. Poot, and K. O'Neill. Electromigrated molecular junctions. *Phys. Status Solidi B*, 243(13):3408–3412, 2006.

[98] J. O. Island, A. Holovchenko, M. Koole, P. F. A. Alkemade, M. Menelaou, N. Aliaga-Alcalde, E. Burzurí, and H. S. J. van der Zant. Fabrication of hybrid molecular devices using multi-layer graphene break junctions. *J. Phys.: Condens. Matter*, 26(47):474205, 2014.

[99] F. Prins, A. Barreiro, J. W. Ruitenberg, J. S. Seldenthuis, N. Aliaga-Alcalde, L. M. K. Vandersypen, and H. S. J. van der Zant. Room-temperature gating of molecular junctions using few-layer graphene nanogap electrodes. *Nano Lett.*, 11(11):4607–4611, 2011.

[100] C. S. Lau, J. A. Mol, J. H. Warner, and G. A. D. Briggs. Nanoscale control of graphene electrodes. *Phys. Chem. Chem. Phys.*, 16(38):20398–20401, 2014.

[101] J. A. Mol, C. S. Lau, W. J. M. Lewis, H. Sadeghi, C. Roche, A. Cnossen, J. H. Warner, C. J. Lambert, H. L. Anderson, and G. A. D. Briggs. Graphene-porphyrin single-molecule transistors. *Nanoscale*, 7(31):13181–13185, 2015.

[102] Q. Xu, G. Scuri, C. Mathewson, P. Kim, C. Nuckolls, and D. Bouilly. Single electron transistor with single aromatic ring molecule covalently connected to graphene nanogaps. *Nano Lett.*, 17(9):5335–5341, 2017.

[103] C. Jia, A. Migliore, N. Xin, S. Huang, J. Wang, Q. Yang, S. Wang, H. Chen, D. Wang, B. Feng, et al. Covalently bonded single-molecule junctions with stable and reversible photoswitched conductivity. *Science*, 352(6292):1443–1445, 2016.

[104] K. Ullmann, P. B. Coto, S. Leitherer, A. Molina-Ontoria, N. Martín, M. Thoss, and H. B. Weber. Single-molecule junctions with epitaxial graphene nanoelectrodes. *Nano Lett.*, 15(5):3512–3518, 2015.

[105] X. Guo, J. P. Small, J. E. Klare, Y. Wang, M. S. Purewal, I. W. Tam, B. H. Hong, R. Caldwell, L. Huang, S. O'Brien, et al. Covalently bridging gaps in single-walled carbon nanotubes with conducting molecules. *Science*, 311(5759):356–359, 2006.

[106] D. J. Wold and C. D. Frisbie. Formation of metal-molecule-metal tunnel junctions: microcontacts to alkanethiol monolayers with a conducting AFM tip. *J. Am. Chem. Soc.*, 122(12):2970–2971, 2000.

[107] W. Li, L. Sepunaru, N. Amdursky, S. R. Cohen, I. Pecht, M. Sheves, and D. Cahen. Temperature and force dependence of nanoscale electron transport via the Cu protein azurin. *ACS Nano*, 6(12):10816–10824, 2012.

[108] C. Wagner, N. Fournier, F. S. Tautz, and R. Temirov. Measurement of the binding energies of the organic-metal perylene-teracarboxylic-dianhydride/Au (111) bonds by molecular manipulation using an atomic force microscope. *Phys. Rev. Lett.*, 109(7):076102, 2012.

[109] C. Z. Li, H. X. He, and N. J. Tao. Quantized tunneling current in the metallic nanogaps formed by electrodeposition and etching. *Appl. Phys. Lett.*, 77(24):3995–3997, 2000.

[110] Y. Wu, W. Hong, T. Akiyama, S. Gautsch, V. Kolivoska, T. Wandlowski, and N. F. de Rooij. Batch fabrication of gold–gold nanogaps by e-beam lithography and electrochemical deposition. *Nanotechnology*, 24(23):235302, 2013.

[111] X. L. Li, H. X. He, B. Q. Xu, X. Y. Xiao, L. A. Nagahara, I. Amlani, R. Tsui, and N. J. Tao. Measurement of electron transport properties of molecular junctions fabricated by electrochemical and mechanical methods. *Surf. Sci.*, 573(1):1–10, 2004.

[112] A. P. Bonifas and R. L. McCreery. 'Soft' Au, Pt and Cu contacts for molecular junctions through surface-diffusion-mediated deposition. *Nat. Nanotechnol.*, 5(8):612–617, 2010.

[113] A. P. Bonifas and R. L. McCreery. Assembling molecular electronic junctions one molecule at a time. *Nano Lett.*, 11(11):4725–4729, 2011.

[114] L. Sun, Y. A. Diaz-Fernandez, T. A. Gschneidtner, F. Westerlund, S. Lara-Avila, and K. Moth-Poulsen. Single-molecule electronics: from chemical design to functional devices. *Chem. Soc. Rev.*, 43(21):7378–7411, 2014.

[115] S. Kubatkin, A. Danilov, M. Hjort, J. Cornil, J.-L. Brédas, N. Stuhr-Hansen, P. Hedegård, and T. Bjørnholm. Single-electron transistor of a single organic molecule with access to several redox states. *Nature*, 425(6959):698, 2003.

[116] B. Limburg, J. O. Thomas, G. Holloway, H. Sadeghi, S. Sangtarash, Ian C.-Y. Hou, J. Cremers, A. Narita, K. Mllen, C. J. Lambert, G. A. D. Briggs, J. A. Mol, and H. L. Anderson. Anchor groups for graphene-porphyrin single-molecule transistors. *Adv. Funct. Mater.*, 28(45):1803629, 2018.

[117] E. A. Osorio, K. O'Neill, N. Stuhr-Hansen, O. F. Nielsen, T. Bjørnholm, and H. S. J. van der Zant. Addition energies and vibrational fine structure measured in electromigrated single-molecule junctions based on an oligophenylenevinylene derivative. *Adv. Mater.*, 19(2):281–285, 2007.

[118] A. Danilov, S. Kubatkin, S. Kafanov, P. Hedegård, N. Stuhr-Hansen, K. Moth-Poulsen, and T. Bjørnholm. Electronic transport in single molecule junctions: Control of the molecule-electrode coupling through intramolecular tunneling barriers. *Nano Lett.*, 8(1):1–5, 2008.

[119] K. Kaasbjerg and K. Flensberg. Strong polarization-induced reduction of addition energies in single-molecule nanojunctions. *Nano Lett.*, 8(11):3809–3814, 2008.

[120] Y. Zang, S. Ray, E.-D. Fung, A. Borges, M. H. Garner, M. L. Steigerwald, G. C. Solomon, S. Patil, and L. Venkataraman. Resonant transport in single-diketopyrrolopyrrole junctions. *J. Am. Chem. Soc.*, 140(41):13167–13170, 2018.

[121] M. Galperin, M. A. Ratner, A. Nitzan, and A. Troisi. Nuclear coupling and polarization in molecular transport junctions: beyond tunneling to function. *Science*, 319(5866):1056–1060, 2008.

[122] K. W. Hipps and U. Mazur. Inelastic electron tunneling: an alternative molecular spectroscopy. *J. Phys. Chem.*, 97(30):7803–7814, 1993.

[123] A. Troisi, M. A. Ratner, and A. Nitzan. Vibronic effects in off-resonant molecular wire conduction. *J. Chem. Phys.*, 118(13):6072–6082, 2003.

[124] M. Galperin, M. A. Ratner, and A. Nitzan. Inelastic electron tunneling spectroscopy in molecular junctions: Peaks and dips. *J. Chem. Phys.*, 121(23):11965–11979, 2004.

[125] H. Song, Y. Kim, J. Ku, Y. H. Jang, H. Jeong, and T. Lee. Vibrational spectra of metal-molecule-metal junctions in electromigrated nanogap electrodes by inelastic electron tunneling. *Appl. Phys. Lett.*, 94(10):103110, 2009.

[126] T. Yamamoto, K. Watanabe, and S. Watanabe. Electronic Transport in Fullerene C_{20} Bridge Assisted by Molecular Vibrations. *Phys. Rev. Lett.*, 95:065501, 2005.

[127] R. Härtle, C. Benesch, and M. Thoss. Multimode vibrational effects in single-molecule conductance: A nonequilibrium Green's function approach. *Phys. Rev. B*, 77:205314, 2008.

[128] J. I. Pascual, J. J. Jackiw, Z. Song, P. S. Weiss, H. Conrad, and H.-P. Rust. Adsorbate-substrate vibrational modes of benzene on Ag (110) resolved with scanning tunneling spectroscopy. *Phys. Rev. Lett.*, 86(6):1050, 2001.

[129] W. Wang, T. Lee, I. Kretzschmar, and M. A. Reed. Inelastic electron tunneling spectroscopy of an alkanedithiol self-assembled monolayer. *Nano Lett.*, 4(4):643–646, 2004.

[130] N. Okabayashi, M. Paulsson, and T. Komeda. Inelastic electron tunneling process for alkanethiol self-assembled monolayers. *Prog. Surf. Sci.*, 88(1):1–38, 2013.

[131] C. R. Arroyo, T. Frederiksen, G. Rubio-Bollinger, M. Vélez, A. Arnau, D. Sánchez-Portal, and N. Agraït. Characterization of single-molecule pentanedithiol junctions by inelastic electron tunneling spectroscopy and first-principles calculations. *Phys. Rev. B*, 81:075405, 2010.

[132] Y. Kim, T. J. Hellmuth, M. Burkle, F. Pauly, and E. Scheer. Characteristics of amine-ended and thiol-ended alkane single-molecule junctions revealed by inelastic electron tunneling spectroscopy. *ACS Nano*, 5(5):4104–4111, 2011.

[133] N. Ogawa, G. Mikaelian, and W. Ho. Spatial Variations in Submolecular Vibronic Spectroscopy on a Thin Insulating Film. *Phys. Rev. Lett.*, 98:166103, 2007.

[134] J. Koch and F. von Oppen. Franck-Condon blockade and giant Fano factors in transport through single molecules. *Phys. Rev. Lett.*, 94(20):206804, 2005.

[135] J. Koch, F. von Oppen, and A. V. Andreev. Theory of the Franck-Condon blockade regime. *Phys. Rev. B*, 74(20):205438, 2006.

[136] M. Galperin, M. A. Ratner, and A. Nitzan. Molecular transport junctions: vibrational effects. *J. Phys.: Condens. Matter*, 19(10):103201, 2007.

[137] A. Zazunov, D. Feinberg, and T. Martin. Phonon-mediated negative differential conductance in molecular quantum dots. *Phys. Rev. B*, 73:115405, 2006.

[138] R. Härtle and M. Thoss. Resonant electron transport in single-molecule junctions: Vibrational excitation, rectification, negative differential resistance, and local cooling. *Phys. Rev. B*, 83(11):115414, 2011.

[139] A. N. Pasupathy, J. Park, C. Chang, A. V. Soldatov, S. Lebedkin, R. C. Bialczak, J. E. Grose, L. A. K. Donev, J. P. Sethna, D. C. Ralph, et al. Vibration-assisted electron tunneling in C_{140} transistors. *Nano Lett.*, 5(2):203–207, 2005.

[140] A. Riss, S. Wickenburg, L. Z. Tan, H.-Z. Tsai, Y. Kim, J. Lu, A. J. Bradley, M. M. Ugeda, K. L. Meaker, K. Watanabe, et al. Imaging and tuning molecular levels at the surface of a gated graphene device. *ACS Nano*, 8(6):5395–5401, 2014.

[141] V. Rabache, J. Chaste, P. Petit, M. L. Della Rocca, P. Martin, J.-C. Lacroix, R. L. McCreery, and P. Lafarge. Direct observation of large quantum interference effect in anthraquinone solid-state junctions. *J. Am. Chem. Soc.*, 135(28):10218–10221, 2013.

[142] J. J. Parks, A. R. Champagne, G. R. Hutchison, S. Flores-Torres, H. D. Abruña, and D. C. Ralph. Tuning the Kondo Effect with a Mechanically Controllable Break Junction. *Phys. Rev. Lett.*, 99:026601, 2007.

[143] T. Böhler, A. Edtbauer, and E. Scheer. Conductance of individual C_{60} molecules measured with controllable gold electrodes. *Phys. Rev. B*, 76(12):125432, 2007.

[144] R. Leturcq, C. Stampfer, K. Inderbitzin, L. Durrer, C. Hierold, E. Mariani, M. G. Schultz, F. von Oppen, and K. Ensslin. Franck–Condon blockade in suspended carbon nanotube quantum dots. *Nat. Phys.*, 5(5):327–331, 2009.

[145] L. H. Yu, Z. K. Keane, J. W. Ciszek, L. Cheng, M. P. Stewart, J. M. Tour, and D. Natelson. Inelastic electron tunneling via molecular vibrations in single-molecule transistors. *Phys. Rev. Lett.*, 93(26):266802, 2004.

[146] N. P. de Leon, W. Liang, Q. Gu, and H. Park. Vibrational excitation in single-molecule transistors: deviation from the simple Franck–Condon prediction. *Nano Lett.*, 8(9):2963–2967, 2008.

[147] S. Ballmann, W. Hieringer, D. Secker, Q. Zheng, J. A. Gladysz, A. Görling, and H. B. Weber. Molecular Wires in Single-Molecule Junctions: Charge Transport and Vibrational Excitations. *Chem. Phys. Chem.*, 11(10):2256–2260, 2010.

[148] D. Secker, S. Wagner, S. Ballmann, R. Härtle, M. Thoss, and H. B. Weber. Resonant Vibrations, Peak Broadening, and Noise in Single Molecule Contacts: The Nature of the First Conductance Peak. *Phys. Rev. Lett.*, 106:136807, 2011.

[149] R. Härtle, C. Benesch, and M. Thoss. Vibrational nonequilibrium effects in the conductance of single molecules with multiple electronic states. *Phys. Rev. Lett.*, 102(14):146801, 2009.

[150] B. Dong, X. L. Lei, and N. J. M. Horing. Robust negative differential conductance and enhanced shot noise in transport through a molecular transistor with vibration assistance. *IEEE Sensors Journal*, 8(6):885–890, 2008.

[151] A. Erpenbeck, R. Härtle, M. Bockstedte, and M. Thoss. Vibrationally dependent electron-electron interactions in resonant electron transport through single-molecule junctions. *Phys. Rev. B*, 93:115421, 2016.

[152] M. Esposito and M. Galperin. Transport in molecular states language: Generalized quantum master equation approach. *Phys. Rev. B*, 79:205303, 2009.

[153] J. Koch and F. von Oppen. Effects of charge-dependent vibrational frequencies and anharmonicities in transport through molecules. *Phys. Rev. B*, 72(11):113308, 2005.

[154] M. A. Karimi, S. G. Bahoosh, M. Herz, R. Hayakawa, F. Pauly, and E. Scheer. Shot noise of 1,4-benzenedithiol single-molecule junctions. *Nano Lett.*, 16(3):1803–1807, 2016.

[155] D. Djukic and J. M. Van Ruitenbeek. Shot noise measurements on a single molecule. *Nano Lett.*, 6(4):789–793, 2006.

[156] O. Tal, M. Krieger, B. Leerink, and J. M. van Ruitenbeek. Electron-Vibration Interaction in Single-Molecule Junctions: From Contact to Tunneling Regimes. *Phys. Rev. Lett.*, 100:196804, 2008.

[157] M. Kiguchi, O. Tal, S. Wohlthat, F. Pauly, M. Krieger, D. Djukic, J. C. Cuevas, and J. M. van Ruitenbeek. Highly conductive molecular junctions based on direct binding of benzene to platinum electrodes. *Phys. Rev. Lett.*, 101(4):046801, 2008.

[158] B. K. Agarwalla, J.-H. Jiang, and D. Segal. Full counting statistics of vibrationally assisted electronic conduction: Transport and fluctuations of thermoelectric efficiency. *Phys. Rev. B*, 92:245418, 2015.

[159] M. Galperin, A. Nitzan, and M. A. Ratner. Inelastic tunneling effects on noise properties of molecular junctions. *Phys. Rev. B*, 74(7):075326, 2006.

[160] S. Takei, Y. B. Kim, and A. Mitra. Enhanced Fano factor in a molecular transistor coupled to phonons and Luttinger-liquid leads. *Phys. Rev. B*, 72:075337, 2005.

[161] D. S. Kosov. Waiting time distribution for electron transport in a molecular junction with electron-vibration interaction. *J. Chem. Phys.*, 146(7):074102, 2017.

[162] R. Stones and A. Olaya-Castro. Non-perturbative electron counting statistics. *arXiv preprint arXiv:1705.02320*, 2017.

[163] H. I. Jørgensen, K. Grove-Rasmussen, J. R. Hauptmann, and P. E. Lindelof. Single wall carbon nanotube double quantum dot. *Appl. Phys. Lett.*, 89(23):232113, 2006.

[164] N. Mason, M. J. Biercuk, and C. M. Marcus. Local gate control of a carbon nanotube double quantum dot. *Science*, 303(5658):655–658, 2004.

[165] M. Jung, J. Schindele, S. Nau, M. Weiss, A. Baumgartner, and C. Schönenberger. Ultraclean single, double, and triple carbon nanotube quantum dots with recessed re bottom gates. *Nano Lett.*, 13(9):4522–4526, 2013.

[166] D. P. S. McCutcheon and A. Nazir. Coherent and incoherent dynamics in excitonic energy transfer: Correlated fluctuations and off-resonance effects. *Phys. Rev. B*, 83(16):165101, 2011.

[167] A. Nazir. Correlation-dependent coherent to incoherent transitions in resonant energy transfer dynamics. *Phys. Rev. Lett.*, 103(14):146404, 2009.

[168] F. Fassioli, A. Nazir, and A. Olaya-Castro. Quantum state tuning of energy transfer in a correlated environment. *J. Phys. Chem. Lett.*, 1(14):2139–2143, 2010.

[169] R. Doll, M. Wubs, P. Hänggi, and S. Kohler. Limitation of entanglement due to spatial qubit separation. *EPL*, 76(4):547, 2006.

[170] E. Mariani and F. von Oppen. Electron-vibron coupling in suspended carbon nanotube quantum dots. *Phys. Rev. B*, 80(15):155411, 2009.

[171] S. Sapmaz, P. Jarillo-Herrero, Ya. M. Blanter, C. Dekker, and H. S. J. van der Zant. Tunneling in suspended carbon nanotubes assisted by longitudinal phonons. *Phys. Rev. Lett.*, 96:026801, 2006.

[172] E. M. Gauger, A. Nazir, S. C. Benjamin, T. M. Stace, and B. W. Lovett. Robust adiabatic approach to optical spin entangling in coupled quantum dots. *New J. Phys.*, 10(7):073016, 2008.

[173] D. Malz and A. Nunnenkamp. Current rectification in a double quantum dot through fermionic reservoir engineering. *Phys. Rev. B*, 97(16):165308, 2018.

[174] P. P. Hofer, M. Perarnau-Llobet, L. D. M. Miranda, G. Haack, R. Silva, J. B. Brask, and N. Brunner. Markovian master equations for quantum thermal machines: local versus global approach. *New J. Phys.*, 19(12):123037, 2017.

[175] M. T. Mitchison and M. B. Plenio. Non-additive dissipation in open quantum networks out of equilibrium. *New J. Phys.*, 20(3):033005, 2018.

[176] A. Greenbaum. *Iterative methods for solving linear systems*, volume 17. Siam, 1997.

[177] R Härtle and M Thoss. Resonant electron transport in single-molecule junctions: Vibrational excitation, rectification, negative differential resistance, and local cooling. *Phys. Rev. B*, 83(11):115414, 2011.

[178] B. J. LeRoy, S. G. Lemay, J. Kong, and C. Dekker. Electrical generation and absorption of phonons in carbon nanotubes. *Nature*, 432(7015):371, 2004.

[179] T. Krause, T. Brandes, M. Esposito, and G. Schaller. Thermodynamics of the polaron master equation at finite bias. *J. Chem. Phys.*, 142(13):134106, 2015.

[180] R. Pariser and R. G. Parr. A semi-empirical theory of the electronic spectra and electronic structure of complex unsaturated molecules. II. *J. Chem. Phys.*, 21(5):767–776, 1953.

[181] R. Pariser and R. G. Parr. A Semi-Empirical Theory of the Electronic Spectra and Electronic Structure of Complex Unsaturated Molecules. I. *J. Chem. Phys.*, 21(3):466–471, 1953.

[182] J. A. Pople. Electron interaction in unsaturated hydrocarbons. *Trans. Faraday Soc.*, 49:1375–1385, 1953.

[183] K. Ohno. Some remarks on the Pariser-Parr-Pople method. *Theor. Chim. Acta*, 2(3):219–227, 1964.

[184] W. Barford. *Electronic and optical properties of conjugated polymers*, volume 159. Oxford University Press, 2013.

[185] H. E. Simmons and T. Fukunaga. Spiroconjugation. *J. Am. Chem. Soc.*, 89(20):5208–5215, 1967.

[186] R. Hoffmann, A. Imamura, and G. D. Zeiss. Spirarenes. *J. Am. Chem. Soc.*, 89(20):5215–5220, 1967.

[187] C. Batich, E. Heilbronner, E. Rommel, M. F. Semmelhack, and J. S. Foos. Equivalence of the energy gaps. $\Delta I(1,2)$ and $\Delta E(1,2)$ between corresponding bands in the photoelectron (I) and electronic absorption (E) spectra of spiro[4.4]nonatetraene. Amusing consequence of spiroconjugation. *J. Am. Chem. Soc.*, 96(25):7662–7668, 1974.

[188] R. J. Bursill, C. Castleton, and W. Barford. Optimal parametrisation of the Pariser–Parr–Pople Model for benzene and biphenyl. *Chem. Phys. Lett.*, 294(4):305–313, 1998.

[189] S. Ramasesha, I. D. L. Albert, and B. Sinha. Optical and magnetic properties of the exact PPP states of biphenyl. *Mol. Phys.*, 72(3):537–547, 1991.

[190] A. Hansson and S. Stafström. Intershell conductance in multiwall carbon nanotubes. *Phys. Rev. B*, 67(7):075406, 2003.

[191] M. Hultell and S. Stafström. Impact of ring torsion on the intrachain mobility in conjugated polymers. *Phys. Rev. B*, 75(10):104304, 2007.

[192] C. A. Coulson and G. S. Rushbrooke. Note on the method of molecular orbitals. *Math. Proc. Camb. Phil. Soc.*, 36(2):193–200, 1940.

[193] E. Haselbach, M. Allan, T. Bally, P. Bednarek, A.-C. Sergenton, A. De Meijere, S. Kozhushkov, M. Piacenza, and S. Grimme. Spiro[4.4]nonatetraene and its positive and negative radical ions: Molectronic structure investigations. *Helv. Chim. Acta*, 84(6):1670–1693, 2001.

[194] M. J. Frisch, G. W. Trucks, H. B. Schlegel, G. E. Scuseria, M. A. Robb, J. R. Cheeseman, G. Scalmani, V. Barone, B. Mennucci, G. A. Petersson, et al. Gaussian 09, Revision A. 02. *Inc., Wallingford, CT*, 200, 2009.

[195] A. D. Becke. Density-functional thermochemistry. III. The role of exact exchange. *J. Chem. Phys.*, 98(7):5648–5652, 1993.

[196] Z. G. Soos and S. Ramasesha. Valence-bond theory of linear Hubbard and Pariser-Parr-Pople models. *Phys. Rev. B*, 29(10):5410, 1984.

[197] J. A. Vergés, E. SanFabián, G. Chiappe, and E. Louis. Fit of Pariser-Parr-Pople and Hubbard model Hamiltonians to charge and spin states of polycyclic aromatic hydrocarbons. *Phys. Rev. B*, 81(8):085120, 2010.

[198] Z.-L. Cheng, R. Skouta, H. Vazquez, J. R. Widawsky, S. Schneebeli, W. Chen, M. S. Hybertsen, R. Breslow, and L. Venkataraman. In situ formation of highly conducting covalent Au-C contacts for single-molecule junctions. *Nat. Nanotechnol.*, 6(6):353–357, 2011.

[199] A. K. Mitchell, K. G. L. Pedersen, P. Hedegård, and J. Paaske. Kondo blockade due to quantum interference in single-molecule junctions. *Nat. Commun.*, 8, 2017.

[200] K. G. L. Pedersen, M. Strange, M. Leijnse, P. Hedegård, G. C. Solomon, and J. Paaske. Quantum interference in off-resonant transport through single molecules. *Phys. Rev. B*, 90(12):125413, 2014.

[201] Y. Tsuji, R. Hoffmann, M. Strange, and G. C. Solomon. Close relation between quantum interference in molecular conductance and diradical existence. *Proc. Natl. Acad. Sci. U.S.A.*, 113(4):E413–E419, 2016.

[202] G. Begemann, D. Darau, A. Donarini, and M. Grifoni. Symmetry fingerprints of a benzene single-electron transistor: Interplay between Coulomb interaction and orbital symmetry. *Phys. Rev. B*, 77(20):201406, 2008.

[203] J. P. Bergfield and C. A. Stafford. Thermoelectric signatures of coherent transport in single-molecule heterojunctions. *Nano Lett.*, 9(8):3072–3076, 2009.

[204] D. Darau, G. Begemann, A. Donarini, and M. Grifoni. Interference effects on the transport characteristics of a benzene single-electron transistor. *Phys. Rev. B*, 79(23):235404, 2009.

[205] M. G. Schultz and F. von Oppen. Quantum transport through nanostructures in the singular-coupling limit. *Phys. Rev. B*, 80(3):033302, 2009.

[206] M. H. Hettler, W. Wenzel, M. R. Wegewijs, and H. Schoeller. Current collapse in tunneling transport through benzene. *Phys. Rev. Lett.*, 90(7):076805, 2003.

[207] D. Rai, O. Hod, and A. Nitzan. Magnetic field control of the current through molecular ring junctions. *J. Phys. Chem. Lett.*, 2(17):2118–2124, 2011.

[208] B. Xu and Y. Dubi. Negative differential conductance in molecular junctions: an overview of experiment and theory. *J. Phys.: Condens. Matter*, 27(26):263202, 2015.

[209] A. Donarini, G. Begemann, and M. Grifoni. Interference effects in the Coulomb blockade regime: Current blocking and spin preparation in symmetric nanojunctions. *Phys. Rev. B*, 82(12):125451, 2010.

[210] I. B. Bersuker. *The Jahn-Teller Effect*. Cambridge University Press, 2006.

[211] I. Bersuker and V. Polinger. *Vibronic interactions in molecules and crystals*, volume 49. Springer Science & Business Media, 2012.

[212] M. G. Schultz. Quantum transport through single-molecule junctions with orbital degeneracies. *Phys. Rev. B*, 82(15):155408, 2010.

[213] M. J. Frisch, G. W. Trucks, H. B. Schlegel, G. E. Scuseria, M. A. Robb, J. R. Cheeseman, G. Scalmani, V. Barone, G. A. Petersson, H. Nakatsuji, et al. Gaussian 16 Revision A. 03. 2016; Gaussian Inc. *Wallingford CT*, 2016.

[214] N. Treitel, R. Shenhar, I. Aprahamian, T. Sheradsky, and M. Rabinovitz. Calculations of PAH anions: When are diffuse functions necessary? *Phys. Chem. Chem. Phys.*, 6(6):1113–1121, 2004.

[215] S. Fatayer, B. Schuler, W. Steurer, I. Scivetti, J. Repp, L. Gross, M. Persson, and G. Meyer. Reorganization energy upon charging a single molecule on an insulator measured by atomic force microscopy. *Nat. Nanotechnol.*, 13:376–380, 2018.

[216] N. J. Kay, S. J. Higgins, J. O. Jeppesen, E. Leary, J. Lycoops, J. Ulstrup, and R. J. Nichols. Single-molecule electrochemical gating in ionic liquids. *J. Am. Chem. Soc.*, 134(40):16817–16826, 2012.

[217] J. Zhang, A. M. Kuznetsov, I. G. Medvedev, Q. Chi, T. Albrecht, P. S. Jensen, and J. Ulstrup. Single-molecule electron transfer in electrochemical environments. *Chem. Rev.*, 108(7):2737–2791, 2008.

[218] B. Choi, B. Capozzi, S. Ahn, A. Turkiewicz, G. Lovat, C. Nuckolls, M. L. Steigerwald, L. Venkataraman, and X. Roy. Solvent-dependent conductance decay constants in single cluster junctions. *Chem. Sci.*, 7(4):2701–2705, 2016.

[219] V. Fatemi, M. Kamenetska, J. B. Neaton, and L. Venkataraman. Environmental control of single-molecule junction transport. *Nano Lett.*, 11(5):1988–1992, 2011.

[220] D. C. Milan, O. A. Al-Owaedi, M.-C. Oerthel, S. Marqués-González, R. J. Brooke, M. R. Bryce, P. Cea, J. Ferrer, S. J. Higgins, C. J. Lambert, et al. Solvent dependence of the single molecule conductance of oligoyne-based molecular wires. *J. Phys. Chem. C*, 120(29):15666–15674, 2015.

[221] M. B. Plenio and S. F. Huelga. Dephasing-assisted transport: quantum networks and biomolecules. *New J. Phys.*, 10(11):113019, 2008.

[222] I. Kassal and A. Aspuru-Guzik. Environment-assisted quantum transport in ordered systems. *New J. Phys.*, 14(5):053041, 2012.

[223] D. Taherinia, C. E. Smith, S. Ghosh, S. O. Odoh, L. Balhorn, L. Gagliardi, C. J. Cramer, and C. D. Frisbie. Charge Transport in 4 nm Molecular Wires with Interrupted Conjugation: Combined Experimental and Computational Evidence for Thermally Assisted Polaron Tunneling. *ACS Nano*, 10(4):4372–4383, 2016.

[224] M. Koole, J. C. Hummelen, and H. S. J. van der Zant. Spin excitations in an all-organic double quantum dot molecule. *Phys. Rev. B*, 94(16):165414, 2016.

[225] H. Valkenier, C. M. Guédon, T. Markussen, K. S. Thygesen, S. J. van der Molen, and J. C. Hummelen. Cross-conjugation and quantum interference: a general correlation? *Phys. Chem. Chem. Phys.*, 16(2):653–662, 2014.

[226] P. Zedler, G. Schaller, G. Kiesslich, C. Emary, and T. Brandes. Weak-coupling approximations in non-markovian transport. *Phys. Rev. B*, 80(4):045309, 2009.

[227] C. Flindt, T. Novotnỳ, A. Braggio, M. Sassetti, and A.-P. Jauho. Counting statistics of non-markovian quantum stochastic processes. *Phys. Rev. Lett.*, 100(15):150601, 2008.

[228] L. D. Contreras-Pulido, M. Bruderer, S. F. Huelga, and M. B. Plenio. Dephasing-assisted transport in linear triple quantum dots. *New J. Phys.*, 16(11):113061, 2014.

[229] P. Rebentrost, M. Mohseni, I. Kassal, S. Lloyd, and A. Aspuru-Guzik. Environment-assisted quantum transport. *New J. Phys.*, 11(3):033003, 2009.

[230] A. Nazir and D. P. S. McCutcheon. Modelling exciton–phonon interactions in optically driven quantum dots. *J. Phys.: Condens. Matter*, 28(10):103002, 2016.

[231] A. Nazir. Photon statistics from a resonantly driven quantum dot. *Phys. Rev. B*, 78(15):153309, 2008.

[232] A. G. Redfield. On the theory of relaxation processes. *IBM J. Res. Dev.*, 1(1):19–31, 1957.

[233] D. P. S. McCutcheon, N. S. Dattani, E. M. Gauger, B. W. Lovett, and A. Nazir. A general approach to quantum dynamics using a variational master equation: Application to phonon-damped rabi rotations in quantum dots. *Phys. Rev. B*, 84(8):081305, 2011.

[234] S. Jang, Y.-C. Cheng, D. R. Reichman, and J. D. Eaves. Theory of coherent resonance energy transfer. *J. Chem. Phys.*, 129(10):101104, 2008.

[235] M. L. Perrin, E. Burzurí, and H. S. J. van der Zant. Single-molecule transistors. *Chem. Soc. Rev.*, 44(4):902–919, 2015.

[236] S. A. Gurvitz and Y. S. Prager. Microscopic derivation of rate equations for quantum transport. *Phys. Rev. B*, 53(23):15932, 1996.

[237] T. H. Stoof and Y. V. Nazarov. Time-dependent resonant tunneling via two discrete states. *Phys. Rev. B*, 53(3):1050, 1996.

[238] G. Kießlich, E. Schöll, T. Brandes, F. Hohls, and R. J. Haug. Noise enhancement due to quantum coherence in coupled quantum dots. *Phys. Rev. Lett.*, 99(20):206602, 2007.

[239] B. Elattari and S. A. Gurvitz. Shot noise in coupled dots and the fractional charges. *Phys. Lett. A*, 292(4):289–294, 2002.

[240] M. Mohseni, P. Rebentrost, S. Lloyd, and A. Aspuru-Guzik. Environment-assisted quantum walks in photosynthetic energy transfer. *J. Chem. Phys.*, 129(17):174106, 2008.

[241] A. W. Chin, A. Datta, F. Caruso, S. F. Huelga, and M. B. Plenio. Noise-assisted energy transfer in quantum networks and light-harvesting complexes. *New J. Phys.*, 12(6):065002, 2010.

[242] F. Caruso. Universally optimal noisy quantum walks on complex networks. *New J. Phys.*, 16(5):055015, 2014.

[243] S. Ballmann, R. Härtle, P. B. Coto, M. Elbing, M. Mayor, M. R. Bryce, M. Thoss, and H. B. Weber. Experimental evidence for quantum interference and vibrationally induced decoherence in single-molecule junctions. *Phys. Rev. Lett.*, 109(5):056801, 2012.

[244] R. Härtle and M. Thoss. Vibrational instabilities in resonant electron transport through single-molecule junctions. *Phys. Rev. B*, 83(12):125419, 2011.

[245] L. I. Glazman and R. I. Shekhter. Inelastic resonant tunneling of electrons through a potential barrier. *Sov. Phys. JETP*, 67:163, 1988.

[246] N. S. Wingreen, K. W. Jacobsen, and J. W. Wilkins. Inelastic scattering in resonant tunneling. *Phys. Rev. B*, 40(17):11834, 1989.

[247] A.-P. Jauho, N. S. Wingreen, and Y. Meir. Time-dependent transport in interacting and noninteracting resonant-tunneling systems. *Phys. Rev. B*, 50(8):5528, 1994.

[248] K. Flensberg. Tunneling broadening of vibrational sidebands in molecular transistors. *Phys. Rev. B*, 68(20):205323, 2003.

[249] H. Wang, I. Pshenichnyuk, R. Härtle, and M. Thoss. Numerically exact, time-dependent treatment of vibrationally coupled electron transport in single-molecule junctions. *J. Chem. Phys.*, 135(24):244506, 2011.

[250] C. Schinabeck, A. Erpenbeck, R. Härtle, and M. Thoss. Hierarchical quantum master equation approach to electronic-vibrational coupling in nonequilibrium transport through nanosystems. *Phys. Rev. B*, 94(20):201407, 2016.

[251] W. Dou, C. Schinabeck, M. Thoss, and J. E. Subotnik. A broadened classical master equation approach for treating electron-nuclear coupling in non-equilibrium transport. *J. Chem. Phys.*, 148(10):102317, 2018.

[252] M. Galperin, A. Nitzan, and M. A. Ratner. Inelastic effects in molecular junction transport: scattering and self-consistent calculations for the seebeck coefficient. *Mol. Phys.*, 106(2-4):397–404, 2008.

[253] A. Mitra, I. Aleiner, and A. J. Millis. Phonon effects in molecular transistors: Quantal and classical treatment. *Phys. Rev. B*, 69:245302, 2004.

[254] Y.J. Yan. Quantum Fokker-Planck theory in a non-Gaussian-Markovian medium. *Phys. Rev. A*, 58(4):2721, 1998.

[255] M. Esposito and M. Galperin. Self-Consistent Quantum Master Equation Approach to Molecular Transport. *J. Phys. Chem. C*, 114(48):20362–20369, 2010.

[256] J. Jin, J. Li, Y. Liu, X.-Q. Li, and Y.J. Yan. Improved master equation approach to quantum transport: From Born to self-consistent Born approximation. *J. Chem. Phys.*, 140(24):244111, 2014.

[257] M. Leijnse and M. R. Wegewijs. Kinetic equations for transport through single-molecule transistors. *Phys. Rev. B*, 78(23):235424, 2008.

[258] N. A. Zimbovskaya. *Transport properties of molecular junctions*, volume 254. Springer, 2013.

[259] J. S. Seldenthuis, H. S. J. van der Zant, M. A. Ratner, and J. M. Thijssen. Vibrational excitations in weakly coupled single-molecule junctions: A computational analysis. *ACS Nano*, 2(7):1445–1451, 2008.

[260] V. Barone, J. Bloino, M. Biczysko, and F. Santoro. Fully integrated approach to compute vibrationally resolved optical spectra: from small molecules to macrosystems. *J. Chem. Theory Comput.*, 5(3):540–554, 2009.

[261] F. Duschinsky. The importance of the electron spectrum in multi-atomic molecules. Concerning the Franck-Condon principle. *Acta Physicochim. URSS*, 7:551–566, 1937.

[262] J. Roden, W. T. Strunz, K. B. Whaley, and A. Eisfeld. Accounting for intramolecular vibrational modes in open quantum system description of molecular systems. *J. Chem. Phys.*, 137(20):204110, 2012.

[263] V. May and O. Kühn. *Charge and energy transfer dynamics in molecular systems*. John Wiley & Sons, 2008.

[264] R. A. Marcus and N. Sutin. Electron transfers in chemistry and biology. *Biochimi. Biophys. Acta*, 811(3):265–322, 1985.

[265] R. A Marcus. On the theory of oxidation-reduction reactions involving electron transfer. I. *J. Chem. Phys.*, 24(5):966–978, 1956.

[266] C. E. D. Chidsey. Free energy and temperature dependence of electron transfer at the metal-electrolyte interface. *Science*, 251(4996):919–922, 1991.

[267] Y. Zeng, R. B. Smith, P. Bai, and M. Z. Bazant. Simple formula for Marcus–Hush–Chidsey kinetics. *J. Electroanal. Chem.*, 735:77–83, 2014.

[268] H. O. Finklea, K. Yoon, E. Chamberlain, J. Allen, and R. Haddox. Effect of the metal on electron transfer across self-assembled monolayers. *J. Phys. Chem. B*, 105(15):3088–3092, 2001.

[269] M. C. Henstridge, E. Laborda, N. V. Rees, and R. G. Compton. Marcus–Hush–Chidsey theory of electron transfer applied to voltammetry: A review. *Electrochim. Acta*, 84:12–20, 2012.

[270] A. Migliore and A. Nitzan. Irreversibility and hysteresis in redox molecular conduction junctions. *J. Am. Chem. Soc.*, 135(25):9420–9432, 2013.

[271] A. Migliore, P. Schiff, and A. Nitzan. On the relationship between molecular state and single electron pictures in simple electrochemical junctions. *Phys. Chem. Chem. Phys.*, 14(40):13746–13753, 2012.

[272] A. M. Kuznetsov and I. G. Medvedev. Coulomb repulsion effect on the tunnel current through the redox molecule in the weak tunneling limit. *Phys. Rev. B*, 78(15):153403, 2008.

[273] A. M. Kuznetsov, I. G. Medvedev, and J. Ulstrup. Coulomb repulsion effect in two-electron nonadiabatic tunneling through a one-level redox molecule. *J. Chem. Phys.*, 131(16):164703, 2009.

[274] L. Yuan, L. Wang, A. R. Garrigues, L. Jiang, H. V. Annadata, M. A. Antonana, E. Barco, and C. A. Nijhuis. Transition from direct to inverted charge transport Marcus regions in molecular junctions via molecular orbital gating. *Nat. Nanotechnol.*, 13:322–329, 2018.

[275] P. R. Bueno, T. A. Benites, and J. J. Davis. The mesoscopic electrochemistry of molecular junctions. *Sci. Rep.*, 6:18400, 2016.

[276] A. Migliore and A. Nitzan. Nonlinear charge transport in redox molecular junctions: A Marcus perspective. *ACS Nano*, 5(8):6669–6685, 2011.

[277] H. Sadeghi, S. Sangtarash, and C. J. Lambert. Robust molecular anchoring to graphene electrodes. *Nano letters*, 17(8):4611–4618, 2017.

[278] J. G. Simmons. Generalized formula for the electric tunnel effect between similar electrodes separated by a thin insulating film. *J. Appl. Phys.*, 34(6):1793–1803, 1963.

[279] Z.-F. Liu and J. B. Neaton. Voltage dependence of molecule–electrode coupling in biased molecular junctions. *J. Phys. Chem. C*, 121(39):21136–21144, 2017.

[280] J. O. Thomas. Private communication.

[281] X. Chen, M. Roemer, L. Yuan, W. Du, D. Thompson, E. del Barco, and C. A. Nijhuis. Molecular diodes with rectification ratios exceeding 10^5 driven by electrostatic interactions. *Nat. Nanotechnol.*, 12(8):797, 2017.

[282] P. Reddy, S.-Y. Jang, R. A. Segalman, and A. Majumdar. Thermoelectricity in molecular junctions. *Science*, 315(5818):1568–1571, 2007.

[283] L. Cui, R. Miao, C. Jiang, E. Meyhofer, and P. Reddy. Perspective: Thermal and thermoelectric transport in molecular junctions. *J. Chem. Phys.*, 146(9):092201, 2017.

[284] Y. Kim, W. Jeong, K. Kim, W. Lee, and P. Reddy. Electrostatic control of thermoelectricity in molecular junctions. *Nat. Nanotechnol.*, 9(11):881, 2014.

[285] P. Gehring, A. Harzheim, J. Spiece, Y. Sheng, G. Rogers, C. Evangeli, A. Mishra, B. J. Robinson, K. Porfyrakis, J. H. Warner, et al. Field-effect control of graphene–fullerene thermoelectric nanodevices. *Nano Lett.*, 17(11):7055–7061, 2017.

[286] R. S. Mulliken. Formulas and numerical tables for overlap integrals. *J. Chem. Phys.*, 46(12):675–713, 1949.

[287] R. S. Mulliken, C. A. Rieke, D. Orloff, and H. Orloff. Formulas and numerical tables for overlap integrals. *J. Chem. Phys.*, 17(12):1248–1267, 1949.

[288] R. J. Glauber. Coherent and incoherent states of the radiation field. *Phys. Rev.*, 131(6):2766, 1963.